

Steel corrosion and actinide sorption by iron corrosion products under saline conditions.

Zur Erlangung des akademischen Grades einer
DOKTORIN DER NATURWISSENSCHAFTEN
(Dr. rer. nat.)

von der KIT-Fakultät für Chemie und Biowissenschaften
des Karlsruher Instituts für Technologie (KIT)
genehmigte

DISSERTATION

von

Nikoleta Morelová

aus

Bratislava, Slowakei

Dekan: Prof. Dr. Manfred Wilhelm

Referent: Prof. Dr. Horst Geckeis

Korreferent: Prof. Dr. Thorsten Schäfer

Tag der mündlichen Prüfung: 20.07.2020

Declaration of Originality

Ich versichere hiermit die vorliegende Arbeit selbstständig verfasst zu haben und keine anderen Quellen oder Hilfsmittel verwendet zu haben als die hier angegebenen. Außerdem versichere ich, dass alle Stellen der Arbeit, die aus anderen Quellen wörtlich oder sinngemäß übernommen wurden, als solche kenntlich gemacht worden sind und die schriftliche Version der Arbeit mit der digitalen übereinstimmt. Die Arbeit wurde in gleicher oder ähnlicher Form noch bei keiner anderen Prüfungsbehörde vorgelegt. Die Satzung des Karlsruher Instituts für Technologie zur Sicherung guter wissenschaftlicher Praxis wurde in der jeweils gültigen Fassung beachtet.

Acknowledgments

This PhD work was performed at Institute for Nuclear Waste Disposal (INE) of the Karlsruhe Institute of Technology (KIT). I would like to express my gratitude to Prof. Horst Geckeis for giving me the opportunity to perform my PhD at his institute and for offering his supervision after I have unexpectedly changed faculty. I have gathered a lot of valuable scientific experience and was given a chance to contribute to high-level scientific research.

I would also like to thank Dr. Marcus Altmaier, head of the Radiochemistry Division at INE, which I was part of. I am grateful for his positive attitude, guidance and many fruitful scientific discussions.

I especially would like to express my gratitude to my direct supervisor, Dr. Nicolas Finck for always finding time for my questions, ideas and discussions, and for his endless support when I was doubting myself. I feel very lucky and honoured to be supervised by such great scientist and kind person.

I am also delighted to thank Dr. Johannes Lützenkirchen for his guidance, lot of dedicated time and sharing his knowledge on surface complexation modelling.

I would like to thank my colleagues, Dr. Dieter Schild for SEM, XPS measurements, Ms. Eva Soballa for SEM measurements, Mr. Frank Geyer for ICP-MS measurements, Ms. Stephanie Kraft for AFM and ICP-OES measurements, Ms. Tanja Kissely for BET measurements, Ms. Elke Bohnert for MS measurements and KIT-INE beamline scientists Dr. Jorg Rothe and Kathy Dardenne for XAS measurements at INE beamline for actinide research.

I would like to acknowledge the Soleil synchrotron and thank DIFFABS beamline scientist Solenn Réguer for assistance with XAS, XRD and XRF measurements and help with XRD data evaluation. I would like to thank Dr. Michel Schlegel for his assistance with steel samples preparation for synchrotron measurements and his guidance in corrosion science.

I am very grateful to the Radioprotection group at INE, especially Mr. Gerhard Christill for helping me with samples transfers, many lovely chats and his endless optimism.

I would also like to thank the Workshop group, especially Mr. Volker Krepper for always managing to fulfil my demands for equipment construction and endless samples cutting.

I would like to thank the members of my Secondary Phases group, Tim and Pelin for their support, knowledge sharing and optimism. I would like to thank my student Eleanor, who has helped me with sorption experiments during her Internship stay.

I am very grateful to my girlfriends, Alexandra, Emi and Sohae for their patience and never ending support whenever I needed it.

A huge thank you goes to my dear parents, Milan and Nad'a, and my lovely sister Natália for their endless support and understanding during stressful periods.

The biggest thank you goes to my amazing husband Sylvain for his limitless love and patience. He never stopped taking care of me, supported me and trusted in me when times were difficult, which kept me going.

This work has been supported within the framework of KORSO project, funded by the German Federal Ministry of Economic Affairs and Energy (BMWi) under contract no. 02 E 11496 B.

Abstract

In deep geological repositories for nuclear waste disposal, the canister of the spent fuel or vitrified waste provides temporarily a barrier against radionuclide migration from the repository near-field. Some countries consider salt rock as potential host rock for a nuclear waste disposal repository, among those Germany and the US. In case of unlikely but possible groundwater intrusion, the conditions in this repository type are expected to evolve into reducing and mildly alkaline with groundwater containing high salt content. Corrosion rates determine the integrity of the container. In turn, secondary corrosion phases form, which may contribute to the retention of radionuclides. The role of such secondary corrosion phases is widely unexplored.

The first part of this PhD thesis addresses **the corrosion behaviour of the two different materials used for spent fuel canister and vitrified waste canister under conditions relevant for the repository in salt rock, with a focus laid on the examination of corrosion rates and corrosion mechanisms.**

The stainless steel 309S (Cr-Ni steel) used to construct coquilles containing vitrified waste and the spheroidal graphite iron GGG 40.3 (SGI), one constituent of the POLLUX container for heat generating high-level radioactive waste in Germany, were corroded under anoxic conditions in dilute to concentrated NaCl and MgCl₂ brines in the presence and absence of sulfate at room and at elevated temperature (90 °C) for various exposure times.

The corrosion rate was estimated for these systems, allowing better predictions of the integrity of the canister under repository conditions. The corrosion rates for the SGI in 5 M NaCl brine were found 1.22±0.05 µm/a at 90 °C and 1.11±0.05 µm/a at room temperature, considering 42 weeks and 49 weeks exposure time, respectively. For the 5 M NaCl brine in the presence of accessory components (e.g. K⁺, Ca²⁺, SO₄²⁻) representing realistic brine composition, the corrosion rates were 9.6±1.0 µm/a at 90 °C and 0.79±0.05 µm/a at room temperature considering 26 weeks exposure time. In the dilute brines at 90 °C (0.1 M NaCl and 0.033 M MgCl₂), the corrosion rate was found 10.0±1.0 µm/a for both brine types. The corrosion rates for the SGI in 3.4 M MgCl₂ based brines were substantially higher, 16.9±1.5 µm/a after 42 weeks and 26.3±1.5 µm/a after 26 weeks at 90 °C in the absence and presence of sulfate respectively. For the room temperature, the corrosion rate in the 3.4 M MgCl₂ brine without sulfate presence was found similar to NaCl brine, 1.22±0.05 µm/a after 49 weeks. For the same system with the sulfate presence, the

corrosion rate was found $3.65 \pm 0.05 \mu\text{m/a}$ after 26 weeks. For the systems, in which the corrosion rate evolution with time was followed, the corrosion rate has decreased with increasing time due to precipitates passivating the steel and hindering iron oxidation. The observed corrosion rates can be clearly related to the measured pH_M values, with higher rates corresponding to lower pH_M . Furthermore, the MgCl_2 based concentrated brines at elevated temperature showed significantly higher corrosion rates compared to NaCl concentrated brines.

The corrosion rates obtained for the Cr-Ni steel are very low, $<0.1 \mu\text{m/a}$ for almost all systems. Two systems run at 90°C , showed slightly higher corrosion rates of $0.49 \pm 0.05 \mu\text{m/a}$ for the 5 M NaCl system with sulfate and $0.44 \pm 0.05 \mu\text{m/a}$ for 3.4 M MgCl_2 system with sulfate, respectively. For this steel type, no considerable effect of brine or temperature on corrosion rate has been observed.

The solid phase characterization allowed identifying the nature of the formed corrosion products, while the pH , E_h evolution and analysis of metal ions in the aqueous phase allowed setting up a preliminary thermodynamic model, which could predict the long-term stability of corrosion products and thus their relevance as potential radionuclide sorbents in the context of waste disposal. A corrosion mechanism was subsequently derived for the two steel types in various brines. A part of this study was performed at the synchrotron light source SOLEIL (Saint-Aubin, France), allowing the application of spectroscopic techniques with high spatial resolution (μXRF , μXAS , μXRD) for detailed characterisation of the corrosion front.

For SGI, the presence of the corrosion product magnetite was verified in dilute to concentrated NaCl brines at elevated under mildly alkaline (pH_M 9.0) and reducing conditions (E_h of -210 mV). The thermodynamic model suggests stability of this phase under strongly reducing conditions ($E_h \sim -400 \text{ mV}$), thus its formation hints at locally different environments and the role of kinetic effects on solid phase formation. Other corrosion phases were identified, such as silicate phase cronstedtite, co-present with magnetite in dilute NaCl and MgCl_2 systems to concentrated NaCl systems in the absence and presence of sulfate at elevated temperature. Additionally, iron(II) hydroxychloride was found at the bulk steel/corrosion layer interface by the techniques with high spatial resolution for concentrated NaCl brine at elevated temperature. This phase, along with cronstedtite, is not relevant as potential radionuclide sorbent in the NaCl systems due to its lower stability compared to magnetite. The presence of green rust chloride was also established in concentrated NaCl brine at room temperature for this steel type as an intermediate iron corrosion product, which likely transforms into magnetite.

Similarly, the presence of iron(II) hydroxychloride was established in the concentrated MgCl_2 brine at room and elevated temperature in the absence of sulfate and at elevated temperature in the presence of sulfate in the pH_M range of 6.6-8.6 and reducing conditions with E_h of -110 to -300 mV as a dominant corrosion product. The stability of this phase has been proposed in the thermodynamic model under the experimental conditions, provided sufficient iron oxidation, highlighting its possible relevance under very high ionic strength conditions.

For the Cr-Ni steel, the precipitated films were very thin, but hint at the presence of trevorite (nickel iron oxide) and chromite (iron chromium oxide) as a part of the passive layer formed on the surface in dilute and concentrated NaCl brines at elevated temperature. At room temperature for all brines and at elevated temperature in the dilute to concentrated MgCl_2 brines, presence of chromium oxide and chromium hydroxide has been confirmed by techniques applied to the analysis of the surface and crosscut. Upon penetration of the passive film, the local Cl^- accumulation at the metal/oxide interface favours the formation of green rust chloride. The thermodynamic model suggests trevorite, chromite and chromium oxide as the relevant long-term stable phases in NaCl solutions under corresponding experimental conditions of pH_M of 5.6-7.7 and E_h values in the range of -80 mV to +210 mV. The thermodynamic model for MgCl_2 brine was not developed but it is assumed that chromite and trevorite will also contribute to the passive film once conditions in the solution reach the stability region of these compounds, which is shifted to higher pH_M due to high I .

Spent nuclear fuel contains long-lived americium and plutonium, contributing significantly to the long-lived part of the alpha radiotoxic actinide content. Upon canister failure, they can be potentially released in their trivalent oxidation state, prevalent under very reducing conditions. The behaviour of trivalent americium and europium as a chemical actinide analogue is exemplarily investigated here. Adequate understanding of radionuclide migration behaviour is essential for the safety case of nuclear waste repositories in salt rock. The second part of this thesis is devoted to the trivalent radionuclide **uptake by relevant corrosion products, identified in the corrosion part, and the examination of underlying mechanisms under saline conditions.**

Synthesis and thorough characterization of selected compounds (magnetite, iron(II) hydroxychloride, trevorite, chromium oxide and green rust chloride) were performed, followed by batch experiments with quantitative analysis of europium sorption onto these phases in dilute to concentrated NaCl brines for trevorite, chromium oxide and green rust chloride and additionally in dilute to concentrated MgCl_2 brines

for iron(II) hydroxychloride and magnetite. Advanced spectroscopic technique (XAS) provided insight into structures of sorbed trivalent americium and showed the absence of structural incorporation and only surface complexation contribution to the uptake by magnetite in concentrated NaCl brines. The large difference in ionic strength between the dilute and concentrated NaCl brines did not significantly affect the europium uptake by magnetite, trevorite, chromium oxide and green rust chloride, while europium uptake by iron hydroxychloride was strongly affected in concentrated $MgCl_2$ brine. Experimental findings indicate that the investigated solid phases play an important role in the retention of trivalent actinides and lanthanides.

A charge distribution (multi-site) surface complexation model was developed for trevorite, chromium oxide and magnetite, using the information on the solid phase from acid/base titrations, experimental europium uptake data and in the case of magnetite americium surface speciation information from XAS, to obtain the complexation constants at infinite dilution.

As a conclusion, slow corrosion of the canister under specific water access scenarios will lead to a loss of container integrity only after a long contact time. New secondary corrosion phases are generated, where the nature of these phases depend on steel type and geochemical conditions. Those corrosion phases may act as sorbents for radionuclides. In this work, strong retention of trivalent radionuclides (actinides, lanthanides) was observed for many corrosion phases, highlighting that even though corrosion is an undesirable process, it has a beneficial effect on the retention of the radionuclides.

The mechanistic and quantitative information achieved for the sorption processes of trivalent radionuclides onto long-term stable corrosion phases under repository conditions for salt rock represent a first step towards a more comprehensive understanding of the relevant processes ultimately aiding the long-term safety performance assessment in nuclear waste repositories.

Table of Contents

Acknowledgments	i
Abstract	iii
1 Introduction	1
1.1 Background of the work & motivation.....	1
1.2 Aim of present work.....	3
1.3 State of the art.....	5
1.3.1 Basic corrosion chemistry	5
1.3.2 Corrosion of steels under saline anoxic conditions	8
1.3.2.1 Clay.....	9
1.3.2.2 Crystalline rock	10
1.3.2.3 Salt rock.....	12
1.3.2.4 Irradiation	15
1.3.3 Sorption processes	18
1.3.4 Sorption of radionuclides and metal ions onto minerals	19
1.3.5 Modelling	24
1.3.5.1 Solubility	26
1.3.5.2 Activity models and databases	27
SIT (Specific Interaction Theory) approach.....	27
Pitzer approach	28
Databases.....	30
1.3.5.3 Surface complexation modelling	32
2 Experimental.....	35
2.1 Materials and chemicals	35
2.1.1 Chemicals	35
2.1.2 Steels.....	35
2.1.3 Mineral phases.....	36
2.1.4 Europium / Americium.....	37
2.2 Analytical methods.....	37
2.2.1 pH measurements	37

2.2.1.1	General definition & Measurements in saline solutions	37
2.2.1.2	pH measurements and corrections in this work	39
2.2.2	Eh measurements	41
2.2.3	Determination of gas phase composition & dissolved metals concentration in solutions	42
2.2.4	Corrosion phase/ Solid phase characterization	43
2.3	Iron granules corrosion experiments	45
2.4	Autoclave corrosion experiments	45
2.5	Sorption of trivalent actinides onto secondary phases detected in corrosion experiments	49
2.5.1	Solid phase titrations	49
2.5.2	Europium uptake	52
2.6	Measurements at synchrotron light sources	53
2.6.1	KIT Synchrotron Light Source, INE-beamline	53
2.6.1.1	Sample preparation	53
2.6.1.2	EXAFS measurements	54
2.6.1.3	Data evaluation	54
2.6.2	SOLEIL, DIFFABS-beamline	54
2.6.2.1	Sample preparation	55
2.6.2.2	μ XRF, μ XANES and μ XRD measurements	56
2.6.2.3	Data evaluation	57
3	Corrosion Studies	59
3.1	Spheroidal graphite iron corrosion in dilute to concentrated NaCl and MgCl ₂ solutions	59
3.1.1	Initial characterization	59
3.1.2	Dissolved metals evolution	60
3.1.3	pH / Eh evolution	62
3.1.4	Corrosion rate	63
3.1.5	Secondary phase characterization and evolution	65
3.1.6	Corrosion mechanism	87
3.2	Cr-Ni steel corrosion in dilute to concentrated NaCl and MgCl ₂ solutions	95
3.2.1	Initial characterization	95
3.2.2	Dissolved metals evolution	96
3.2.3	pH / Eh evolution	98
3.2.4	Corrosion rate	100

3.2.5	Secondary phase characterization and evolution	101
3.2.6	Corrosion mechanism	110
3.3	Corrosion under flowing conditions (in collaboration with SNL).....	115
4	Sorption studies	117
4.1	Solubility and speciation of europium and americium in dilute to concentrated NaCl and MgCl ₂ solutions.....	119
4.1.1	Solubility	119
4.1.2	Speciation	121
4.2	Uptake of europium/americium by Fe (Ni, Cr) minerals	122
4.2.1	Magnetite (Fe ₃ O ₄).....	122
4.2.2	Iron hydroxychloride (Fe ₂ (OH) ₃ Cl).....	139
4.2.3	Green rust chloride (Fe ₄ (OH) ₈ Cl)· nH ₂ O (GR-Cl)	145
4.2.4	Trevorite (NiFe ₂ O ₄)	148
4.2.5	Chromium oxide (Cr ₂ O ₃).....	156
	Conclusions and Outlook	165
	References	171
	Annex	193

1 Introduction

1.1 Background of the work & motivation

In today's civilization, all human activities are somehow associated with consuming naturally occurring resources and thus producing waste materials. The waste produced in the production of electricity, whichever fuel is used, must be responsibly managed in a way to minimize the impact on environment and effects on human health. In case of applying nuclear energy, reduction of waste volumes, fuel recycling in some countries and finally residual waste containment technologies and disposal strategies have been developed quite early. Politics and nuclear industry has been aware of its long-term responsibility since the early days and have always pursued a careful management of the spent fuel and radioactive waste produced by about 450 reactors providing about 10 % of world's electricity [WNA, 2019_a]. Radioactive waste originates as well from other industries and processes using radioactive materials such as medical applications, agriculture, non-destructive testing, nuclear research or decommissioning of nuclear weapons. Radioactive waste types generated by energy production consist largely of actinides, fission and activation products partly with long half-lives and pose a radiological risk to human health and the environment.

The safe disposal of the long-lived radioactive waste for extended timescale is one of the crucial elements in the application of nuclear energy as well as its public acceptance. The development of robust disposal concepts, its safety demonstration and throughout understanding of the behaviour of various engineered and natural barriers is involved in safe waste disposal issues. Deep geological repositories are considered the safest and widely accepted option for the final disposal of long-lived intermediate level (ILW) and high-level radioactive waste (HLW). Deep geological repositories are located underground in depths between 250 m and 1000 m for mined repositories in stable geological formations [BGR, 2007; Brady et al., 2012; Chen et al., 2017; WNA, 2019_b]. Recently, deep borehole disposal in 2000 m to 5000 m depths has also been proposed. In all those cases, the isolation is provided by natural barriers such as host rock in combination with engineered and geo-engineered barriers providing a high degree of passive safety after closure of the site. Such disposal concepts ease the burden for the future generations. One of the remaining major challenges is to obtain data, which allow assessing the safety of a disposal site for long periods of time. In final disposal facilities, high-level nuclear waste is foreseen to be encapsulated in thick-walled steel or copper containers. The waste

canister is then emplaced in selected host rock depending on which buffer and backfill materials are selected. Preferred host rock types vary internationally with three main formations being sedimentary clay rock, crystalline (mostly granite) rock and salt rock. Clay rock formations have been selected in Switzerland (Opalinus Clay), Belgium (Boom Clay) and France (Callovo-Oxfordian). They fulfil many of the required properties stated above, such as high sorption capacity, low permeability and fracture self-healing. However, drawbacks are their low thermal conductivity and low mechanical stiffness requiring additional reinforcement efforts during excavation and construction. Canada, China, Finland and Sweden are among those countries, which have selected crystalline rock. These hard rocks are self-supporting and minimal engineering effort is required to stabilize rock walls in emplacement and access drifts. However, fractures in the relatively brittle rock may have high permeability, thus allowing the radionuclides (RN) to potentially migrate via advective water flow. Salt host rocks, considered as potential host rocks for repositories in Germany and the US, benefit from high thermal conductivity, favourable mechanical and viscoplastic properties, which cause the rock to deform under lithostatic pressure leading to compaction of crushed salt used as backfill material and, thus, to the encapsulation of the waste containers in emplacement cells. Furthermore, genuine salt rock is impermeable towards fluids rendering water intrusion unlikely in comparison to the other two host rocks. The disadvantage is a limited sorption capacity and the relatively high solubility in water in the case of contact with unsaturated aqueous solutions [BGR, 2007; IAEA, 2009; Jobmann et al., 2017]. In Germany, LLW (low-level waste) and ILW have been disposed in former salt mines at Asse, which after water intrusion is under preparation for waste retrieval, and Morsleben, which is currently prepared for closure. The Gorleben site (about 900 m below ground) is not anymore a reference for geological disposal of HLW but still remains in the newly started site selection process, which is planned to be completed in 2031 [BGR, 2019; IAEA, 1997; WNA, 2019_b]. In the US, the Waste Isolation Pilot Plant (WIPP) repository, also in salt rock, has been operational since 1999 for disposal of long-lived ILW [WIPP, 2019; WNA, 2019_b].

The extent of potential migration of radionuclides from the repository to the biosphere needs to be quantified for the long-term safety assessment of repositories. Intrusion of water to the emplacement caverns is a possible scenario discussed for all repository types. Water access will lead to container corrosion and affect container integrity up to its possible failure. A safety case requires the knowledge of corrosion rates and corrosion mechanisms. On one side, data on corrosion rates will allow estimating the time frame of waste package integrity. On the other side, quantitative insight into corrosion mechanisms may allow for the assessment of corrosion products as additional barriers against radionuclide migration to the far field. Radionuclide retention can be provided by two mechanisms:

development of very reducing conditions due to metallic corrosion, which is known to reduce mobility and solubility of many redox sensitive RNs, and interaction with the corrosion products and subsequent retardation or retention [Kim & Grambow, 1999]. The latter processes have so far not been considered in safety assessment for radioactive waste repositories. The composition of the intruding groundwater varies depending on the host rock formation. Relatively low ionic strength solutions ($I \leq 0.5$ M) are encountered in many clay and crystalline environments, while aqueous systems in salt rock formations may have salinities of up to 5 M for NaCl and 10 M for MgCl₂ containing also relatively low concentrations of K⁺, SO₄²⁻ and Ca²⁺ [Kienzler & Loida, 2001]. Iron corrosion causes changes in many geochemical conditions such as pH, redox potential (E_h), affecting not only oxidation states and solubility of radionuclides, but also favouring stability of different corrosion products, which in turn can affect RN mobility by sorption. The corrosion reactions and RN solution chemistry in systems with high ionic strength cannot be directly derived from data obtained for dilute systems. The presence of chloride at high concentration levels may for instance accelerate corrosion processes and favour the formation of Cl⁻ bearing species and solid phases. Solubilities of many solid phases increase in concentrated brines due to ion activity effects and sorption at mineral surfaces in solutions of elevated ionic strength is different from that in dilute aqueous solutions. In a deep geological repository environment, the residual oxygen is expected to be consumed within a couple of tens to hundred years after closure of the emplacement cell, buffering the environment of the system to reducing conditions. Therefore, experimental effort should be dedicated to a better understanding of the salt brine effects on corrosion and solution chemistry, and migration behaviour of radionuclides under anoxic conditions.

1.2 Aim of present work

This PhD thesis focuses on two processes affecting the migration of the radionuclides, the corrosion of steel and subsequent sorption of radionuclides onto formed secondary phases. The study aims at a comprehensive description of corrosion processes including corrosion phase identification and corrosion rate estimation of two types of steel under anoxic, stagnant and dilute to concentrated saline conditions, with a major focus on concentrated brine systems. The second investigated process is the retention of radionuclides onto corrosion products formed under anoxic, elevated temperature and dilute to concentrated saline conditions to establish the ionic strength effect on the sorption capability (*Figure 1*). This data is of relevance in the context of salt rock repositories and may aid the safety performance assessment of radioactive waste disposal under saline ground- or porewater conditions.

The main objectives of this work are summarized below:

- A detailed investigation of the corrosion behaviour of stainless steel 309S and spheroidal graphite iron GGG40.3, which are used as materials for canisters for vitrified waste and spent fuel in Germany and other countries, respectively, in dilute to concentrated NaCl and MgCl₂ brines at elevated (90 °C) and room temperature with various exposure times in closed autoclaves. The pH and E_h evolution is followed and the corresponding values are along with the experimentally identified corrosion products compared to the thermodynamically stable corrosion phase in *Pourbaix* diagrams. The effect of different steel, brine compositions and temperature on corrosion phase formation and corrosion rates is evaluated and the underlying reaction mechanisms are identified. Note that the impact of irradiation effects is not considered within the context of this thesis.
- The uptake of trivalent radionuclides by Fe (Cr/Ni) corrosion products identified in corrosion experiments is investigated in dilute to concentrated NaCl and MgCl₂ systems. Batch experiments are performed with a radioactive europium and americium tracer added to equilibrated saline suspensions of well characterized synthetic corrosion phases. At sorption equilibrium, pH is measured and sorption is quantified via solid-liquid distribution coefficients using gamma counting. The dissolution of the investigated minerals in the experimental pH range is quantified by the measurements of dissolved Fe (Ni, Cr) amounts. RN uptake by certain solid phases is subsequently modelled using a surface complexation model to obtain complexation constants. The model is supported by experimentally obtained surface charge data for the solid phases, and where applicable, advanced spectroscopic techniques are applied to aid the evaluation of underlying mechanisms, binding modes and surface speciation.

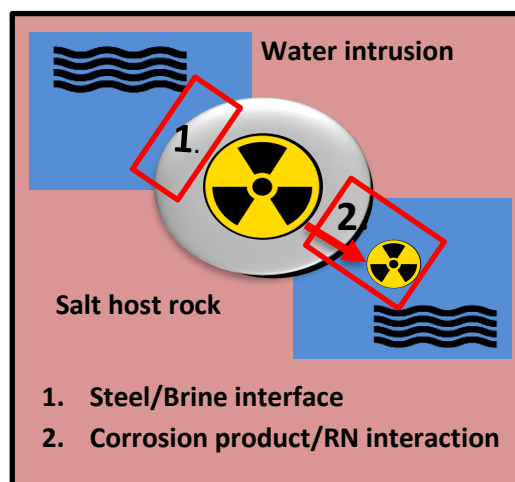
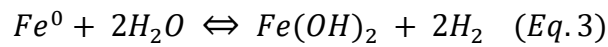
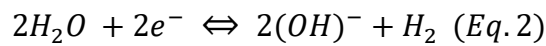
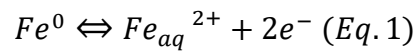


Figure 1: Schematic of the objectives for this thesis.

1.3 State of the art

1.3.1 Basic corrosion chemistry

Corrosion is a chemical reaction between a material (metal in this work) and its surrounding environment leading to the deterioration of the material, the result of which is the corrosion damage. The present thesis restricts to phenomena related to the chemical corrosion of iron based metals and does not consider damage related to mechanical overstressing. The corrosion process involves two simultaneous half-cell redox reactions: oxidation (anodic) and reduction (cathodic) reactions. These are coupled through electron exchange and are generally known as electrochemical reactions. For the iron corrosion under anoxic conditions, these are coupled as follow: the anodic iron oxidation (**Eq. 1**) and the cathodic water reduction (**Eq. 2**).



Thus in the corrosion process, anode, cathode and an electrolyte are always present. In case of aqueous corrosion in real systems, the electrolyte usually contains additional corrosive agents such as ions. The equilibrium potential between the two half-cell reactions is called *corrosion potential*. Although the two reactions must proceed at the same time and rate, they are spatially separated. The separation is caused by a difference in voltage at an anode and at a cathode. This potential difference in the solution then gives rise to electron migration. As mentioned above, the iron dissolution occurs in the anodic area while no corrosion damage occurs at the cathodic area (**Figure 2**). The corrosion of various metals produces hydrogen gas as seen in **Eq. 2**, buffering the system to lower potentials and establishing reducing conditions.

Uniform corrosion is a process where active metal dissolution is the dominant corrosion mechanism. The locations of anode and cathode tend to move randomly over the surface and thus, on average, the metal dissolution is uniform. If the precipitated corrosion product is electrically insulating, the rate of dissolution and corrosion rate will decrease. Depending on the porosity of the film, it may give rise to localized attacks [Lyon, 2012; McCafferty, 2010; Sato, 2012].

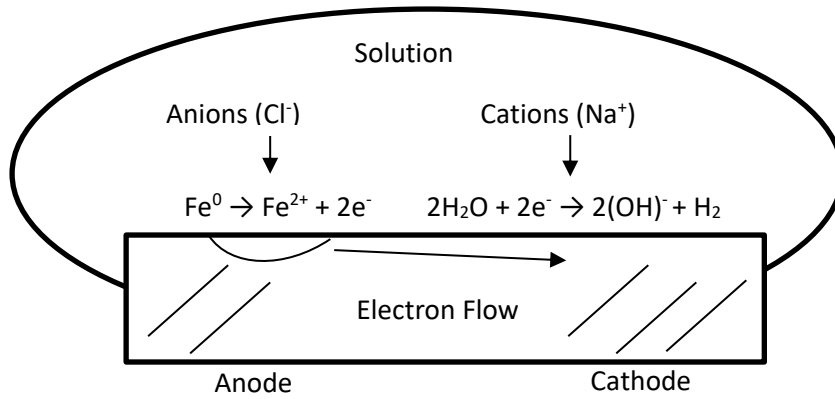


Figure 2: Schematic diagram showing spatial separation of anode and cathode and corresponding migration of ions in the solution.

Stainless steels are known for their good corrosion resistance due to a protective, passivating layer formed at the surface. Passivity is caused by a solid-state electrochemical oxidation of a metal to solid species that are largely stable against dissolution under specific pH and E_h conditions. However, for these steel types, the anodic area tends to be strongly localized giving rise to localized corrosion damage such as pitting corrosion, crevice corrosion or stress corrosion cracking. Furthermore, the hydroxyl ions produced by the cathodic reaction may cause local pH increase in the surface solution layer. This can alter the corrosion behaviour of the substance or favour the precipitation of different solid phases. The passive film on stainless steel is usually made of a several nanometres thick layer of metal oxides and hydroxides containing bound water. From the electrochemical point of view, the passive film is stable when the metal is in the so called passivation region where the dissolution current of the metal is extremely small and is independent from the potential. Pitting corrosion occurs due to localized breakdown of the passive film, usually induced by chloride ions. After the passive film breakdown, re-passivation, growth of metastable pits (limited pit growth) or growth of stable pits are possible. In the presence of an applied mechanical stress, the pit can serve as a site for stress corrosion cracking. Furthermore, discovering of pits can be challenging if the corrosion products cover them. As pits may require months to years to occur, the short-term absence does not mean that the steel is immune to this type of attack. Chloride is particularly unique in causing pitting corrosion, as it is a small anion and a strong electron donor, which tends to interact with electron acceptors such as metal cations and has high diffusivity. The critical *pitting potential* (the potential where pitting will occur) is characteristic to every metal and is dependent on chloride concentration, pH and temperature. The higher the pitting potential the higher the resistance to pitting. Higher chloride concentrations, lower pH and higher temperature decrease the pitting potential to lower values. The addition of inhibitors

such as sulfate in solution or molybdenum in the alloy composition raises the pitting potential [King, 2012; Ramya et al., 2010; Sato, 2012].

Pit formation can generally be divided into three possible mechanisms: the penetration, the film thinning and the film rupture. These three mechanisms are not mutually exclusive and the pit initiation may be a result of their combination. Once the pit is initiated, the local current density is very high due to small geometrical area. The dissolved metal cations are confined within the pit and do not diffuse to the bulk due to restricted geometry which results in hydrolysis and development of local acidity. Once the corrosive pit electrolyte rich in chloride and hydrogen ions is formed, the environment is capable of sustaining further pit growth [Marcus, 2011; McCafferty, 2010]. Crevice corrosion is another form of localized corrosion attack, which occurs within narrow and confined clearances such as seals or within screw threads or under deposits such as corrosion products. The various forms of corrosion are shown in *Figure 3*.

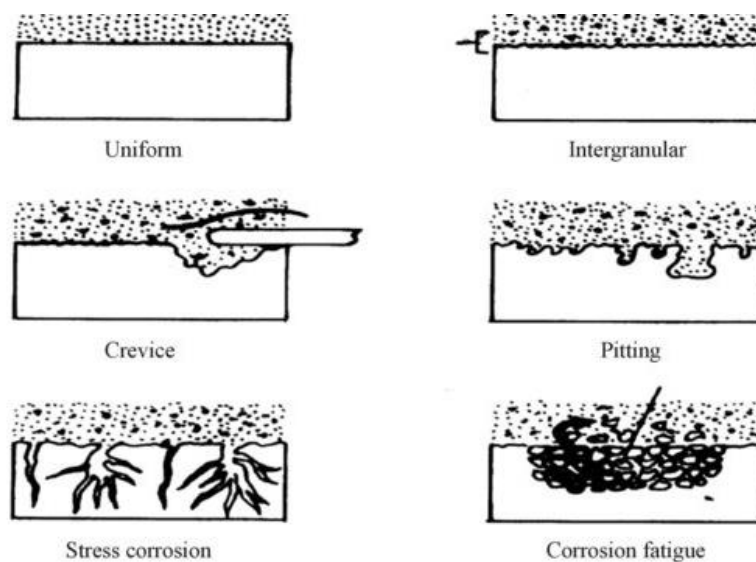


Figure 3: Various forms of corrosion [Chaturvedi, 2009].

Different types of corrosion can occur depending on environmental factors. In the context of waste disposal, the localized corrosion is the most undesirable corrosion mechanism, potentially causing the failure of the canister even though most of the steel surface remains intact. Although localized attacks are more common for alloyed steels, they may also be observed in non-alloyed steel (carbon steel) if a formed iron oxide layer is sufficiently thick to act as an insulator with cracks formation giving way for pitting attack with corresponding pitting potential.

The redox reactions are the core of the corrosion process, with the potential playing a crucial role in corrosion type, stability of formed phases and films, and at the same time, the redox state and with it associated solubility and sorption behaviour of radionuclides.

The Nernst equation (*Eq. 4*) defines the relationship between the half-cell or full-cell potential of a redox couple and the standard electrode potential, temperature and activity of the involved species.

$$E = E^0 - \frac{2.303 \times RT}{nF} \log\left(\frac{a_{red}}{a_{ox}}\right) \quad (Eq. 4)$$

Where E is the redox potential of the given medium, E^0 is the redox potential under standard conditions, n is the number of transferred electrons, T is the absolute temperature in Kelvin, R is the ideal gas constant, F is the Faraday constant, and a_{red} , a_{ox} are the activities of the reducing and oxidizing species, respectively.

Since a single potential cannot be experimentally measured, in practice a potential difference is measured, with hydrogen electrode taken as a primary standard. The electrochemical potential of the standard hydrogen electrode (E_h) at a hydrogen gas pressure of 1 bar at 298 K, with activity equal to 1 is 0 V. Potential measured with respect to the hydrogen electrode is referred to as the S.H.E scale [Lyon, 2012; McCafferty, 2010]. In the nuclear waste repository the oxygen is expected to be consumed after a certain amount of time and reducing conditions will develop. Hence, this work is focused on anoxic conditions.

1.3.2 Corrosion of steels under saline anoxic conditions

In the past years, research has been performed into the various types of barriers to immobilize the radioactive waste, including spent fuel canisters, glass for high-level waste (HLW) and cement. The canisters for nuclear waste are in most disposal concepts made of steel. The corrosion of many steel types has been internationally investigated in different media. The most relevant steel types can be summarized in *Table 1*.

Low alloyed steels such as fine grained steel (TStE 355), major candidate for container material in salt rock, clay and granitic rock, spheroidal graphite iron (GGG40.3), candidate for container material in salt and clay rock, and copper, one of the major candidates in granitic rock are so called “corrosion

allowance materials”. These are considered relevant for the repository due to exhibition of active, but uniform corrosion with predictable corrosion rates and can be used economically in sufficient thickness for a desired lifetime [Kusten et al., 2004]. Furthermore, copper is known to achieve thermodynamic stability under reducing conditions [Shoesmith, 2006].

Nickel based Hastelloy C4 and Ti-99.8Pd, major candidates for container materials in salt rock, clay and in case of Ti99.8-Pd also in granitic rock, along with the stainless steel 309S, candidate mainly in salt rock are so called “corrosion resistant materials” [Kusten et al., 2004]. They exhibit high corrosion resistance in the disposal environment, corroding at a very low corrosion rate due to instantaneous formation of a protective adherent oxide layer, called the passive surface film. They can be used in relatively small thickness. The “corrosion resistant material” should prove absence of the localized corrosion or at least its propagation resistance [Van Iseghem, 2012].

Table 1: Composition of most relevant materials investigated in the context of waste disposal.

Material/ Composition wt %	Cr	Ni	Mo	Ti	Pd	C	Si	Mn	Fe
Ti99.8-Pd (3.7025)	-	-	-	99.77	0.17	0.01	-	-	0.05
Hastelloy C4 (2.4610)	16.8	66.77	15.9	0.33	-	0.006	0.05	0.09	0.05
Fine-grained steel TStE 355 (1.0566)	-	-	-	-	-	0.17	0.44	1.49	97.9
Spheroidal Graphite iron GGG40.3 SGI (0.7043)	-	-	-	-	-	3.7	1.83	0.21	94.26
Stainless steel 309S, Cr-Ni steel (1.4833)	22-24	13	-	-	-	0.08	0.75	2	60-62

1.3.2.1 Clay

Steel corrosion, particularly low alloyed steels (AISI 1050, P235GH, A37, SA516, P235), in conditions representative of disposal in clay-based repositories (e.g., under consideration in France and Belgium) has been reported [El Mendili et al., 2014; King, 2012; Necib et al., 2016; Schlegel et al., 2008; 2018]. The corrosion rates depend on the type of clay, backfill material contact, and aerobic or anaerobic environment. A great overview of corrosion rates under various conditions is done by Kursten et al. [2004] and King [2008]. King [2008] reported decreasing corrosion rate with time due to formation of protective surface film, with the rate anodically limited by transport of species across

this film. Furthermore, a difference in behaviour was observed in the presence of compacted bentonite and in bulk solution. In the compacted clay systems, the decrease in corrosion rate with time is slow, and steady-state is not reached even after several years of exposure. The anaerobic corrosion rate in these systems is 1-2 $\mu\text{m/a}$. In the bulk solution, the corrosion rate reaches steady-state rate after 6 months and the long-term corrosion rate is 0.1 $\mu\text{m/a}$ [King, 2008]. Kursten et al. [2004] reported strong dependence of corrosion rate on temperature with carbon steel average corrosion rate in Boom clay formation of 1.81 $\mu\text{m/a}$ at 16 °C, while the rate reached 8.59 $\mu\text{m/a}$ at 170 °C. These studies also demonstrated susceptibility of the carbon steel to pitting with pit depths of 100-200 μm after 5 years exposure period at 16 °C and 240 μm after 2 years exposure period at 90 °C.

Regarding the formed corrosion products, various authors found the formation of magnetite, siderite (FeCO_3) and various silicate phases such as greenalite ($\text{Fe}_{2-3}\text{Si}_2\text{O}_5(\text{OH})_4$), cronstedtite ($\text{Fe}_3(\text{Si,Fe})\text{O}_5(\text{OH})_4$) or berthierine ($(\text{Fe,Al})_3(\text{Si,Al})_2\text{O}_5(\text{OH})_4$) due to presence of silicate and carbonate in the groundwater. A good summary of numerous experimental studies with various bentonite types was reported by Kaufhold et al. [2015].

These studies also showed that despite low Cl^- concentration in aquatic systems in clay formations, the formed secondary phases (traces) on mild steels contain Cl^- , such as iron hydroxychloride, $\beta\text{-Fe}_2(\text{OH})_3\text{Cl}$. Under acidic conditions (pH of 4.5), this phase was found at the metal surface (inner corrosion layer), while siderite and mackinawite (FeS) phases were found in the external corrosion layer with corrosion rate of 250 $\mu\text{m/a}$ at 85 °C. The coupons exposed to near neutral pH conditions, $\beta\text{-Fe}_2(\text{OH})_3\text{Cl}$ was found at the metal surface with magnetite and silicate compounds observed in the external layer with corrosion rate of 10 $\mu\text{m/a}$ at 85 °C. This was explained by electrophoretic concentration of Cl^- near the metal surface. Furthermore, the stability of this phase hints at neutral to alkaline conditions at the metal surface [Schlegel et al., 2018]. The Si phases inhibit the corrosion by the formation of protective films, while Cl^- phases favour active corrosion [Necib et al., 2017; Schlegel et al., 2016].

Stainless steels (309, 316), Ni- based and Ti- based alloys remained unaffected by the interaction with clay. This findings were reported based on the situ experiments under various conditions [Gaudin et al., 2009; Kursten et al., 2004].

1.3.2.2 Crystalline rock

Similarly, corrosion of various steel types in crystalline rock based repository has been investigated by various authors [Anantatmula & Fish, 1986; Hung et al., 2017; Marsh et al., 1986] showing low corrosion rates and the formation of iron smectite clay and magnetite films on the surface for low

alloyed steels. However, low alloyed steels are not suitable for use without a buffer or backfill due to likely microbial induced corrosion [King et al., 2016].

The concept of disposal in Sweden considers fuel assemblies fixed in a cast iron insert surrounded by copper canister [Shoesmith, 2006; Van Iseghem, 2012]. Copper is thermodynamically stable in oxygen-free water and does not corrode. However, in water containing Cl^- or HS^- species, copper is no longer immune to corrosion. Under repository conditions, the copper canister surface will be covered by duplex bilayer corrosion product film. This layer consists of an inner layer of Cu_2O formed during the initial aerobic period and outer layer of malachite ($\text{Cu}_2\text{CO}_3(\text{OH})_2$), atacamite ($\text{CuCl}_2 \cdot 3\text{Cu}(\text{OH})_2$) or Cu_2S depending on the Cl^- or CO_3^{2-} concentration in the porewater and bentonite presence, as many types of bentonite contain sulphide minerals. Under long-term reducing conditions, Cu_2S is the most thermodynamically stable phase. This layer composition is also applicable on the Cu-Ni alloys in deaerated water in the presence of sulphides. The in-situ experiments in the Aspo Hard Rock Laboratory showed corrosion rate of copper specimen exposed to bentonite clay of $3 \mu\text{m/a}$. The laboratory immersion experiments of copper exposed to compacted bentonite-sand mixture saturated with saline synthetic groundwater revealed corrosion rates of $30\text{-}50 \mu\text{m/a}$ [Kursten [2004]. In all those cases residual oxygen is assumed to be responsible for the high corrosion rates. Under expected anoxic repository conditions, longer copper corrosion rates lie in the $< 1 \mu\text{m/a}$ range [King & Lilja, 2011]. A great overview of copper corrosion in volcanic rock systems has been reported by Shoesmith [2006].

The studies performed in two geological media representative of the near field repository in granite (Spanish disposal concept) include granitic-bentonite water with varying chloride content and saturated bentonite. The corrosion rate of carbon steel TStE 355 in granitic-bentonite water was reported $6 \mu\text{m/a}$ at $90 \text{ }^\circ\text{C}$ increasing to $14 \mu\text{m/a}$ at $120 \text{ }^\circ\text{C}$. The temperature had no significant effect on the corrosion rate after 18 months of exposure to saturated bentonite, which reached $10 \mu\text{m/a}$ at $50 \text{ }^\circ\text{C}$ and $100 \text{ }^\circ\text{C}$. The carbon steel was found resistant to pitting corrosion in the aqueous bentonite buffered granitic groundwater, but susceptible to pitting (up to $100 \mu\text{m}$) in compacted and saturated bentonite. This behaviour was attributed to the inhomogeneity of the electrolyte surrounding the metallic specimen. The compacted bentonite environment leads to creation of zones with different corrosion potential on the surface leading to local attack as opposed to uniform attack observed in homogenous medium – granitic-bentonite water. The XRD analyses of the corrosion products revealed formation of hematite for the specimen exposed to granitic-bentonite water, which could have been formed due to the air interaction during the XRD measurement with previously formed corrosion products under anaerobic conditions. The corrosion products formed on specimen exposed to saturated bentonite consisted of siderite (due to CO_2 presence in saturated bentonite) and magnetite. The

stainless steel 316L was found resistant to stress corrosion cracking, localised corrosion and corrosion rate was less than 0.1 $\mu\text{m/a}$ in both geological media mentioned above [Kursten et al., 2004].

1.3.2.3 Salt rock

Research into corrosion under saline conditions has mainly been conducted in countries with saline rock geologies: Germany and part of United States. Composition of the fluids inclusions in the salt rock vary essentially from pure NaCl solutions to MgCl_2 , CaCl_2 dominated solutions along with other components in low amounts. The thermal gradient produced by the heat generated by the waste could cause brine (fluid pockets in the salt) migration towards the container. The extent of the corrosion will then be determined by the brine composition, volume and container material [Winterle et al., 2012].

The thermal conductivity in the salt rock is very high, which allows higher surface temperature of the canister, up to 200 °C. Nevertheless, recent studies showed that the initial disposal temperature of the canister in salt rock should not exceed 100 °C [Kommission Lagerung hoch radioaktiver Abfallstoffe, 2016].

In the early 80's, extensive research into corrosion of materials shown in *Table 1* has been done at INE, KIT, previously Kernforschungszentrum Karlsruhe, where the major focus was on the corrosion rate estimation. Saline and anoxic conditions were of interest due to the fact that disposal in a salt dome was under consideration as the reference concept for high-level radioactive waste in Germany. The mechanism of formation and identification of secondary phases were not of primary interest, though secondary phase analysis was performed in some cases. The corrosion tests were performed in airtight autoclaves with brines either saturated in NaCl with additions of 0.02 M MgCl_2 and CaSO_4 , or saturated MgCl_2 with additions of 0.3 M NaCl, 0.8 M KCl and 0.15 M MgSO_4 [Kienzler, 2017a; Smailos et al., 1987] at various temperatures for duration of 2 years.

An in-situ study was performed at INE [Kursten et al., 2004; Smailos & Fiehn, 1995], where specimen of various materials were exposed for five years in an electrically heated borehole in the Asse mine at temperatures between 170 °C and 190 °C. The composition of the Asse salt mine rock is mainly halite thus the brine is saturated in NaCl. A similar in-situ experiment "DEBORA" was performed in the Asse environment for 504 days at 180 °C without irradiation. A third in-situ experiment "BAMBUS II" was also performed, where steels were corroded in Asse environment for 3740 days at 90 °C without irradiation.

In the laboratory tests, the corrosion of **fine-grained steel TStE 355** showed a strong temperature dependence, particularly for MgCl_2 based brine. The estimated corrosion rate was 56 $\mu\text{m/a}$ at 90 °C

increasing to 186 $\mu\text{m/a}$ at 170 °C in MgCl_2 solution, whereas in NaCl solution it was only 25 $\mu\text{m/a}$ at 90 °C and the increase with temperature was minimal, 35 $\mu\text{m/a}$ at 170 °C, considering a volume to surface area ratio of 2 mL/cm^2 and pH of the solution being 5. Increasing the volume to surface area ratio to 5, the corrosion rate increases to 220 $\mu\text{m/a}$ at 170 °C for the MgCl_2 brine and 46 $\mu\text{m/a}$ at 170 °C for the NaCl brine. The presence of magnetite and hematite was found as formed secondary phases in NaCl rich brines and $(\text{Fe,Mg})(\text{OH})_2 / \text{Fe}(\text{OH})_3\text{Cl}$ with traces of magnetite was found in Mg-rich brines at 90 °C and 150 °C [Grambow et al., 1996]. The presence of hematite could be due to sample oxidation during XRD measurements. The presence of sulphides (0-200 mg/L H_2S) did not influence the general corrosion behaviour independent of the brine. The formed corrosion products were the same in the sulphide containing and sulphide free brines.

In the field studies, the fine-grained steel TStE 355 showed uniform corrosion with rates in the range of 13-37 $\mu\text{m/a}$. The variation in the corrosion rates is related to different contact time with brine. The specimen part at the bottom of the borehole had longer brine contact time than that in the top part, thus giving rise to different local corrosion rates. Furthermore, the gas phase measurement evidenced the presence of oxygen, which could affect the corrosion process and associated corrosion rate. In DEBORA, the corrosion rate of fine-grained steel was around 17 $\mu\text{m/a}$ [Kurstien et al., 2004]. In BAMBUS II, the fine-grained steel corrosion rates were very low 0.02-1.7 $\mu\text{m/year}$. It must be noted that the variation of corrosion rates, particularly for unalloyed materials, in in-situ vs. laboratory experiment may be attributed to the fact that in the in-situ experiments only small amounts of brine were present while in the laboratory experiments, large amounts of brine were used.

A study by Wang et al. [2000] focused on corrosion product identification of a low-alloyed steel A36 (similar to fine-grained steel TStE 355) under saline anaerobic conditions corresponding to WIPP brines at 25 °C, at pH 9.5 and found formation of non-homogenous film of magnetite and green rust bearing SO_4^{2-} and Cl^- species. The brines compositions in WIPP are not too different from the ones used in experiments at INE.

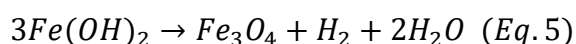
Green rust (GR) is a member of the Fe(II), Fe(III) layered double hydroxide family of minerals. GRs contain both Fe(II) and Fe(III) cations in brucite-like layers along with anions and water structurally arranged in the interlayer. i.e., sulfate (SO_4^{2-}), carbonate (CO_3^{2-}), or chloride (Cl^-) [Refait et al., 1998]. Green rusts are metastable with respect to magnetite under anoxic conditions in the pH range of 7-9 [Tosca et al., 2018].

More work summarizing the corrosion of canister materials in saline systems in the context of the WIPP was reported by Winterle et al. [2012]. The authors found strong dependence of corrosion rate

of low carbon steel (A216 steel) on MgCl₂ content and exponential increase in corrosion rate for temperatures ranging from 100 °C to 200 °C. The corrosion product identification confirmed presence of mixed magnesium iron hydroxychloride, also observed in INE studies for fine-grained steel in MgCl₂ rich brines.

In the laboratory tests, the **spheroidal graphite iron** (GGG 40.3) exhibited a strong dependence on brine composition, with corrosion rates of 25 µm/a at 150 °C for NaCl-rich brine, and 46 µm/a at 90 °C to 91 µm/a at 170 °C for MgCl₂-rich brine. The presence of cathodic graphite particles promote localised dissolution of adjacent ferrite independent of the environment [King et al., 2016]. Due to this mechanism, pits up to 1.3 mm were found after exposure to MgCl₂-rich brine for 465 days at 90 °C [Smailos et al., 1987]. In the field studies, the corrosion rates after 10 years of exposure to salt host rock in Asse mine were 0.09 µm/a at 90 °C and 0.08 µm/a at 170 °C, respectively, with no indication of pitting. The difference in the corrosion rate between the field and the laboratory studies is a consequence of a lower amount of brine in the actual host rock and lower corrosivity of brine in Asse compared to MgCl₂ rich brine [King et al., 2016]. Spheroidal graphite iron corrosion under mildly saline conditions were studied by Hsu and Chen [2010], confirming the presence of graphitic corrosion and the formation of FeCl₂.

Higher corrosion rates in the MgCl₂-rich brines in comparison to the NaCl-rich brines are attributed to the higher chloride concentration and to the presence of magnesium ions. It seems that the Mg²⁺ ions intrude into the ferrous hydroxide layers of Fe²⁺ and cause interference with the normally expected conversion of Fe(OH)₂ to magnetite by the Schikorr reaction [Kursten et al., 2004; King, 2008]. This reaction involves the anaerobic oxidation of Fe²⁺ into Fe³⁺, and to the formation of a more stable Fe(II,III) oxide phase, magnetite (**Eq. 5**). A corrosion layer of Fe(OH)₂ does not passivate the steel as a layer of magnetite would, and thus the steel continues to corrode. Low pH corrosion would force similar effect as it would prohibit the formation of a layer of precipitated corrosion products [Kursten et al., 2004].



Hastelloy C4, showed in the laboratory studies very low corrosion rate, 0.05-1.2 µm/a; depending on the brine and temperature. However, at 200 °C, crevice and pitting corrosion were noticeable. [Kienzler, 2017b; Kusten et al., 2004; Smailos et al., 1987]. In all the field studies, the hastelloy C4 showed high corrosion resistance, corrosion rate below detection limit, but formations of small pits were observed (10 µm in depth).

Ti99.8-Pd seems as a great candidate for the canister material as it has high corrosion resistance to general and localized corrosion due to formed protective layer of TiO_2 . In the laboratory studies, change of temperature and change of brine composition showed no effect, all corrosion rates were under $0.1 \mu\text{m/a}$ [Kusten et al., 2004; Smailos et al., 1987]. The field studies showed that Ti99.8-Pd is highly resistant to pitting and crevice corrosion, its general corrosion rate was below the detection limit.

Ti99.8-Pd seems to be best suited as HLW packaging material; however, hydrogen embrittlement needs to be considered as well as the economic aspect. Hydrogen cracking could be a concern for titanium alloys as hydrogen can precipitate as titanium hydrides, which causes material embrittlement [Winterle et al., 2012]. Hydrogen embrittlement is less relevant in the case of carbon steel [Nagies, & Heusler, 1998].

Stainless steel 309S showed in the laboratory studies high susceptibility to stress corrosion cracking (SCC) and pitting (around $30 \mu\text{m}$ depth independent of the brine after 2 years), but exhibited low corrosion rates at $150 \text{ }^\circ\text{C}$ of $4.4 \mu\text{m/a}$ decreasing to below $1.9 \mu\text{m/a}$ in MgCl_2 brine, and below $0.62 \mu\text{m/a}$ in NaCl brine after 3 months [Kienzler, 2017_b].

In the field studies, stainless steel 309S suffered from pitting corrosion (up to $200 \mu\text{m}$ in depth) and stress corrosion cracking but showed very low corrosion rates, $0.3\text{-}0.7 \mu\text{m/a}$. DEBORA showed corrosion rate of stainless steel 309S of about $1 \mu\text{m/a}$. However, also in this experiment, pitting was observed ($30 \mu\text{m}$) [Kursten et al., 2004; Smailos & Fiehn, 1995]. In BAMBUS II, the corrosion rates of $0.30\pm 0.20 \mu\text{m/a}$ with $50 \mu\text{m}$ deep pits were obtained.

The low corrosion rates are attributed to the formation of protective Cr_2O_3 layer. This property is the reason for stainless steels being alloyed with Cr [Ramya et al., 2010]. Furthermore, Zhang et al. [2017] investigated the formed oxide film on stainless steels by transmission electron microscopy and found that in addition for Cr, Fe is also present in the passive films and the Fe/Cr ratio increases with the applied potential. Additionally, they detected Ni in the film in marginal amounts, attributing it to originate from NiFe_2O_4 spinel.

1.3.2.4 Irradiation

Un-alloyed materials may exhibit low-moderate corrosion rates in the absence of irradiation but the corrosion rate can increase as much as 15 times if certain radiation levels are present [Kursten et al., 2004; Shoesmith & King, 1999]. Sets of experiments were performed under gamma irradiation in the spent fuel storage pool of KFA Jülich to investigate the effect of radiolytic products formed in salt brines (H_2O_2 , ClO^- , and ClO_3^-) on the corrosion process. The dose rate of 1000 Gy/h corresponds to

the gamma dose rate on the surface of the HLW canister (~5 mm), while much lower dose rate of 10 Gy/h is relevant for thick unalloyed containers. For spheroidal graphite iron, under a high gamma dose rate of 1000 Gy/h, the corrosion rate increased from 46 $\mu\text{m/a}$ to 165 $\mu\text{m/a}$ at 90 °C in MgCl_2 based brine. For fine-grained steel TStE355 in MgCl_2 based brine at 90 °C, the corrosion rate reached under irradiation of 1000 Gy/h 464 $\mu\text{m/a}$. There is a negligible effect on corrosion rate when the dose rate is low, 1-10 Gy/h, which is the likely absorbed dose rate for these steel types. For Hastelloy C4, irradiation of 1000 Gy/h increased the corrosion rate to 3.5 $\mu\text{m/a}$ with 1 mm deep pits after 1 year at 90 °C. Irradiation had negligible effect on Ti99.8-Pd. The effect of irradiation on corrosion product formation was not investigated.

Corrosion studies performed in this thesis focus on the detailed investigation of the two types of steel, which are used for canisters for vitrified waste and spent fuel. High-level waste is a waste form, which contains elements from reprocessing of spent nuclear fuel, which are through a vitrification process incorporated into a borosilicate glass matrix. This glass is then poured into a stainless steel canister (4-5 mm thick) (**Figure 4 A**) and if necessary, a steel overpack is added later on upon cooling, usually made of spheroidal graphite iron [Kursten et al., 2004]. The stainless steel 309S (from now on referred as Cr-Ni steel) examined in this work is currently used for the vitrified waste container due to its high temperature resistance [King, 2008]. Recent study by Guo et al. (2020) reported that under simulated repository conditions, corrosion could be significantly accelerated at the interfaces of different barrier materials (using stainless steel 316), which has not been considered in the current safety and performance assessment models. If this phenomenon is also applicable on stainless steel 309S, it may potentially lead to its failure.

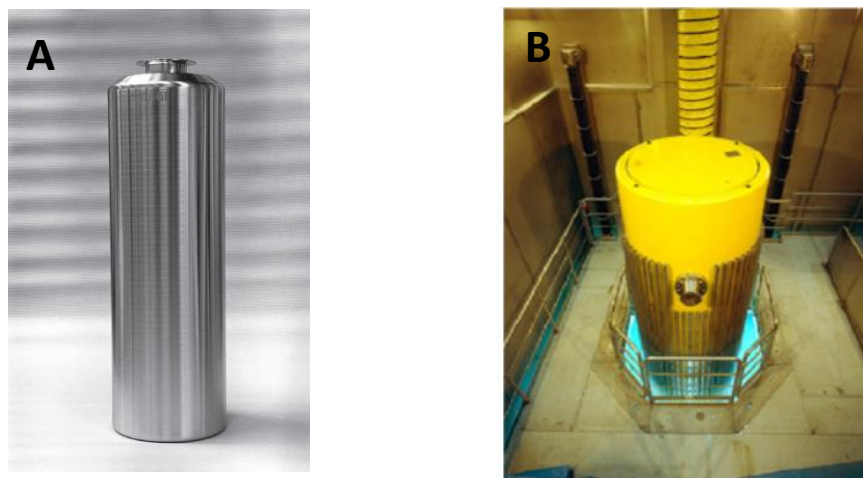


Figure 4: High-level vitrified waste canister (left) [Van Iseghem, 2012] and spent fuel canister (right) [Filbert et al., 2011].

In cases of spent fuel being directly disposed without reprocessing, a different concept (POLLUX container) is adopted, where the assemblies are encapsulated in an un-alloyed or low alloyed steel (**Figure 4 B**), which if necessary can be surrounded by 3-4 mm layer of corrosion resistant steel. This inner cask is additionally surrounded by 265 mm of spheroidal graphite iron. [Kursten et al., 2004; GNS, 2020]. The second material of interest is spheroidal graphite iron (GGG40.3) (from now on referred as SGI). This material is a great candidate due to its high impact and fatigue resistance as well as its cost-effectiveness.

Many of the reported studies looked very systematically at corrosion under saline conditions at room and elevated temperatures, microbial activity effect and effects of other factors on corrosion of many alloys. Furthermore, many studies have looked into corrosion of steels in brines corresponding to German repository site conditions at elevated temperature but here no systematic evolution of corrosion mechanism, including anoxic corrosion phases identification, pH, E_h and gas phase was done for the two steels of interest. This work provides this missing information and allows better understanding of the corrosion mechanism under repository conditions in salt rock.

The relevant corrosion mechanism for low alloyed steel in low saline media found in the literature consist of initial stage of corrosion, random oxidation of the surface until the monolayer of the corrosion product is complete. The film thickening process then proceeds by ion transport through the film under the influence of the electric field gradient established in the film. As the film is thickening, the field decreases and with it the rate of the film growth. A net constant corrosion rate (of metal loss) is reached when the rate of the film thickening is equal to the rate of film dissolution. The resulting corrosion product layer consists of inner and outer film. Inner film is formed by a solid-state process, and is made of magnetite [Diomidis, 2014] or iron hydroxychloride due to electrophoretic concentration of Cl^- at the metal surface [Schlegel et al., 2018]. The thicker outer part is formed by dissolution-precipitation mechanism. The outer layer consist of magnetite, siderite or other carbonate and calcium containing products [Diomidis, 2014] or silicate containing products [Schlegel et al., 2018]. The composition of the outer part depends on the local conditions at the surface, electrolyte chemistry and temperature. The presence of surface layer leads to mass-transport controlled corrosion process. A specific mechanism applies on the spheroidal graphite iron, which due to presence of graphite inclusion undergoes graphitic corrosion, form of galvanic corrosion under which the iron in the proximity of cathodic graphite dissolves preferentially. This mechanism is only of concern when the corrosion rate is low [King et al., 2016]. The porosity of the formed film and initial heterogeneous film formation in the low alloyed steels can lead to localised damage. The presence and composition of the double layer for low alloyed steels has not yet been reported in highly saline conditions.

Nevertheless, due to high Cl^- concentration, the electrophoretic accumulation at the surface can be expected. The identified corrosion products in the literature under saline conditions are magnetite and hematite in NaCl rich brines and $(\text{Fe,Mg})(\text{OH})_2 / \text{Fe}(\text{OH})_3\text{Cl}$ with traces of magnetite in Mg-rich brines.

The highly alloyed steels along Ti99.8-Pd exhibit low corrosion rates due to formation of protective Cr/Ti oxide layers. Due to negligible corrosion damage for these materials, no corrosion product information is available. In Cr-Ni alloyed steels, the literature reports formation of a passive double layer made of inner Cr oxide/Cr containing spinel oxide formed by a solid-state growth mechanism and an outer layer of Fe, Ni spinel oxide formed by metal dissolution and corrosion product precipitation mechanism [Zhang et al., 2017].

1.3.3 Sorption processes

Sorption processes at solid / water interfaces belong to the most relevant mechanisms regarding the retardation and retention of radionuclides. Sorption processes can be categorized into several types of interaction mechanisms: incorporation into the structure of the sorbent, inner-sphere and outer-sphere surface complexation of ionic species, surface induced redox reaction, surface precipitation and ion exchange reactions. The difference between the inner-sphere and the outer-sphere complexes on a metal oxide and water interface is the type of chemical bonding between the aqueous ionic species and the surface site. In the inner sphere complex the ion is partially dehydrated and binds directly to the surface while in the outer sphere complex the ion keeps its hydration sphere and is attached to the surface only via electrostatic forces [Geckeis et al., 2013; Payne et al., 2013].

The sorption of a pollutant/ RN onto a mineral surface is usually empirically expressed in terms of distribution coefficient $K_D (\frac{L}{kg})$ representing the distribution of the contaminant between the solid surface and the aqueous phase. As performance assessment calculations for radioactive waste disposal use distribution coefficients it is crucial to have robust arguments for the selected values. The K_D can be further incorporated into transport models, from which further parameters for the assessment of RN migration behaviour can be obtained. The experimental sorption results can be converted into a K_D value using the relationship in **Eq. 6**:

$$K_D = \frac{[M]_s}{[M]_e} \times \frac{V}{m} = \frac{[M]_i - [M]_e}{[M]_e} \times \frac{V}{m} \quad \left(\frac{L}{kg}\right) \quad (\text{Eq. 6})$$

$[M]_i$ and $[M]_e$ are the initial and equilibrium concentration of radionuclide in solution respectively, $[M]_s$ is the concentration of the sorbed / incorporated radionuclide in the solid, V is the solution volume (L) and m is the mass of the sorbent (kg). Sorption experiments can be performed at various pH, ionic strength levels and solid to liquid ratios in order to examine the dependence of $\log K_D$ values on such variations. Additional sorption data (amount of sorbed metal per unit sorbent) are often determined as a function of metal concentration, so called sorption isotherms. The underlying uptake mechanism: sorption vs. incorporation and type of sorption can be identified applying complimentary spectroscopic techniques. There are numerous studies providing the K_D values intended for nuclear waste disposal safety assessment applications, summarized e.g. by Jung et al. [2001] and Lee et al. [2013] and while they describe the range of K_D values for specific RNs and cover various factors affecting these values, they cannot be extrapolated to a wide range of conditions. Therefore, a development of a thermodynamic sorption model, which includes relevant sorption reactions and aqueous RN species with associated equilibrium constants is beneficial because it allows extrapolation of existing data and direct estimation of contaminant K_D values for a wide range of geochemical conditions.

1.3.4 Sorption of radionuclides and metal ions onto minerals

Spent fuel consists of 96 wt. % uranium which can be reprocessed. The remaining matrix consists of minor actinides, plutonium and long/short-lived fission products. In the context of final repository short-lived fission products are not considered. From this remaining matrix, plutonium accounts for 25 wt. %, minor actinides (neptunium, americium and curium) for 2.5 wt. % and the remaining matrix (72.5 wt. %) consists of fission products such as technetium, zirconium and cesium [Oecd-nea.org, 2017]. These radionuclides are covering the whole range of oxidation states, while trivalent state is of interest in this work.

Plutonium is a constituent of high-level radioactive waste. The 1.15 % present in the spent fuel from a commercial pressurized light water reactor with a burn up of 42 GWd/t consists of 53 % ^{239}Pu , 25 % ^{240}Pu , 15 % ^{241}Pu (which decays beta minus to ^{241}Am with $t_{1/2} = 14$ a), 5 % ^{242}Pu and remaining amounts of ^{238}Pu [WNA, 2019c]. Plutonium is the main source of heat and radioactivity in the spent fuel after several hundred years. Its environmental chemistry is important due to the long half-life of its main isotope ^{239}Pu ($t_{1/2} = 24,000$ a) and high solubility and mobility in its oxidation state 5^+ , which is dominant under very oxidizing conditions. Plutonium is redox sensitive with reduction potentials being

strongly pH dependent. Its tetravalent oxidation (4^+) state, which is considered immobile and sorbs strongly to minerals, prevails under oxidizing to mildly reducing conditions [Kirsch et al., 2011; Marsac et al., 2017; Powell et al., 2004]. Under very reducing conditions, the reduction can partially or entirely reach trivalent oxidation state in presence of a corroding iron based container. The *Pourbaix* diagram for plutonium is shown in **Figure 5**.

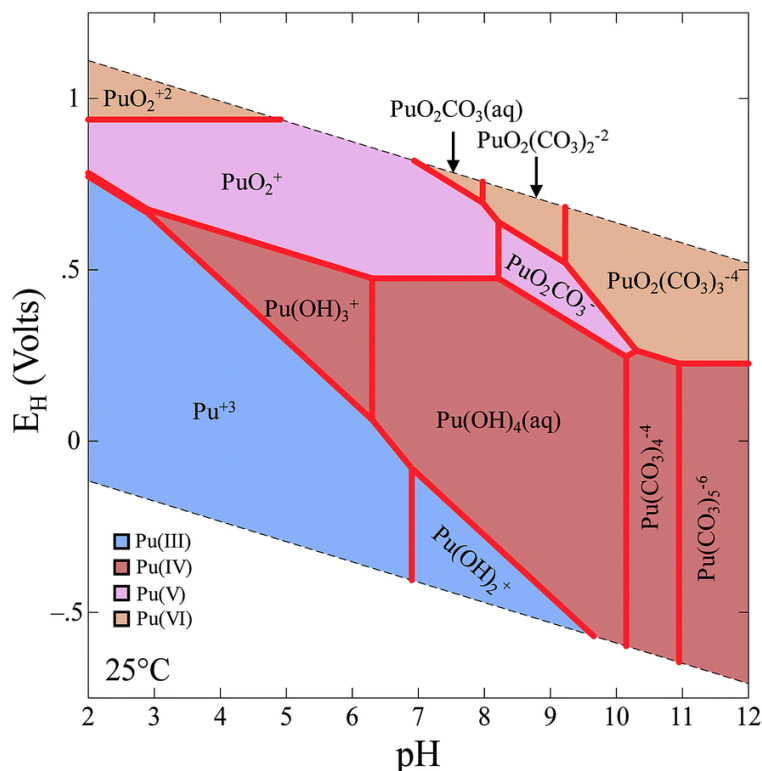


Figure 5: The *Pourbaix* diagram for plutonium taken from Hixon & Powell [2018].

The separation of the minor actinide americium from spent fuel during fuel reprocessing is challenging and not practiced on commercial scale yet, thus it remains in the waste matrix, which is disposed in the final waste repository. Here it is strongly contributing to the heat generation and radiotoxicity for quite some time. Europium is frequently taken as a chemical homologue to these trivalent actinides (americium, curium and plutonium). Those trivalent metal ions show comparable aquatic chemistry characteristics.

Assuming that the canister is subject to corrosion, which results in breaching of this barrier and radionuclides come in contact with the corrosion products on the surface, the sorption process may result in their capture. The thermodynamic sorption constants are thus important data, which are needed for the safety performance assessment. The second part of this thesis is focused on retention of

trivalent radionuclides onto formed secondary phases observed in the first part (corrosion experiments) if considered important with respect to the long-term disposal under saline conditions.

Many countries consider radioactive waste disposal in argillaceous or sedimentary host rock; therefore numerous studies regarding sorption of heavy metals onto clay have been performed. Clay minerals were found to sorb heavy metals well either through ion exchange reaction in their interlayer or through inner-sphere surface complex formation [Bauer et al., 2005; Bradbury & Baeyens, 2006; Coppin et al., 2002; Finck et al., 2015; Finck et al., 2017; Franco et al., 2016; Hartmann et al., 2008; Kowal-Fouchard et al., 2004; Lujanienė et al., 2010; de Pablo et al., 2011; Rabung et al., 2005; Stumpf et al., 2007]. These works focus on low ionic strength conditions. As certain pore waters in clay rock e.g. in Northern Germany and in Canada may contain high salt contents up to 4.9 *m* [Brewitz, 1980], Schnurr et al. [2015] and Vilks & Yang [2018] investigated the sorption of trivalent radionuclides onto several clay minerals in brines with NaCl concentration up to 3.9 *m* and found that an increase in the ionic strength decreases the extent of the uptake in the low pH region (< 7). Radionuclides with different oxidation states exhibited different sorption behaviour onto clays [Vilks & Yang, 2018].

There are few studies reporting sorption data of radionuclides onto various surfaces at high *I*, which are modelled with a surface complexation model. Ams et al. [2013] investigated neptunium sorption onto bacteria under moderately saline conditions, while Schnurr et al. [2015] evaluated and modelled europium sorption onto clay minerals in up to nearly saturated NaCl solution. Scholze et al. [2019] and Banik et al. [2017] examined neptunium sorption onto various clays in solution with *I* up to 3 M. A similar approach was adopted by Marsac et al. [2017] who studied plutonium sorption onto clay particles under similar conditions. In all these studies, a non-electrostatic surface complexation model was sufficient to describe the experimental data when applying the SIT and Pitzer approach to calculate activity coefficients in solution. Strontium adsorption onto clay minerals in systems with *I* up to 4 *m* was modelled by Mahoney & Langmuir [1991] using a surface complexation triple layer model. Recently, García et al. [2019] used a basic Stern model combined with the Pitzer approach to describe the uptake of europium on quartz up to high *I*.

There are many available data describing the sorption of trivalent metal ions and RNs onto iron hydr(oxides) under variety of conditions. A study summarizing possible retention mechanisms of radionuclides on mineral surfaces and approaches to geochemical modelling of actinide sorption was done by Geckeis et al. [2013] with data obtained by various complexation models available in HZDR database [HZDR, 2018]. A good overview of the sorption coefficients for Pu, Am, U, Np and Tc onto Fe hydroxides and oxides was published by Li and Kaplan [2012]. The oxidation states of investigated

Pu and Np are mainly 4^+ and 5^+ , thus not of interest in the framework of this thesis. Sorption of trivalent radionuclides onto Fe(III) minerals under oxic conditions were investigated by various authors [Estes et al., 2013; Naveau et al., 2005; Rabung et al., 1998; Stumpf et al., 2006]. All these studies found strong sorption capacity of the iron hydr(oxide) phases under low ionic strength and oxic conditions.

Sorption onto nickel ferrites (NiFe_2O_4) has been reported for divalent ions such as Co, Ni [Martin Cabañas et al., 2011] and tetravalent Tc [Wang et al., 2019] at low ionic strength, but no sorption of trivalent pollutants or radionuclides has been reported. The pure iron analogue of nickel ferrite, magnetite ($\text{Fe(II)Fe(III)}_2\text{O}_4$) has been investigated by many authors as potential sink for numerous pollutants due to its ability to reduce higher valent, usually mobile, species into trivalent or tetravalent species which are likely to sorb on its surface already at acidic to neutral pH values [Latta et al., 2011]. This ability is due to the presence of Fe(II) in the structure. Magnetite is a stable crystalline iron corrosion product in moderately to strongly reducing environments and under neutral to alkaline conditions, and was mentioned as an observed corrosion product in the corrosion literature review *section 1.3.2*. Magnetite can be formed either by the Schikorr reaction (*Eq. 5*) or by transformation of metastable phases such as layered double hydroxides (green rusts) [Cornell & Schwertmann, 1996].

The affinity and redox behaviour of uranium in presence of magnetite was studied by Huber et al. [2012], Ilton et al. [2010], Latta et al. [2011], Missana et al. [2003], Pidchenko et al. [2017], Rovira et al. [2007], Scott et al. [2005] and Yuan et al. [2015]. The sorption of pentavalent neptunium was investigated by Nakata et al. [2002], while sorption of tetravalent thorium onto magnetite was reported by Rojo et al. [2009]. Powell et al. [2004] studied the redox and retention behaviour of pentavalent plutonium, while Kirsch et al. [2011] investigated interaction of trivalent plutonium with magnetite and found strong retention by formation of inner sphere surface complexes. Another recent study by Dumas et al. [2019] showed that precipitation of magnetite in presence of pentavalent plutonium results in its reduction into Pu^{3+} and retention of plutonium partly by incorporation into the magnetite structure and partly by sorption on the surface by formation of tridentate surface complexes. Limited literature is available on europium or americium and its respective sorption behaviour on magnetite [Catalette et al., 1998; Lujanienė et al., 2010; Singh et al., 2009]. Singh et al. [2009] investigated the sorption of europium onto magnetite (2 g/L) for and Eu concentration of 2×10^{-9} M and observed complete sorption at pH 5.5 in background electrolyte with $I = 0.1$ M. These authors used magnetite with high surface area, $72 \text{ m}^2/\text{g}$. Similarly, in the work of Catalette et al [1998], the authors used higher europium concentration (2×10^{-4} M) and magnetite with a specific surface area of $18.3 \text{ m}^2/\text{g}$ and a solid to liquid ratio of 2 g/L. They found complete sorption above pH 7 and modelled the sorption with diffuse layer surface complexation model. Finck et al, [2016_{a,b}] who investigated Am retention by

adsorption or co-precipitation with magnetite by X-ray diffraction and X-ray absorption spectroscopy found that the fate and type of entrapment of Am depends on the circumstance whether the radionuclide is present during (incorporation) or after (surface sorption) formation of magnetite. None of these data sets focused on environments with high ionic strength. To our knowledge, only sorption and reduction behaviour of uranium in the presence of magnetite under reducing saline conditions has been reported [Grambow et al., 1996].

Green rust chloride ($\text{Fe(II)}_3\text{Fe(III)(OH)}_8\text{Cl} \cdot n\text{H}_2\text{O}$) or sulfate are other minerals observed as corrosion products of carbon steel [Refait et al., 1998]. Their formation and possible transformation mechanisms into magnetite are described in a review by Usman et al. [2018]. Similarly as for magnetite, its nature of mixed Fe^{2+} and Fe^{3+} allows reduction of higher valent radionuclides to lower oxidation states, however compared to magnetite it contains stoichiometric two times more structural Fe^{2+} which makes it more powerful reductant. A great summary of green rusts interaction with various elements, with focus on uranium was reported by Latta et al. [2015], while Bach et al. [2014], Christiansen et al. [2011], Römer et al. [2011] and Roberts et al. [2019] studied the green rust retention capacity with neptunium. They found out, that once the radionuclide is reduced to tetravalent oxidation state, it is retained at the green rust edge sites. Jönsson & Sherman [2008] found that green rust retains trivalent arsenic by forming bidentate inner sphere surface complexes. Reduction and retention of technetium by green rust was studied by Pepper et al. [2003]. Americium sorption and incorporation into green rust chloride was also studied by Finck et al. [2016_a], who demonstrated that formation of green rust in presence of americium via a precipitation route retains the americium as it substitutes for Fe^{3+} within the green rust octahedral sheet. The immobilisation via this mechanism was also confirmed by Refait et al. [2017], who has demonstrated the incorporation of Al^{3+} or Cr^{3+} into the structure of green rust sulfate upon formation while replacing Fe^{3+} in the brucite layer. Yet again, all these works were performed in suspensions with low ionic strength. To our knowledge, no sorption data for green rusts in solutions with high ionic strength are available.

Beside the above mentioned phases, other Fe phases frequently detected in corrosion experiments may be of interest, but for which hardly any work on RN retention has been reported. For example, only one publication is existing describing sorption data for ferrous hydroxychloride ($\text{Fe}_2(\text{OH})_3\text{Cl}$) [Grambow et al., 1996], a mineral that is often found on archaeological artefacts corroded in seawater and corrosion product in clay formations [Necib et al., 2017; Nemer et al., 2011; Réguer et al., 2015; Schlegel et al., 2018]. The work by Grambow et al. [1996] describes in-situ reduction and retention of U^{6+} on corroded carbon steel (TStE 355) in MgCl_2 rich brine, which results in formation of $(\text{Mg,Fe})_2(\text{OH})_3\text{Cl}$ and traces of magnetite. These corrosion products immobilized 98 % of dissolved,

now reduced to tetravalent, uranium within one day. However, magnetite appears to be the main sorbent phase and no uptake quantification on ferrous hydroxychloride was performed.

As Cr_2O_3 forms instantaneously on Cr containing stainless steels and plays an important role regarding its passivity, it is likely that even during a canister failure due to pitting corrosion, the layer of Cr_2O_3 will still cover a large area of the canister surface. There are limited sorption data regarding this mineral, mainly focusing on H_2 and CO_2 as pollutants [Borello et al., 1972; Kuhlenbeck et al., 1992; Zhou et al., 2019]. The affinity of radionuclides to this phase has not yet been reported.

In the context of safety case, strong sorption capacity and reducing power of Fe(II) containing minerals have been reported for low I (clay) environment. However, there is clearly a lack of sorption data of radionuclides under highly saline conditions for various metal hydr(oxides). This work aims to provide these information for the various corrosion phases observed in the corrosion experiments under stagnant saline anoxic conditions.

1.3.5 Modelling

Pourbaix diagrams (showing equilibrium potentials between a metal/radionuclide and its various oxidized aqueous species and solid compounds) are systematically used in the corrosion focused part of this work to compare the identified formed corrosion phases from experiments to thermodynamically stable solid compounds under corresponding conditions (pH, E_h , T, I and dissolved metal concentrations). The equilibrium lines correspond to a 50:50 % distribution between the species [Pourbaix, 1974]. The outcome then shows whether the given compound is stable in long-term or is prone to further transformation. The diagram is crucial to check whether these found corrosion phases are relevant in the long-term (provided geochemical conditions will not change). Such phases will specifically be of interest for the radionuclide retention studies. In addition, the measured potential will be compared to passivation/pitting potentials of the steels in given brines to establish the possible corrosion type and relate these to the observed corrosion damage. A simplified general *Pourbaix* diagram for Fe and Cr are shown in **Figure 6** giving an overview of the passivity and corrosion domains [McCafferty, 2010; Pourbaix, 1974]. In no cases throughout this work is the potential externally forced to reducing values by addition of buffers.

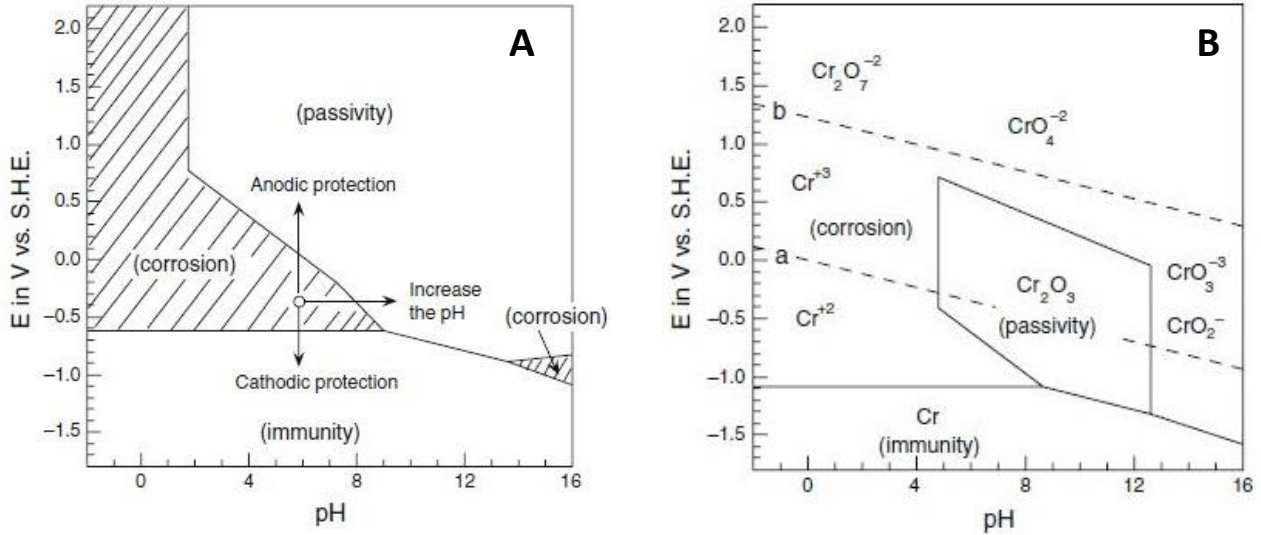


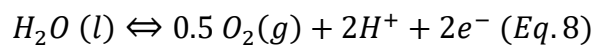
Figure 6: Simplified *Pourbaix* diagrams for Fe showing general domains (A) and Cr with species and solid compounds (B) [McCafferty, 2010]. The dashed lines in figure B correspond to borders of the stability region of water described below.

In the *Pourbaix* diagram the redox potential of a system may be defined as the negative logarithm of the electron activity: $pe = -\log a_{e^-}$. The correlation between E_h and pe values is shown in *Eq. 7*.

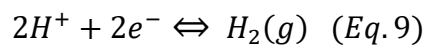
$$E_h = -\frac{RT}{F} \ln(a_{e^-}) = \frac{2.303 \times RT}{F} pe = 0.059 pe [V] \text{ at } 25^\circ\text{C} \text{ (Eq. 7)}$$

The redox potential of an aqueous solution is limited in the *Pourbaix* diagram by the upper stability line of water corresponding to water oxidation and by the lower stability line corresponding to water reduction [Pourbaix, 1974].

The oxidation of water to O_2 according to reaction in *Eq. 8* corresponds to an oxygen partial pressure of 1 bar.



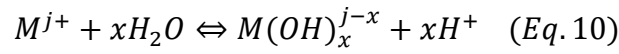
The reduction of water to H_2 according to reaction in *Eq. 9* corresponds to a hydrogen partial pressure of 1 bar.



The oxidation and reduction of water above the upper and below the lower stability lines are kinetically very slow processes thus it is possible to obtain potential values in solutions even above and below the lines.

1.3.5.1 Solubility

The thermodynamic stability of solid phases in aqueous environment is determined by its solubility. In the absence of other complexing ligands than OH⁻ ions, the aqueous metal species (M^{j+}) reacts with water by hydrolysis as shown in **Eq. 10**.



The formation constant of the hydroxide complex in a given medium is given by K_H or $\log K_H$ as shown below in **Eq. 11** and **12**.

$$K_H = \frac{[M(OH)_x^{j-x}][H^+]^x}{[M^{j+}]} \quad (\text{Eq. 11})$$

$$\log K_H = \log[M(OH)_x^{j-x}] + x \log[H^+] - \log[M^{j+}] \quad (\text{Eq. 12})$$

The standard state hydrolysis constant at dilute conditions $I = 0$ and $T = 25$ °C is expressed as a function of activity coefficients of an ion (γ_i) and activity of water (a_w) (**Eq. 13**).

$$\log K_H^\circ = \log K_H + \log \gamma_{M(OH)_x^{j-x}} + x \log \gamma_{H^+} - \log \gamma_{M^{j+}} - x \log a_w \quad (\text{Eq. 13})$$

Similarly, the solubility of metal hydroxides is conventionally defined as shown in **Eq. 14** with conditional constant K_S (**Eq. 15**) in a given medium and standard state conditions constant $\log K_S^\circ$ (**Eq. 16**).



$$K_S = \frac{[M^{j+}]}{[H^+]^b} \quad (\text{Eq. 15})$$

$$\log K_S^\circ = \log K_S + \log \gamma_{M^{j+}} - b \log \gamma_{H^+} + (b+x) \log a_w \quad (\text{Eq. 16})$$

The values of $\log K_s$ in a given medium and under the standard state conditions $\log K_s^\circ$ are interconnected and can be obtained using the activity coefficients calculated with SIT, Pitzer or other activity models. The ionic strength (I) can be calculated using **Eq. 17**.

$$I = \frac{1}{2} \times \sum_i M_i z_i^2 \quad (\text{mol/L}) \quad (\text{Eq. 17})$$

Where M_i is the molarity (mol/L) of all aqueous solute species and z_i is its electrical charge.

1.3.5.2 Activity models and databases

In deep geological repositories with salt rock formations, the aqueous systems will have high ionic strength up to 10 M. Although experiments in this thesis are also performed at low ionic strength $I = 0.1$ M, most of the work focuses on highly saline systems. Consequently, the activity coefficients must be taken into account due to non-negligible interactions between the ions in the solution. The subsections below give a short overview of the SIT and Pitzer activity models, which are used in this work for the activity coefficients calculations.

SIT (Specific Interaction Theory) approach

A popular method for treatment of ion interaction processes and ionic strength effects in real systems with $I > 0$ is the SIT approach. It is based on the Debye-Hückel model which is able to express the activity coefficients in dilute solutions and accounts for long range electrostatic interactions [Brönsted, 1922; Scatchard, 1936]. However, at higher salt concentration also short range non-electrostatic interactions between ions need to be taken into account. This is commonly done by adding a further ionic strength dependence term. The calculation of an activity coefficient is shown in **Eq. 18** where D is the Debye-Hückel term shown in **Eq. 19**.

$$\log \gamma_i = -z_i^2 \times D + \sum_k \varepsilon(i, k, I_m) \times m_k \quad (\text{Eq. 18})$$

$$D = \frac{A \times \sqrt{I_m}}{1 + 1.5 \times \sqrt{I_m}} \quad (\text{Eq. 19})$$

Here z_i is the charge of ion i , $\varepsilon(i, k, I_m)$ is the specific ion interaction coefficient for a given electrolyte with molal ionic strength I_m (mol/kg) between the examined ion i and the ion k of opposite charge,

and m_k is the molality (mol/kg) of the oppositely charged ion k . The Debye-Hückel constant A is temperature and pressure dependent and equals $0.509 \pm 0.001 \text{ kg}^{1/2} \times \text{mol}^{-1/2}$ at $25 \text{ }^\circ\text{C}$ and $0.600 \pm 0.001 \text{ kg}^{1/2} \times \text{mol}^{-1/2}$ at $100 \text{ }^\circ\text{C}$ at a pressure of 1 bar [Bretti et al., 2004; Grenthe et al., 2013]. The specific ion interaction coefficient is not a constant and may vary with the ionic strength. The extent of the variation is small for 1:1, 1:2 and 2:1 electrolytes as long as the molality is less than 3.5 m and for these cases it may be assumed constant. Thus, the SIT model validity is limited to $I_m \leq 3.5 m$ [Grenthe et al., 2013]. A study by Bretti et al. [2004] introduced an additional two parameters SIT equation for the specific ion interaction coefficient calculation, which makes it possible to calculate activity coefficients correctly up to ionic strength of at least 6 m . Another option to take into account the significant effect of the concentration on ion interaction coefficients and to correctly calculate the activity coefficients at high ionic strength is the use of Pitzer model.

Pitzer approach

In order to accurately describe the activity coefficients in aqueous solutions, Pitzer [1973; Pitzer & Kim, 1974] proposed a set of semi empirical equations which could deal with the thermodynamics of concentrated solutions. As these have proven successful, many models based on these equations have been developed to describe ion-ion interactions in solution [Harvie et al., 1984]. Pitzer's equations are based on the virial expansion for the excess Gibbs Energy (G^{ex}) principally made up of two parts (**Eq. 20**).

$$\frac{G^{ex}}{RT} = \left(w_w f(I_m) + \frac{1}{w_w} \sum_{ij} \lambda_{ij}(I_m) n_i n_j + \frac{1}{w_w^2} \sum_{ijk} \mu_{ijk} n_i n_j n_k \right) \quad (\text{Eq. 20})$$

Where w_w is the number of kilograms of solvent water, $f(I_m)$ is the Debye-Hückel function describing the first order long range electrical interactions between ions (**Eq. 21**) and n is the number of moles of solute species i, j or k . The virial coefficients λ_{ij} and μ_{ijk} are second order and third order interaction coefficients. The Debye-Hückel part is dependent on ionic strength and solvent properties but not on individual species, while the second part considers the binary interactions giving the effect of short range forces between solutes and the ternary interactions between the three solutes i, j and k . The virial coefficients λ_{ij} for the ion-ion interaction are also function of ionic strength, while this dependence can be neglected for the μ_{ijk} virial coefficients. The Pitzer approach allows more realistic modelling, but at the same time it increases significantly the number of parameters required for calculation.

The empirical form chosen by Pitzer for the first part $f(I_m)$ is:

$$f(I_m) = -A_\phi \frac{4I}{1.2} \ln(1 + 1.2\sqrt{I_m}) \quad (\text{Eq. 21})$$

Where A_ϕ is the Debye-Hückel constant for the osmotic coefficient and can be found in tables [Silvester & Pitzer, 1976] as a function of temperature.

Pitzer modified the equation for strong electrolyte systems to allow addition of more directly observable parameters (**Eq. 22**).

$$\begin{aligned} \frac{G^{ex}}{RTw_w} = f(I_m) &+ \sum_{cc'} n_c n_{c'} \left(\theta_{cc'} + \sum_a n_a \psi_{cc'a} \right) + \sum_{aa'} n_a n_{a'} \left(\theta_{aa'} + \sum_c n_c \psi_{aa'c} \right) \\ &+ 2 \sum_{ca} n_c n_a \left(B_{ca}(I_m) + \frac{\sum_c Z_c m_c}{\sqrt{Z_c Z_a}} C_{ca} \right) \quad (\text{Eq. 22}) \end{aligned}$$

Where c, c', a, a' and Z stand for cations, anions and absolute values of ionic charges respectively. New parameters θ and $B(I_m)$ are binary ion-ion interaction parameters, and ψ and C are ternary ion-ion parameters. The B and C parameters are characteristic of each aqueous *single* electrolyte system and are determined by properties of pure electrolytes, while the θ and ψ parameters are characteristic of each aqueous *mixed* electrolyte system [Chen et al., 1979; Pitzer & Mayorga, 1973; Pitzer & Kim, 1974]. The B parameter can be further expanded (**Eq. 23**).

$$B_{ca}(I_m) = \beta_{ca}^0 + \frac{\beta_{ca}^1}{2I_m} \left[1 - (1 + 2\sqrt{I_m}) \exp(-2\sqrt{I_m}) \right] \quad (\text{Eq. 23})$$

The activity coefficient can thus be expressed as:

$$\ln \gamma_i = \frac{1}{RT} (\delta G^{ex} / \delta n_i) \quad (\text{Eq. 24})$$

The adjustable parameters that have to be determined for given solution composition are β^0 , β^1 , θ , ψ and C . The binary parameter β_{ij}^0 describes the effect of repulsive forces between similar ions, while β_{ij}^1 describes the attractive force between oppositely charged ions. An additional term including β_{ij}^2 is considered for 2-2 and higher valence electrolytes. θ_{ij} and ψ_{ij} are mixing parameters in case of ternary and higher electrolyte systems and are not expected to contribute significantly in systems examined in this work. The full description of Pitzer equations can be found elsewhere [Chen et al., 1979; Koh et

al., 1985; Pitzer, 1973; Pitzer & Kim, 1974]. The obtained molal activity coefficients were recalculated into molar activity coefficient in this work where needed.

Databases

Geochemical calculations are some of the key tools being used for performance assessment studies, which allow quantification of geo/chemical reactions and RN speciation. Comprehensive and complete thermodynamic databases are crucial for any model or thermodynamic assessment. There are various databases with sets of thermodynamic data of radionuclides and other elements relevant to be used for the nuclear waste disposal safety case. The criteria for adequate database are completeness, tractability, consistency and ideally include various ionic strength models and temperature dependence. The most quality-assured thermodynamic database available for actinides and fission products is the NEA-TDB, the Thermochemical Database Project of the Nuclear Energy Agency. For instance, americium data were initially reviewed by Silva et al. [1995] and further updated in Volume 5 by Guillaumont et al. [2003]. The thermodynamic data for europium were reviewed by Hummel et al. [2002], who found that the majority of the selected constants were fairly close to the corresponding values of americium as expected due to similar chemical properties of the two elements. Hummel et al. [2002] at PSI were acquiring data and compiling a database for the National Cooperative for the Disposal of Radioactive Waste (NAGRA) supporting the safety assessment of possible Swiss nuclear waste repositories. The selection of thermodynamic data of iron was summarized by Lemire et al. [2013; 2020].

Within this thesis, speciation and solubility of europium and americium species were calculated using the PhreeqC software (version 3.4.0.12927) [Parkhurst & Appelo, 1999]. Guillaumont et al. [2003] and Hummel et al. [2002] provided the equilibrium constants for europium and americium for all used databases. For activity corrections, SIT and Pitzer approaches were used. The ThermoChimie database with SIT parameters [Grivé et al., 2015] was used for calculation of activity coefficients using the Debye-Hückel approach, while the Harvie-Moller-Weare database [Harvie et al., 1984] was chosen for the Pitzer approach.

ThermoChimie is a thermodynamic database developed by the French National Radioactive Waste Management Agency (ANDRA). Belgium and the UK later joined the ThermoChimie consortium. This database provides ion interaction parameters for ionic strength up to SIT capabilities [Grivé et al., 2015], therefore its applicability is constrained to low-intermediate ionic strength. This database is comprehensive, reliable regarding values for transition metals as well as radionuclides, and used in

this thesis for all calculations for low-intermediate ionic strength. It will be referenced when used as [TC]. The SIT parameters for Eu/Am species were provided by Neck et al. [2009].

THEREDA, the Thermodynamic Reference Database developed by various German research institutions aims at providing reliable thermodynamic data allowing geochemical modelling in high ionic strength solutions [Moog et al., 2015]. This database is applicable to saline solutions, uses Pitzer approach for activity coefficients calculations and to a large extent the Harvie-Moller-Weare database [Harvie et al., 1984]. THEREDA provides reliable ready to use databases for mainly actinides in solutions with high ionic strength [Neck et al., 2009]. This database is used for solubility and speciation calculations for high ionic strength in sorption part of this thesis as well as for surface complexation modelling and is referenced when used as [TPA].

PhreeqC was further used for temperature correction calculations for pH (explained in experimental part) and to obtain activities of all aqueous species in the corrosion experiments at 25 °C and 90 °C, which further served as an input for the Geochemist's Workbench (GWB) software (version 8.0) [Bethke, 1996; Bethke and Yeakel, 2018]. Act2 module of GWB was then used to obtain *Pourbaix* diagrams. For low-intermediate ionic strength, the Thermochimie database was used, however obtaining correct activity coefficients at high ionic strength was difficult, as no reliable Pitzer database for transition metals is available. Fortunately, PhreeqC and GWB offer a database largely based on Harvie et al. [1984;] with Pitzer parameters for iron, collected from various literature [Appelo, 2015; Millero et al., 1995; Pitzer and Mayorga, 1973; Plummer et al., 1988]. The data are however unconfirmed and thus a source of uncertainty for these calculations. This database will be referred to as [PI]. The aqueous species for the elements of interest in each database are shown in ***Annex Table A1***.

Surface complexation modelling of sorption and surface titration data (explained in ***section 1.3.5.3***) was done with FITEQL 2 code [Westall, 1982]. The Pitzer database [Harvie et al., 1984] with parameters from Neck et al. [2009] was used for calculations at $I > 0.1$ M and the Davies approach [Davies, 1962] for $I \leq 0.1$ M. Activity coefficients obtained using Davies and Debye-Hückel approach do not differ at such low ionic strength, thus no inconsistencies were created using different activity coefficient approaches under these conditions.

1.3.5.3 Surface complexation modelling

RN sorption onto mineral surfaces can be described by thermodynamic sorption models yielding equilibrium constants for the relevant sorption reactions under varying geochemical conditions. Surface complexation modelling is a powerful tool widely used to describe the sorption behaviour of RNs and other ionic species. One of its advantages is the ability to consider charges at surfaces as well as of the solutes in aqueous solutions and thus to take ionic strength effects into account [Lützenkirchen, 2006].

In order to choose the appropriate model a series of decisions on the model features such as electrostatic factors, type and number of surface sites and sorption reactions need to be made depending on the complexity of the system and objective of the study. Furthermore, a comprehensive model should be calibrated by experimental sorption data as a function of pH, ionic strength and sorbent concentration. Minerals should be characterized in terms of surface area, impurities and structure [Payne et al., 2013]. In this work, cation sorption to various metal oxides up to highly saline conditions based on own experimental data is modelled and under this scenario the surface charge and surface electrostatic play a significant role. Thus, an electrostatic model was adopted [Lützenkirchen, 2006].

Iron oxides are considered primarily in this work. They are known exhibiting variable charge surfaces on their different exposed surface planes. The many available electrostatic models differ in the treatment of the surface charge or the number of planes and sites. The different treatment of the surface charge is based on the description of the electric double layer forming at the solid-liquid interface. A Helmholtz double layer consists of two layers of opposite charges located on opposite sides of an interface [Helmholtz, 1853]. Thus, the charge on the mineral surface is compensated by the charge of a layer of ions on the solution side. This was the basis for Gouy and Chapman who introduced a diffuse layer of ions into the model, which extends further from the surface, also called Diffuse Layer Model. Stern then combined the two approaches and developed what is nowadays called the Basic Stern Model.

In the various models, the electrostatic potential varies with the distance from the surface in different ways. Regardless of the model, the specific surface area and site capacity must be specified and the formation constants of surface complexes are adjustable parameters which have usually to be fitted to experimental data. The Constant Capacitance Model has one immobile layer of specifically adsorbed ions and the capacitance is in this case either optimized or set to a recommended literature value. The diffuse layer model includes a diffuse layer of electrostatically bound counter-ions. A capacitance is not required in this model, only the intrinsic stability constants. The popular Triple Layer Model

includes two immobile layers (planes) and a diffuse layer of ions. Only hydroxyl groups are found on metal oxide surfaces. The inner plane contains ions that are specifically bound to surface groups of opposite charge while the outer plane is regarded as the head end of the diffuse layer. The two capacitances, one for each layer, are either optimized in the model alongside formation constants for the interaction of surface groups with the ions in the inner plane or set to literature values if known [Lützenkirchen, 2006]. A schematic representation of the triple layer model is shown in **Figure 7** with corresponding potentials and surface charge densities.

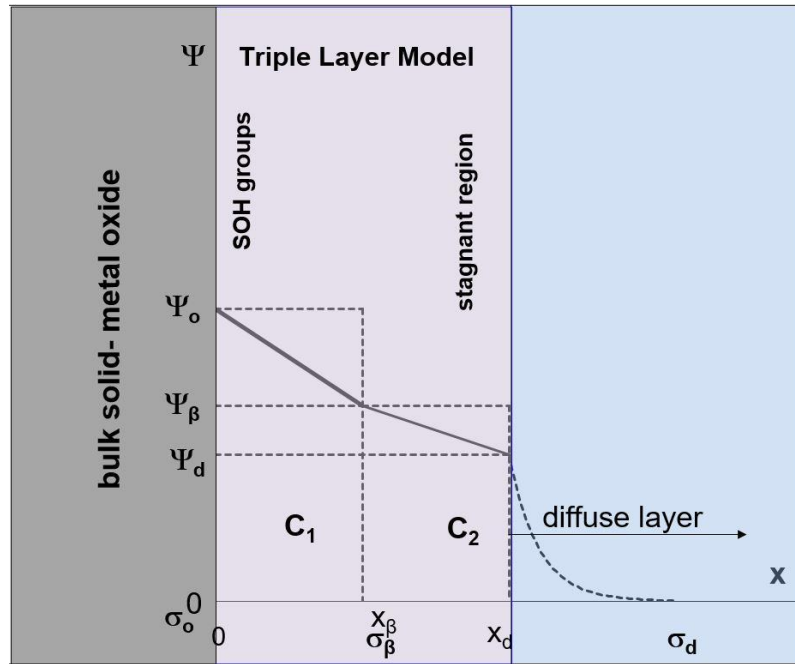


Figure 7: Schematic representation of the triple layer model with planes 0, β and d, with corresponding potentials ψ_0 , ψ_β , ψ_d , surface charge densities σ_0 , σ_β , σ_d , two capacitances in the Stern layer and a diffuse layer.

The effective surface charge density σ , the charge of the surface region equals to surface charge density of the diffuse layer but with an opposite sign. $\sigma = -\sigma_d$, which is also the sum of the surface charge densities of the 0 and β planes, $\sigma = -\sigma_d = \sigma_0 + \sigma_\beta$ [Lützenkirchen et al., 2012].

In this work, charge distribution generic site or multi-site complexation triple layer models [Davis et al., 1978] were used depending on the available information on the solid phase. The general approach developed by Hiemstra & Van Riemsdijk [1996] treats surface complexes as having a spatial charge distribution in the interfacial region over two electrostatic planes rather than considering them as point charges located in one electrostatic plane. Such point charges are a feature of a simple diffuse layer model and are known to lead to physically unrealistic results. The charge distribution multi side

complexation (CD-MUSIC) model is best suited to address known complex crystal structures. The development of the model used in this work was based on the following strategy.

1. The specific surface area is determined for a given sorbent. This is done using the Brunauer-Emmett-Teller (BET) method.
2. The relevant crystal planes, binding site types and site concentrations are defined. If this is not known from literature in combination with known particle morphology, generic sites are used to describe the surface functional groups. The number of generic sites may range from a single type of binding site to multiple sites possibly including “strong” and “weak” sites. Initial values for site concentrations are set to reasonable values and the model is iteratively redefined to better fit the experimental data.
3. The suitable surface reactions on the surface sites (point 2.) are defined.
4. The protonation/ deprotonation (titration) data on the specific sorbent and with it associated parameters (e.g. capacitances) are optimized. These are then fixed in the model.
5. Suitable surface reactions with the radionuclide are defined. In case of known surface complex structures, e.g. binding mode (obtained by spectroscopic techniques), these are incorporated.
6. The activity coefficients of all species in the solution and the dielectric constants of solutions are estimated for all used ionic strengths and applied in the model for all sorbents.
7. The uptake data of the radionuclide on the solid are modelled in various sites configurations until a satisfactory fit is achieved and associated complexation constants and charge distribution factors are obtained.

Overall, the final model is usually a compromise between the model complexity (number of sites and reactions) and fit to the experimental data.

2 Experimental

2.1 Materials and chemicals

2.1.1 Chemicals

All sample preparation and handling was performed in an Ar-filled glovebox with O₂ and H₂O content below 1 ppmv at 22 ± 2 °C. Ultrapure water (MilliQ system, 18.2 MΩ/cm at 25 °C) was used to prepare suspensions and electrolyte solutions which were further purged with Ar for 4 hours to remove traces of CO₂ and O₂ prior storage in the Ar glovebox or prior use. The pH electrode was calibrated using reference buffer solutions of pH 4, 7, and 10 (Radiometer Analytical) and the response of the E_h electrode was checked using standard buffer from Hach giving 220 mV at 25 °C. All other chemicals used in this work are summarized in *Annex Table A2*.

2.1.2 Steels

The two steel types used for corrosion experiments in this work were obtained from commercial suppliers ThyssenKrupp Acciai Speciali Terni (SS 309S - referred in this work as Cr-Ni steel) and Mittelrheinische Metallgießerei Heinrich Beyer GmbH (GGG40.3 - referred in this work as SGI). The steel specimen (coupons) were cut from a block of steel to obtain dimensions of 4 mm x 18 mm x 10 mm and 4 mm x 14 mm x 8 mm with 3 mm holes, providing surface area of ~ 10 cm². In order to reach low roughness and adequate morphology, all sides of each coupon were grinded on 500 SiC sheet (Struers, Knuth-Rotor 3) and polished with diamond containing paste up to ¼ µm (Buehler, Ecomet 1 Polisher). After polishing, ultrasound with ethanol was used to remove impurities, the samples were dried, weighted and put into an Ar glovebox to avoid oxidation. The initial state of the coupons was examined by various analytical techniques described in *section 2.2.4* to obtain an overview of the initial surface. The chemical composition of the steels according to the certificates provided by the manufacturers is shown in *Table 2*.

Table 2: Chemical composition of the steels according to the certificates/ wt. %.

Steel	C	Mn	Si	Cr	Ni	Mo	Cu	Mg	Fe
Cr-Ni steel	0.06	1.15	0.35	22.45	13.17	0.23	0.23	-	62.36
SGI	3.46	0.29	3.39	0.042	-	-	0.038	0.052	92.73

2.1.3 Mineral phases

As not all compounds of interest were available commercially, certain minerals were synthesised in house, usually oxygen sensitive or metastable compounds. The secondary phases for use in the sorption experiments and as reference compounds in spectroscopic studies were synthesized according to the routes described in **Table 3**. This table also shows few naturally occurring mineral phases used in this work. After the synthesis, all the compounds except of magnetite for sorption (already available as suspension with no salt content) were centrifuged for 15 mins at 14,500 rpm (~ 14,130 g). The supernatant was removed, the compound washed with deionized water and dried under argon atmosphere. The iron hydroxychloride batch 2 was synthesized by GRS Braunschweig and sent to INE under anoxic conditions. This batch yielded bigger particle size, 400 nm.

Table 3: Synthesis routes for secondary phases and references.

Secondary Phase	Synthesis Route	Particle size	Reference
Magnetite for Sorption Fe_3O_4	Heat 0.3 M (560 mL) of iron sulfate to 90 °C, 240 mL of 3.33 M KOH + 0.27 M KNO_3 . Heat for 60 minutes. Follow with dialysis, available in house.	100 nm	Cornell & Schwertmann, [1996]
Magnetite for Reference Fe_3O_4	45 mL MilliQ, 0.3 g $\text{FeCl}_2 \cdot 4\text{H}_2\text{O}$, 0.49 g FeCl_3 , 12.3 mL of 1 M NaOH.	-	Cornell & Schwertmann, [1996]
Green Rust Chloride –Pure $\text{Fe}_4(\text{OH})_8\text{Cl} \cdot n\text{H}_2\text{O}$	90 mL MilliQ, 2 g of FeCl_2 , 0.4 g FeCl_3 , 15 mL of 0.8 M NaOH.	500 nm	Génin et al., [1998]; Usman et al., [2018]
Green Rust Chloride –Doped $(\text{Ni,Cr,Fe})_4(\text{OH})_8\text{Cl} \cdot n\text{H}_2\text{O}$	42.5 mL MilliQ, 0.35 g of $\text{NiCl}_2 \cdot 6\text{H}_2\text{O}$, 0.49 g $\text{FeCl}_2 \cdot 4\text{H}_2\text{O}$, 0.06 g FeCl_3 , 0.085 g of CrCl_3 , 7.5 mL of 1 M NaOH.	-	Same path as pure GR added Cr and Ni ions
Iron hydroxychloride $\text{Fe}_2(\text{OH})_3\text{Cl}$	100 mL MilliQ, 47.7 g of $\text{FeCl}_2 \cdot 4\text{H}_2\text{O}$, 100 mL of 0.8 M NaOH. Let age for 24 hours.	200 nm	Réguer et al., [2015]
Nickel hydroxide $\text{Ni}(\text{OH})_2$	0.52 g of NiO in 50 mL of 3 M HCl, heat for 1 hour at 80 °C, 21 mL of 6 M NaOH.	-	Hall et al., [2015]
Akaganeite for Reference	Heat 2 l of 0.1 M FeCl_3 in closed vessel at 70 °C for 48 hours, available in house.	-	Cornell & Schwertmann, [1996]
Naturally occurring mineral phases used in this work			
Mineral	Formula	Molar mass	Origin
Greenalite	$\text{Fe}_{2-3}\text{Si}_2\text{O}_5(\text{OH})_4$	371.73	Excalibur-Cureton, US
Cronstedtite	$\text{Fe}_3(\text{Si,Fe})\text{O}_5(\text{OH})_4$	399.49	Muséum national d'histoire naturelle
Iron Chromium Oxide-Chromite	FeCr_2O_4	223.84	KIT-AGW, Karlsruhe, Germany

2.1.4 Europium / Americium

Europium was used for batch sorption experiments as a chemical analogue to trivalent actinides such as americium, curium and plutonium. Use of radioactive isotope allowed for direct gamma measurements and avoided dilution due to salt content, which would be needed for other quantification techniques such as high resolution (HR) inductively coupled plasma mass spectrometry (ICP-MS) (Thermo Element XR). The radioactive europium stock solution consisted of dissolved EuCl_3 obtained from Eckert & Ziegler Nuclitec with a composition of $> 95\%$ ^{152}Eu ($t_{1/2} = 13.5$ y), 3.76% ^{153}Gd and 0.55% ^{154}Eu , and an activity of 1×10^4 MBq/L on 15.3.2016. Inactive europium isotope ^{153}Eu stock solution used alongside active europium for experiments with high europium concentrations was obtained by dissolving Eu_2O_3 in 0.5 M HCl. In order to obtain structural information by application of XAS, americium was used to better fit the needs of the experiments as europium Eu L₃-edge (6977 eV) and iron Fe K-edge (7112 eV) have very close excitation energies, while americium Am L₃-edge (18,510 eV) is well above the Fe K-edge excitation energy. The isotopic composition of the Am stock solution was 99.5% ^{243}Am ($t_{1/2} = 7370$ y), 0.5% ^{241}Am ($t_{1/2} = 432.2$ y) and had an activity of 1.11×10^4 MBq/L. The concentrations of Am and inactive Eu in the respective stock solutions were confirmed by HR ICP-MS. ^{243}Am is a preferred isotope in research due to its lower specific activity and gamma emission compared to ^{241}Am .

2.2 Analytical methods

2.2.1 pH measurements

2.2.1.1 General definition & Measurements in saline solutions

The pH is defined as a negative decimal logarithm of hydrogen ion activity in a solution (*Eq. 25*), where M_{H^+} is a molar (molal) concentration of H^+ , γ_{H^+} is the molar (molal) activity coefficient of H^+ and M^0 is a constant representing the standard state conditions, either 1 mol/L or 1 mol/kg depending on the chosen scale. The difference between the two scales can be ignored for dilute systems [Buck et al., 2002; Covington et al., 1985]. In saline systems, attention must be paid to activity coefficients and whether molal or molar scale is used.

$$pH = -\log(a_{H^+}) = -\log\left(\frac{M_{H^+} \gamma_{H^+}}{M^0}\right) \quad (\text{Eq. 25})$$

As any other single ion activity, it is not directly measurable, as thus it is defined operationally by the means of an operational cell where potential difference between two electrodes, one hydrogen electrode and one reference electrode, is measured [Buck et al., 2002; Covington et al., 1985; Lützenkirchen et al., 2012]. Potential (mV) can be related to the activity of hydrogen ions via the Nernst equation (**Eq. 26**), which also explains strong temperature dependence of pH.

$$E = E^0 + \frac{RT}{F} \ln(a_{H^+}) \quad (\text{Eq. 26})$$

Where E^0 is the standard potential difference of the cell.

A combined glass electrode has a built in reference electrode, which can be calibrated against buffer solutions at low ionic strength with known hydrogen ion activity. This electrode is connected to a pH-meter which measures the potential between the two internal electrodes. This type of electrode has been used in this work for all pH measurements. The operational cell of this electrode type is:

Reference electrode (Ag/AgCl) | salt bridge KCl (c ≥ 3.5 mol/L) || solution [pH(Buffer) or pH(Sample)] | glass electrode.

The reference electrode is calibrated against 2-3 buffers in this work. In case of two reference buffers (B1, B2), the pH of the sample (S) is then obtained by the voltage difference between the sample and the standard buffer solution (**Eq. 27**) where calculation of the potential of the sample is shown in **Eq. 28** [Lützenkirchen et al., 2012]:

$$pH(S) = \frac{[E(S) - E(B1)]}{[E(B2) - E(B1)]} \times [pH(B2) - pH(B1)] + pH(B1) \quad (\text{Eq. 27})$$

$$E(S) = E^0(Ref) - E^0(Glass) - E_A + \frac{RT}{F} \ln(a_{H^+}) + E_j(S) \quad (\text{Eq. 28})$$

The same principle then applies for calculation of the potential for buffer 1 and 2. The $E^0(Ref)$, $E^0(Glass)$ and E_A , standard potentials of the reference electrode and glass electrode as well as asymmetry potential of the glass electrode remain the same for buffers and sample and thus cancel out. The difference in the liquid junction potential E_j (potential at the interface between electrolyte in the reference electrode and the sample/buffer solution) between the sample and the buffers requires low ($I \leq 0.1 M$) and similar ionic strength for all buffers and sample solution. [Buck et al., 2002; Covington et al., 1985]. In the case of samples with elevated/ high ionic strength, not only is the junction potential difference significant, but also the activity coefficient is affected and thus this method is no longer valid for accurate pH determination.

In saline solutions, $I \geq 0.1$ M, the pH is expressed in terms of concentration rather than activity (*Eq. 29*). This value is calculated from the measured experimental pH (pH_{EXP}) and an empirical correction factor (A) which accounts for the liquid junction potential effect and activity coefficients changes of H^+ (*Eq. 30, 31*) for a given electrolyte system.

$$pH = -\log(a_{H^+}) = -\log M_{H^+} - \log \gamma_{H^+} \quad (\text{Eq. 29})$$

$$pH_M = -\log M_{H^+} = pH_{EXP} + A_M \quad (\text{Eq. 30})$$

$$A_M = \log \gamma_{H^+} + \Delta E_j \frac{F}{RT} \ln 10 \quad (\text{Eq. 31})$$

A values are experimentally determined as a function of the brine type and concentration, and can be calculated from the empirical polynomial published in literature for various salts [Altmaier et al., 2003; 2008]. All pH_M values in this work refer to the molar concentration of protons.

2.2.1.2 pH measurements and corrections in this work

The electrode used for pH_{EXP} measurements in corrosion and sorption experiments is a Metrohm solitrode pH electrode with reference electrolyte 3 M KCl. The pH_{EXP} measurements were performed in corrosion and sorption studies in Ar gloveboxes at room temperature. The pH electrode was conditioned in 0.5 M HCl solution for 10 minutes, stored in 3 M KCl solution and rinsed with deionized water prior every use. The pH electrode was calibrated using reference buffer solutions at pH 4, 7 and 10 (Radiometer Analytical) prior pH measurement. No buffer additions or pH adjustments were performed in the corrosion studies.

In all samples in the sorption studies, one of the following buffers (MES, MOPS or TRIS) was used. The middle pH (pK_a) values for the buffers are shown in *Table 4*.

Table 4. The buffering range and pK_a values of pH buffers used in this work.

Buffer	Name	pH range (25 °C)	pK_a value
MES	2-(<i>N</i> -Morpholino)-ethanesulfonic acid	5.5 - 6.7	6.10
MOPS	3-(<i>N</i> -Morpholino)-propanesulfonic acid	6.5 - 7.9	7.14
TRIS	Tris (hydroxymethyl)-aminomethane	7.5 - 9.0	8.06

pH_{EXP} adjustments were done using 0.1 M and 0.5 M HCl, and 0.1 M and 0.5 M NaOH.

The A factors used in this work for NaCl and MgCl₂ brines at room temperature are summarized in **Table 5** [Altmaier et al., 2003]. The pH_{EXP} was measured for 10 minutes in sorption samples and up to 1 hour for corrosion samples to allow stabilization.

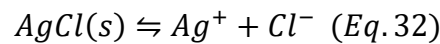
Table 5: Correction factors for ionic strength (A factors).		
Background Electrolyte		Experiment
Molarity	Molar A Factor	Corrosion/Sorption/Titration
0.1 M NaCl	-0.076	Corr/ Sorp/Titr
0.94 M NaCl	0.075	Sorp
0.95 M NaCl	0.077	Sorp
0.96 M NaCl	0.08	Sorp
1 M NaCl	0.087	Titr/Corr
2.8 M NaCl	0.45	Sorp
2.9 M NaCl	0.47	Sorp
3 M NaCl	0.49	Corr
4.7 M NaCl	0.88	Sorp
4.8 M NaCl	0.9	Sorp
5 M NaCl	0.95	Corr
0.033 M MgCl₂	-0.06	Corr/Sorp
0.31 M MgCl₂	0.06	Sorp
0.33 M MgCl₂	0.07	Corr
0.95 M MgCl₂	0.37	Sorp
3 M MgCl₂	1.6	Corr
3.25 M MgCl₂	1.8	Sorp
3.4 M MgCl₂	1.9	Corr

As the pH_M electrodes were not mounted on the autoclaves, it was not possible to measure the in-situ pH_{EXP} at 90 °C, but only after cooling down at room temperature. As mentioned in **section 2.2.1.1** the pH_M is dependent on the temperature and a significant shift was expected between the two temperatures. In order to get a meaningful pH_M of the system, the initial and final pH_M values for experiments at 90 °C were recalculated using the PhreeqC software. The software can use the measured pH_M, E_h and dissolved metals content determined by HR ICP-MS at 25 °C as an input and recalculate the values for pH_M for the same system at 90 °C. Depending on the systems, either the [TC] database with SIT approach was used (all Cr-Ni steel systems and low I systems for SGI) or the [PI] database with Pitzer approach (high I systems for SGI). The pH_M uncertainty at room temperature was determined as ± 0.05 unit after repeated measurements and calibrations at various times. The recalculated pH_M at 90 °C has much larger uncertainty, which comes from HR ICP-MS uncertainty and database completeness and reliability. The value for the maximum uncertainty for the recalculated

pH_M was estimated as 0.5. As the sorption experiments are performed at room temperature, no temperature correction is applied in this case.

2.2.2 E_h measurements

The potential was introduced in *section 1.3.1*. It can be expressed by Nernst equation (*Eq. 4*). The electrode used for redox potential measurements is a Radiometer Analyticals Ag/AgCl combined platinum E_h electrode with 3 M KCl internal electrolyte. The corresponding electrochemical reaction can be presented as follows:



with the potential depending on the activity of chloride ions. The conversion of measured E_h into potential of standard hydrogen electrode (S.H.E.) is calculated from the Nernst equation with $E^0_{Ag/AgCl} = 0.22249$ V [Bates & Macaskill, 1978] (*Eq. 33*).

$$E = E^0_{Ag/AgCl} - \frac{RT}{F} \ln a_{Cl^-} = 0.208 \text{ V at } 25 \text{ }^\circ\text{C} \quad (Eq. 33)$$

This factor (+208 mV) is also confirmed in the literature [Friis et al., 1997]. Same cleaning steps as for the pH electrode were applied on the E_h electrode. The response of the electrode was tested using a reference buffer solution of +220 mV vs. Ag/AgCl (Hach) prior measurements. In case of deviation (usually below 20 mV), this was taken into account and the final values were corrected for the offset. The E_h was measured without agitation up to 1 hour in corrosion samples to allow stabilization and achieve a drift in E_h below 0.5 mV/min. All E_h values reported in this work are with respect to S.H.E. In PhreeqC, the potential values needed for pH_M recalculations are input as pe values, and are recalculated from E_h using the *Eq. 7*.

The correction for pH_M with respect to temperature was described in *section 2.2.1.2*. The E_h correction with respect to temperature is not as straightforward and cannot be recalculated as the exact contribution of different dissolved species in the solution is not known. The variation of the standard electrode potential for various pairs (Fe²⁺/Fe³⁺; Cr⁰/Cr³⁺ etc.) with temperature is summarized in work of Bratsch [1989], but also in this study it is constrained to water and not ionic solutions. No empirical correction factor is available for the E_h measured in solutions with high ionic strength, which would account for variations in liquid junction potential. Liquid junction potentials should not exceed 50 mV

in the conditions of this study [Barry, 1994; Yalçıntaş et al., 2015]. This can be considered as an uncertainty for the E_h measurements.

2.2.3 Determination of gas phase composition & dissolved metals concentration in solutions

The gas phase in the corrosion experiments was characterized by a quadrupole gas mass spectrometer (GAM400, In Process Instruments, Pfeiffer Vacuum). The gas sample was collected in an Ar glovebox using a gas sampling cylinder which was previously evacuated to vacuum of 10^{-11} Pa (**Figure 8**). Then it was mounted onto the experimental equipment and the vent was open. A steel filter between the equipment and the sampling cylinder was used to prevent potential moisture from entering the gas sampling cylinder. The spectrometer was calibrated on a known gas mixture and the mass spectrometer was pumped overnight to vacuum to remove any residual moisture coming from the sample. The mass spectrometer measures the mass to charge ratio of gas components and produces results in terms of the intensity as a function of the mass which gives the composition of the gas.



Figure 8: The gas sampling cylinder used for sampling of the gas phase.

The main gases of interest were H_2 and O_2 . Low oxygen content in the gas phase confirmed tightness of the setup, while high hydrogen content hinted at higher degree of corrosion. The tightness of the setup was a crucial property as oxygen intrusion indicated oxidizing environment, which would no longer represent the repository conditions.

High resolution inductively coupled plasma mass spectrometry (HR) ICP-MS (Thermo Element XR) was used in this work to quantify the total concentration of metals in the aqueous phase. The ICP-MS uses an inductively coupled plasma to ionize the sample. In the corrosion and sorption studies the liquid phase was ultracentrifuged (Beckman Coulter XL-90 K) for 30 minutes at 90,000 rpm (~700,000 g) and a 2 mL acidified aliquot was given for the analysis. The samples were diluted to achieve salt content below 50 mg/L due to the equipment limit for the salt matrix. The concentration of dissolved metals was then recalculated back in mg/L. In corrosion and sorption studies, Fe, Ni and Cr were

quantified, depending on the steel type/ solid phase used as a sorbent. Additionally, elements of interest in stock solutions were quantified as mentioned in *section 2.1.4*.

2.2.4 Corrosion phase/ Solid phase characterization

The initial steel samples, the formed corrosion phases on the steel samples in the corrosion experiments and the secondary phases used as sorbents in sorption experiments were characterized using the following methods:

- Atomic force microscopy: AFM determines an average surface roughness, it was applied on the initial steel surfaces. The RMS (root mean square) roughness was evaluated for both steels.
- Scanning electron microscopy (SEM, Quanta 650 FEG, FEI) - Energy dispersive X-ray spectroscopy (EDX, Thermo Scientific NORAN System 7) analysis was used to obtain the morphology and elemental composition of the secondary phases on corroded steels and synthesised or purchased compounds. The obtained elemental spectra were analysed and quantified using the NSS software (Thermo Scientific). The samples were prepared in an Ar box and positioned inside the microscope with short air exposure.
- X-ray photoelectron spectroscopy (XPS, VersaProbe II, ULVAC-PHI, Al K α monochromatic X-ray excitation) determined the elemental composition and oxidation states of the identified elements aiding with identification of secondary phases on corroded samples and characterisation of impurities in synthesised and purchased compounds used in sorption experiments. XPS probes only couple nm of the examined surface in comparison to EDX, which samples the depth in the range of μm . The samples were prepared in an Ar box and directly placed inside the XPS equipment without air exposure.
- X-ray diffraction (XRD, D8 Advance from Bruker AXS, Cu-K α radiation, Sol-X /LynxEye XE-T detector) was used to determine the purity of certain commercially obtained compounds, confirm the identity and possible impurities of the synthesised compounds and to characterize the crystalline secondary phases on the corroded steels. The redox sensitive compounds and all corrosion samples were measured encapsulated in a special anoxic holder, which was closed in an argon atmosphere. The measurements were performed in angles of 2θ ranging from 2 to 80° with incremental step of 0.02° and a measurement time of 0.5-1s per step. This duration avoided the diffusion of oxygen and ensured anoxic conditions throughout the measurement. The obtained spectra were analysed with the Diffrac.Eva software [version 5.0] and compared to a JCPDS database (Joint Committee on Powder Diffraction Standards) [1970].

- Raman spectroscopy is another technique which could provide information about chemical structure and directly identify a compound. It is not restricted to crystalline powders which is a limitation of the XRD technique. Certain synthesised compounds were measured by Raman spectroscopy. Special anoxic copper holders were developed in house and used for redox sensitive samples. Various spots of $1000 \times 500 \mu\text{m}^2$ using a 532 nm wavelength laser were measured for 20-40 minutes using 10x magnification. The obtained spectrum was then compared to various literature data due to the absence of database in the OPUS software [version 7.5, Bruker Optik].
- Certain corroded samples were embedded in epoxy resin (Buehler), crosscut and polished with 500 SiC grinding paper and further $1 \mu\text{m}$ diamond paste under air. SEM-EDX measurements were done on the crosscut allowing better examination of the steel-corrosion products interface.
- The specific surface area of solid compounds is an essential information needed for the surface complexation model and for the sorption experiments allowing exposure of the same surface area for various compounds and thus direct comparison. The determination of specific surface area is done using a Brunauer-Emmett-Teller (BET) technique performed in house using Autosorb 1 equipment from Quantachome. This technique was performed on all **not** redox sensitive compounds used for sorption experiments, as the complete analysis is not performed under anoxic conditions.
- The last technique performed on the corroded steel samples was weight loss measurement allowing the estimation of the corrosion rate. The steel coupon was dipped several times in a solution of 50 wt. % de-ionized water and 50 wt % 6 M HCl containing 5 g/L hexamethylene tetramine, which hinders dissolution of non-corroded steel surface and only allows dissolution of the hydr(oxides) under acidic conditions [Bayol et al., 2007]. Subsequently the weight was measured and the weight loss allowed determination of the corrosion rate (CR) in m/a (*Eq. 34*).

$$CR = \frac{\Delta m}{S \times \rho_S \times t} \quad (\text{Eq. 34})$$

Where Δm is the weight loss in kg, S is the surface area of the steel coupon in m^2 , ρ_S is the steel density and t is the exposure time in years. Initial steels were likewise tested in the removal solution to obtain the mass loss of the non-corroded surface if any and thus compensate for the error. The post corrosion cleaning of the specimen follows the ASTM G1-03 standards [2003].

2.3 Iron granules corrosion experiments

As iron is the major constituent of the two steels investigated in this work, a set of preliminary experiments including pure zero valent iron was done to get an approximate idea of the corrosion evolution and formed secondary phases. Furthermore, this simple system would further allow comparison to the more complex steel compositions and the effect of various other constituents on corrosion and secondary phases' formation. The starting material were commercially obtained 2 mm large iron granules, which were cleaned by washing shortly with 5 mM HCl. The granules were estimated as spheres and the surface area of the solid to brine volume ratio 1:5 was used (2.64 g of granules and 50 mL of brine). Experiments were performed in PFA (perfluoroalkoxy alkane) containers with screw closing considering contact times of (2), 6, 12 and 18 weeks. For the liquid phase, various brines were compared: NaCl solutions with $I = 1$ M and 3 M, and MgCl₂ with $I = 1$ M and 9 M for experiments performed in an oven at 60 °C. The preparation of the experiments as well as the sampling was done inside an Ar-filled glovebox to ensure anoxic conditions. pH_{EXP} and E_h were measured initially prior the experiments and then prior each sampling. The pH_M was recalculated for 60 °C with PhreeqC software using Pitzer approach for activity coefficients calculations and [PI] database. The pH_{EXP} and E_h were measured after cooling down to room temperature in the Ar glovebox. After pH_{EXP} and E_h measurements, part of the granules and of the brine were removed in such manner to allow the surface area to volume ratio remaining constant (15 mL of brine and 0.8 g of iron granules). After sampling the containers were closed again and placed back into the oven. The various analytical techniques were applied on the removed granules, which were briefly washed to remove dried salt content (XPS and SEM-EDX) and on the liquid phase (ICP-MS). The precipitates in the liquid phase were examined by X-ray diffraction (XRD). The results of these experiments are reported in the *Annex*.

2.4 Autoclave corrosion experiments

The long-term corrosion experiments were performed for the two types of steels described in depth in *sections 1.3.2* and *2.1.2*, the stainless steel 309S used for the vitrified waste container and the spheroidal graphite iron (GGG40) used for the spent fuel canister. The specimen preparation was described in *section 2.1.2*. The polished steels were initially characterized using the XPS, AFM, XRD and SEM-EDX analytical techniques. Raman spectroscopy cannot be performed on metals, only on metallic oxides/hydroxides. The corrosion experiments were performed in tightly closed vessels

(autoclaves), which were designed and built according to the experimental needs. The autoclaves are small reactors consisting of a stainless steel body, a Teflon and tantalum internal liner (tantalum is a highly corrosion resistant metal), fluorocarbon rubber Viton O-ring, underlid steel plate and a stainless steel lid. The tight closing is ensured via 6 screws. The fluorocarbon rubber Viton O-ring was chosen due to its ability to prohibit the escape of hydrogen, which is expected to form. In order to follow the evolution of the gas phase during the corrosion process as well as to avoid the overpressure, some of the autoclaves were modified and the lid was fitted with a manometer, an overpressure valve and a valve for sampling of the gas phase for mass spectrometry measurements (fittings also made of tantalum). All parts were ordered from PARCOM (Bad Schönborn, Germany) and mounted on the autoclaves in house (**Figure 9**). After fitting the lid with tantalum connections, the autoclaves were tested for tightness of the connection welds with water at 62 bars for 30 mins. Additional tightness test was conducted after the autoclaves were fully mounted with fittings, with nitrogen up to 10 bars for 10 mins. Both tests confirmed the tightness of the setup. Prior to the experiments, the autoclaves were thoroughly cleaned with ethanol. The total volume of the autoclave was 90 mL.

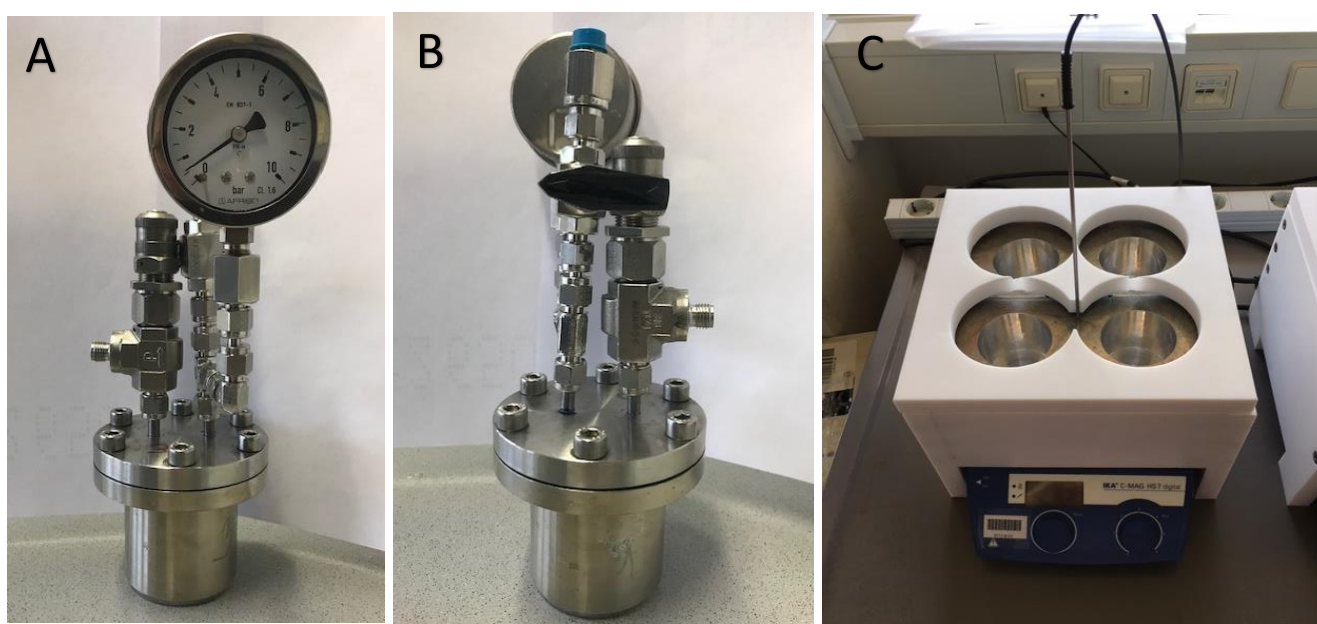


Figure 9: The autoclave setup with fittings (A, B) and the heating setup (C).

The steel coupons were placed onto a Teflon stand and fully submerged in the brine, not touching the bottom and not touching each other to avoid galvanic corrosion. In each autoclave, the setup consisted of two coupons (surface area of 9.50 cm^2) and 48 mL of brine giving the 1:5 surface area to brine volume ratio. This also allowed for additional free space for the formed gas. This steel surface area to brine volume ratio has been adopted in some of the previous corrosion studies [Smailos et al.]. There

are studies confirming the effect of the ratio on corrosion, particularly higher volume to surface area ratio causing higher availability of H⁺ ions and hence higher corrosion rate [Smailos, 1985].

The brines used in the corrosion experiments were taken from the literature describing the Asse [Kienzler & Loida, 2001] and Gorleben [Kursten et al., 2004] salt dome brine composition. In case of groundwater coming in contact with the canister, the composition of the brine is either saturated NaCl or MgCl₂, with NaCl being more likely. There are also traces of calcium, sulfate and potassium present. In order to distinguish the effect of NaCl and MgCl₂ with regard to the additional elements, four brines were prepared: brine saturated with respect to NaCl, brine saturated with respect to MgCl₂ and two so called solutions 1 and 3, which correspond to saturated NaCl or MgCl₂ with addition of respective salts as found in the literature. The solutions were prepared from high purity reagents described in **Table A2**. All solutions were diluted to 95 % saturation in order to avoid precipitation. **Table 6** shows the composition of the respective brines. One set of experiments was also performed with dilute brines with $I = 0.1$ M NaCl and $I = 0.1$ M MgCl₂ to allow the comparison of the corrosion phases formation and corrosion rates with respect to the chloride concentration.

Table 6: Composition of brines used in the corrosion experiments.

Salts	Solution 3/M	Saturated NaCl/M	Salts	Solution 1/M	Saturated MgCl ₂ /M
NaCl	5	5	NaCl	0.31	-
CaCl ₂ ·2H ₂ O	0.0188	-	KCl	0.8	-
Na ₂ SO ₄	0.0188	-	MgCl ₂ ·6H ₂ O	3.4	3.4
K ₂ SO ₄	0.015	-	MgSO ₄ ·7H ₂ O	0.15	-
MgSO ₄ ·7H ₂ O	0.015	-	-	-	-

Prior the filling of the autoclaves, the polished coupons were weighted. The coupons were hanged onto the Teflon stand including spacers and the autoclaves were filled with respective brines. The pH_{EXP} and E_h were measured as described in *sections 2.2.1.2* and *2.2.2* and the autoclaves were closed inside the Ar glovebox. The pressure for the experiments is atmospheric (1 atm).

Our corrosion experiments focused on room temperature and on 90 °C [Kommission Lagerung hoch radioaktiver Abfallstoffe, 2016], as the groundwater is not expected to enter the repository chamber in the beginning of the disposal but rather later on when the temperature already decreased.

For the experiments performed at elevated temperature, it was not possible to use the oven to heat the autoclaves with fittings due to the limitation of the manometer material which could not withstand the temperature of 90 °C. A different setup was developed. Two aluminium blocks with 4 holes each to fit the autoclaves were manufactured in house and set onto heating plates with dimensions of 215 x 215 mm². 8 autoclaves could therefore be heated simultaneously. The whole setup was carefully isolated by an additional block of Teflon leaving the bottom free for cooling of the heating plate. A hole was made in the aluminium and Teflon to accommodate the heating element for the temperature control (*Figure 9*). The heating plate setup was tested to obtain the temperature offset within the autoclave. As the temperature was not measured directly in the autoclave, but rather within the aluminium block, the vapour pressure of water on the manometer allowed determination of the temperature within the autoclave and further correction with respect to the heating block temperature. Additional tests with an open autoclave and thermometer were done to confirm the temperature offset. The uncertainty for the temperature in the autoclave was determined as ± 3 °C. One set of experiments, run in the laboratory outside of the glovebox, showed that in long-term, oxygen may intrude inside the autoclave and the whole setup was placed inside of a newly built glovebox continuously flushed with nitrogen to minimize possible oxygen intrusion over extended period of time. The experiments run at the room temperature were placed in either argon filled or nitrogen filled box. The environment of the autoclaves for various experimental batches is summarized in *Annex Table A4*.

Since corrosion is a slow process, long-term corrosion experiments were performed in this PhD study. The aim of these experiments is to obtain the corrosion rate, to identify which secondary phases are formed, what is the underlying corrosion mechanism and additional effects of temperature, sulfate presence and various brine compositions. Corrosion process of the waste package as well as the solubility of the waste matrix in the groundwater is affected by many parameters such as pH, E_h , partial pressure of CO₂, and presence of various cationic, anionic and other species. Additional factors influence corrosion processes in the repository such as defects in welds, radiation from the waste package, which produces certain oxidizing species as well as the reducing effect of bacteria. These are beyond the scope of this thesis.

The set of 4 autoclaves without fittings and 12 autoclaves mounted with fittings were used, in which the experiments were run batch wise in various configurations of brines, temperatures and exposure summarized in *Annex Table A4*. Experiments at various temperatures allow the observation of the temperature effect on the corrosion rate, while the different exposure times aids observation of the corrosion front progress and possible corrosion phases' transformation as well as determination of the mean corrosion rate.

At the end of the experiment, the heated autoclaves were cooled down to the room temperature inside the argon or nitrogen filled glovebox. Next, the sampling cylinder was mounted onto the fittings, the gas phase was sampled and subsequently the composition determined by mass spectrometry. Once opened, the E_h and pH_{EXP} measurements took place prior to the removal of the coupons. The pH_{M} for heated experiments was recalculated as described in *section 2.2.1.2*. The brine was sampled and examined for concentration of dissolved Fe (Ni, Cr) using the HR ICP-MS technique. The corroded coupons were quickly washed by de-ionized water and then blown dry to get rid of the salt content on the surface. Subsequently the smaller coupon was taken for XPS measurement followed by SEM-(EDX) measurement. The larger coupon was for examination by XRD technique. All the measurements as well as the transport were performed under anoxic conditions or vacuum. Some of the samples were then embedded in resin, crosscut and send for additional SEM-EDX measurement. At last, the weight loss of the coupons was determined and corrosion rate calculated after which the coupons were discarded.

2.5 Sorption of trivalent actinides onto secondary phases detected in corrosion experiments

2.5.1 Solid phase titrations

The surface charge behaviour of the solid in the solution as a function of pH is one of the crucial inputs into a surface complexation model. A method for measuring the surface charge is acid-base titration, examining the number of protons sorbed/desorbed by the solid particles as a function of the pH. Ideally, the titration is performed on the specific solid used in the sorption experiments and the protonation /deprotonation constants are determined directly from the model. In this case, the specific surface area needs to be known. These constants may also be found in the literature, but are not available for many solids. Within the framework of this thesis, the titration should be performed at various ionic strengths because this parameter affects the electrostatic forces, as ions of opposite charge to that of the surface create a shielding effect of the surface charge. In this work, five different solid phases were used for sorption experiments: green rust chloride, iron hydroxychloride, magnetite, trevorite and chromium oxide. There are no titration data available for iron hydroxychloride due to its very narrow stability pH range [7.6-9] and its strong reactivity with oxygen. Very scarce titration data is available for green rust sulfate and carbonate [Guilbaud et al., 2013], also due to metastability of green rust and its narrow stability pH range [7-9]. The titration was not performed for green rust chloride and iron hydroxychloride as it was not possible to accurately determine the specific surface area by the BET

method due to the sensitive nature of these two phases. The titration was however performed on the remaining three solid phases.

In case of trevorite, 0.04 g of solid was added to 30 mL of NaCl for various molarities (0.1 M and 1 M) and 50 μ L of 1 M NaOH was added to obtain alkaline initial conditions. This equilibrated mixture (10 hours) was titrated using the Metrohm 907 Titrando with Metrohm 801 Stirrer by injecting 10 μ L of 0.25 M HCl every 1-2 minutes (drift < 0.3 mV/min) until pH 4.5 was achieved. The raw data from the titration set-up were measured electrode potentials vs. cumulative volume of the added acid (base). The titration was done under humidified argon that was passed through a NaOH solution to avoid interference from carbon dioxide.

Using an excel-macro (Titrator Journal), the titration raw data (in most cases the number of data points was reduced prior to using the macro) were used to calibrate the measurement set-up (i.e. to transfer measured potentials to proton concentrations) and to calculate the relative amount of protons on the target surface. The input parameters required for this treatment on proton (molar) concentration scale were the pK_w (dissociation constant of water) for a given ionic strength. These values were a priori calculated using Geochemist's Workbench with the appropriate ion-activity model. The activity coefficients involved in these calculations are self-consistent with those used in the surface complexation model calculations.

For the calculation of the relative surface charge density, the raw data were converted to molar proton concentration, which were then, in combination with the known total proton concentration, used to calculate the amount of protons consumed or released by the surface. This amount was recalculated to charge density using the Faraday constant, the known mass of mineral in the suspension, the known volume at each titration point and the independently determined specific surface area of the mineral of interest [Lützenkirchen et al., 2012]. In this, the theoretical blank (which is consistent with the calibration/blank titration in the absence of the mineral surface but otherwise identical conditions) is subtracted. The equation is given below:

$$\sigma = \frac{F}{S \times A} \times [(C_A - C_{B_I}) - (C_{H^+} - C_{OH^-})] \times \frac{V_I}{V_2} \quad (Eq. 35)$$

Here, the σ is the relative surface charge density in C/m², F is the Faraday constant (96485 C/mol), S is the solid content in g/L, A is the specific surface area determined by BET method in m²/g, C_A and C_{B_I} are the cumulative acid and initial base concentrations in moles respectively, C_{H^+} and C_{OH^-} are

the free concentrations of H^+ and OH^- in the solution in moles and V_I and V are the initial and cumulative volume in litres accounting for the dilution of S and acid at every step.

The new output was the pH_M vs. relative surface charge density. To obtain absolute values the point of zero charge is needed. In the case of magnetite the independently measured isoelectric point was used, while in other cases the values of point of zero charge were taken from the literature.

The commercially obtained trevorite mineral has a large surface area, as determined by BET, thus less solid was required for titration. The point of zero charge (PZC) at 25°C for trevorite was taken from the literature as 8.3 [Barale et al., 2008; Martin Cabañas et al., 2011]. A value measured directly for the specific solid was unobtainable as the equipment for zeta potential measurements was unavailable. In the literature, the point of zero charge is given in terms of activity, but the model incorporates the pH as a molar proton concentration pH_M , so this correction was made using the calculated activity coefficients. The point of zero charge was corrected for the molar proton concentration for each ionic strength used in the titration experiments, and the charge was shifted to get the point of zero charge according to the corrected pH_M for each ionic strength. This then gave the absolute surface charge density. The logarithm of the activity coefficient was obtained as -0.1 for 0.1 M and -0.05 for 1 M.

Similar procedure was followed for the titration of Cr_2O_3 . Due to a small surface area, 0.56 g of chromium oxide was titrated. The other quantities remained as in the case of trevorite. The point of zero charge for this solid was taken as 7.9 [Blesa et al., 2000; Wiśniewska & Szewczuk-Karpisz, 2013] and corrected to pH_M as described above.

Magnetite was titrated manually in an argon box due to its sensitivity towards oxidation. The background electrolyte solutions were 0.1 M and 1 M NaCl (25 mL each) with 1.08 g of magnetite giving an exposed surface area of magnetite of 14 m². Similarly in this case, 35 µL of 1 M NaOH was added and the solution was equilibrated for 24 hours. Next, 100 µL of 0.01 M HCl were added every 2 minutes and the pH_{EXP} was recorded until pH_{EXP} around 5 was achieved. It was preferential to start at alkaline conditions to avoid dissolution of magnetite in acidic pH region. The point of zero charge was found at $pH_M = 6.4$, which is in agreement with the independently measured isoelectric point. This is also in agreement with various published data summarized in a recent review by Vidojkovic & Rakin [2017].

For the three solids the obtained pH_M vs. absolute surface charge density values served as the experimental input for the surface complexation models.

2.5.2 Europium uptake

The uptake of europium by various solid phases was investigated in batch type experiments in background electrolytes of NaCl and MgCl₂ brines with various ionic strength. The percentage of sorbed Eu and solid-liquid distribution coefficients (K_D values) for europium were obtained as a function of pH_M for several fixed Eu concentrations (5.1×10^{-10} M, 1×10^{-7} M, and 1×10^{-5} M). The examined pH_M range was depending on the mineral and limited at the lower limit by the solubility of the phase and at the upper limit to avoid precipitation of Eu(OH)₃ and other europium phases. The solid to liquid ratio was varying with respect to different solid phases to obtain same exposed surface area or in case of very soluble phase to prevent dissolution prior sorption. In the screw-cap vial (PP, 20 mL, Zinsser Analytic), the solid phase and the background electrolyte were equilibrated for 24 hours, after which the respective buffer was added (MES, MOPS, TRIS) to reach 20 mM in the solution. The use of buffer was required to avoid undesirable pH shift in samples.

After a further equilibration time of 5 hours, the europium was added. For europium concentration of 5.1×10^{-10} M, only active europium was used, while for the higher concentrations (1×10^{-7} M and 1×10^{-5} M) the inactive europium was added as well. The pH_M was adjusted using 0.5 M and 0.1 M HCl, 0.5 M and 0.1 M NaOH to obtain the desired pH_M value. Usually for each system all three buffers were used due to different pH (pKa) values of different buffers, thus fewer adjustments with acid or base were needed to cover the required pH_M range. The summary of the experimental conditions for the sorption samples is shown in *Annex Table A5*.

A brief kinetic study was done for all systems, where phase separation took place after 2, 4, 24 and 72 hours to confirm the time needed to reach equilibrium. After the pH_M adjustment and further equilibration period of 24 hours (for magnetite, green rust, chromium oxide) or 72 hours (for trevorite, iron hydroxychloride), a given suspension was ultracentrifuged (Beckman Coulter XL-90 K) at 90,000 rpm (~700,000 g) for 30 minutes. After the phase separation, the solid phase was disposed and the supernatant (2 mL) was acidified with concentrated HCl or HNO₃ (50 μ L) to avoid wall sorption. The concentration of the radionuclide in the supernatant was quantified using a gamma counter (Packard Cobra Auto-Gamma 5003). In the case of use of inactive europium, the ratio of active/inactive europium in addition to the gamma counting results was used to obtain the total europium concentration in the solution. An aliquot of the supernatant was also analysed by HR ICP-MS to quantify the content of dissolved Fe/Ni/Cr to conclude whether dissolution of the solid phase had occurred and to which degree.

The sorption isotherm studies performed only for magnetite followed similar experimental procedure, separation and measurement processes. In the latter, the amount of europium sorbed at the magnetite surface (in mol/g) was obtained for $I = 0.96$ M, 2.9 M and 4.8 M NaCl at constant solid to liquid ratio (0.5 g/L) and Eu concentration ranging from 1×10^{-4} M to 5.1×10^{-10} M at constant $\text{pH}_M \sim 6$ and ~ 7 . The data was then plotted as a function of initial Eu concentration in the liquid phase.

An additional experimental set was performed with magnetite and americium, which aimed at determining the binding mode of the americium to the magnetite surface, possible incorporation and potential effect of ionic strength on the retention mechanism. The solid phase from this set of experiments was used for EXAFS measurements at the INE beamline at KIT synchrotron light source and is explained in depth below.

2.6 Measurements at synchrotron light sources

Sorption and corrosion samples were characterized by application of synchrotron-based techniques at the KIT (INE beamline for Actinide Research, Karlsruhe, Germany) and SOLEIL (DIFFABS beamline, Gif-sur-Yvette, France) synchrotron light sources. The measurements were completed in cooperation with the respective beamline scientists.

2.6.1 KIT Synchrotron Light Source, INE-beamline

EXAFS measurements allow exploring in-situ molecular structure of surface species by determination of near neighbour coordination number and interatomic distance of the neighbouring atom in the sample. The obtained information on the potential ionic strength effect, retention mechanism and binding mode also allow formation of an accurate and realistic surface complexation model. In this work, americium was contacted with pre-formed magnetite under anoxic and saline conditions. Information on the local environment was obtained by probing the Am L_3 -edge.

2.6.1.1 Sample preparation

In order to observe the possible ionic strength effect on retention mechanism, four samples were examined at a fixed solid to liquid ratio of 1 g/L magnetite at pH_M values of 6.1 and 7.1 for $I = 0.95$ M NaCl, as well as 6.1 and 7.0 for $I = 4.7$ M NaCl. The Am concentration was 7.8×10^{-6} M, with MES (20 mM) used to buffer the pH_M . The equilibration time of the solid phase and the electrolyte as well

as the buffer were identical to europium batch experiments. After pH_M correction and an equilibration period of 24 hours, the solid phase (wet paste) was transferred into 250 μL polyethylene vial. This vial was sealed and mounted inside a tight cell with Kapton (polyimide) film windows. The sample preparation and encapsulation took place inside an argon glovebox. This setup (four samples in one cell) was transported to the INE beamline [Rothe et al., 2012] where the measurements were done under continuous argon flow.

2.6.1.2 EXAFS measurements

Am L_3 -edge (18510 eV) XAFS spectra (5-6 scans to achieve adequate signal-to-noise ratio) were collected on the solid phase. The spectra were energy calibrated using the Zr K-edge XANES of a Zr foil measured simultaneously by assigning the first inflection point to 17998.0 eV. The XAFS signal was recorded in fluorescence detection mode at room temperature using a 5-element low energy germanium solid state detector (Canberra-Eurisys).

2.6.1.3 Data evaluation

The collected data were analysed and modelled following standard procedures using Athena (Demeter version 0.9.26) and Artemis (version 0.8.012) interfaces of the Ifeffit software [Ravel & Newville, 2005]. Structural information was obtained by applying the multi-shell approach for the data fitting. The coordination number (CN), interatomic distance (ΔR), relative shift in ionization energy (ΔE_0) and Debye-Waller term (σ^2) were the fitting parameters for each shell. For the four samples of interest, the amplitude reduction factor (S_0^2) was fixed during the fit to the experimental data and set to the value obtained for the americium solution without solid phase, which was used as reference. The k^2 and k^3 weighted Fourier transformed spectra were fitted in R space using a combination of single Am-Cl, Am-Fe and Am-O scattering paths [Ravel & Newville, 2005]. The misfit between data and model is expressed by the factor F representing the figure of the merit of the fit [Ravel, 2000].

2.6.2 SOLEIL, DIFFABS-beamline

The long-term corrosion experiments in this work aim at estimating the corrosion rate and identifying the formed corrosion products. This information will help the estimation of the period of the container integrity, which is an important input for safety performance assessment of disposal sites. Identification of corrosion products is also important with respect to retention of radionuclides (RN) dissolved from the waste matrix. Due to the nature of our corrosion samples, the analytical techniques

used to determine the nature of the corrosion products are applied on the surface. Embedding in resin and crosscutting of the sample is possible but only SEM-EDX analysis can be performed on the crosscut, which does not allow overall characterization of the corrosion front. The corrosion interface on the crosscut is too thin for XRD analysis and the geometry would not allow for anoxic measurement by Raman spectroscopy at INE laboratories. For these reasons, XRF (X-ray fluorescence), XRD and XANES measurements were performed on the crosscuts of selected corrosion samples to allow obtaining a complete picture of the elements distribution, phase characterization and corrosion front progression. DIFFABS beamline has the capability to apply various techniques, diffraction and absorption on the same region of the sample under identical conditions with micro focused beam, size below $5 \times 9 \mu\text{m}^2$ (reached in our case), which is essential for the corroded samples where the corrosion front is very thin.

2.6.2.1 Sample preparation

The preparation of the specimen followed the identical procedure as in the case of the long-term corrosion experiments. The polished Cr-Ni steel and SGI coupons (4 mm x 18 mm x 10 mm) were contacted with 5 M NaCl or 3.4 M MgCl₂ for 31 weeks at 90 °C (in the oven) in closed autoclaves under anoxic conditions without additional fittings for the gas phase sampling. The 31 weeks contact time should ensure sufficient coverage by the secondary phases for the analysis by synchrotron-based methods. The autoclaves were cooled down and opened in an argon glovebox where the corroded samples were cleaned off salt and embedded in epoxy resin (Buehler). The four embedded coupons were put in an airtight transfer vessel and transported to CEA (Commissariat à l'énergie atomique et aux énergies alternatives) Saclay SEARS Laboratory in France. The vessel was opened in an argon box, where each sample was transversally cut with a small saw (Minitom, Struers). The cutting took about 2 hours to minimize the strain on the sample. After the cut, the sample was polished with a diamond containing paste to 1 μm providing a study area of 10 mm x 4 mm. No grinding paper was used for the specimen preparation. In order to get a good overview of the different areas on the crosscut and select best areas for the synchrotron measurements, optical microscopy was performed on all samples. This revealed one small spot of interest for Cr-Ni steel corroded in 5 M NaCl, no corrosion for Cr-Ni steel in 3.4 M MgCl₂ and various spots of interest for the SGI in both brines. μRaman spectroscopy and SEM-EDX measurements were then performed on the spots of interest. All measurements were performed on the samples encapsulated in an anoxic holder with argon atmosphere. After these measurements were completed the crosscut samples were placed again in the transfer vessel in the argon box and transported to another argon glovebox in the synchrotron Soleil chemical

laboratory, where conditioning in an appropriate sample holder for the measurements at beamline took place.

2.6.2.2 μ XRF, μ XANES and μ XRD measurements

In the synchrotron laboratory argon box, the cut samples were encapsulated inside a specially designed cell with Kapton windows to fit the required geometry for the measurements (**Figure 10**). These were brought to the DIFFABS beamline where the measurements took place without additional argon flow.

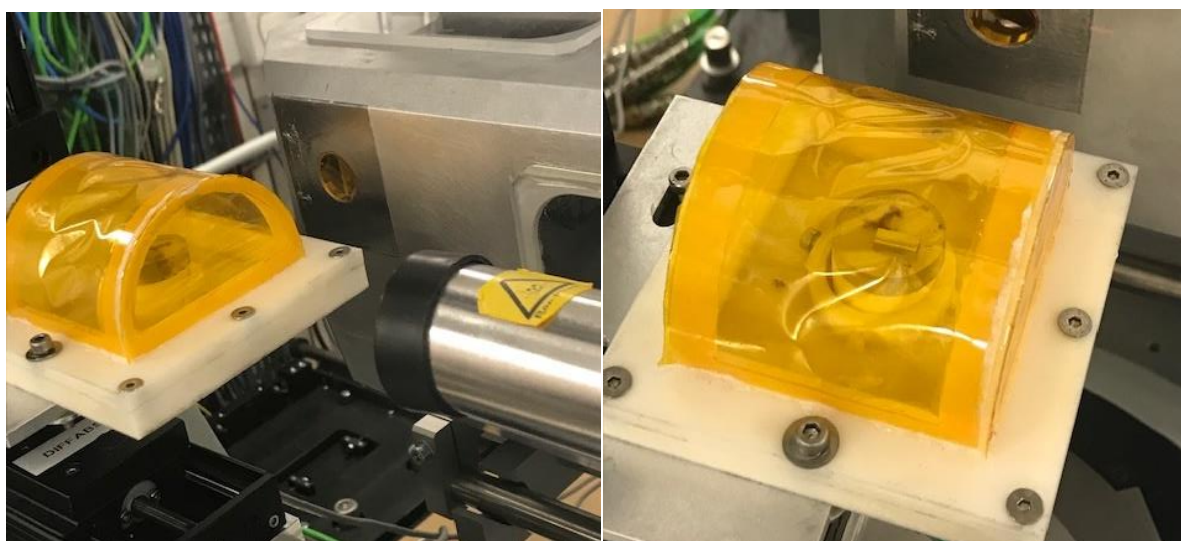


Figure 10: The corroded sample encapsulated in an anoxic cell built for the measurements.

As the main constituents of the steels are Cr, Ni and Fe for the Cr-Ni steel and only Fe for the SGI, these three elements were of interest for the synchrotron measurements.

The energy of incoming X-ray beam was calibrated by Fe K-edge of an iron foil (7112 eV) was measured for calibration purposes, where a 10 eV offset (7122 eV) was determined. This was taken into account during data evaluation for all samples. Spatial distribution of the elements was determined by recording μ XRF maps. The μ XRF maps were recorded for the three samples (Cr-Ni steel corroded in 3.4 M MgCl_2 was not measured due to lack of corrosion front), at specific excitation energies, above the edge of the element of interest, at 7.2 keV for Fe (K-edge at 7112 eV) for the SGI and additionally at 8.4 keV for Ni (K-edge at 8333 eV) and at 6.2 keV for Cr (K-edge at 5989 eV) for the Cr-Ni steel. According to the maps, showing local enrichments of elements, the points of interest were selected to perform further μ XRD and μ XANES analyses. μ XANES spectra (2 scans per point) were collected at Fe K-edge, Ni K-edge and Cr K-edge for the following range of energies: 7000-7320 eV for Fe, 5890-6200 eV for Cr and 8280-8450 eV for Ni. μ XRD measurements were performed as a line scan though the corrosion front and at selected points at a discrete energy of 8.4 keV for all samples to identify the

present crystalline phases. At last, as XANES is characteristic of a local environment surrounding the probed element and valence state, one or several reference compound spectra are needed for the spectra fitting. A linear combination of XANES spectra of known species allows determination of the compounds nature and proportion in the measured sample. Various reference compounds (purchased or synthesised) were measured (not with μ focused beam) at a Fe K-edge and compared to the μ XANES spectra obtained for the steel samples. The selection of reference compounds (*Annex Table A6*) was based on earlier analyses in the laboratory of steel specimen corroded for 13 weeks under identical chemical conditions and other thermodynamically stable compounds based on *Pourbaix* diagrams for iron, nickel and chromium. The Fe K-edge XANES of reference compounds were measured at SOLEIL while the Ni and Cr K-edge XANES of reference compounds were measured at INE-beamline at KIT synchrotron light source due to insufficient time at synchrotron SOLEIL.

2.6.2.3 Data evaluation

The obtained μ XRF maps were opened using the PyMca software (version 5.4.2) [Solé et al., 2007] and exported to Origin with the corresponding coordinates. The μ XANES spectra were analysed following standard procedures using the Athena (Demeter version 0.9.26) interface of the Ifeffit software [Ravel & Newville, 2005]. The energy calibration was done to account for the 10 eV offset determined at the beamline. Further self-absorption correction using the appropriate steel composition was done for each spectrum to account for the fluorescence absorption by the bulk steel, which affects the amplitude of the edge data. A linear combination fitting in Athena allowed the identification of the corrosion phases or their partial contribution at various points of interest shown directly in the μ XRF map. The obtained μ XRD data were converted from the wavelength used at the beamline (1.476 Å (8.4 keV)) to the wavelength used in the laboratory (Cu-K α radiation at 1.5406 Å) to allow better comparison and data treatment in the Diffrac.Eva software.

3 Corrosion Studies

3.1 Spheroidal graphite iron corrosion in dilute to concentrated NaCl and MgCl₂ solutions

3.1.1 Initial characterization

The examination of the initial sample surface was an important first step to allow observation of the morphological changes as corrosion progresses. **Figure 11** shows the SEM images of polished non-corroded spheroidal graphite iron. The light material is the iron whereas the dark spots are carbon inclusions (particle size ~ 50 μm in diameter), which are typical for spheroidal graphite iron. Closing up onto the carbon inclusion, the sheet like structure is clear, confirming presence of graphite, which is not homogeneously distributed. As expected, XPS analysis showed the presence of Fe(0) (**Figure 12 A**). EDX results show the chemical composition of the selected points (**Table 7**), first focused on the iron surface and then on the graphite inclusion. The Si amount is slightly lower compared to the certificate when looking at the composition of the bulk steel. The X-ray diffractogram of spheroidal graphite iron (**Figure 12 B**) shows a good match with cubic iron, while the small peaks correspond to the graphite. Finally, the surface roughness of the starting material was assessed by AFM. A value for the root mean square (RMS) roughness of 15 nm was obtained for a scanned area of 30 x 30 μm^2 .

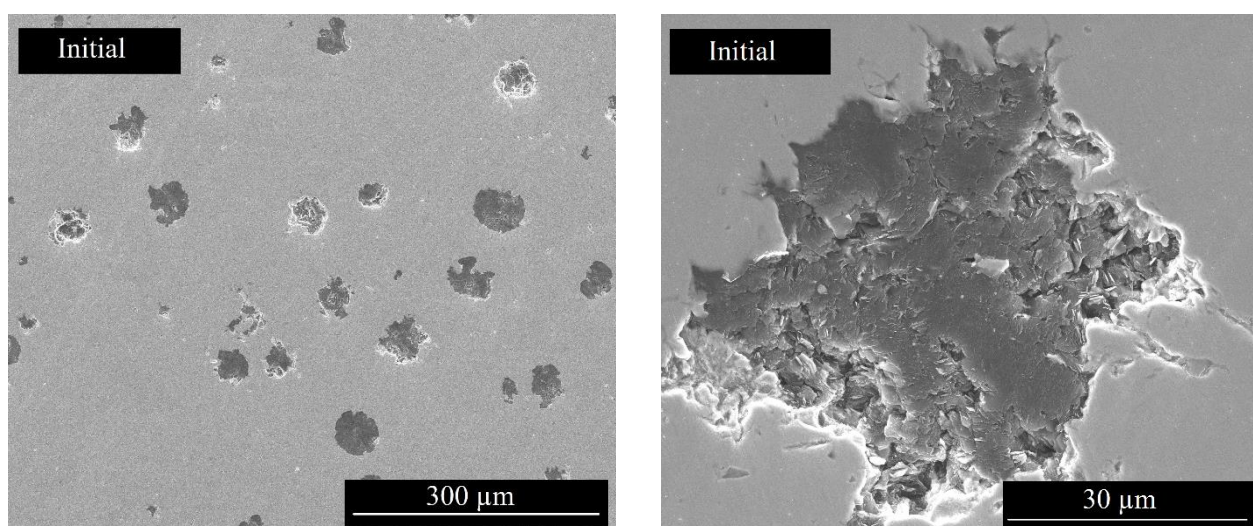


Figure 11: SEM images of the initial spheroidal graphite iron showing the graphite inclusions.

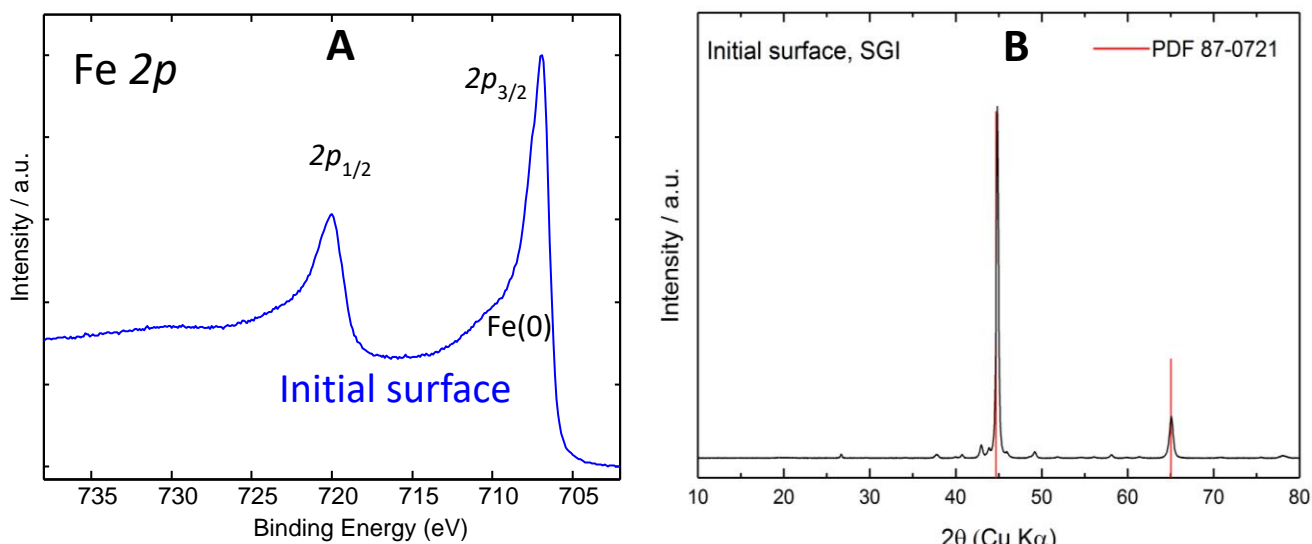


Figure 12: Fe 2p XPS spectrum (A) and X-ray diffractogram (B) of the initial spheroidal graphite iron; reflections correspond to cubic iron.

Table 7: Chemical composition of the spheroidal graphite iron.

Element / wt. %	C	Mn	Si	Cr	Mg	Cu	Fe
Certificate	3.46	0.29	3.39	0.042	0.052	0.038	92.691
EDX of overall surface/ (Error: +/- 3 Sigma)	3.79±0.60	-	2.47±0.14	-	-	-	93.73±0.56
EDX focused onto graphite/ (Error: +/- 3 Sigma)	99.67±1.91	-	-	-	-	-	0.33±0.09

3.1.2 Dissolved metals evolution

The quantification of the dissolved metals in the solution at the end of the experiments was done using HR ICP-MS following the procedure for sample preparation described in *section 2.2.3*. In case of SGI, only iron dissolution was of interest. The silica and carbon dissolution were not followed, but it was later found that silica contributes to the corrosion product formation. As we do not possess the exact amounts of dissolved silica in these dynamic systems, we have calculated the amounts of dissolved Si from the corresponding weight loss for all systems (*Table 8*). As the weight loss of silica from the steel accounts in addition to the dissolved amount of silicon also for the corrosion products formation by precipitation, taking this value as corresponding to the dissolved amount on silica in the solution is overestimating the real dissolved amount. This contributes to the uncertainty of the recalculated pH_M at elevated temperature, as the sensitivity study has shown that changing the aqueous silica

concentration by 1 order of magnitude can shift the recalculated pH_M by 0.02-0.4 unit. **Table 9** shows the dissolved amounts of iron given by HR ICP-MS.

Table 8: Dissolved amounts of silica in the solution for SGI estimated from weight loss.

System/ Amounts in $\mu\text{g/L}$	13 weeks	26 weeks	28 weeks	42 weeks	49 weeks
5 M NaCl, 90 °C	2121±70	1202±70	-	2758±70	-
3.4 M MgCl ₂ , 90 °C	24822±70	34016±70	-	44270±70	-
5 M NaCl, 25 °C	-	-	-	-	2121±70
3.4 M MgCl ₂ , 25 °C	-	-	-	-	3253±70
0.1 M NaCl, 90 °C	-	-	10183±70	-	-
0.033 M MgCl ₂ , 90 °C	-	-	10182±70	-	-
Solution 3, 90 °C	-	14285±70	-	-	-
Solution 1, 90 °C	-	38683±70	-	-	-
Solution 3, 25 °C	-	1202±70	-	-	-
Solution 1, 25 °C	-	5233±70	-	-	-

Table 9: Iron concentrations in the solution for SGI experiments. The numbers in parentheses correspond to the relative standard deviation in %.

System/ Amounts in $\mu\text{g/L}$	13 weeks	26 weeks	28 weeks	42 weeks	49 weeks
5 M NaCl, 90 °C	102.9 (24)	130.8 (7.6)	-	151(5.6)	-
3.4 M MgCl ₂ , 90 °C	216945.4 (2.2)	61874.1 (0.7)	-	105000 (2.1)	-
5 M NaCl, 25 °C	-	-	-	-	300(2.6)
3.4 M MgCl ₂ , 25 °C	-	-	-	-	42730 (2.3)
0.1 M NaCl, 90 °C	-	-	16500 (0.2)	-	-
0.033 M MgCl ₂ , 90 °C	-	-	11800 (0.9)	-	-
Solution 3, 90 °C	-	4867.5 (1.5)	-	-	-
Solution 1, 90 °C	-	360991.7 (1.2)	-	-	-
Solution 3, 25 °C	-	<10	-	-	-
Solution 1, 25 °C	-	63238 (0.3)	-	-	-

The dissolved iron amounts in 5 M NaCl at 90 °C were quite low. This is also applicable for the 5 M NaCl system at room temperature. Interestingly, in solution 3 (rich in NaCl), the dissolved amount is an order of magnitude higher. In the corrosion experiments in 3.4 MgCl₂ and solution 1 (rich in MgCl₂), independent of the temperature, the dissolved amounts were 2-3 orders of magnitudes higher compared to those in NaCl systems. Finally, the experiments performed in more dilute electrolyte solutions showed surprisingly high dissolution of iron, with similar concentrations for both electrolyte types. The values are all likely related to the pH_M of each system.

3.1.3 pH / E_h evolution

The accurate pH_M and E_h values of a system are along dissolved metals amounts crucial parameters allowing identification of thermodynamically stable corrosion phase(s) in *Pourbaix* diagram under those conditions.

The pH_M values (**Figure 13**) either remain stable or increase to a more or less extent in most of the investigated systems. The largest increase in pH_M ($\Delta\text{pH}_M \sim 2.5$) is observed in 5 M NaCl solution at 90 °C. Significant pH_M increase is, however, also noticed in 3.4 M MgCl_2 solution and solutions 1 and 3 at room temperature. A small decrease is observed for one system, solution 3 at 90 °C.

The initial pH_M is different for each system, even in case of the same brine at different temperatures, as the pH_M values for room temperature systems are the measured ones, while the pH_M values for the systems at 90 °C are the recalculated values from the measured values using the dissolved amounts of metals.

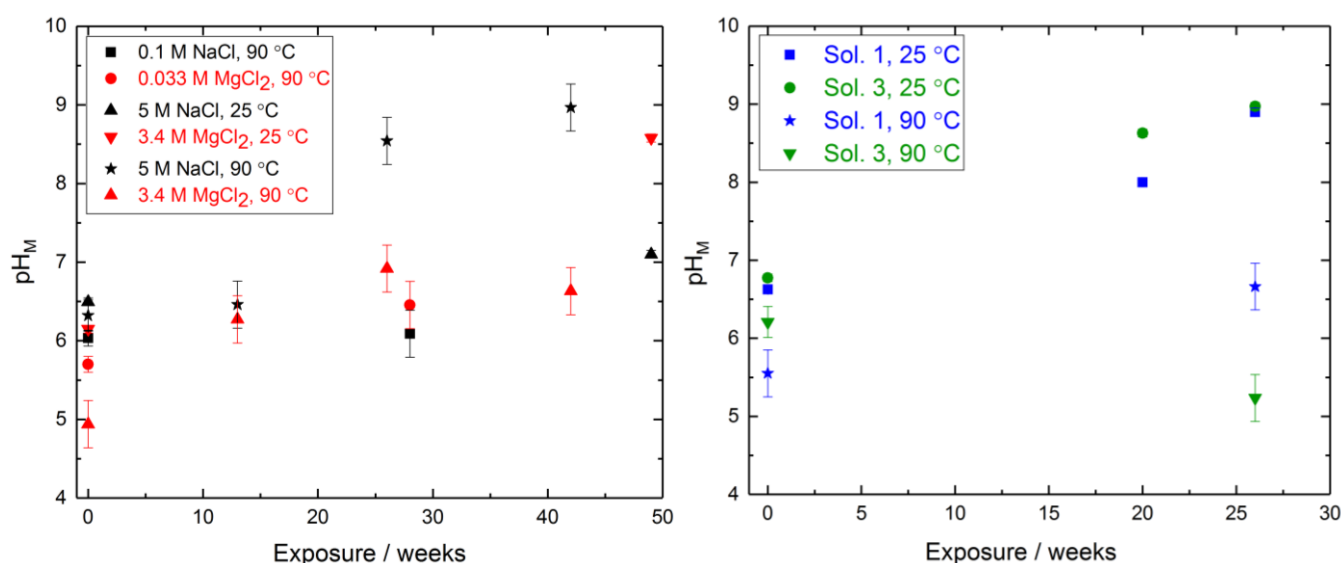


Figure 13: The pH_M evolution for the spheroidal graphite iron corroded in various brines with time.

In similar manner, the E_h evolution was followed for all systems, and is shown in **Figure 14**. Redox potentials in all solutions clearly decrease and finally reach reducing conditions. With the exception of experiment in solution 1, E_h values level out at ~ -200 mV. In the case of E_h , the initial values are the same for the identical brines at 90 °C and 25 °C. The uncertainties for the redox potentials lie in the ± 50 mV range. Corroding iron is known to have the redox potential on the stability line of water, which in this pH_M range is around -300 to -400 mV. The higher values in the experiments could be related to ionic strength correction, but most likely to the hydrogen escape over time. Moderate

amounts of hydrogen were found in the gas phase, however, not sufficient to correspond to the observed corrosion rate confirming that the setup is not hydrogen tight over longer period.

In house potentiodynamic polarization measurements by Dr. P. Cakir-Wuttke determined preliminary values of the corrosion potential, E_{corr} , described in the *section 1.3.1* [McCafferty, 2010; Popov, 2015] for steels investigated in this study. The values of the corrosion potential for SGI in 5 M NaCl and 3.4 M MgCl₂ brines with pH approximately 7 were estimated in the range of -400 to -450 mV, close to the stability line of water. These values are with respect to S.H.E. and compared to values obtained in this study, the measured potentials (-160 mV for 5 M NaCl and -300 mV for 3.4 M MgCl₂ at 25 °C) are above the corrosion potentials, as expected.

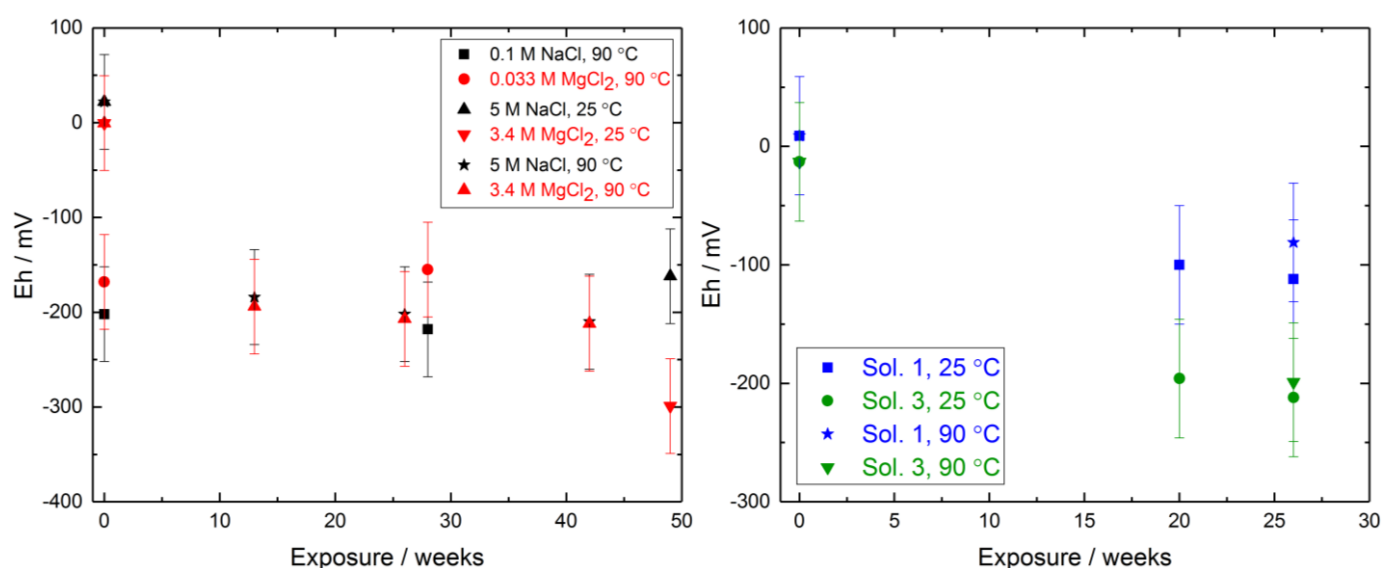


Figure 14: The E_h evolution for the spheroidal graphite iron corroded in various brines with time.

3.1.4 Corrosion rate

The corrosion rates of spheroidal graphite iron for all systems were calculated from the weight loss and are shown in *Table 10* along with pH_M values. The procedure for post-corrosion sample cleaning was described in *section 2.2.4*. The corrosion in MgCl₂ brines is in general faster than in NaCl solutions and pH_M is an important driver for corrosion rates with lower pH_M values resulting in faster corrosion.

The decrease of the rate with time observed in 5 M NaCl and 3.4 M MgCl₂ brine is due to corrosion product formation, which protects the surface and puts the steel in the passivation region, thus the dissolution of iron/silica from the steel is slower and dependent on the oxide film porosity/

homogeneity. The rates after 42 weeks are not necessarily final values and longer exposure is needed to obtain the steady-state, where the corrosion rates are no longer changing with time.

The low pH_M of the solution 3 system run at 90 °C justifies high corrosion rate. In this case $MgCl_2$ at 90 °C and solution 1 system at 90 °C, the pH_M is similar and the same corrosion product was forming in significant coverage in both cases, thus similar corrosion rates were expected (after 26 weeks).

The corrosion rate of the steel corroded in solution 1 at 25 °C for 26 weeks is much lower than the rate in solution 1 at 90 °C after 26 weeks (likely due to kinetics and higher pH_M), but higher than in 3.4 M $MgCl_2$ at 25 °C after 49 weeks. If the corrosion rate in solution 1 at 25 °C will decrease with time, it may reach similar values after 49 weeks as the 3.4 M $MgCl_2$ brine at 25 °C. The pH_M evolution in these two solutions is similar and hence, the sulfate presence does not seem to play a role with respect to the corrosion rate.

The relatively low pH_M values in dilute systems could explain quite high corrosion rate, $10 \pm 1.0 \mu m/a$ for both brines. It was expected that the corrosion rate for the two brines with identical ionic strength would be similar as the same corrosion product is formed, similar pH_M is established and similar amounts of dissolved iron were found.

Table 10: The corrosion rate CR and (pH_M) of SGI for various systems.

System/ CR in $\mu m/a$	13 weeks	20 weeks	26 weeks	28 weeks	42 weeks	49 weeks
5 M NaCl, 90 °C	2.89±0.05 (6.5±0.3)	-	1.01±0.05 (8.5±0.3)	-	1.22±0.05 (9.0±0.3)	-
3.4 M MgCl₂, 90 °C	38.1±2.0 (6.3±0.3)	-	23.1±1.5 (6.9±0.3)	-	16.9±1.5 (6.6±0.3)	-
5 M NaCl, 25 °C	-	-	-	-	-	1.11±0.05 (7.10±0.05)
3.4 M MgCl₂, 25 °C	-	-	-	-	-	1.22±0.05 (8.60±0.05)
Solution 3, 90 °C	-	-	9.6±1.0 (5.2±0.3)	-	-	-
Solution 1, 90 °C	-	-	26.3±1.5 (6.7±0.3)	-	-	-
Solution 3, 25 °C	-	1.26±0.05 (8.63±0.05)	0.79±0.05 (8.97±0.05)	-	-	-
Solution 1, 25 °C	-	2.07±0.05 (8.00±0.05)	3.65±0.05 (8.90±0.05)	-	-	-
0.1 M NaCl, 90 °C	-	-	-	10.0±1.0 (6.1±0.3)	-	-
0.033 M MgCl₂, 90 °C	-	-	-	10.0±1.0 (6.4±0.3)	-	-

In the literature [Smailos et al., 1987], in solution 1 the corrosion rate of SGI was reported 46 $\mu\text{m/a}$ at 90 °C, considering identical brine volume to surface area ratio used in this work, but much lower pH of ~ 4.0 . We have observed a corrosion rate of $26.3 \pm 1.5 \mu\text{m/a}$ at 90 °C at $\text{pH}_M 6.7 \pm 0.3$ and $3.65 \pm 0.05 \mu\text{m/a}$ at 25 °C at $\text{pH}_M 8.90 \pm 0.05$, clearly demonstrating the importance of pH_M on iron corrosion. Considering solution 3 system, the corrosion rate in the literature is 25 $\mu\text{m/a}$ at 150 °C at pH of ~ 6.0 -7.0, while we have observed a corrosion rate of $9.6 \pm 1.0 \mu\text{m/a}$ at 90 °C at pH_M of 5.2 ± 0.3 . Similarly, the corrosion rate of cast steel in Ar-purged synthetic seawater at 90 °C, pH ~ 8.0 was reported 6-8 $\mu\text{m/a}$ [Marsh et al., 1983; King, 2008].

The technical report by King [2008] describes carbon steel and cast steel long-term anaerobic corrosion rates of the order of 1-2 $\mu\text{m/a}$ in systems containing compacted clay and 0.1 $\mu\text{m/a}$ in bulk solution (simulated and natural groundwaters) considering ambient temperature to 100 °C. Carbon steel and cast iron corrosion rates in dilute Allar granitic groundwater (low I , pH 8.1) at 90 °C were reported $< 1 \mu\text{m/a}$.

3.1.5 Secondary phase characterization and evolution

3.1.5.1 NaCl brine

The SEM images show a nice evolution with respect to time in 5 M NaCl at 90 °C (**Figure 15**). The white area in the image after 13 weeks corresponds to the initially non-corroded surface. After 26 and 42 weeks this area is not visible anymore, while the coverage by the formed corrosion products is increasing, highlighting the corrosion progress. After 13 weeks, very few phases with platelet like morphology can be observed. After 26 weeks, two different morphologies can be observed, a clustered platelet one and small octahedral structures. After 42 weeks, the octahedral structure has clustered into big octahedral arrangement of 20 μm in size, while the platelet like structures are present in less significant quantities. XPS analysis (**Figure 16**) showed very similar Fe 2p spectra for all samples, showing a mixed contribution from Fe(III), Fe(II) and absence of Fe(0). O 1s spectra (not shown) for samples after 26 and 42 weeks showed hydroxide and oxide contributions, while after 42 weeks, the oxide peak is dominant.

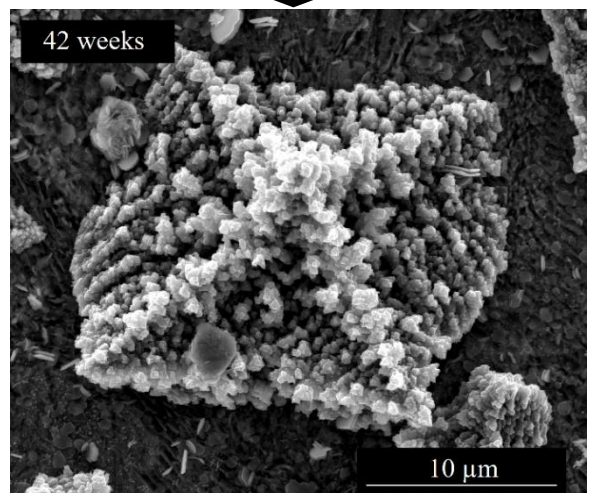
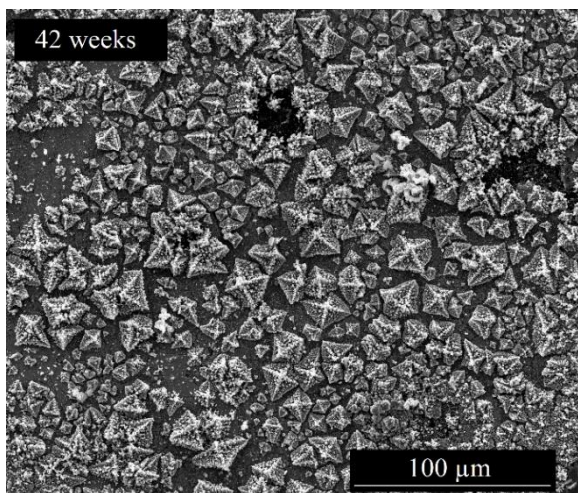
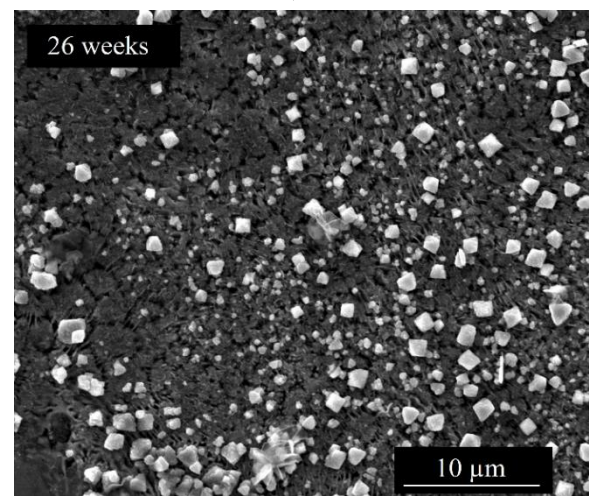
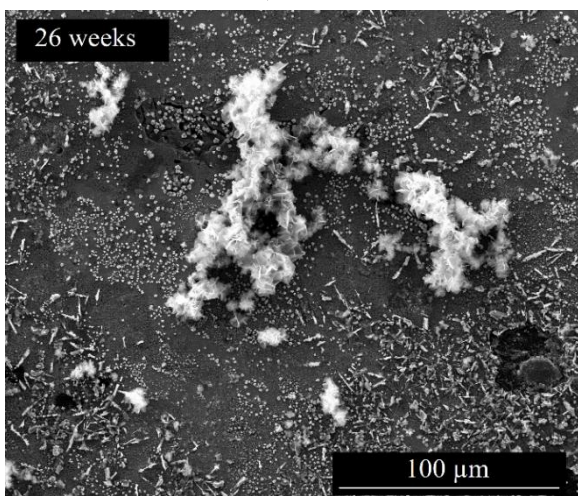
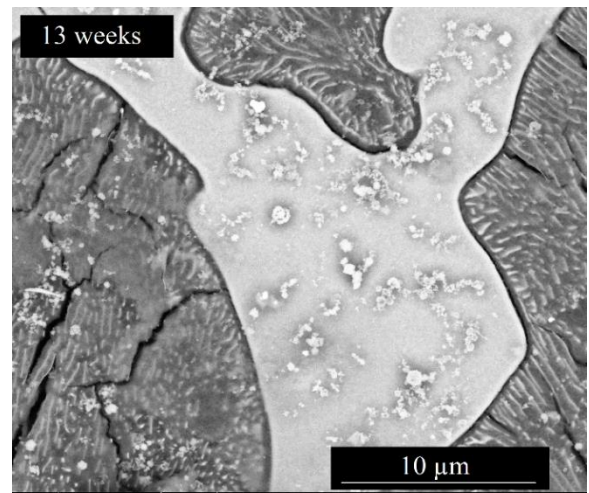
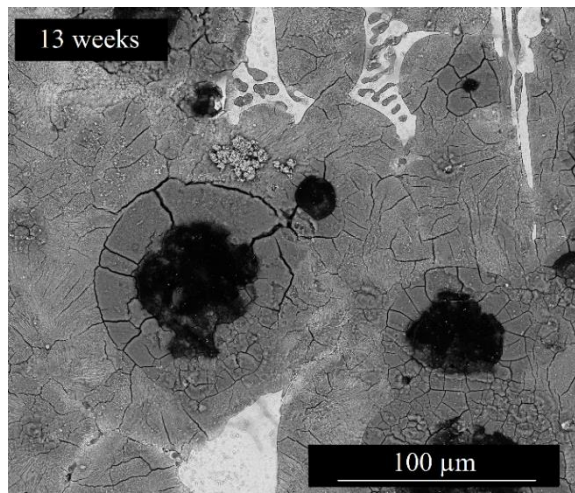


Figure 15: SEM images of the evolution of the solid phase morphology of the SGI in the 5 M NaCl brine ($I = 5$ M) exposed for 13 weeks (top) to 42 weeks (bottom), $T = 90$ °C applying two microscope magnifications.

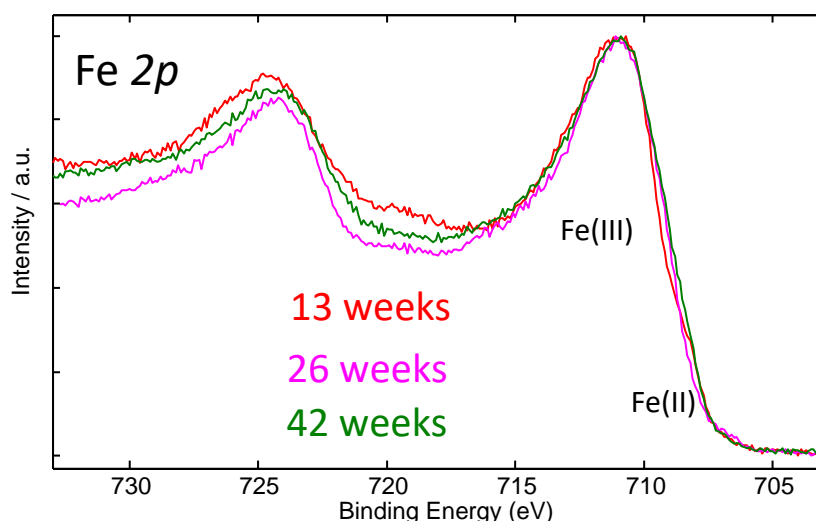


Figure 16: The XPS Fe 2p spectra of the corrosion products in 5 M NaCl.

According to the EDX analyses (**Table 11**), the platelet like corrosion phase formed after 13 weeks is an iron silicate phase, likely greenalite ($\text{Fe}_{2-3}\text{Si}_2\text{O}_5(\text{OH})_4$) or cronstedtite ($\text{Fe}_3(\text{Si},\text{Fe})\text{O}_5(\text{OH})_4$), with Si/Fe and Si/O ratios pointing rather to the cronstedtite phase. This phase does not transform and is present also after 26 and 42 weeks as shown by EDX, however as noted by SEM analysis in much lower quantities than the octahedral phase, corresponding to magnetite. Small amounts of ~2 wt. % Si are found in the magnetite structure. Various spots after 26 and 42 weeks were examined to investigate whether this is an anomaly. The Si could originate from iron silicate impurities in the magnetite or from the Si in the steel below the corrosion product.

Table 11: The chemical composition of the observed corrosion products on SGI according to their morphology in 5 M NaCl brine at 90 °C.

Element / Atomic %	Si	Fe	O
13 weeks - Platelet structure	9.3 ±0.2	27.5±0.7	63.2±1.0
26 weeks - Platelet structure, Spot 1	7.54±0.27	28.91±0.82	63.55±1.16
26 weeks - Platelet structure, Spot 2	7.86±0.28	30.03±0.85	62.11±1.16
26 weeks - Octahedral structure, Spot 1	2.3±0.31	41.39±1.29	56.3±1.37
26 weeks - Octahedral structure, Spot 2	2.49±0.31	40.83±1.27	56.68±1.41
42 weeks - Octahedral structure, Spot 1	2.33±0.15	40.56±0.73	57.11±1.03
42 weeks - Octahedral structure, Spot 2	2.73±0.26	42.13±1.31	55.14±1.37
42 weeks - Octahedral structure, Spot 3	2.58±0.15	40.63±0.73	56.79±1.01
42 weeks - Platelet structure	8.12±0.19	31.22±0.66	60.35±1.07

The XRD analyses corroborate the EDX and SEM findings. Initially (up to 13 weeks), only the initial cubic iron surface (PDF card 87-0721) could be identified (*Annex Figure A8*). As the corrosion product layer is thin and the steel surface is not completely covered, the initial surface is also observed after 26 and 42 weeks. Small peaks matching magnetite (PDF card 88-0315) are present after 26 weeks and the intensity gets higher after 42 weeks. A small peak with low intensity is present at $2\theta = 12.5^\circ$ after 13 and 26 weeks and in moderate intensity along another peak at $2\theta = 25^\circ$ after 42 weeks. These two peaks are consistent with both silicate phases, greenalite and cronstedtite, and cannot be differentiated.

Pourbaix diagrams for SGI were constructed using GWB software and the Pitzer approach with [PI] database except for ionic strength 0.1 M where the Debye-Hückel approach and [TC] database was used to calculate the activity coefficients. The points in the diagram correspond to the pH (in activity, defined in *Eq. 25, 29*) and E_h values measured in this work for each system. For the purposes of this thesis, it is of interest to establish which corrosion phases of thermodynamic stability are relevant for the sorption studies.

The *Annex Figure A9 A* shows the *Pourbaix* diagram for 5 M NaCl system corroded at 90 °C using dissolved amounts of Fe and Si after 42 weeks and the [PI] database. The diagram suggests hematite as a long-term thermodynamically stable phase under our conditions and no precipitation after 13 weeks. However, minnesotaite, iron silicate mineral containing structural Fe(II) is shown as stable phase under more reducing conditions considering the Si activity calculated from the weight loss. Constructing the *Pourbaix* diagram with lower Si activity, magnetite as stable phase under reducing conditions along with minnesotaite (*Annex Figure A9 B*). Lowering the Si activity further reveals stability of magnetite and greenalite (instead of minnesotaite), which is another iron silicate phase very similar to cronstedtite (containing structural Fe(II) and Fe(III)). This highlights the importance of accurate quantification of aqueous silica. Crystalline hematite has a very high thermodynamic stability, however, its formation under various conditions can be kinetically hindered so that other Fe-phases can be found in many systems [Chesworth et al., 2008]. It is revealed that cronstedtite is stable under similar conditions as magnetite, as these are both mixed Fe(II)/Fe(III) phases, which are stable under reducing and neutral to alkaline conditions. As magnetite is more stable, cronstedtite is not appearing on the *Pourbaix* diagrams. Apparently, thermodynamic calculations do not reflect the experimental findings. The experimental observation of a corrosion layer composed of different, heterogeneously distributed Fe-corrosion phases is an indication for locally different conditions and the role of kinetic effects on solid phase formation (see discussion below).

As discussed previously, in iron corroding systems, the E_h values should be at the water stability line. Considering our experimental data points, this is not the case. This could be due to the insufficient tightness of the autoclaves or difficulties with the used redox electrode (high ionic strength, temperature correction). Considering the uncertainty of the silica activity calculated from the weight loss and uncertainties surrounding the E_h values, experimentally observed corrosion phases magnetite and Fe-silicate phases could be of long-term relevance in a repository system and their role as potential radionuclide sinks should be investigated.

This section describes the characterization of steel sample crosscut interface corroded for 31 weeks in 5 M NaCl at 90 °C in the CEA Saclay SEARS laboratory and the results obtained by the synchrotron-based microscopic (μ XRF, μ XAS and μ XRD) techniques. The aim of the synchrotron-based experiments was to obtain information on the distribution of the elements in the corrosion layer and therefore possibly conclude on the corrosion reaction pathway from the iron surface to the solution. The additional measurements performed on the crosscut sample in the CEA SEARS laboratory by optical microscopy prior the synchrotron measurements revealed heterogeneous corrosion layer with one region of interest (*Figure 17*). The SEM (*Figure 18*) - EDX (*Table 12*) and μ Raman analysis (*Figure 19*) on this region of interest further suggested phase distribution of silicate phase cronstedtite (spots 3,4) at the former place of the graphite inclusion removed upon corrosion, magnetite (spots 5,6,8, A) at the rim close to the non-corroded steel and iron hydroxychloride is found close to the steel/corrosion layer interface (spots 1,2,7,9,10,B). As the corrosion layer is detached from the steel upon crosscutting, the spots 7, 9 and 10 were likely close to the bulk steel before the cutting and thus it could explain why this phase is not detected by the surface analysis of non-embedded samples.



Figure 17: The optical image of the crosscut with the red circle highlighting the interface of interest in SGI sample corroded in 5 M NaCl for 31 weeks at 90 °C.

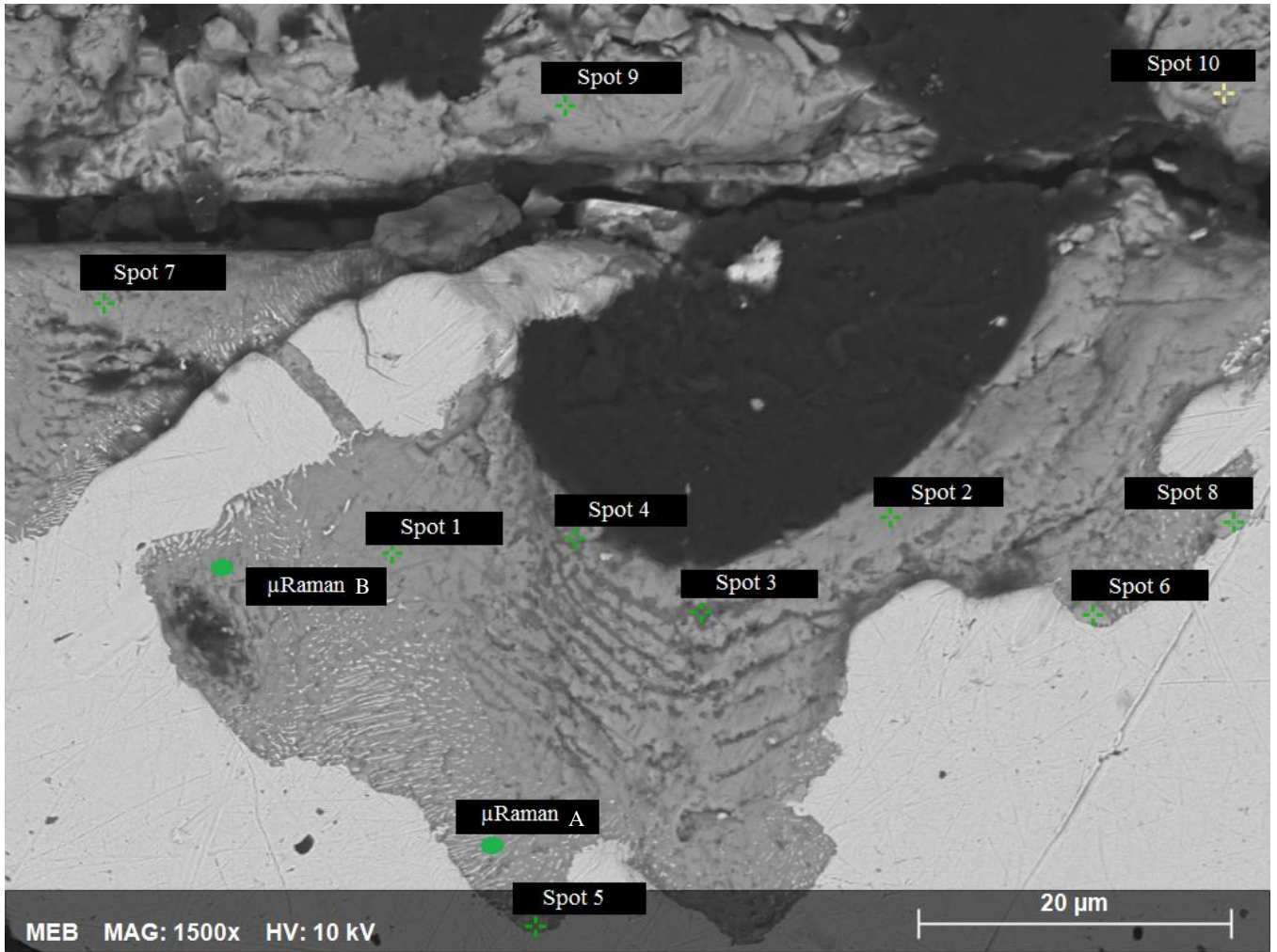


Figure 18: SEM image of the crosscut for the SGI corroded in 5 M NaCl for 31 weeks. The spots shown in the figure correspond to the spots in the *Table 12*. T = 90 °C.

Table 12: The chemical composition of the phases observed for SGI crosscut corroded in 5 M NaCl for 31 weeks at 90 °C.

Element/ Atomic %	O	Si	Cl	Fe
Spot 1	51.6±1.2	0.5±0.1	17.6±2.6	30.3±2.0
Spot 2	54.8±1.2	0.09±0.03	16.7±2.6	28.4±1.9
Spot 3	62.3±1.3	16.05±1.75	0.12±0.05	21.5±1.6
Spot 4	60.9±1.3	15.39±1.75	0.10±0.04	23.5±1.7
Spot 5	56.7±1.3	1.3±0.3	0.3±0.1	41.5±2.1
Spot 6	59.1±1.3	0.4±0.1	0.10±0.03	40.3±2.1
Spot 7	50.7±1.2	0.8±0.1	17.2±2.6	31.3±2.0
Spot 8	58.0±1.3	0.6±0.1	0.12±0.03	41.2±2.1
Spot 9	47.6±1.2	0.05±0.03	19.7±2.6	32.6±2.1
Spot 10	48.9±1.2	0.08±0.03	19.1±2.6	31.8±2.0

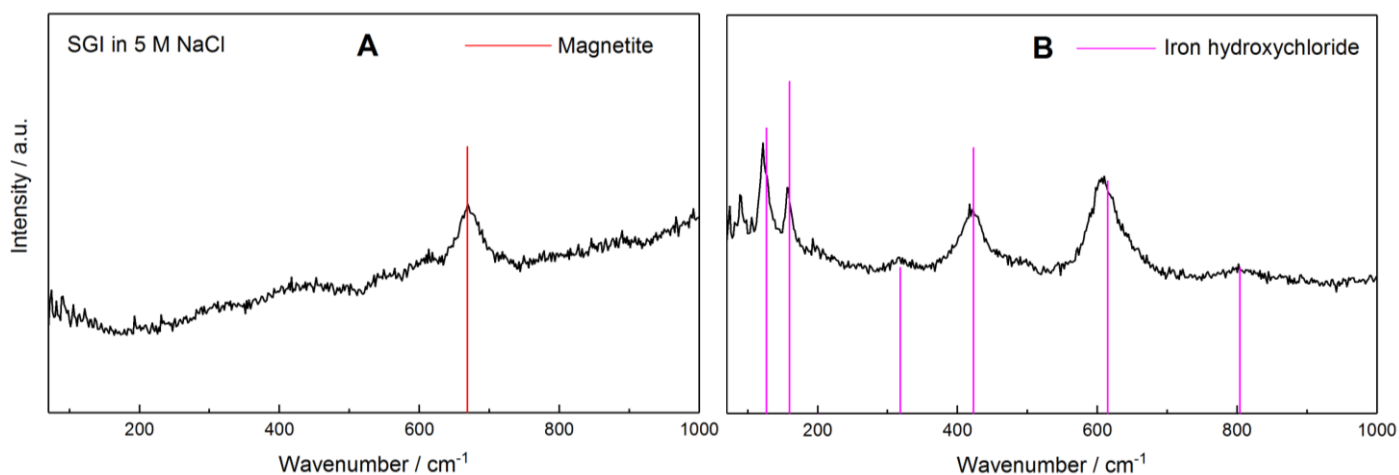


Figure 19: μ Raman spectra of the SGI crosscut corroded in 5 M NaCl.

At the synchrotron, the μ XRF technique provided map of iron distribution in the sample (*Figure 20*). The yellow spots correspond to the graphite inclusions in the steel, while the yellow/green rim shows the corrosion layer, which thickness clearly varies along the rim. Several points of interest were selected in the map, at which the μ XANES spectra were collected. The linear combination fitting was performed on the collected spectra using a linear combination of XANES spectra of reference compounds and best fits are shown along the samples' spectra in *Figure 20*. The point 1 matches the pristine steel spectrum, while the point 2 shows the presence of iron silicate phase cronstedtite (63 %) and iron hydroxychloride (37 %). As point 3 shows only the presence of cronstedtite as a corrosion product, it seems that iron hydroxychloride is forming in thickest areas of the corrosion layer and is not uniformly distributed. Furthermore, as this phase was not observed by the surface analysis, only on the crosscut (consistent with findings by μ Raman and SEM-EDX), it appears to be forming close to the bulk steel.

The findings clearly show the heterogeneity of the corrosion phase layers. Furthermore, they suggest initial precipitation of cronstedtite, followed by more thermodynamically stable magnetite considering solution conditions. These two phases co-exist and no systematic spatial separation has been identified. Upon cracks in the layer of these corrosion products, Cl^- diffusion and accumulation at the steel/corrosion product interface favours formation of iron hydroxychloride phase. These findings aid with the determination of the corrosion sequence.

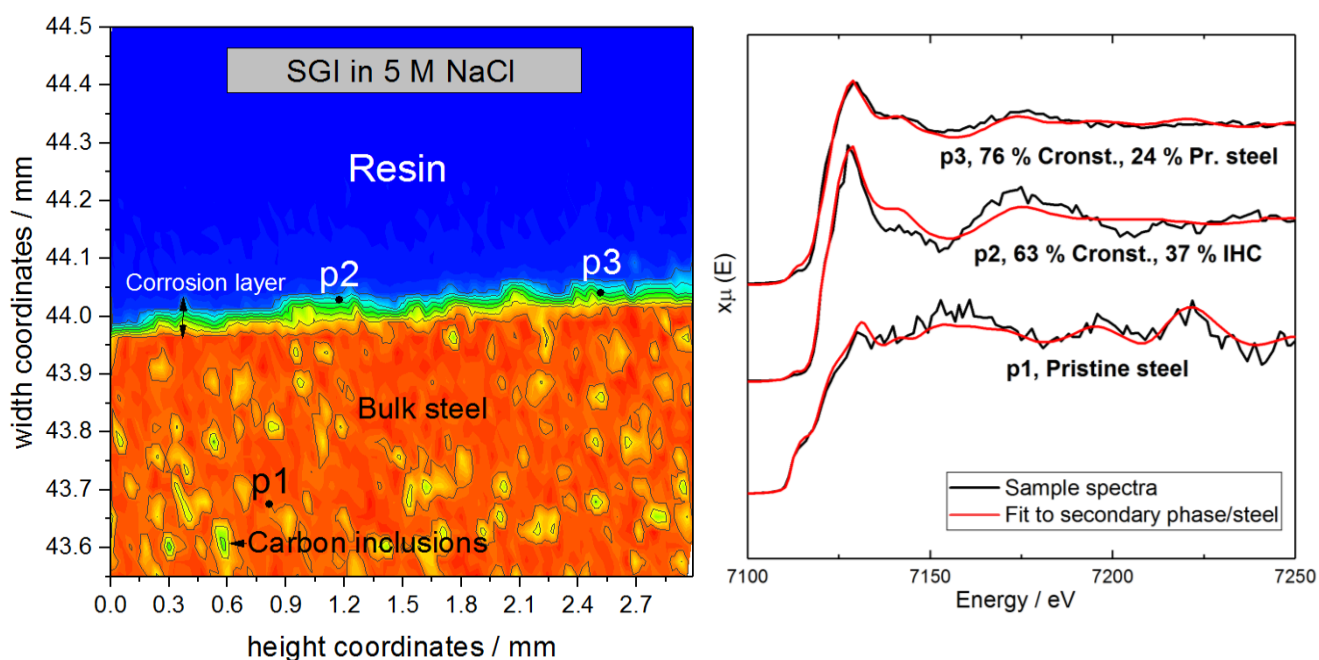


Figure 20: The μ XRF map showing iron distribution and the μ XANES spectra of the 5 M NaCl sample. The μ XANES spectra corresponding to the respective reference compounds are shown in *Annex Figure A10*. I.H.C. in the μ XANES spectra refers to iron hydroxychloride phase.

In order to observe the effect of temperature on the corrosion progress, an experiment was performed in concentrated brine under similar long exposure (49 weeks) at room temperature. The SEM images of the corrosion phases (*Figure 21*) show the presence of crystals with hexagonal platelet morphology with uniform and significant surface coverage and occasional octahedral crystallites sitting on top of the hexagonal structures. XPS shows presence of Fe(II) and Fe(III) in the narrow Fe $2p$ spectrum (*Annex Figure A11*). Furthermore, a significant chloride peak was also found for the sample corroded at 25 °C, hinting at presence of green rust chloride, which would match the hexagonal morphology. The Fe/O/Cl ratio and absence of sodium and thus salt evaluated by EDX analysis and shown in *Table 13*, suggest that the octahedral structure is in fact iron hydroxychloride. The platelet structure also shows the presence of chloride and a Fe/Cl ratio is matching green rust chloride matching the XPS analysis. The oxygen amount is however too low to match the ratio. The XRD analysis (*Figure 22*) showed peaks matching green rust chloride in addition to peak corresponding to the initial surface. As overall the hexagonal phase was covering way larger area than the octahedral iron hydroxychloride phase, the XRD analysis showing only the presence of green rust chloride peaks was anticipated.

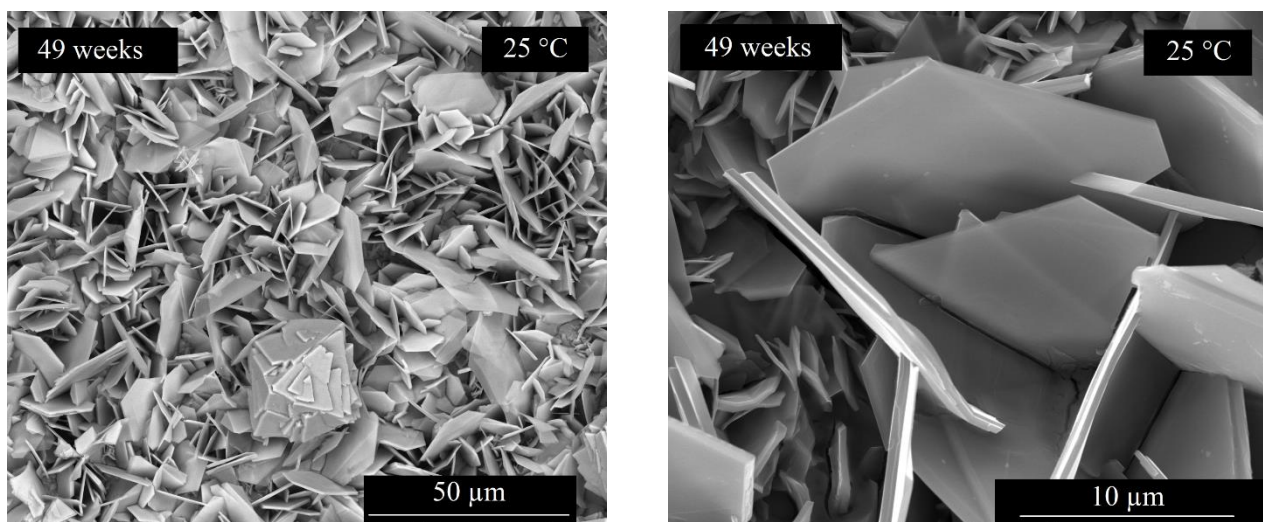


Figure 21: SEM images of the solid phase morphology in 5 M NaCl brine at 25 °C, applying two microscope magnifications.

Table 13: The chemical composition of the observed corrosion products on SGI according to morphology in 5 M NaCl brine at 25 °C.

Element / Atomic %	Cl	Fe	O
49 weeks - Octahedral structure, Spot 1	15.46±0.30	21.60±0.68	62.94±1.30
49 weeks - Octahedral structure, Spot 2	15.36±0.29	26.06±0.66	58.58±1.21
49 weeks - Octahedral structure, Spot 3	16.8±0.49	31.11±1.20	52.09±1.61
49 weeks - Hexagonal structure, Spot 1	10.64±0.31	42.79±1.02	46.17±1.10
49 weeks - Hexagonal structure, Spot 2	9.52±0.26	37.37±0.85	52.90±1.09

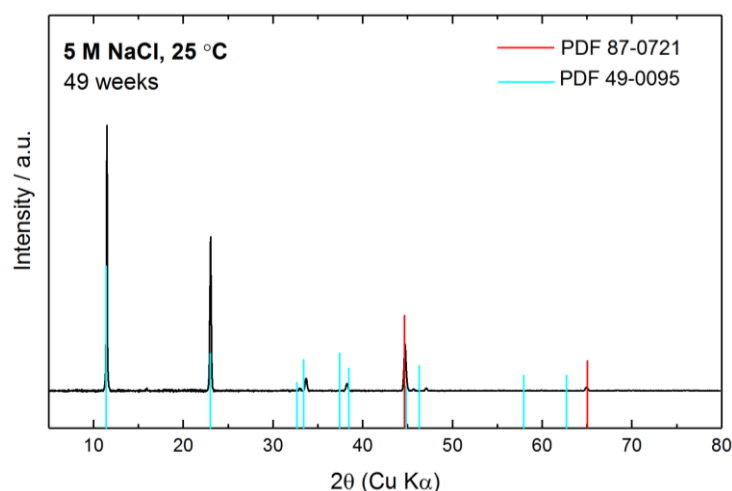


Figure 22: X-ray diffractograms of the spheroidal graphite iron corroded in 5 M NaCl for 49 weeks at 25 °C. PDF card 87-0721 refers to non-corroded steel surface, cubic iron and 49-0095 to green rust chloride.

In this case, the neutral pH_M values favour green rust chloride phase [Refait et al., 1998] in competition with iron hydroxychloride considering the present chloride concentrations and established equilibrium.

At elevated temperature, the moderately alkaline pH_M favours the precipitation of magnetite and cronstedtite. Overall, in both cases, the coverage by secondary phases is significant and corrosion rates are more or less identical.

Green rust chloride is a metastable phase and would never be shown as a long-term thermodynamically stable phase in the *Pourbaix* diagram. According to the *Pourbaix* diagram of Refait et al. [1998] shown in *Annex Figure A12*, the stability window of green rust chloride is fitting to the experimental conditions of the room temperature system. It may however in the long-term transform to magnetite [Usman et al., 2018].

An experiment performed at elevated temperature of 90 °C included solution 3; saturated NaCl with addition of small amounts of sulfate and was run for 26 weeks. The graphs corresponding to the results are shown in *Annex Figures A13, A14* and *A15*. The specimen coverage by secondary phases observed in SEM was lower than in the saturated NaCl brine in the absence of sulfate with the phase having hexagonal morphology. The lower coverage by precipitated phases compared to the saturated 5 M NaCl solution without sulfates is likely due to different pH_M values (5.2 vs. 8.5). No magnetite matching octahedral structure was found in solution 3, as the pH_M is too low for this phase to precipitate. The XPS showed presence of Fe(II) and Fe(III) in Fe 2p spectrum of the precipitated particles. The XRD showed due to low coverage only peaks matching the presence of initial steel. The EDX analyses (*Annex Table A7*) of the hexagonal particles showed compositions, which seem to correspond to iron silicate with Mg(II) replacing for Fe(II). In solution 3, the Mg amount accounts only for 0.015 M but it seems sufficient for the partial Fe-Mg replacement. The steel specimen from this experiment was embedded in resin, cut and polished and additional SEM analysis was performed on the crosscut (*Annex Figure A16*). The corrosion dissolution depth is uniform, 23-26 μm . In comparison, the corrosion rate for this system was obtained $9.6 \pm 1.0 \mu\text{m/a}$.

Two sets of experiments in solution 3 were performed at 25 °C. The exposure in these experiments was 20 and 26 weeks. The SEM image of the SGI corroded in solution 3 for 20 weeks (*Annex Figure A17*) show small circular abrasions looking like pits around the graphite inclusion. The steel further away from the inclusion is less attacked, most of it intact, showing preferential place of corrosion in the vicinity of the graphite inclusion, as mentioned earlier, likely due to position of cathode (graphite) and anode (steel). No distinct corrosion products were observed on the surface. The SEM images after 26 weeks show similar behaviour, a non-corroded surface with no corrosion products present on the smooth polished area. Upon zooming into the hole, which is used for hanging the coupon in the experimental setup, it seems that the rough area inside the hole and crevice environment caused crevice

corrosion. A structure with hexagonal morphology of 10 μm in size was observed. The XPS analysis of the sample after 20 weeks showed only Fe(0) confirming the non-corroded surface but zooming into the dissolved (pit) area a small Fe(II) peak was obtained along Fe(0) peak, likely from a small amount of Fe(OH)₂ precipitated from the solution within the dissolved structure. The low E_h and high pH_M conditions of this sample would fit with presence of this compound prior transforming into more thermodynamically stable iron silicate or magnetite phase later on. The XPS Fe 2p spectra of the 26 weeks sample showed the presence of Fe(II), a small peak of Fe(III), sulfate and hydroxide when focused on the hexagonal structure. The EDX analysis of the hexagonal particles (*Annex Table A8*) suggest presence of precipitated sodium sulfate from the solution along with possible Fe(OH)₂. The EDX and XRD analyses of the polished sample area (*Annex Figure A18*) showed composition and peaks matching the initial SGI.

According to existing data shown in *Pourbaix* diagram in *Annex Figure A19*, pyrite should be thermodynamically stable in those experiments performed in presence of sulfate. However, it is well known that pyrite will not form under given conditions. Sulfate reduction is usually microbially induced, kinetically strongly hindered and might play a role on the very long-term.

One experiment was performed in dilute brine with ionic strength of 0.1 M NaCl at 90 °C for 28 weeks. The results of various analyses are shown in the *Annex Figures A14, A15, A20* and *Table A9*. Overall, the SEM showed presence of crystallites with octahedral morphology of 10 μm in size, small bright crystals of undefined morphology and hexagonal stack layered crystals of about 1-2 μm in size. XPS analysis of this sample showed the presence of Fe(II) and Fe(III) in Fe 2p spectrum. The EDX analysis showed Fe/O ratio matching magnetite for the octahedral and undefined morphology particles and Fe/Si/O ratio matching cronstedtite for the stacked hexagonal particles. The X-ray diffractogram shows peaks matching the initial steel, magnetite and cronstedtite (greenalite XRD pattern is similar, but EDX suggested cronstedtite from the Si/O ratio), confirming the observations of SEM and EDX techniques. Increasing the chloride concentration does not change the behaviour for the examined NaCl systems, showing that the brine with $I = 5$ M NaCl favours the same secondary phases as the dilute NaCl solution with $I = 0.1$ M NaCl, which are not Cl⁻ bearing phases.

The *Pourbaix* diagram generated for the low ionic strength system, 0.1 M NaCl at 90 °C run for 28 weeks is shown in the *Annex Figure A21*. Overall, lower ionic strength of the system moves the FeCl⁺ (FeCl₂)/ solid phase border line to the lower pH values.

Overall, it seems that in NaCl based systems, magnetite, and depending on the silica activity likely minnesotaite, are the long-term phases of interest, taking into account the redox potentials of corroding iron, which lie below the values obtained in this work.

3.1.5.2 MgCl₂ brine

In 3.4 M MgCl₂ brine the surface developed completely differently with time as compared to observations made in NaCl brine. The SEM images show the presence of the same pyramid shaped corrosion phase of 50 μm in diameter after 13, 26 and 42 weeks (**Figure 23**) and a significantly higher coverage of the surface. From the morphology of the secondary phases, it can be concluded that this phase is not magnetite. The XPS narrow 2*p* spectra (**Figure 24**) show the presence of Fe(II) only, while the narrow O 2*s* spectra (not shown here) show the presence of hydroxide only, thus suggesting that the structure with pyramid morphology is a Fe(II) hydroxide phase.

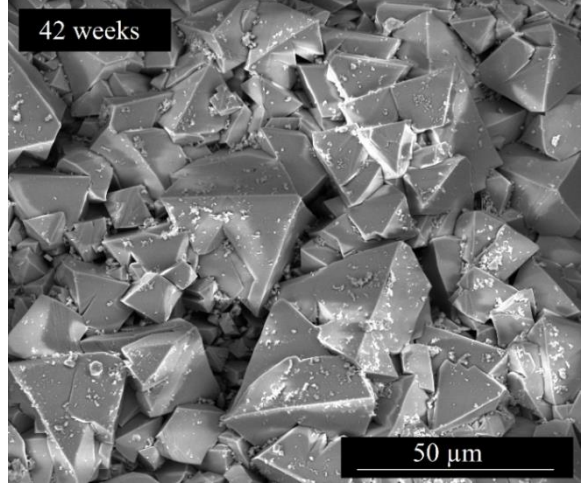
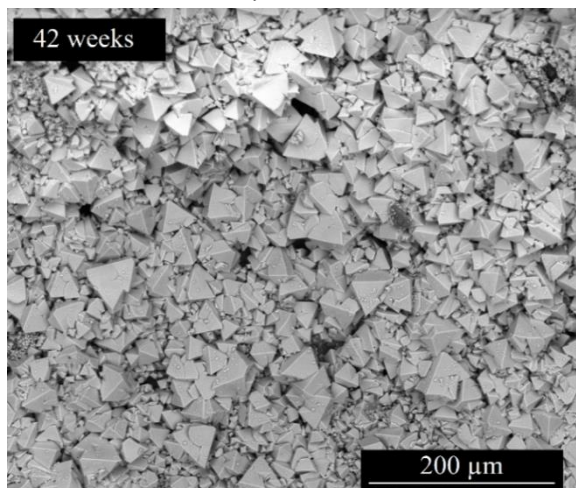
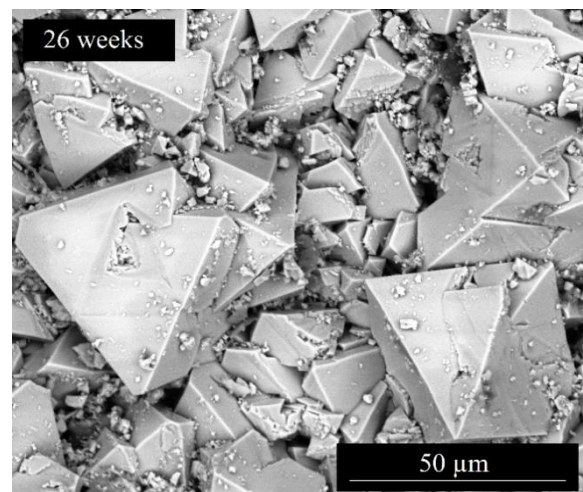
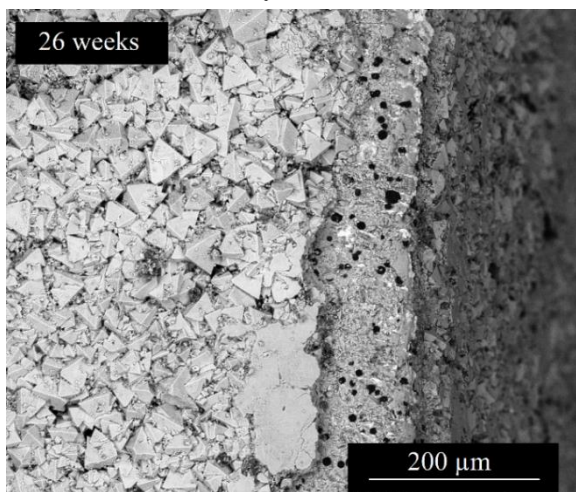
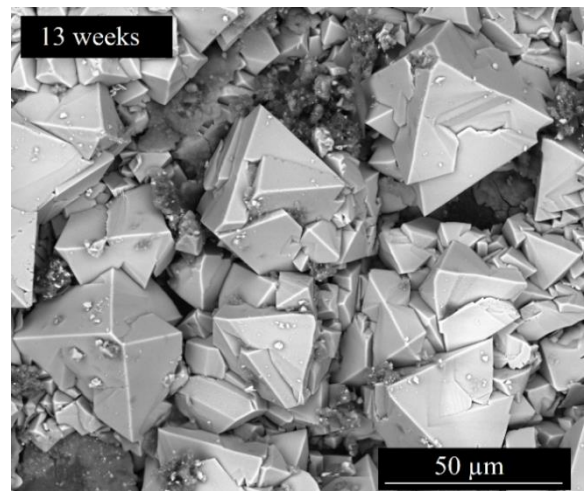
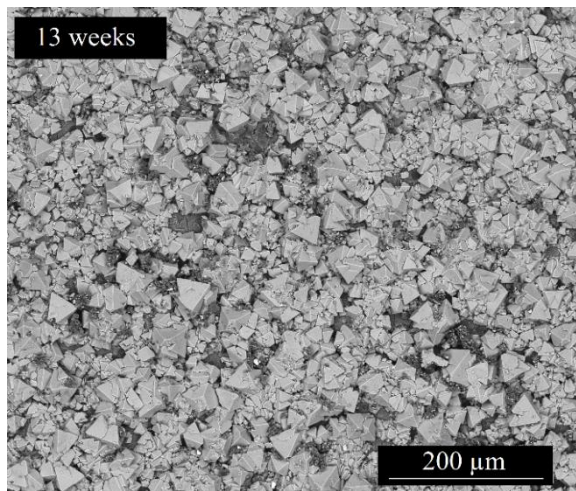


Figure 23: SEM images of the evolution of the solid phase morphology of the SGI in the 3.4 M MgCl_2 ($I = 10.2 \text{ M}$) brine exposed for 13 weeks (top) to 42 weeks (bottom), $T = 90 \text{ }^\circ\text{C}$, applying two microscope magnifications.

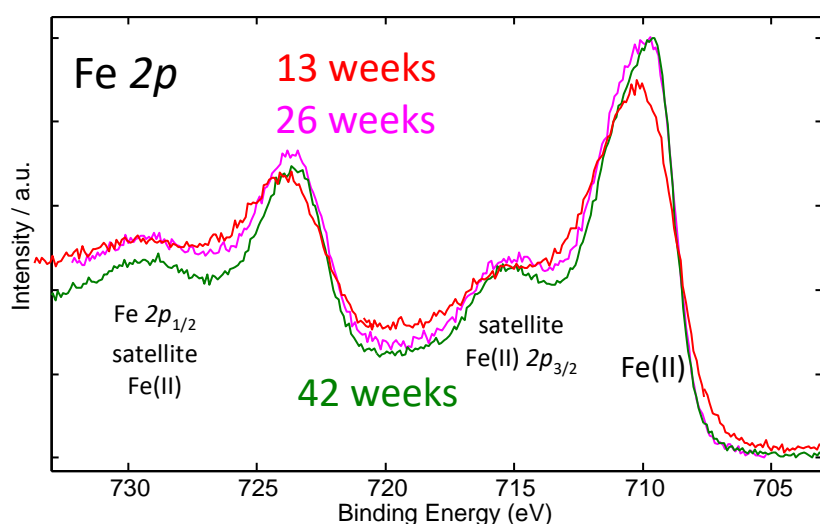


Figure 24: XPS narrow Fe 2p spectra of the spheroidal graphite iron surface/corrosion phase evolution with time in 3.4 M MgCl₂ at 90 °C.

The EDX analyses in **Table 14** show absence of Si and presence of Mg and Cl in the structure with the pyramid morphology. The absence of Si is an additional confirmation that corrosion in MgCl₂ and NaCl brine favour the generation of different secondary phases. This could be due to difference in ionic strength or due to the different pH ranges establishing. The Mg to Cl ratio could be residual salt. However, no salt crystals were observed in SEM and samples were carefully washed thus rendering the presence of crystallised salt unlikely.

Table 14: The chemical composition of the observed corrosion products on SGI according to their morphology in 3.4 M MgCl₂ brine at 90 °C.

Element / Atomic %	Cl	Fe	O	Mg
13 weeks - Pyramid structure	14.91±0.44	17.57±0.83	62.33±1.68	5.19±0.36
26 weeks - Pyramid structure	14.04±0.44	13.35±0.77	65.78±1.76	6.83±0.39
42 weeks - Pyramid structure	13.12±0.26	14.76±0.52	64.94±1.29	7.19±0.24

The XRD analyses (**Annex Figure A22**), show the occurrence of Fe₂(OH)₃Cl, iron hydroxychloride (PDF card 34-0199) as a dominant phase after 13, 26 and 42 weeks. EDX analysis suggests Mg(II) replacing about 25 % of Fe(II) in the structure. This substitution is possible due to similar atomic radius sizes between the two, 71 pm vs. 77 pm, respectively [Shannon, 1976]. The two small peaks present at 2θ = 56.4° and 70.2° after 26 and 42 weeks match with amakinite, which is a (Mg,Fe)(OH)₂ phase (PDF card 15-0125). This phase may correspond to the precursor of the iron hydroxychloride phase. It appears that under given conditions, the Fe₂(OH)₃Cl is more stable than magnetite or silicate phases.

The sample corroded for 13 weeks in saturated MgCl_2 at $90\text{ }^\circ\text{C}$ was embedded in resin, crosscut and polished following the procedure described in detail in *section 2.2.4* and examined by SEM-EDX. The images in *Figure 25* show the steel coupon (light) and surrounding resin (black) with the corrosion layer in-between. The corrosion layer detached from the steel upon cutting. The thickness of the layer is between $14.2\text{--}17.9\text{ }\mu\text{m}$, highlighting rather uniform corrosion. The graphite inclusion at the exposed surface is removed (hole at the rim), which likely occurred upon polishing. *Annex Figure A23* shows the elemental distribution obtained by EDX analysis of the crosscut, corroborating the obtained results on the magnesium/iron hydroxychloride phase.

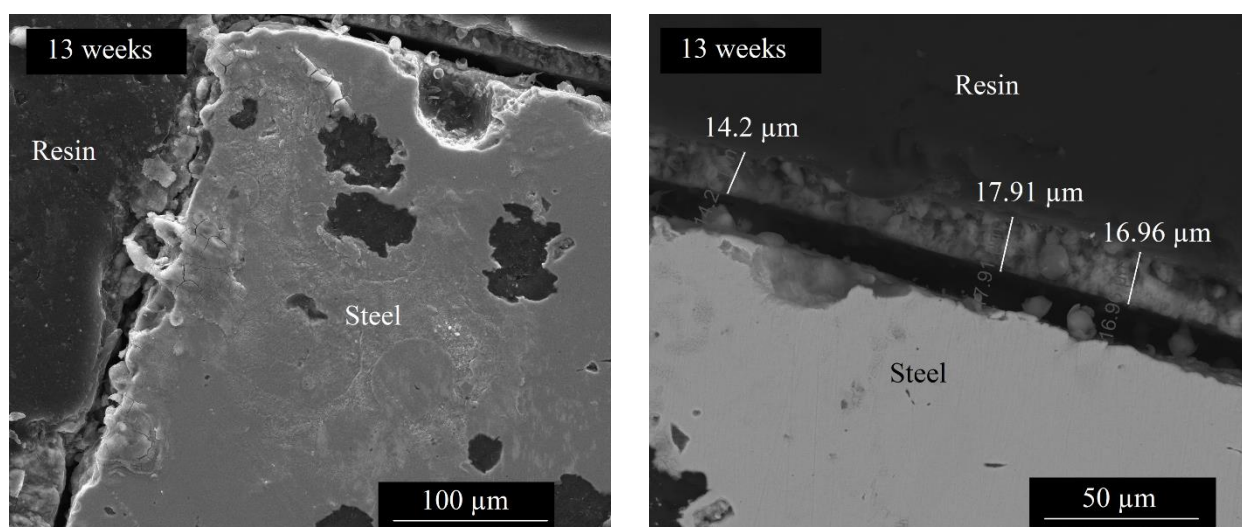


Figure 25: SEM images of the SGI crosscut corroded in 3.4 M MgCl_2 for 13 weeks at $90\text{ }^\circ\text{C}$.

Iron hydroxychloride is known as being metastable and oxidizes into green rust chloride, sulfate [Nemer et al., 2011; Rémazeilles & Refait, 2008] or magnetite [Schlegel et al., 2016], depending on the environment. The *Pourbaix* diagram generated for 3.4 M MgCl_2 system using the dissolved metals amounts after 42 weeks shows that no phase is thermodynamically stable under conditions corresponding to our data (*Figure 26 A*), with minnesotaite mineral stability window being the closest. Iron hydroxychloride has been found on many archaeological artefacts. However, the data for this compound are very limited and the $\log K$ value is only available at $25\text{ }^\circ\text{C}$. Running this system at $25\text{ }^\circ\text{C}$ with low activity of silica and high activity of iron then shows the stability window of iron hydroxychloride close to our data points (*Figure 26 B*). This highlights that this compound may actually be thermodynamically stable under high ionic strength, in the slightly acidic-neutral pH range and could be of relevance in the repository, provided high availability of aqueous iron. The mismatch between the experimentally observed and thermodynamically stable phases could, also in this case be, attributed to locally different conditions and/or kinetic effects on solid phase formation. Additionally, the silica activity in this system was calculated from the dissolved amounts based on the weight loss,

thus in reality it may be quite low in MgCl_2 systems. Furthermore, the calculated activity of iron is closely depending on the database, while the used [PI] database may be a source of uncertainty due to lack of reliable and complete iron data for activity calculations based on the Pitzer approach.

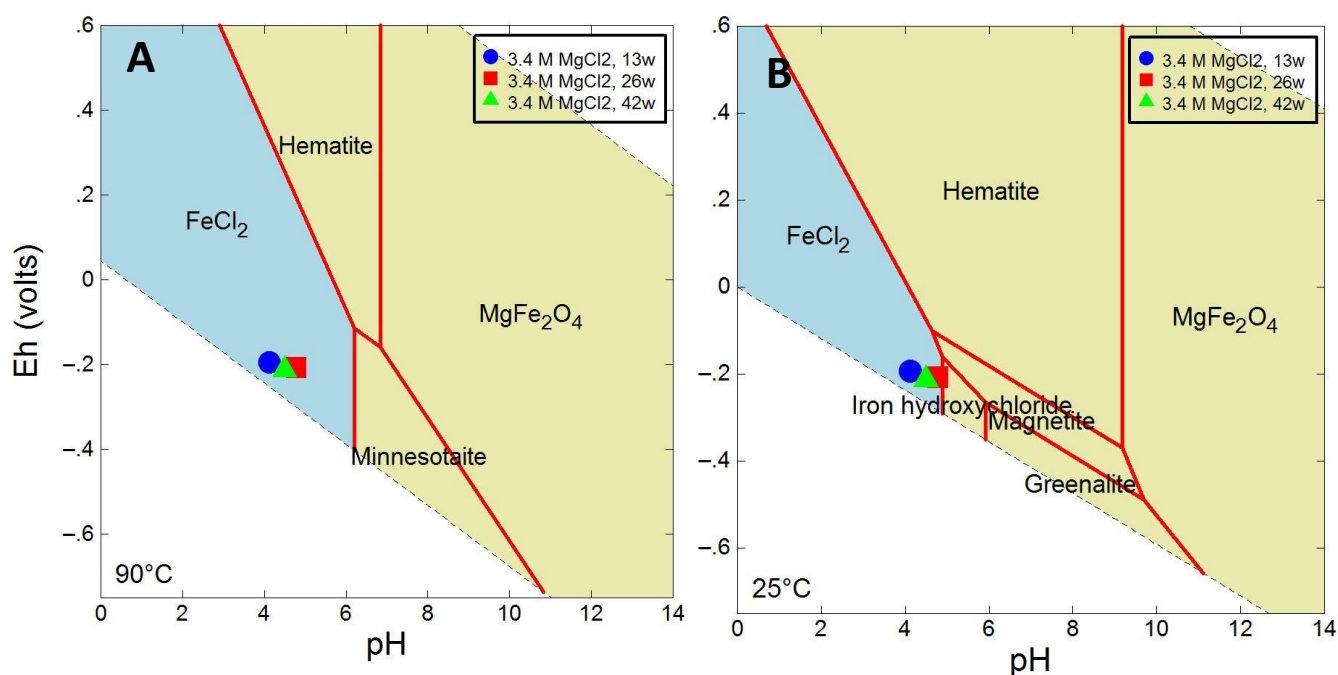


Figure 26: *Pourbaix* diagrams for the 3.4 M MgCl_2 system at 90 °C calculated with Pitzer approach and [PI] database. Iron (Fe^{2+}) activity taken from ICP-MS of $\log a = -3.65$ and silica ($\text{SiO}_{2,\text{aq}}$) activity taken from the weight loss of $\log a = -1.87$ (A). High iron activity $\log a = 3$ and low silica activity $\log a = -5$ (B).

This section describes the characterization of SGI crosscut sample corroded in the 3.4 M MgCl_2 for 31 weeks at 90 °C in the CEA Saclay SEARS laboratory and the results obtained by the synchrotron-based μXRF , μXAS and μXRD techniques. The optical microscopy on the crosscut of the sample (**Figure 27**) revealed a homogenous corrosion attack matching the surface analysis finding of the thick corrosion layer of iron hydroxychloride. The whole interface along the sample was selected as the region of interest.



Figure 27: The optical images of the crosscut with the red circle highlighting the interface of interest for SGI sample corroded in 3.4 M MgCl_2 for 31 weeks at 90 °C.

The μ Raman spectra of this sample (**Figure 28**) showed the presence of iron hydroxychloride in various spots in the corrosion layer (A, B) shown in **Figure 29**. One spectrum (C) showed in addition to iron hydroxychloride peaks corresponding to potentially FeO (wüstite) phase [Hazan et al., 2013] Additional peaks at $\sim 385\text{ cm}^{-1}$ and $\sim 712\text{ cm}^{-1}$ were not matched.

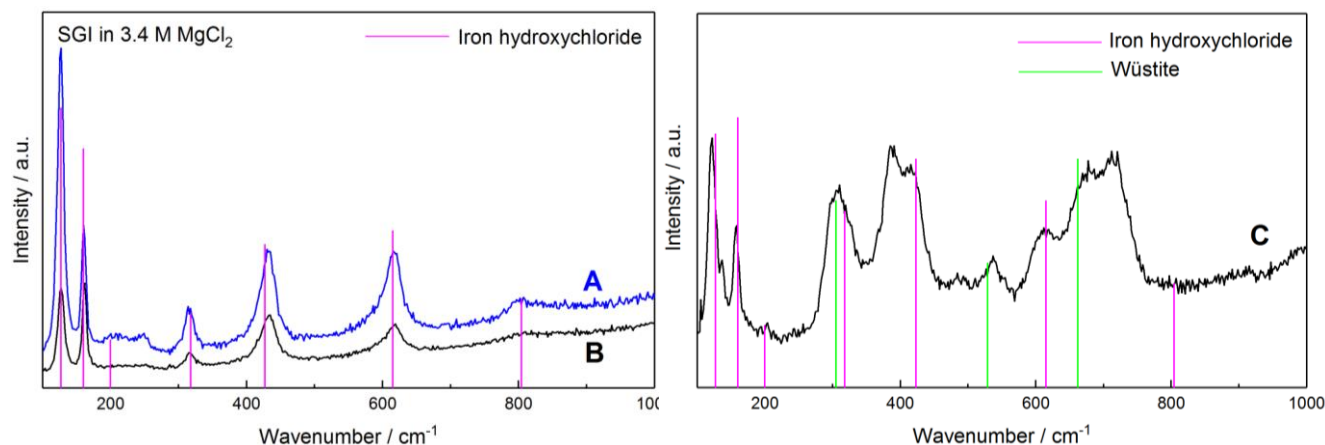


Figure 28: μ Raman spectra of the SGI crosscut corroded in 3.4 M MgCl_2 at $90\text{ }^\circ\text{C}$ for 31 weeks.

The SEM-EDX analysis of this sample showed the chemical composition (**Table 15**) of various examined spots in the corrosion layer shown in **Figure 29**. The Fe/Cl/Si/O ratio hinted at the presence of iron hydroxychloride in spots 5, 6, and 7, where Mg is also present in the structure and replaces approximately 20 % of Fe(II). Spots 3 and 4 were too close to non-corroded surface and are showing mainly the presence of iron. Spots 1, 2 and 8 have various compositions but include Mg, Si and Cl at the same time and could origin from a mixed Mg-Fe silicate phase or $(\text{Mg,Fe})(\text{OH})_2$ phase.

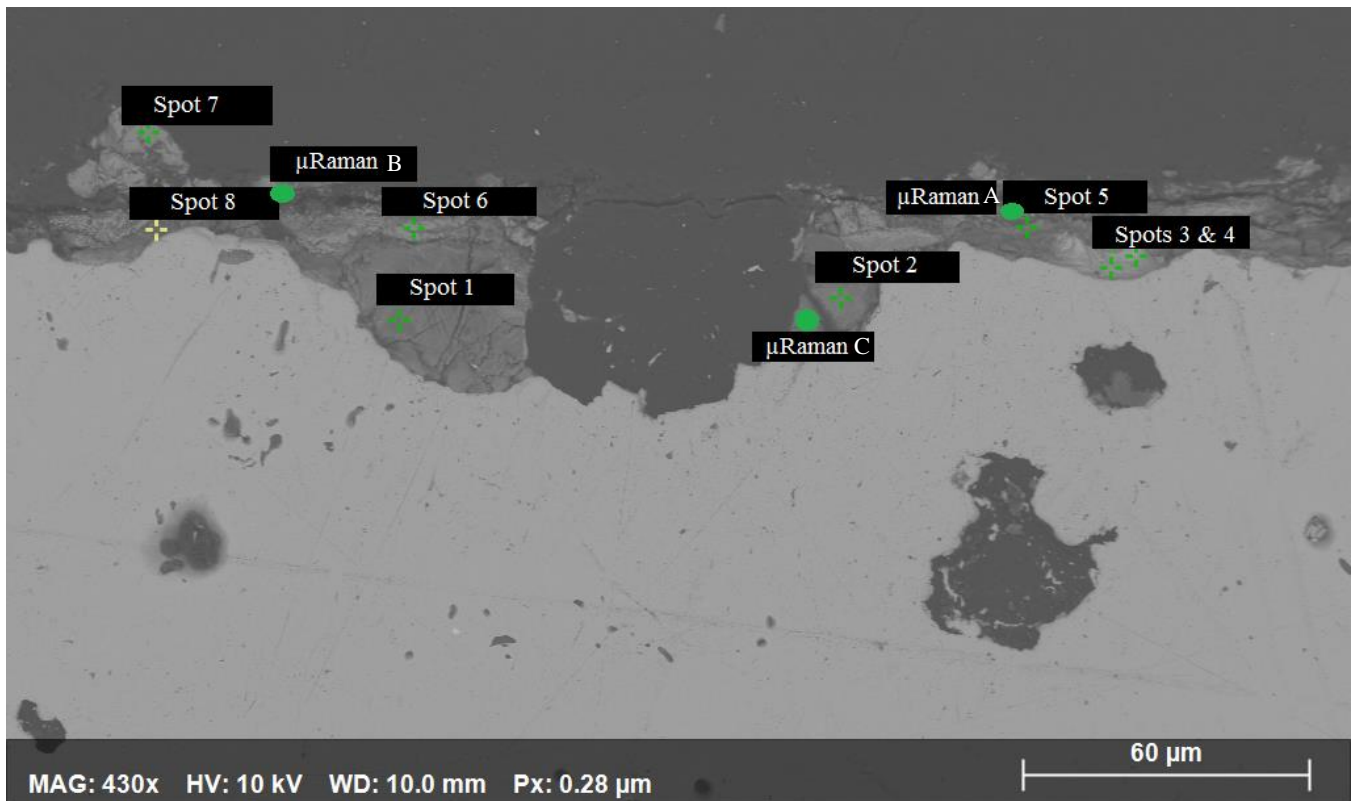


Figure 29: SEM image of the crosscut of the SGI corroded in 3.4 M MgCl₂ at 90 °C for 31 weeks. The spots shown in the figure correspond to the spots in the *Table 15*.

Table 15: The chemical composition of the phases observed for SGI crosscut in 3.4 M MgCl₂.

Element/ Atomic %	O	Mg	Si	Cl	Fe
Spot 1	32.0±3.1	9.2±1.6	16.0±1.8	5.5±0.8	37.2±3.2
Spot 2	57.7±3.5	8.6±1.6	6.6±1.0	0.9±0.1	26.1±2.7
Spot 3	6.3±1.0	0.13±0.07	6.4±1.0	0.3±0.1	86.7±6.1
Spot 4	6.7±1.0	1.2±0.1	6.3±1.0	0.4±0.1	85.3±6.1
Spot 5	52.6±3.3	7.1±1.4	0.7±0.2	13.1±2.3	26.4±2.8
Spot 6	50.7±3.3	7.1±1.4	0.3±0.1	14.4±2.3	27.4±2.8
Spot 7	47.8±3.2	6.5±1.2	0.1±0.07	15.9±2.4	29.5±2.8
Spot 8	60.4±3.6	14.8±2.3	6.4±1.0	5.4±0.8	12.9±2.1

The μXRF map shows a homogenous thick corrosion layer (*Figure 30*). The fitted XANES spectra in *Figure 30* are corresponding to the locations shown in the XRF map. The point 4 corresponds to pristine steel. The spectrum in point 5 matches iron hydroxychloride, while point 6 shows FeO as a corrosion product close to the bulk steel. FeO (wüstite) was also observed by μRaman, but not by SEM-EDX.

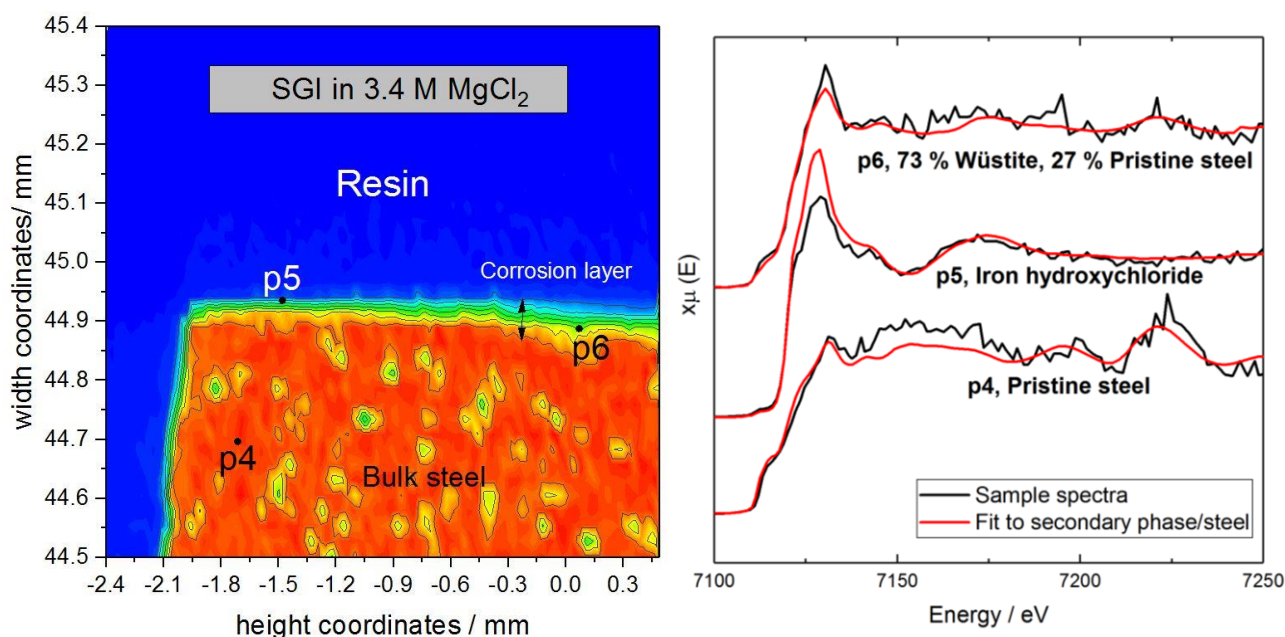


Figure 30: The μ XRF map and μ XANES spectra of the SGI sample crosscut corroded in 3.4 M MgCl_2 . The μ XANES spectra corresponding to the respective reference compounds are shown in *Annex Figure A10*.

The μ XRD line scan through the steel-corrosion product-resin interface (*Annex Figure A24*) was performed showing peaks matching the pristine steel and the iron hydroxychloride. The major peak for wüstite at $2\theta = 42^\circ$ is also present in weak intensity, however this is very close to another peak of iron hydroxychloride ($2\theta = 43^\circ$) and it cannot be distinguished with certainty. The observation of FeO (wüstite) in 3.4 M MgCl_2 sample is novel and was not detected by surface analyses. This observation could help identify the reaction pathway from the steel surface to the solution.

Similarly to NaCl brine, an experiment was run at 25 °C for 49 weeks for the SGI in 3.4 M MgCl_2 ($I = 10.2$ M). The SEM analysis showed the formation of a phase with identical pyramid morphology to iron hydroxychloride but with smaller crystal size, about 10-15 μm in size (*Figure 31*). The XPS Fe $2p$ narrow spectra (*Annex Figure A25*) showed the presence of Fe(II) only, as in the case of elevated temperature. The EDX showed a chemical composition matching the findings of the elevated temperature system, also including the Mg doping (*Table 16*). Finally, the X-ray diffractogram of the system at 25 °C (*Figure 32*) showed peaks matching iron hydroxychloride and additional peak matching the cubic iron due to low surface coverage. In this system, the formation of the secondary phase is independent of temperature. It is likely due to high ionic strength-chloride concentration, and range of pH_M and E_h conditions of the two systems, under which this phase is stable.

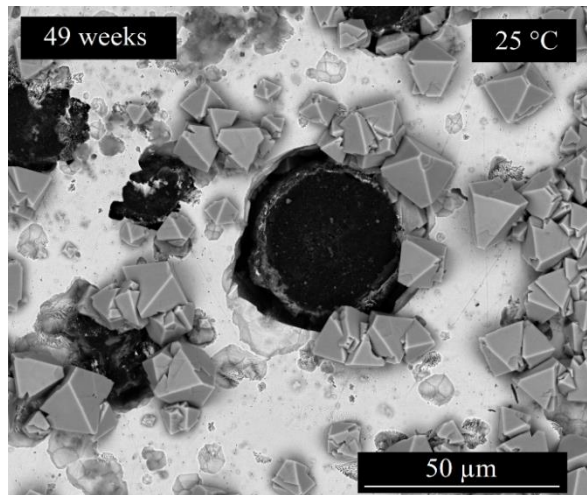


Figure 31: SEM image of the solid phase morphology on SGI in 3.4 M MgCl₂ brine at 25 °C.

Table 16: The chemical composition of the observed corrosion products on SGI according to morphology in 3.4 M MgCl₂ brine at 25 °C.

Element / Atomic %	Cl	Fe	O	Mg
49 weeks - Pyramid structure, Spot 1	15.2±0.4	22.75±0.91	56.63±1.51	5.42±0.33
49 weeks - Pyramid structure, Spot 2	17.66±0.52	31.79±1.27	45.86±1.57	4.69±0.37

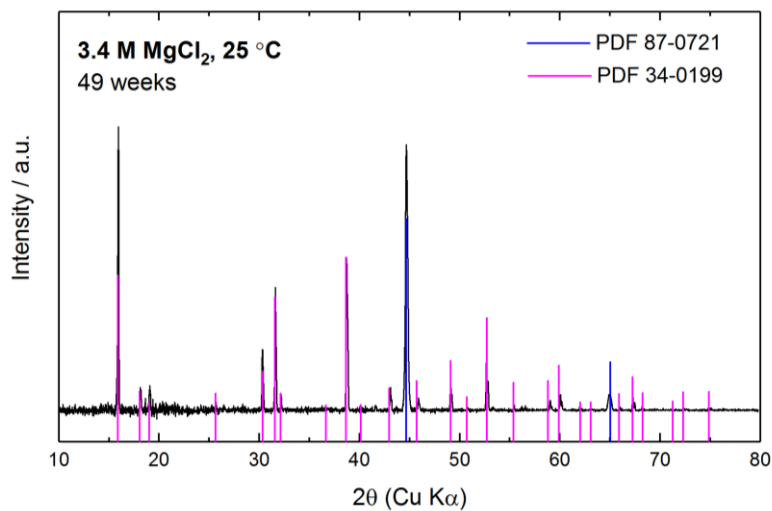


Figure 32: X-ray diffractograms of the spheroidal graphite iron corroded in 3.4 M MgCl₂ for 49 weeks at 25 °C. PDF card 87-0721 refers to the non-corroded steel surface, cubic iron, and 34-0199 to iron hydroxychloride.

One experiment was performed for SGI at 90 °C in solution 1, concentrated MgCl₂ with addition of sulfate. The results of various analytical techniques are shown in the *Annex Figures A26, A27 and A28*. The SEM image of the specimen for this system showed a structure of the consistent pyramid morphology as in the 3.4 M MgCl₂ brine, suggesting the presence of iron hydroxychloride. However,

an additional phase was observed on top of the pyramid structure. A significant Fe(III) peak is present along the Fe(II) peak in the narrow Fe $2p$ spectrum, suggesting that the additional formed phase on top of the presumably iron hydroxychloride is a mixed Fe(II)-Fe(III) or pure Fe(III) phase. This is most likely due to higher E_h measured for solution 1 (- 100 mV) compared to 3.4 M MgCl₂ (- 200 mV). The EDX analysis (*Annex Table A10*) of the pyramid structure particles matches iron hydroxychloride while the additional phase with no distinct morphology matches green rust chloride where Fe(II) is significantly replaced by Mg(II). This is in agreement with the additional Fe(III) peak observation by XPS. The X-ray diffractogram has high background, however pattern matching iron hydroxychloride phase can be identified. The pH_M value of the system with and without sulfate is similar (~ 6.7), while ionic strength is very high for both systems. Under these conditions it appears that the same phase, Mg doped iron hydroxychloride, is favoured. However, due to higher redox potential in solution 1, the competition with green rust chloride takes place.

The corroded coupon from the solution 1 experiment was embedded in resin, cut and polished. The SEM-EDX analysis (SEM image in *Annex Figure A29*) on the cut evaluated the thickness of the corrosion layer to be in the range of 23-32 μm . In comparison, the corrosion rate for this system from weight loss was determined as $26.3 \pm 1.5 \mu\text{m}$.

A set of experiments was performed for SGI in solution 1 at 25 °C. The SEM images of the surface (*Annex Figure A30*) after 20 weeks revealed, as in the case of solution 3, iron dissolution but no clear presence of corrosion phases (occasional precipitate of Na₂SO₄ from the solution after 26 weeks). The dissolution seems to be less concentrated to graphite inclusions proximity and is rather uniform. When focused on the edge of the sample, a strong corrosion attack was found, likely due to the rough surface at the edge, which provides imperfections and defects where dissolution can be initiated easily. The XPS analysis (not shown here) showed a strong peak of Fe(0) in the narrow Fe $2p$ spectra, supporting the absence of precipitated corrosion phases. The EDX and XRD analyses showed results matching the initial steel (*Annex Figure A31*).

As in the case of NaCl, an experiment was performed in dilute brine with ionic strength of 0.1 M MgCl₂ at 90 °C for 28 weeks. The results of various analyses are shown in the *Annex Figures A27, A28 and A32*. The XPS, SEM and XRD results of the steel coupon were identical to the $I = 0.1$ M NaCl system, with formed phases of stacked hexagonal and octahedral morphologies, confirmed as magnetite and cronstedtite. Interestingly, in $I = 0.1$ M MgCl₂ brine, the overall composition determined by EDX analysis (*Annex Table A11*) for the hexagonal phase matches cronstedtite, but part of Fe(II) is replaced by Mg(II) in the structure upon formation. The EDX determined Fe/O ratio of octahedral

structure matches magnetite composition. The corrosion in both dilute solutions of identical ionic strength (0.1 M) progressed similarly, highlighting that at this ionic strength the cation in the salt is not playing a role with regard to corrosion phase formation. Similarly, the *Pourbaix* diagram constructed for this system (not shown) is close to identical to 0.1 M NaCl system due to similar metals dissolved amounts and similar pH_M/E_h values of the two systems.

In the MgCl_2 based systems, the stable phases of interest are magnetite (low I), minnesotaite (depending on the aqueous Si concentration) and potentially iron hydroxychloride (high I).

Table 17 summarizes the experimentally determined secondary phases on SGI in various brines and at different temperatures along with the corresponding pH_M and E_h values. The experimental results discussed above show that various corrosion phases are distributed heterogeneously at the iron corrosion front. Findings point to an ongoing reaction taking place at the iron solution interface and a real equilibrium does most likely not establish under experimental conditions. This is also reflected by the different types of secondary phases suggested by thermodynamic calculations and found in the experiments.

Table 17: The observed secondary phases formed on corroded SGI under various conditions.					
Steel	Brine/ Molarity	T /°C	pH_M	E_h	Experimentally determined secondary phase
SGI	5 M NaCl	90	9.0±0.3	-210±50	Cronstedtite and magnetite. IHC at the steel/corrosion layer interface.
	5 M NaCl	25	7.10±0.05	-162±50	Green Rust Chloride, few iron hydroxychloride particles.
	Sol. 3	90	5.2±0.3	-199±50	Cronstedtite with Mg partially replacing Fe(II).
	Sol. 3	25	8.97±0.05	-212±50	No phase precipitation on the surface, marginal presence of $\text{Fe}(\text{OH})_2$ in the hole of the coupon.
	0.1 M NaCl	90	6.1±0.3	-218±50	Cronstedtite and magnetite.
	3.4 M MgCl_2	90	6.6±0.3	-212±50	Iron hydroxychloride with partial Fe(II) replacement with Mg. $(\text{Fe,Mg})(\text{OH})_2$ as potential precursor. FeO at the steel/corrosion layer interface.
	3.4 M MgCl_2	25	8.58±0.05	-299±50	Iron hydroxychloride with partial Fe(II) replacement with Mg.
	Sol. 1	90	6.7±0.3	-81±50	Iron hydroxychloride with partial Fe(II) replacement with Mg. Green Rust chloride with partial Fe(II) replacement with Mg.
	Sol. 1	25	8.90±0.05	-112±50	No phase precipitation.
	0.033M MgCl_2	90	6.4±0.3	-155±50	Cronstedtite and magnetite.

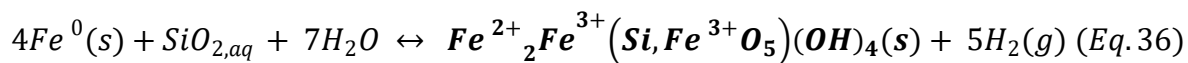
3.1.6 Corrosion mechanism

In case of all SGI samples, graphitic corrosion is taking place, where the iron around the graphite inclusion is preferentially corroded due to the galvanic coupling of iron (anodic sites) and carbon (cathodic sites). This phenomenon has been considerably more observed in certain samples (5 M NaCl at 90 °C, solution 3 at 25 °C) than in others. At some point, due to this phenomenon the graphite inclusion is removed upon corrosion and this contributes to the weight loss increasing the corrosion rate, even though the amounts of dissolved iron or coverage by secondary phases are low. The graphitic corrosion was previously observed for this type of steel by Hsu & Chen [2010]. Overall, uniform corrosion has been observed for SGI in NaCl and MgCl₂ brines, no distinct pitting corrosion was observed in the samples. pH_M has been confirmed as the main driver for iron corrosion in all systems with higher corrosion rates observed in systems with low pH_M.

The main findings in this work could be interpreted by the following corrosion mechanisms: The most general oxidation reaction for metals is specified for iron (*Eq. 1*) and since this reaction is anaerobic, the reduction of water gives rise to the formation of hydrogen (*Eq. 2*). Accumulation of Fe²⁺ in the solution gives rise to formation of iron hydroxide (*Eq. 3*) [Lyon, 2012; Sato, 2012; Tosca et al, 2018]. From the overall mass balance of this reaction, there is no direct change in pH upon formation of Fe(OH)₂.

For SGI corroded in NaCl brines, the 3.4 wt. % Si contained in steel seem to play a significant role. The Si is present as SiO₂ in the steel and its solubility is increasing with the ionic strength [Ahmed et al., 2015] and temperature [Zarrouk & Purnanto, 2015], but is ~ 1 mmol/L at near-neutral pH, room temperature and *I* = 0.3 M NaCl. This is however sufficient to form an iron silicate compounds, such as cronstedtite, under certain conditions. This phase was observed as the only formed phase in the 5 M NaCl system at 90 °C after 13 weeks, dominant phase in the 0.1 M NaCl system at 90 °C and 0.033 M MgCl₂ system at 90 °C after 28 weeks and in solution 3 system at 90 °C after 26 weeks. These four systems have one common feature; the pH_M value is below 6.5. Cronstedtite is likely formed though the following mass balance in *Eq. 36* [Schlegel et al., 2014, 2016; Vacher et al., 2019]. In the case of formation of this mineral, the pH_M with not change. The variation of pH_M considering uncertainty in these systems reached maximum of 0.7 pH_M unit, which can be explained by production of (OH)⁻ by water reduction on cathodic sites or impurities in salt or steel specimen. Hydrogen gas is produced, which drives the *E_h* to lower values. The *E_h* reduction is observable for all systems. The Cl⁻ in this

system is forming iron chloride aqueous species, but no Si-Cl phase has high enough stability under our conditions to precipitate.



Formation of magnetite was observed in 5 M NaCl system after 26 weeks, and bigger magnetite crystals were observed after 42 weeks. At this point, the magnetite and cronstedtite co-existed and no transformation was observed. Furthermore, no systematic spatial separation of the two phases on the surface was identified. The initial formation of cronstedtite in 5 M NaCl system did not passivate the surface sufficiently which led to further iron oxidation and water reduction which drove the pH_M to values of 8.5. Here the magnetite was favoured alongside cronstedtite and the coverage by the secondary phases achieved partial passivation of the steel, thus the pH_M increase levelled out. As only parts of the sample were covered by the corrosion products, a complete oxide monolayer has not yet been formed, thus in this system, the constant corrosion rate has not been reached and oxidation of the uncovered surface contributes to the further pH_M increase. The formation of magnetite, which is described in Schikorr equation (Eq. 5), does not produce or consume any acid or base and thus does not affect the pH_M .

The formation of magnetite alongside cronstedtite was observed also in dilute systems at pH_M 6.1-6.5. This can be explained by looking at the respective *Pourbaix* diagram of these systems, from which it is clear that lower ionic strength shifts the aqueous phase /solid stability border to lower pH_M values.

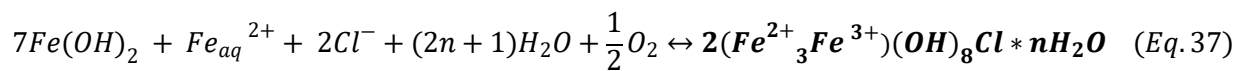
The sequential formation of cronstedtite, and then magnetite, can be explained as follows. At the beginning of the corrosion process, as the fresh surface was exposed, a possible slight excess of Si at the surface reacted with oxidised iron and formed cronstedtite. Afterward, cronstedtite formation was limited by the heterogeneity and concentration of Si in the steel, and the excess of oxidized Fe was eventually incorporated in magnetite. Magnetite formation is likely a result of solid-state transformations. Iron silicates are also stable under neutral - alkaline and reducing conditions as magnetite, but the precipitation of magnetite is solubility driven due to higher iron dissolved amounts compared to silica. The stability fields of magnetite vs. cronstedtite and greenalite as a function of Si concentration and redox potential are shown in work of Vacher et al. [2019], pointing at a very narrow stability window of cronstedtite with respect to the other two phases.

Despite high Cl^- concentration, SGI favours in 5 M NaCl brine the formation of magnetite within a very short period considering the timeframe of the repository evolution. Furthermore, this phase is stable in the *Pourbaix* diagram under the high ionic strength and very reducing conditions (at lower

redox potential than the one measured in this system) showing that it will not transform in long-term but rather grow into large crystals. The *Pourbaix* diagram generated in this work for 5 M NaCl system showed another potentially long-term stable phase under neutral-alkaline and reducing conditions, minnesotaite. Its stability with respect to magnetite is strongly dependent on Si concentration in the solution. Therefore, the accurate determination of silicate concentrations should be envisaged in future experiments.

We do not observe any transformation of cronstedtite into magnetite despite magnetite being more stable phase. Cronstedtite could be temporarily stabilized by cathodic protection due to electrical contact of newly formed cathode (precipitated phase) and anode (steel surface). This could lead to its extended stability, even if it is not favoured by thermodynamics. Nagies, & Heusler [1998] performed electrochemical experiments with low carbon steel in salt brines at elevated temperature of 90-200 °C and also observed the presence of magnetite.

The 5 M NaCl system run at 25 °C showed the presence of green rust chloride. It can be formed via direct precipitation from aqueous Fe²⁺ and Fe³⁺ [Usman et al., 2018] or as shown in **Eq. 37** in the presence of dissolved oxygen [Refaat & Génin, 1993]. This mass balance is similar also for green rust sulfate where each SO₄²⁻ replaces two Cl⁻ in the interlayer of the phase. The pH_M variation upon formation should be minimal (OH⁻ consumed, but produced upon iron oxidation). The pH_M for this system slightly increased over the period of 49 weeks from pH_M 6.5 to 7.1. This change can be attributed to same causes as for cronstedtite described above. Furthermore, lower pH_M compared to the elevated system despite similar corrosion rates could be attributed to the precipitation of (OH)⁻ containing solids. These conditions favour with redox potential of -160±50 mV under this ionic strength the formation of green rust chloride.



The observed coverage by green rust chloride was significant and homogenous, and slowed down steel corrosion by hindering the access of Cl⁻ and water to the metal surface. This film stability will be driven by the low solubility of green rust. However, cracks and pores will develop in the film and water will reach the metal surface leading to further iron oxidation. This will lead to further E_h decrease and possible pH_M increase. According to Jolivet et al. [2004] and Usman et al. [2018], the green rust chloride will transform into a mixture of magnetite and Fe(OH)₂ above pH 10, however depending on the ionic strength and E_h , this transformation could start at lower pH_M from 7.0 [Sagoe-Crentsil & Glasser, 1993; Tosca et al., 2018].

This mechanism may also help explaining the presence of iron hydroxychloride close to the bulk steel, so called internal layer as found by μ XANES spectroscopy in the 5 M NaCl, 90 °C sample. It appears that once cronstedtite and magnetite form a protective layer, Cl^- diffuses through layer voids and cracks to the metal surface where it enhances the anodic reaction. This spatial delocalization of anodic and cathodic reactions leading to the electrophoretic accumulation of Cl^- at the interface thus favour the precipitation of iron hydroxychloride even if the conditions in the solution are unfavourable for this phase [Schlegel et al., 2016; 2018]. The conditions at the steel/corrosion product interface are not the same as in the aqueous phase, thus allow existence of the iron hydroxychloride at the interface, where an electrochemical control is taking place. This also explains why it was found only in the thick areas of the corrosion layer, where additional corrosion phase is also present and why it was not observed by the surface analyses on non crosscut samples. The scheme of the suggested interface for the saturated NaCl system at 90 °C is shown in **Figure 33** with iron hydroxychloride shown as the internal corrosion layer and cronstedtite with magnetite as the external corrosion layer. The presence and composition of the double layer for low alloyed steel under highly saline conditions is reported in this work for the first time.

This phenomenon was observed by Schlegel et al. [2016; 2018], who examined the corrosion of low carbon steel in anoxic clay porewater under slightly alkaline conditions at 85 °C for up to 2 years, finding the formation of iron silicate phases such as greenalite and cronstedtite, and exposed to room temperature transients finding the presence of chukanovite, siderite (external corrosion layer) and iron hydroxychloride (internal corrosion layer), with iron hydroxychloride close to the bulk steel. This study has shown that despite low Cl^- concentration in aquatic systems in clay formations, the formed secondary phases on mild steels may contain Cl due to the mechanism explained above.

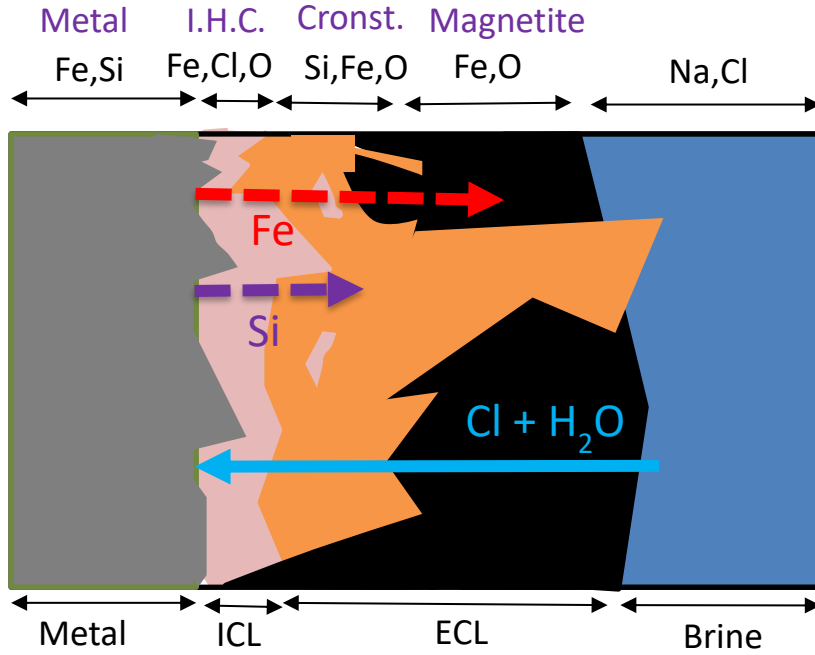
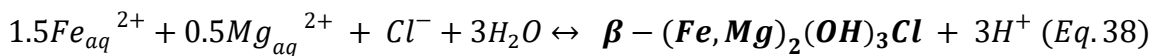


Figure 33: Schematic illustration of the elemental transfer at the steel/brine interface for saturated NaCl system at 90 °C. ICL stands for internal corrosion layer, ECL external corrosion layer and I.H.C. denotes the iron hydroxychloride phase.

In solution 3 and 1 at room temperature, iron corrosion was observed but no distinct precipitated phases were observed. In sulfate-containing solutions, pyrite could potentially be the long-term stable phase but will only form if microbial activity becomes relevant.

In MgCl₂ based systems, iron hydroxychloride was found at 90 °C and 25 °C in the saturated brine and in solution 1 at 90 °C. Mg was found to replace part of Fe(II), so the formation mass balance is proposed in *Eq. 38*. The pH_M is not expected to change upon iron hydroxychloride formation (H⁺ formation is balanced OH⁻ from water reduction).

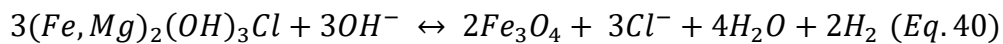
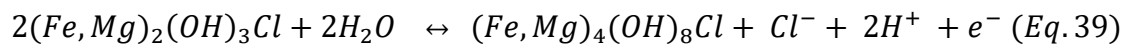


At elevated temperature in 3.4 M MgCl₂ and solution 1, the pH_M increased from ~5.2 to 6.6. In both cases, the coverage by this phase was significant and corrosion rates similar, likely due to similar pH_M values. Once the corrosion layer was thick enough to passivate the surface, the pH_M reached a plateau. At room temperature, the pH_M increase was larger, from 6.2 to 8.6. In this case, the coverage by the phase was too low. The lack of precipitates buffering the system, higher water dissociation constant at 25 °C compared to 90 °C and impurities in the brine/steel could explain the pH_M increase in this system. The corrosion mechanism appears unchanged as identical phases were formed for the two temperatures, with higher corrosion rate at elevated temperature. No Fe silicate compounds were found on SGI in

MgCl₂ brines with high ionic strength, although Ahmed et al. [2015] reported that higher ionic strength increases the silica solubility. Under the ionic strength conditions in these experiments, the Cl⁻ concentration in the solution favours the formation of chloride bearing phases. The formed Fe-Si phases in dilute MgCl₂ brine and Fe-Cl in concentrated MgCl₂ contain structural Mg replacing Fe(II).

The presence of mixed magnesium-iron hydroxychloride as a corrosion product of low carbon steel under highly saline conditions was also confirmed by Westerman & Pitman [1984]. Furthermore, a study performed at INE focusing on the low carbon steel corrosion in saturated MgCl₂ brine at elevated temperature by Grambow et al. [1996] also found the presence of mixed magnesium-iron hydroxychloride and amakinite.

Although iron hydroxychloride was found to be stable in the timespan of our experiments, it has been reported to eventually oxidize and form green rust chloride [Nemer et al., 2011; Refait & Génin, 1997; Rémazeilles & Refait, 2008] or magnetite [Schlegel et al., 2016]. The proposed mass balance for these transformations is detailed in the *Eq. 39* and *40*.



Additionally, green rust chloride is prone to transformation into either of the other GR in the presence of the appropriate anion, ferrous ions and oxygen [Refait & Génin, 1993]. Green rust chloride and iron hydroxychloride are stable under similar pH/ E_h conditions, with higher iron hydroxychloride stability at lower E_h values, as it is a pure Fe(II) phase compared to mixed Fe(II)/Fe(III) green rust chloride phase.

All the outcomes show that iron hydroxychloride remains stable in saturated MgCl₂ brines within the experimental timespan. Although partial iron hydroxychloride transformation into green rust chloride was observed for solution 1 at 90 °C, further transformation into magnetite cannot be confirmed nor ruled out based on the results obtained in this work. Furthermore, the partial transformation observed in solution 1 took place at rather high E_h , which would unlikely be the condition in the repository. The thermodynamic model has shown that under ionic strength corresponding to the saturated MgCl₂ brine, iron hydroxychloride is potentially stable under moderately acidic-neutral and reducing conditions, provided that sufficient iron is oxidised, thus making this phase of interest in the context of the repository.

The paper by Rémazeilles & Refait [2008] also described the equilibrium between Fe(OH)₂ and Fe₂(OH)₃Cl, specifying Fe(OH)₂ as the precursor of iron hydroxychloride. The formation mechanism

was suggested as alternating $\text{Fe}(\text{OH})_2$ and FeCl_2 layers, which are structurally similar and where Cl^- substitutes at random for OH^- ions. This configuration is then rearranged into iron hydroxychloride. The μXANES for the SGI sample in saturated MgCl_2 revealed the presence of FeO at the metal interface. FeO formation is likely a result of solid-state transformation. FeO is metastable and is known to transform into magnetite [Tanei and Kondo, 2017]. The route for this transformation most likely is via anaerobic oxidation into $\text{Fe}(\text{OH})_2$. As Mg is present in the solution, it would likely partially substitute for $\text{Fe}(\text{II})$ upon $\text{Fe}(\text{OH})_2$ formation from FeO , as presence of $(\text{Fe},\text{Mg})(\text{OH})_2$ phase was confirmed by XRD for 3.4 M MgCl_2 system. The presence of this mixed compound alongside FeCl_2 would hinder the transformation into magnetite, and instead favour the formation of iron hydroxychloride.

In terms of which phase should be evaluated as a sink for radionuclides from the point of long-term stability under reducing conditions, it would be magnetite for dilute NaCl , MgCl_2 systems and concentrated NaCl systems and iron hydroxychloride for concentrated MgCl_2 brines. Furthermore, a silica containing phase such as minnesotaite may also be present in long-term in both brines. This would need to be experimentally confirmed in longer experiments and under strictly reducing conditions, where the silica dissolution would be followed. Of course, many other aspects (e.g. oxidizing species effect on the E_h) need to be taken into account to accurately predict the corrosion behaviour in the repository.

3.2 Cr-Ni steel corrosion in dilute to concentrated NaCl and MgCl₂ solutions

3.2.1 Initial characterization

The second type of steel was characterized by the same techniques as SGI. SEM images of the polished initial steel surface show a uniform smooth surface of the Cr-Ni steel (*Figure 34*). At higher magnification, scratches originating from the production as well as small carbon impurity spots were detected. XPS Fe 2*p* spectrum (*Figure 35 A*) shows only the peak of Fe(0), similarly as in the case of the SGI. In case of Cr-Ni steel, the formation of the protective Cr₂O₃ layer is instantaneous and thus the Cr(III) is always present on the surface, even prior to submerging the samples into brines. Comparing the elemental quantification by EDX analysis with the certificate (*Table 18*) shows a good match considering the uncertainty of EDX data. XRD analysis (*Figure 35 B*) was performed under anoxic conditions and compared to the database. The red lines show a match in the database with an alloy of 70 % iron, 11 % Ni and 19 % Cr, close to the composition of the alloy used in this study. As for SGI, the AFM analysis was performed on the Cr-Ni steel, showing lower roughness in comparison to the SGI steel, as due to the carbon inclusions in SGI obtaining a smooth surface is more challenging. A root mean square (RMS) roughness of 5.8 nm was found considering a scanning area of 30 x 30 μm².

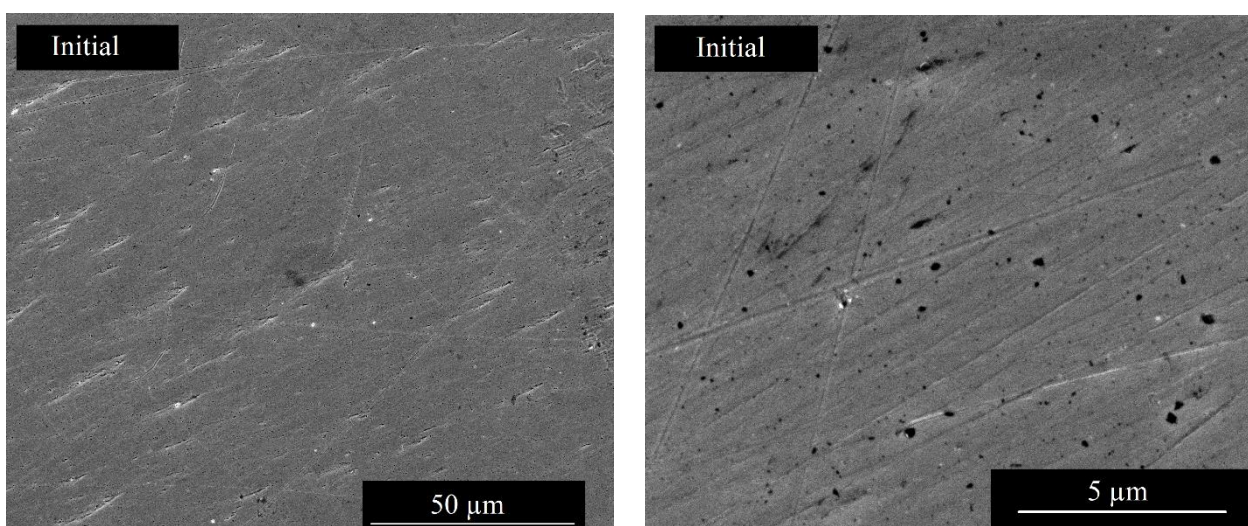


Figure 34: SEM images of the initial Cr-Ni steel surface under various magnifications.

Table 18: Chemical composition of the Cr-Ni steel.

Element / wt. %	C	Mn	Si	Cr	Ni	Mo	Cu	Fe
Certificate	0.06	1.15	0.35	22.45	13.17	0.23	0.23	62.36
EDX (Uncertainty +/- 3 Sigma)	-	1.18±0.32	0.45±0.07	23.13±0.53	13.21±1.05	0.29±0.17	-	61.74±1.13

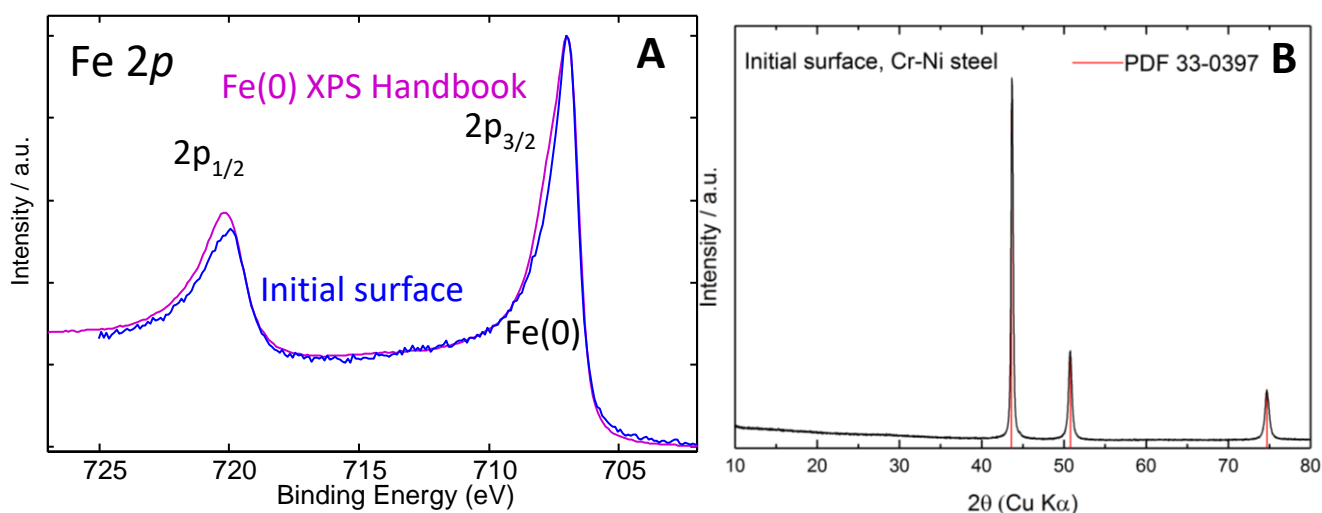


Figure 35: XPS narrow Fe 2p spectrum (A) and X-ray diffractogram (B) of the initial Cr-Ni steel, matching 304 austenitic steel (PDF 33-0397).

3.2.2 Dissolved metals evolution

The *Tables 19, 20, 21* below show the dissolved amounts of Cr, Fe and Ni measured for the Cr-Ni steel by the ICP-MS for all systems. The lowest are the values of chromium, then iron and highest are the ones of nickel.

Chromium concentrations lie either below or close to the detection limit in all solutions. The low concentrations are easily explained by the expected low solubility of Cr(III) oxide solid phases. Low concentrations of iron indicate generally low corrosion rates. The highest amounts of dissolved iron are found in solution 1 and in 3.4 M MgCl₂ at 90 °C. The inconsistent trends for the measured iron concentrations decreasing with time after initial increase are pointing to the precipitation of iron containing solid phases. Fe(II) should not reach solubility limits of pure hydroxide solids at the low concentration level, so that we may assume Fe(III) oxihydroxides or mixed phases forming with time.

The relatively high E_h values measured in the solutions (see section below) could point to oxidation to Fe(III).

Finally, the amounts of dissolved nickel were high after 26 weeks for almost all solutions. The highest dissolution of nickel was found in solution 1 at 90 °C. But also for nickel a clear reduction in concentrations below detection limits is found after 28 weeks for all solutions. As in the case of iron, precipitation of solid phases must be invoked for this observation. As nickel is not redox sensitive under given conditions, one may assume coprecipitation of Ni(II) with Fe(III) oxihydroxides or formation of mixed Ni(II)-Cr(III) or Ni(II)-Fe(III) solid phases (see also the outcome of geochemical calculations below).

Table 19: The dissolved amounts of chromium in the solution for Cr-Ni steel. The numbers in parentheses correspond to the relative standard deviation in %.

System/ Amounts in $\mu\text{g/L}$	13 weeks	26 weeks	28 weeks	42 weeks	49 weeks
5 M NaCl, 90 °C	<10	40.5 (46.4)	-	<10.	-
3.4 M MgCl ₂ , 90 °C	30.7 (21.8)	<10	-	<10	-
5 M NaCl, 25 °C	-	-	-	-	<10
3.4 M MgCl ₂ , 25 °C	-	-	-	-	<10
0.1 M NaCl, 90 °C	-	-	<10	-	-
0.033 M MgCl ₂ , 90 °C	-	-	<10	-	-
Solution 3, 90 °C	-	27.8 (56.0)	-	-	-
Solution 1, 90 °C	-	32.7 (6.0)	-	-	-
Solution 3, 25 °C	-	<10	-	-	-
Solution 1, 25 °C	-	<10	-	-	-

Table 20: The dissolved amounts of iron in the solution for Cr-Ni steel. The numbers in parentheses correspond to the relative standard deviation in %.

System/ Amounts in $\mu\text{g/L}$	13 weeks	26 weeks	28 weeks	42 weeks	49 weeks
5 M NaCl, 90 °C	11.93 (28.2)	61.1 (15.3)	-	<10	-
3.4 M MgCl ₂ , 90 °C	91 (43.9)	1099 (3.9)	-	<10	-
5 M NaCl, 25 °C	-	-	-	-	<10
3.4 M MgCl ₂ , 25 °C	-	-	-	-	<10
0.1 M NaCl, 90 °C	-	-	117(58.6)	-	-
0.033 M MgCl ₂ , 90 °C	-	-	<10	-	-
Solution 3, 90 °C	-	668(23.5)	-	-	-
Solution 1, 90 °C	-	151 (3.0)	-	-	-
Solution 3, 25 °C	-	<10	-	-	-
Solution 1, 25 °C	-	<10	-	-	-

Table 21: The dissolved amounts of nickel in the solution for Cr-Ni steel. The numbers in parentheses correspond to the relative standard deviation in %.

System/ Amounts in $\mu\text{g/L}$	13 weeks	26 weeks	28 weeks	42 weeks	49 weeks
5 M NaCl, 90 °C	228.3 (1.2)	796.7 (3.4)	-	<30	-
3.4 M MgCl ₂ , 90 °C	110.9 (21.2)	542.4 (3.4)	-	<30	-
5 M NaCl, 25 °C	-	-	-	-	<30
3.4 M MgCl ₂ , 25 °C	-	-	-	-	<30
0.1 M NaCl, 90 °C	-	-	<30	-	-
0.033 M MgCl ₂ , 90 °C	-	-	<30	-	-
Solution 3, 90 °C	-	963.9 (2.0)	-	-	-
Solution 1, 90 °C	-	9688.3 (1.8)	-	-	-
Solution 3, 25 °C	-	<30	-	-	-
Solution 1, 25 °C	-	782 (1.7)	-	-	-

3.2.3 pH / E_h evolution

pH_M and E_h values are shown in *Figures 36* and *37*. pH_M remains constant or shows slight increase (largest $\Delta\text{pH}_M \sim 1.0$).

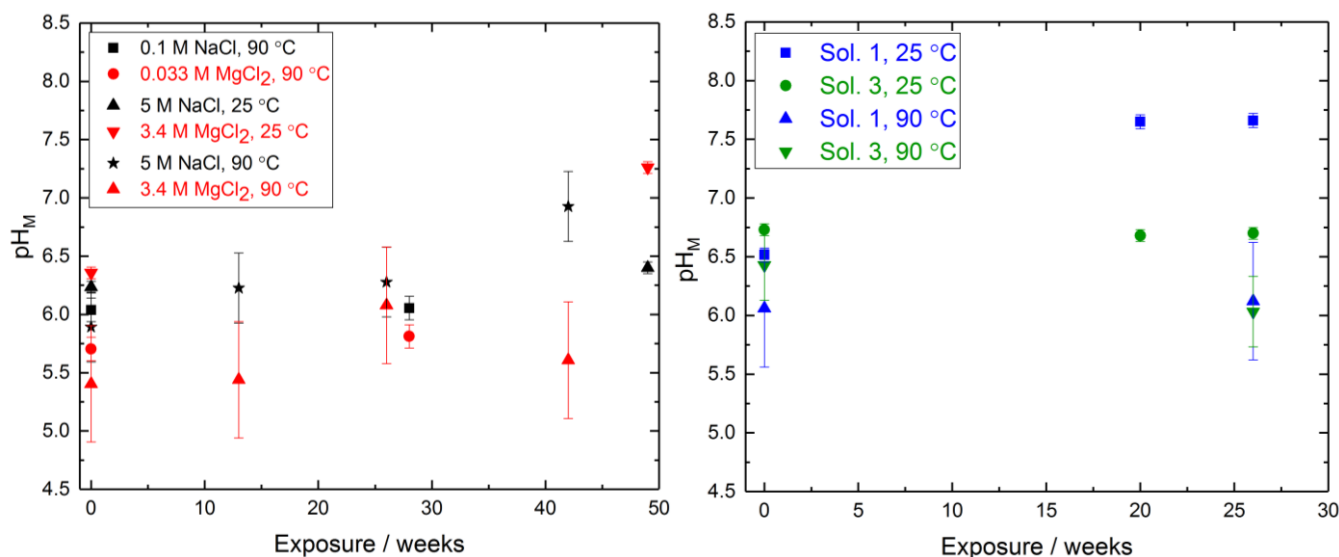


Figure 36: The pH_M evolution for the Cr-Ni steel corroded in various brines with time.

The E_h evolution in experiments with corroding Cr-Ni steel is different to that for SGI. The concentration of the redox buffers Fe(II)/Fe(III) in solutions in general is low, which makes it difficult to measure reliable E_h values. Thus in our case the values may have high uncertainty and have to be considered with care. The E_h decreased in some solutions in others a slight increase is found.

The measured E_h values indicate that not really reducing conditions establish in the solutions. It is, however, unlikely that oxygen intrusion occurs, which would shift the E_h up, as these autoclaves were stored in an inert atmosphere environment, which was regularly controlled over the whole course of the experiments. This is also confirmed by presence of only traces of oxygen in the gas phase. The reason for the relatively high E_h values in solutions, therefore, is assumed to be mainly due to the low Fe(II) concentrations.

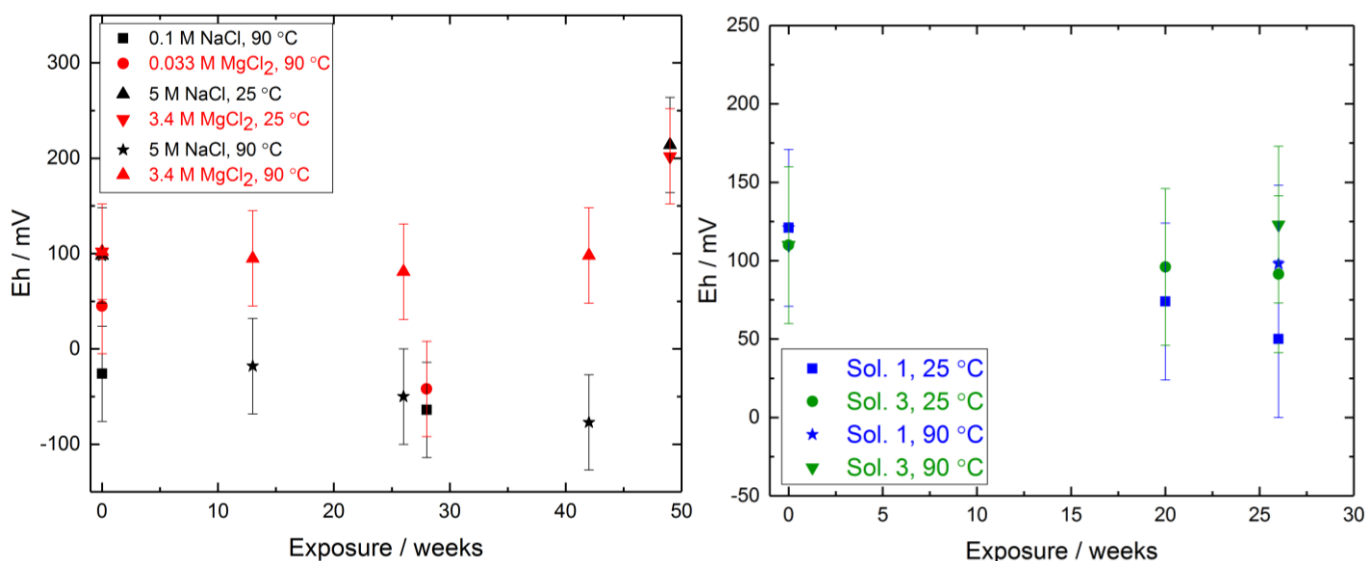


Figure 37: The E_h evolution of the Cr-Ni steel corroded in various brines with time.

As in the case for the SGI, the potentiodynamic polarization measurements [McCafferty, 2010; Popov, 2015] performed by Dr. P. Cekir-Wuttke determined the approximate corrosion potentials (E_{corr}) and pitting potentials (E_{pit}) (described in *section 1.3.1*) for Cr-Ni steel used in this study in two brines. The found values were: $E_{corr} \sim -70$ mV, $E_{pit} \sim 200$ mV for 5 M NaCl, 25 °C and $E_{corr} \sim -440$ mV, $E_{pit} \sim -80$ mV for 3.4 M MgCl₂, 25 °C. The values of redox potentials measured in this work for the corroded steels are above the pitting potentials for both brines at 25 °C (212 ± 50 mV for NaCl and 202 ± 50 mV for MgCl₂). Pit formation, however, can be a slow process and possibly will take place in the long-term but not necessarily in the relatively short experiments of this work.

This general finding that metal ion concentrations remain low in all experiments points to an efficient passivation mechanism and small corrosion rates of the Cr-Ni steel under given experimental conditions.

3.2.4 Corrosion rate

The corrosion rates obtained from the weight loss for this type of steel are very low, $<0.1 \mu\text{m/a}$ for almost all systems (*Table 22*). In these cases, the weight loss was equal to the uncertainty of the scale, which is 0.0001 g. The two systems with sulfate, run at 90°C , showed slightly higher corrosion rates of $0.49\pm 0.05 \mu\text{m/a}$ for solution 3 and $0.44\pm 0.05 \mu\text{m/a}$ for solution 1, respectively. The values for hydrogen evolution obtained from the analysis of the gas phase composition were all in the range of the background, matching the low corrosion rates.

System/ CR in $\mu\text{m/a}$	13 weeks	20 weeks	26 weeks	28 weeks	42 weeks	49 weeks
5 M NaCl, 90°C	<0.1	-	<0.1	-	<0.1	-
3.4 M MgCl₂, 90°C	<0.1	-	<0.1	-	<0.1	-
5 M NaCl, 25°C	-	-	-	-	-	<0.1
3.4 M MgCl₂, 25°C	-	-	-	-	-	<0.1
0.1 M NaCl, 90°C	-	-	-	<0.1	-	-
0.033 M MgCl₂, 90°C	-	-	-	<0.1	-	-
Solution 3, 90°C	-	-	0.49 ± 0.05	-	-	-
Solution 1, 90°C	-	-	0.44 ± 0.05	-	-	-
Solution 3, 25°C	-	<0.1	<0.1	-	-	-
Solution 1, 25°C	-	<0.1	<0.1	-	-	-

In the literature, laboratory autoclaves experiments showed for the Cr-Ni steel used in this study corrosion rate of $1.9 \mu\text{m/a}$ in solution 1 and $0.62 \mu\text{m/a}$ in solution 3 after 2 years at 150°C with small pits of average $30 \mu\text{m}$ depth [Kienzler, 2017_b]. The steel has been found susceptible to stress corrosion cracking and pitting. The comparison to our corrosion rates shows that the rate is dependent on the temperature, particularly in solution 1 and that pits are present already after 2 years of exposure.

Cr-Ni steel showed corrosion rates of $0.3\text{-}0.7 \mu\text{m/a}$ at 170°C after almost 5 years in an electrically heated borehole in the Asse salt mine (solution 3), along with stress corrosion cracking and pitting corrosion (up to $200 \mu\text{m}$ in depth) [Kursten et al., 2004; Smailos & Fiehn, 1995]. Further field studies revealed corrosion rates below $1 \mu\text{m/}$ with pits up to $50 \mu\text{m}$ deep [Kursten et al., 2004].

Due to those findings of pitting corrosion in various studies the investigators considered Cr-Ni a less qualified material for the overpack container wall and preferred the SGI. SGI shows - as also stated in the present study - higher corrosion rates. The absence of pitting corrosion, however, allows for a

better predictability of container integrity over the long-term. The fact that pitting corrosion is not found for Cr-Ni steel in the present work might be due to the relatively short experiment duration.

3.2.5 Secondary phase characterization and evolution

It needs to be noted that XPS analysis is very surface sensitive with an information depth of a few nm while EDX provides rather bulk information on a given sample. XPS, therefore, is able to detect very thin Cr₂O₃ layers, while EDX analysis still “sees” the bulk metal.

3.2.5.1 NaCl brine

Corrosion experiments in 5 M NaCl at an elevated temperature of 90 °C were run up to 42 weeks. The SEM images of the surface in *Figure 38* show the formation of a thin layer on top of the non-corroded surface after 13 and 26 weeks. Its thickness and morphology could not be evaluated. No pits are visible at any spot on the sample after 13 and 26 weeks. After 42 weeks, the SEM image shows a damage point on the surface, but its size and geometry suggest it is from the steel production. The rest of the surface after 42 weeks is also appearing without damage. The XPS analyses of the surface with respect to time show after 13 and 26 weeks presence of Cr(III) (*Annex Figure A33*), Fe(0), Fe(III), Ni(0) and a weak Ni(II) peak, but no significant contribution of Fe(II) in locations with the particles suggesting initial surface with Cr₂O₃, Cr(OH)₃ and/or NiFe₂O₄ (possible solid solution with magnetite) layer. Similarly, after 42 weeks, the XPS shows presence of Cr(III), mixed oxide / hydroxide signal and Fe(0) peak.

The EDX analyses of the particles after 13 and 26 weeks show the presence of Cr, Ni, Fe and O but no compound can be concluded, as the interference from the steel below does not allow obtaining clear composition. The EDX analyses of the locations without the particle layer (including the damage hole) and of the sample after 42 weeks match the composition of the initial steel. At last, the XRD analyses (*Annex Figure A34*) show only peaks matching the initial surface: Cr-Ni steel after 13, 26 and 42 weeks. More detailed information is available from synchrotron based μ XAS studies.

After SEM measurements were completed, the Cr-Ni sample corroded for 13 weeks in saturated NaCl at 90 °C was embedded in resin, crosscut and polished. Additional SEM analysis was performed on the cut (*Annex Figure A35*). No corrosion damage could be observed.

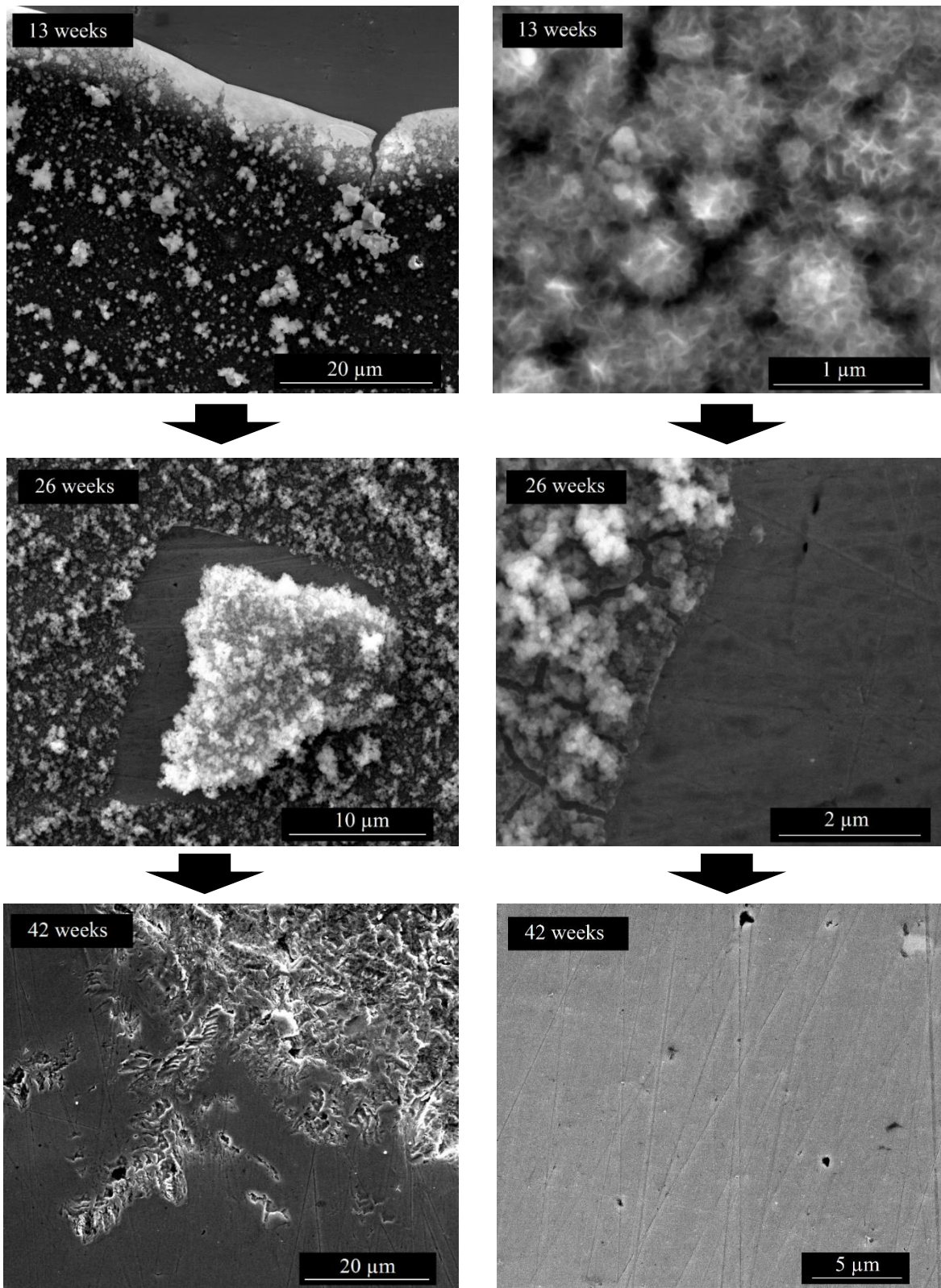


Figure 38: SEM images of the evolution of the solid phase/surface morphology of the Cr-Ni steel in the 5 M NaCl brine ($I = 5 \text{ M}$) exposed for 13 weeks (top) to 42 weeks (bottom), $T = 90 \text{ }^\circ\text{C}$, applying two microscope magnifications.

As in the case of SGI, the Cr-Ni steel corrosion interface of the 5 M NaCl, 31 weeks, 90 °C sample was examined by the same various techniques. **Figure 39** shows the optical image of the crosscut of the Cr-Ni steel sample corroded in 5 M NaCl with two regions of interest with a very thin detached corrosion layer.

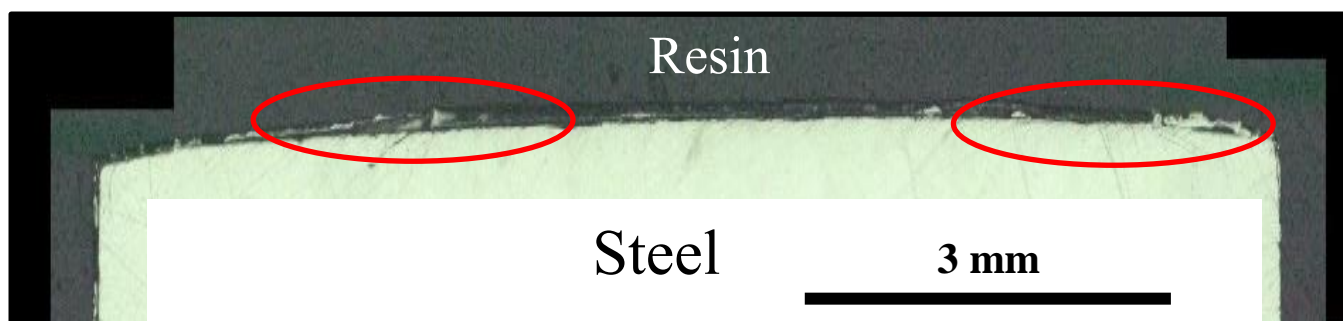


Figure 39: The optical image of the crosscut with the red circles highlighting the interface of interest in Cr-Ni steel sample corroded in 5 M NaCl at 90 °C.

The μ Raman analysis did not provide any conclusive results. The SEM-EDX analyses of the detached corrosion layer shown in **Annex Figure A36, Table A12**, showed composition, which could match a mixed FeCr_2O_4 / NiFe_2O_4 and Cr_2O_3 or $\text{Cr}(\text{OH})_3$ phases. No single phase could be assumed from the elemental ratios.

The μ XRF maps showing the elemental distribution of Ni and Fe are shown along with the positions of the selected points of interest for μ XANES in **Figure 40**. The μ XANES spectra for the two elements with the corresponding fits using the linear combination fitting of reference spectra are shown in **Figure 41**.

The corrosion layer in the examined Cr-Ni steel sample is very thin as shown in optical microscopy. The μ XANES spectra of iron (**Figure 41 A**) are consistent with the presence of green rust chloride along with the pristine steel in points 3, 4, 5 and pristine steel only in point 6. Points 1 and 2 show spectra which can be fitted by a linear combination of spectra for 58-60 % trevorite (NiFe_2O_4) and 40-42 % green rust chloride.

The μ XANES spectra of nickel (**Figure 41 B**) match the pristine steel in points 3 and 4, and show the presence of the same two compounds, trevorite and green rust chloride in points 1 and 2 in different proportions. The point 1, closer to the bulk steel has almost equal distribution of the two compounds, while point 2 in the corrosion layer shows 71 % of trevorite and 29 % of green rust chloride. Considering these findings along with the results of μ XANES of iron, where more spectra matching the green rust chloride along pristine steel were obtained, it appears that there is a systematic

distribution of the phases: GR Cl is forming close to the bulk steel and trevorite in the outer part of the corrosion layer.

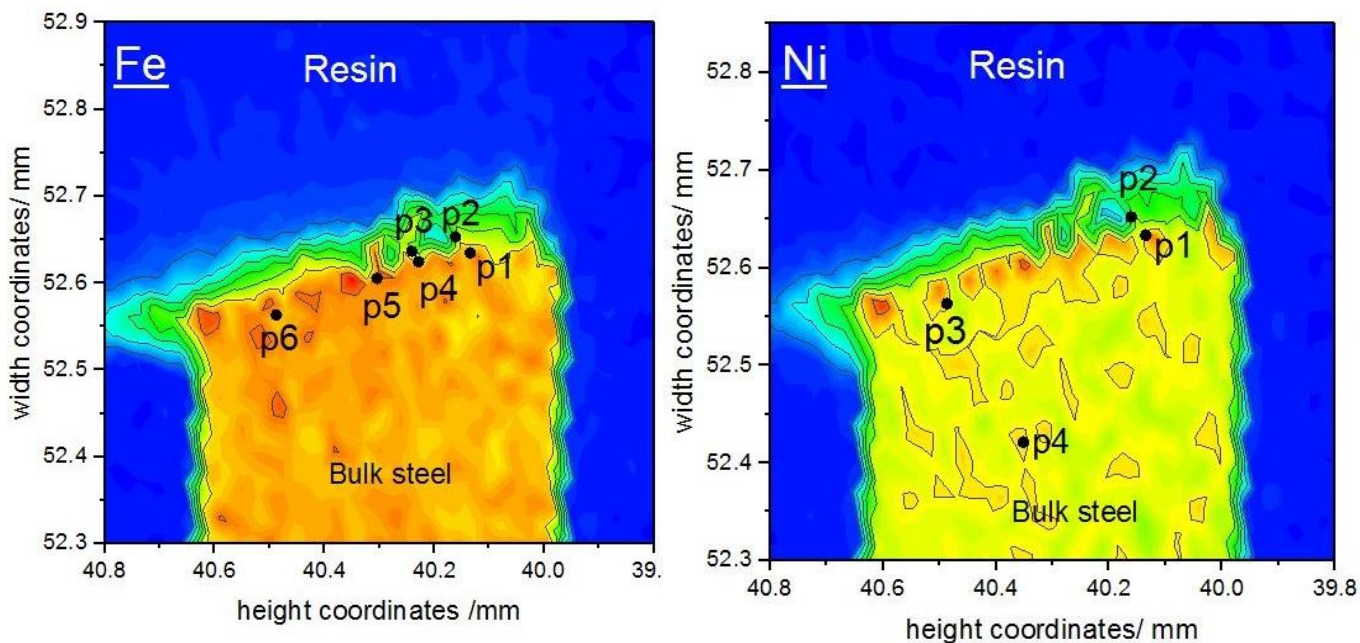


Figure 40: The μ XRF maps of the 5 M NaCl sample showing iron and nickel distribution in the sample.

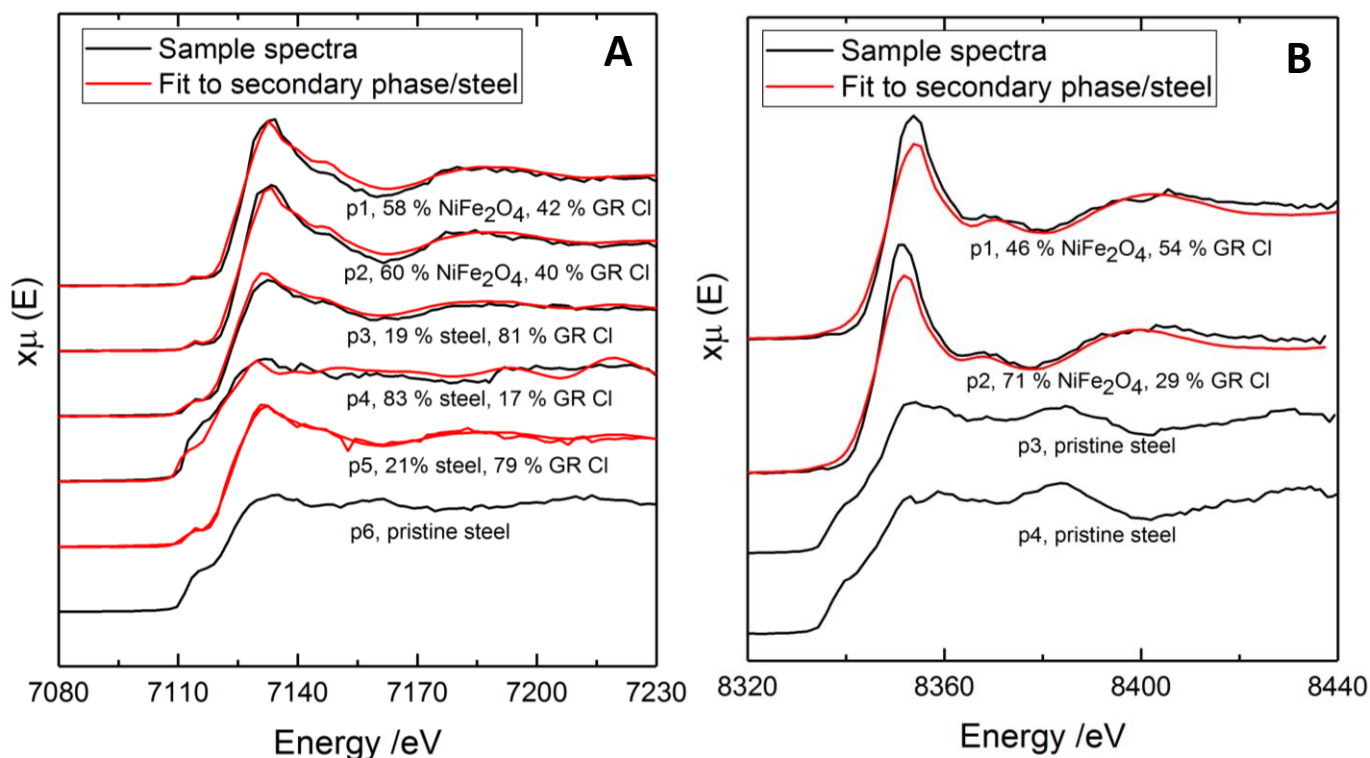


Figure 41: μ XANES spectra of iron (A) and nickel (B) of the Cr-Ni steel crosscut in 5 M NaCl at 90 °C collected at locations shown in corresponding μ XRF maps. The μ XANES spectra corresponding to the respective reference compounds are shown in *Annex Figure A37*.

More μ XANES spectra were collected in the left region of the sample, where nickel and iron show high concentration, but unfortunately, due to the thinness of the corrosion layer, the spectra were only matching the pristine steel.

Similarly, **Figure 42** shows the μ XRF map of the chromium distribution in the sample and the μ XANES spectra at the corresponding points. Points 1 to 4 show spectra matching $\text{Cr}(\text{OH})_3$ and Cr_2O_3 references, with different contributions from the two compounds, but in all cases, the $\text{Cr}(\text{OH})_3$ phase is dominant. No spectra were matching the NiCr_2O_4 or FeCr_2O_4 phases.

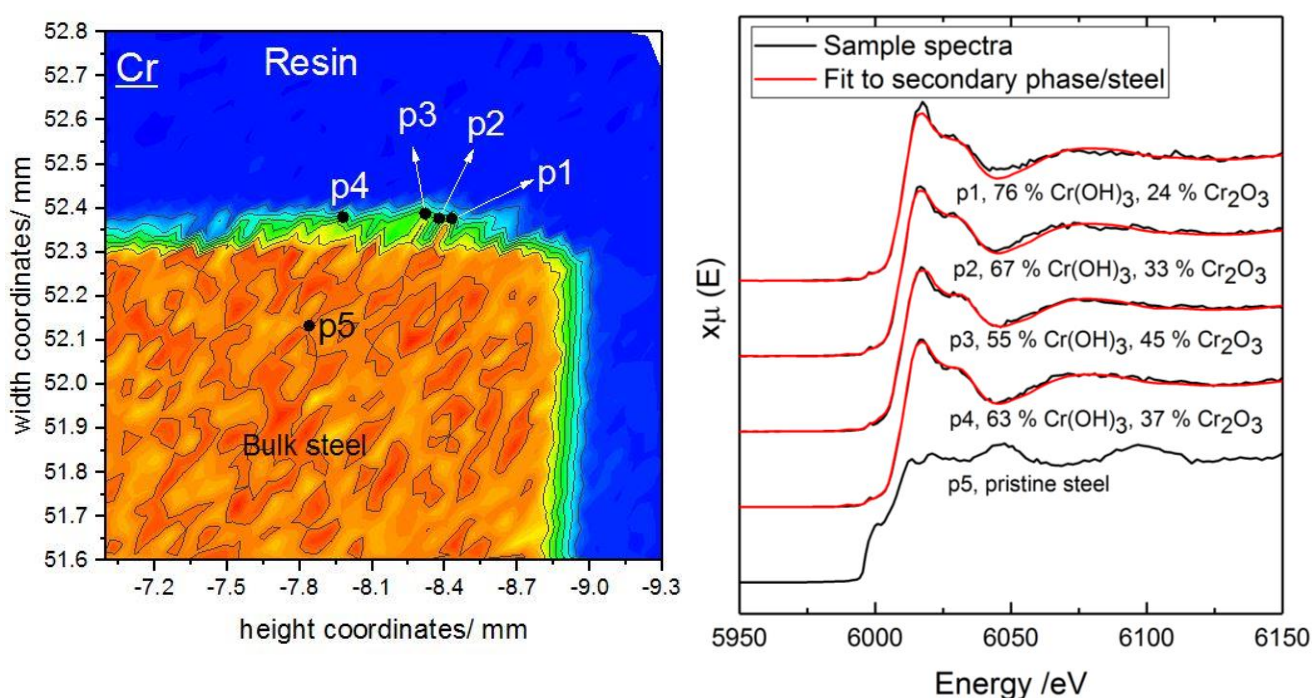


Figure 42: The μ XRF map of the 5 M NaCl sample showing chromium distribution in the sample and the μ XANES spectra collected at the corresponding points. The μ XANES spectra corresponding to the respective reference compounds are shown in **Annex Figure A38**.

Finally, μ XRD line scans through the interface, steel-corrosion layer-resin were performed at the regions of interest. These locations are shown in separate μ XRF maps in **Annex Figure A39**. The X-ray diffractograms are shown in **Annex Figure A40**. The μ XRD line scan through the Cr-rich region showed match with steel, Cr_2O_3 and resin as scanning through the interface. The presence of $\text{Cr}(\text{OH})_3$ was not observed, likely due to the absence of (or too low) crystallinity of this phase. No other phases were detected. The scan through the Fe/Ni-rich region generated diffractograms with absence of clear peaks, showing mainly background, likely due to the thinness of the layer and step size ($20\ \mu\text{m}$).

Overall, the high resolution analysis indicates the presence of different secondary phases and some kind of a corrosion progress scheme/double layer formation: GR-Cl containing structural Ni(II) and

Cr(III) forms at the steel/corrosion layer interface. Transformation to trevorite (NiFe_2O_4) takes place when moving towards the solution. Inhomogeneous distribution of the Cr_2O_3 / $\text{Cr}(\text{OH})_3$ layer is observed.

A thermodynamic model was also developed for the Cr-Ni steel in 5 M NaCl at 90 °C. For the system run for 13, 26 and 42 weeks the amounts of dissolved metals were quite low and generating the *Pourbaix* diagram using the varying amounts with respect to 13 and 26 weeks did not change the stability fields of the diagram in a significant way. The dissolved amounts of metals after 42 weeks were not used for *Pourbaix* diagram construction as they were below the detection limit.

Constructing the *Pourbaix* diagram with respect to iron using the SIT approach for activity coefficient calculations and the [TC] database (**Figure 43 A**), the data points corresponding to our pH activity / E_h conditions were on the border between aqueous region of FeCl_2 and stability field of thermodynamically stable phase chromite (FeCr_2O_4). The presence of this phase as a part of the passive film/corrosion layer is thus very likely. However the surface analyses (XPS) of samples in 5 M NaCl hinted at the presence of phases containing as well Fe(III). The presence of such a phase could, however, not be detected by μXANES and thus remains unclear. When constructing the *Pourbaix* diagram with respect to nickel (**Figure 43 B**), the data points are in the aqueous region of Ni^{2+} , but close to the predominance field of trevorite (NiFe_2O_4). The presence of trevorite is in agreement with the μXANES observations. Finally, constructing the *Pourbaix* diagram for the 5 M NaCl system with respect to Cr (**Figure 44**), the data points are clearly located in the stability field of chromium oxide (Cr_2O_3). This finding is also in the agreement with the μXANES observations. These calculations need to be considered with care as they were done using SIT approach and [TC] database at ionic strength of 5 M, which is above the limit for the *I* for this approach. The observed phases trevorite and chromium oxide are confirmed as thermodynamically stable under neutral and a wide range of oxidizing to reducing conditions. Another issue already discussed previously needs to be considered. The corrosion experiments performed here investigate an ongoing reaction and the forming solid phases do not necessarily need to be identical with those expected from thermodynamic equilibrium calculations.

In most of the remaining systems, the concentrations of dissolved metal ions were below the detection limit and no precipitation of phases was observed. Similar observations as 5 M NaCl were made in the experiments performed in solution 3 for 26 weeks at 90 °C and in dilute solution with $I = 0.1$ M NaCl for 28 weeks at 90 °C. A very thin heterogeneous layer was found by SEM (**Annex Figures A41** and **A42**). XPS analysis of surfaces after contact with NaCl based solutions showed the presence of Fe(0),

Fe(III), Ni(0), Ni(II), Cr(III). The EDX and the XRD analysis could only detect the non-corroded steel in all samples.

According to the *Pourbaix* diagrams of iron and nickel corresponding to the conditions in the solution 3 system run at 90 °C for 26 weeks, chromite or trevorite are the thermodynamically stable phases (*Annex Figure A43*) with XPS analysis favouring trevorite. Also for this steel type, pyrite is shown in *Pourbaix* diagram as thermodynamically stable under reducing conditions in sulfate containing solutions, but will not form under given experimental conditions.

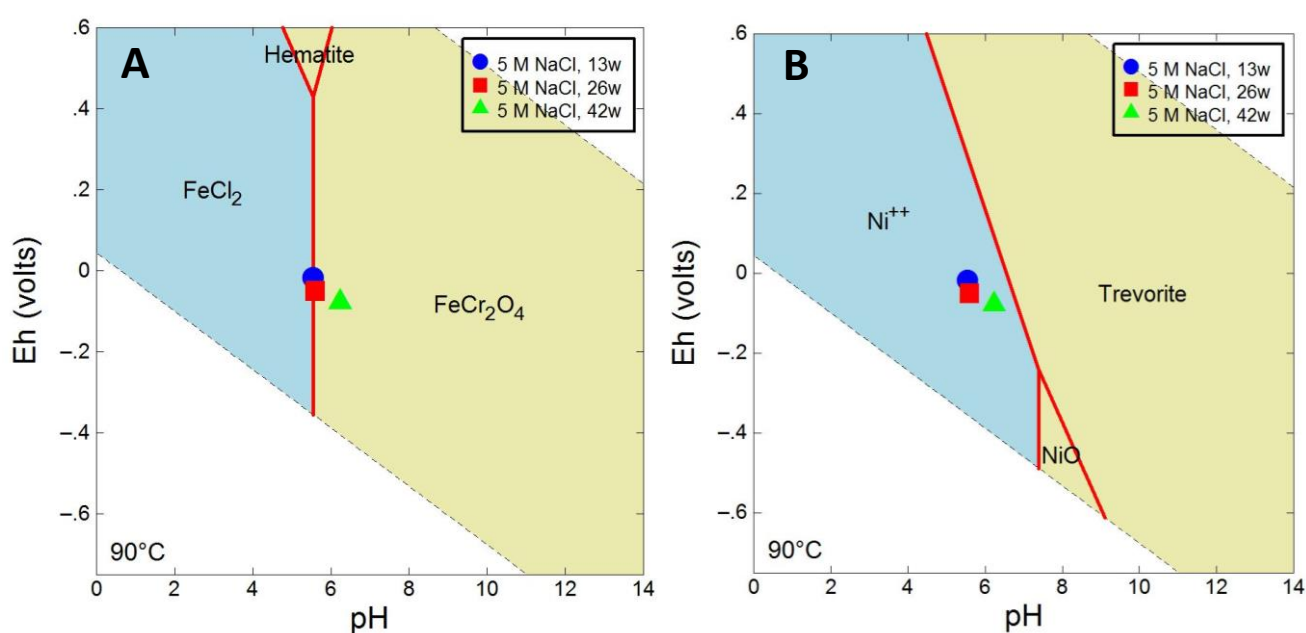


Figure 43: *Pourbaix* diagrams for 5 M NaCl system at 90 °C drawn with respect to Fe (A) and with respect to Ni (B) using dissolved amounts after 26 weeks, SIT approach and [TC] database. No phase suppression.

For the experiments performed at 25 °C in solution 3 for 20 and 26 weeks and in 5 M NaCl run for 49 weeks, the SEM images are matching the initial surface (*Annex Figures A44* and *A45*). The EDX (*Annex Table A13*), XPS and XRD analyses (*Annex Figure A46*) confirmed absence of observable corrosion. Occasional precipitate of sodium sulfate could be found after 26 weeks in solution 3 (by EDX).

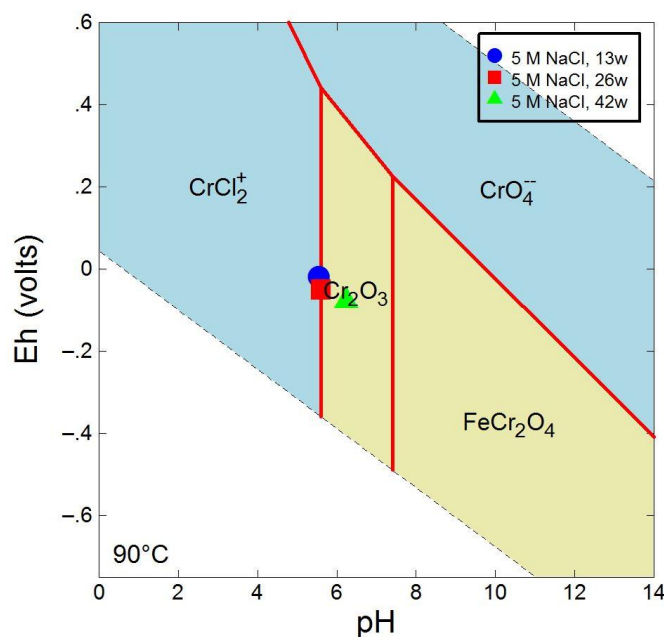


Figure 44: *Pourbaix* diagram for 5 M NaCl system at 90 °C drawn with respect to Cr (A) using dissolved amounts after 26 weeks, SIT approach and [TC] database. No phase suppression.

3.2.5.2 MgCl₂ brine

The evolution of the surface morphology is similar to the NaCl brine, as the surface appears without any significant corrosion damage. A very thin heterogenous layer is formed after 13, 26 and 42 weeks in 3.4 M MgCl₂ brine at 90 °C (*Annex Figure A47*). The XPS analyses show identical spectra for all samples with presence of Fe(0), Ni(0) and Cr(III) (*Annex Figure A48*), which would suggest that the layer is just Cr₂O₃ and/or Cr(OH)₃. The EDX analyses in *Annex Table A14* showed only the composition matching the initial steel after 13, 26 and 42 weeks, Lastly, XRD (*Annex Figure A49*) showed peaks matching the initial steel for all samples. The same behaviour is applicable for the dilute system with $I = 0.1$ MgCl₂ system run at 90 °C for 28 weeks (*Annex Figure A50*) and for the 3.4 M MgCl₂ system run at 25 °C for 49 weeks (*Annex Figure A51*). In solution 1 system run for 20 weeks at 25 °C, the analyses (*Annex Figures A52, A53 and A54, Table A15*) hint at an occasional possible MgFe₂O₄ precipitate on non-corroded surface. These findings are consistent with the optical microscopy observation on the crosscut of the embedded sample corroded for 31 weeks at 90 °C in 3.4 M MgCl₂, where no corrosion damage could be identified.

In the solution 1 system run at 90 °C for 26 weeks, a likely pit initiation was observed along with precipitate forming in its vicinity (*Figure 45 A*). The presence of Ni(II), Fe(II), Fe(III), hydroxide, oxide and chloride were detected by XPS in the precipitate. This configuration could along with the morphology (higher microscope magnification SEM image in *Annex Figure A55*) correspond to green

rust chloride with Ni(II) replacing for Fe(II) (and possibly Cr(III) for Fe(III)), but other compounds are also possible. Additionally, a non-corroded surface is found further away from the pit (presence of Fe(0), Ni(0) and Cr(III) by XPS). The crosscut of this embedded sample revealed stress corrosion cracking with crack depth of 1 mm (**Figure 45 B**). It is likely that the crack was initiated in the pit location upon cutting due to stress. In other locations, where a pit was not initiated, corrosion damage was not observed.

Overall, for both brines, no or a very thin corrosion layer was found, mainly consisting of Cr (hydr)oxide and Ni(II) and Fe(III) phases as visible by SEM and detected by XPS. As no reliable data are available for activity calculations using the Pitzer approach for Cr and Ni, the *Pourbaix* diagrams were not generated for the systems corroded in MgCl₂. As similar behaviour is observed for the Cr-Ni steel in both brines and low degree of corrosion is found, it is assumed that similar phases are favoured, with Ni(II) and Fe(III) phases precipitation onset likely shifted to higher pH_M due to higher ionic strength of 3.4 M MgCl₂ vs. 5 M NaCl. The phases of interest for the for radionuclides retention are trevorite (NiFe₂O₄), chromium hydroxide (Cr(OH)₃), chromium oxide (Cr₂O₃) and chromite (FeCr₂O₄), considering the long-term stability, with the first three phases experimentally confirmed in this work.

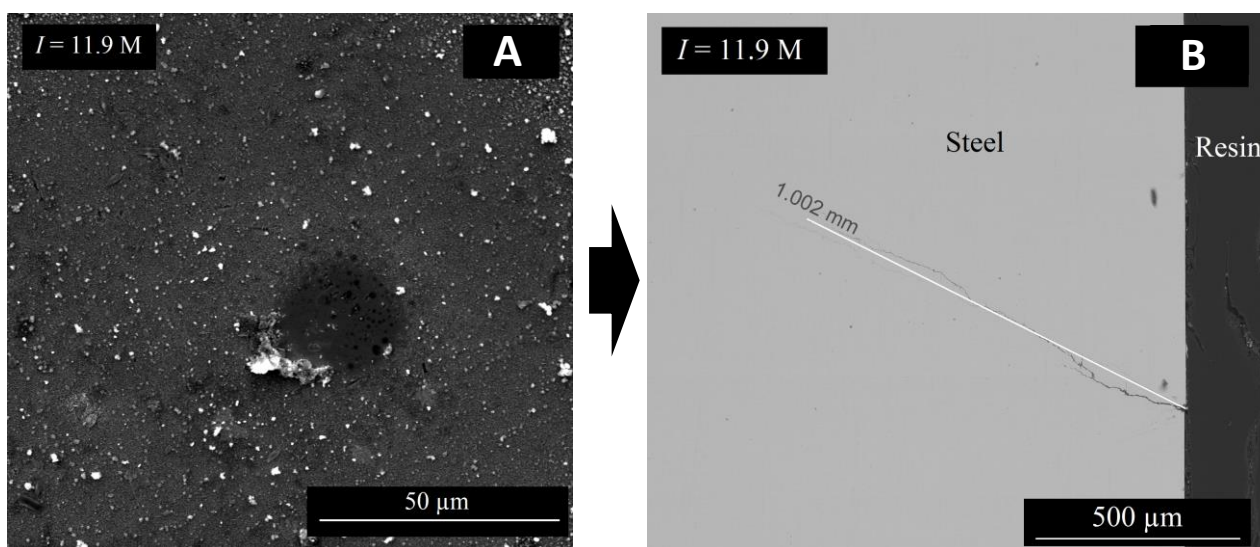


Figure 45: SEM image of the solid phase morphology of Cr-Ni steel sample in solution 1, T = 90 °C with exposure of 26 weeks (A) and the embedded crosscut of the same sample (B).

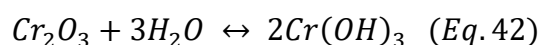
Table 23 below summarizes the experimentally determined secondary phases on Cr-Ni steel in various brines and at different temperatures along with the corresponding pH_M and E_h values.

Table 23: The observed secondary phases formed on corroded Cr-Ni steel under various conditions.

Steel	Brine/ Molarity	T /°C	pH _M	E _h	Experimentally determined secondary phase
Cr-Ni Steel	5 M NaCl	90	6.9±0.3	-77±50	Passive film composed of chromium oxide, chromium hydroxide and trevorite. Green Rust chloride doped with Ni and Cr at the steel/film interface.
	5 M NaCl	25	6.40±0.05	214±50	Chromium oxide and chromium hydroxide layer.
	Sol. 3	90	6.0±0.3	123±50	Passive film composed of chromium oxide, chromium hydroxide and trevorite.
	Sol. 3	25	6.70±0.05	91±50	Chromium oxide and chromium hydroxide layer.
	0.1 M NaCl	90	6.0±0.1	-64±50	Passive film composed of chromium oxide, chromium hydroxide and trevorite.
	3.4 M MgCl ₂	90	5.6±0.5	98±50	Chromium oxide and chromium hydroxide layer.
	3.4 M MgCl ₂	25	7.26±0.05	202±50	Chromium oxide and chromium hydroxide layer.
	Sol. 1	90	6.1±0.5	98±50	Green rust chloride with Ni and Cr near starting pit. Chromium oxide and chromium hydroxide layer away from the pit.
	Sol. 1	25	7.66±0.05	50±50	Chromium oxide and chromium hydroxide layer. Possible MgFe ₂ O ₄ .
	0.033M MgCl ₂	90	5.8±0.1	-42±50	Chromium oxide and chromium hydroxide layer.

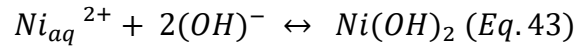
3.2.6 Corrosion mechanism

Stainless steels, such as Cr-Ni steel in this study, are known for instantaneously forming a Cr₂O₃ protective layer (*Eq. 41*). This layer can be hydrated (*Eq. 42*) and therefore a combination of Cr₂O₃ and Cr(OH)₃ is always present in the passive film [Kirchheim et al., 1989; Zhu et al., 2015]. This was also observed by μ XANES technique in 5 M NaCl sample, where both of these compounds were detected.



We have observed this layer by XPS even on the initial samples prior to the corrosion experiments being started and in many systems as sole component of the film. This was particularly the case for room temperature systems: 5 M NaCl at 25 °C, in solution 3 at 25 °C and in solution 1 at 25 °C.

In the case of Cr-Ni steel, the general oxidation of iron (*Eq. 1*) and reduction of water (*Eq. 2*) can also release Ni²⁺ which in turn will hydrolyse (*Eq. 43*).

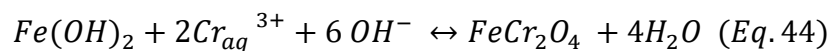


Furthermore, nickel has higher solubility, thus higher amounts of dissolved nickel were found despite lower nickel content in the Cr-Ni steel compared to iron. In all systems with dissolved amounts below detection limits, the pH_M variation is small. This is likely be due to lack of water reduction and OH^- formation.

Other oxide phases depending on the alloy composition may form on the surface and contribute to the passive film. One particular group of formed oxides are spinels. Oxides with spinel structures are corrosion resistant and possess low solubilities [Beverkog & Puigdomenech, 1999]. In case of our Ni-Cr-Fe-O-H system, the four spinels, which could form are magnetite Fe_3O_4 , trevorite $NiFe_2O_4$, chromite $FeCr_2O_4$ and nichromite $NiCr_2O_4$. These compounds appear to be contributing to the passivation film in many of our samples as suggested by XPS and μ XANES analyses, particularly in systems run at elevated temperature.

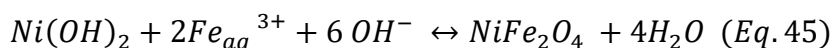
Many studies are looking into the passivation film composition with respect to distribution of these compounds and their interaction [Kirchheim et al., 1989; Pérez et al., 2002; Ramya et al., 2010; Zhang et al., 2017]. All these studies agree that the passivation film is made of a double layer structure, with inner layer made of Cr oxide or Cr-containing spinel oxide formed by a solid-state growth mechanism and an outer layer of Fe, Ni spinel oxide formed by metal dissolution and corrosion product precipitation mechanism [Duan et al., 2015; Terachi et al., 2008]. This is in agreement with the results obtained in this work, showing that a similar passivation mechanism proceeds in solution with low and high ionic strength for stainless steel 309S.

In a recent study by Zhang et al. [2017] it was found that the oxide film is composed of amorphous Cr_2O_3 , which is covered by discontinuous crystalline spinel oxides formed through $Fe(OH)_2$ - initially formed according to **Eq. 3**. The dissociation of $Fe(OH)_2$ leads to formation of chromite according to **Eq. 44**. Magnetite formation from $Fe(OH)_2$ via Schikorr equation was shown in **Eq. 5**, but its presence is unlikely due to higher stability of mixed Ni, Cr, Fe compounds compared to magnetite [Beverkog & Puigdomenech, 1999]. The absence of magnetite was also suggested in our thermodynamic model calculation.



In the similar manner, trevorite can be formed (**Eq. 45**). Upon formation of $2Fe_{aq}^{3+}$, the $6(OH)^{-}$ are formed from water reduction, thus no pH_M variation should occur upon formation of this compound.

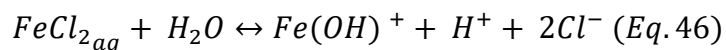
The minor pH_M changes in the systems considering the uncertainty come from $(\text{OH})^-$ from water reduction associated with iron and nickel oxidation and from impurities in steel and salt.



It can be concluded that the observed heterogenous corrosion layer of the spinel group phases was part of the passivation film and no observable pitting corrosion took place in these samples yet. The resolution did not allow for more precise structural evaluation of the passive film.

From the electrochemical point of view, the passive film is stable when the metal is in the passivation region. From the available values for corrosion and pitting potentials ($E_{\text{corr}} \sim -70$ mV, $E_{\text{pit}} \sim 200$ mV for 5 M NaCl, 25 °C and $E_{\text{corr}} \sim -440$ mV, $E_{\text{pit}} \sim -80$ mV for 3.4 M MgCl_2 , 25 °C), pitting corrosion is expected to occur for all MgCl_2 brines systems. The values for the pitting potentials are not known for the systems at 90 °C, but increasing the temperature results in even lower pitting potential values, therefore pitting potentials may be reached in some systems with NaCl brine at 90 °C. Pitting is a slow process and the lack of observable pitting in these relatively short experiments does not mean this steel is immune to pitting.

The only sample with pit initiation was in the solution 1 corroded at 90 °C for 26 weeks. Here, the pit formation was accompanied by the presumably green rust chloride formation in its vicinity. It seems that upon the passive film penetration/dissolution (pure $\text{Cr}_2\text{O}_3/\text{Cr}(\text{OH})_3$ film in this sample), the metal around the pit is under cathodic control, which causes cathodic reduction of water and thus higher local pH_M , along with local Cl^- accumulation allowing for formation of green rust chloride, where structural Fe(II) and Fe(III) are partially substituted by Ni(II) and Cr(III). Inside the pit, the pH_M is lowering due to cation hydrolysis (**Eq. 46**). This acidic chloride environment in the pit thus tends to propagate the pit growth and hinders repassivation [Frankel, 1998].



It is not clear, whether the green rust chloride would transform into trevorite, and whether this phase would be stabilized by electrophoretic accumulation of Cl^- at the interface or upon further metals dissolution from the pit, different compounds would be favoured.

A similar phenomenon was observed in the results from application of synchrotron-based techniques, where according to μXANES of iron and nickel, the green rust chloride (doped with Ni and Cr) was forming close to the bulk steel in 5 M NaCl sample corroded at 90 °C for 31 weeks. The presence of the trevorite phase on the outer part of the layer was also confirmed. It appears that in this case, the Cl^-

diffused through the cracks / pores in the film to the steel/oxide interface once trevorite already contributed to the passive film and at this interface the formation of green rust chloride occurred. It is possible that small/metastable pits were present but not visible in the μ XRF maps. This sample seemed to be in an earlier stage of pitting corrosion compared to the solution 1 sample. This is in agreement with surface analyses of the 5 M NaCl sample corroded at 90 °C, where a layer likely containing trevorite or mixed trevorite - chromite was observed.

However, it needs to be noted that the growth of the outer layer is also governed by the stability of the oxide phases [Bojinov & Beverskog, 2006]. This could explain the presence of trevorite in 5 M NaCl sample with pH_M of 6.3 and absence of trevorite in the passive film in solution 1 sample with pH_M of 6.1, keeping it mind that higher ionic strength shifts the stability region to higher pH_M values. Similarly, it would explain the absence of spinel compounds in the film in concentrated MgCl_2 brines.

It appears every steel sample is unique notably in the initial corrosion phase due to specific imperfections or cracks in the passive film. This can enhance the pit initiation. The presence of green rust chloride was observed in NaCl based (5 M) and in MgCl_2 based (solution 1) brines, highlighting that despite the difference in ionic strength (nevertheless high in both cases), the interface conditions upon film penetration favour, at least initially, the same compound. The presence of sulfate was expected to cause an inhibition of the corrosion due to the reinforcement of the protective film by shifting the pitting potential to higher values [McCafferty, 2010]; nevertheless, the sulfate concentration in solution 1 did not suffice to avoid reaching the pitting potential. Green rust sulfate is more stable than green rust chloride in chloride and sulfate containing solutions [Refait et al., 1997, 2003], however, it seems the interface conditions favour, due to chloride accumulation, green rust chloride.

Finally, from the point of interest for radionuclide retention in dilute to concentrated NaCl and MgCl_2 brines, the thermodynamically stable spinel compounds (trevorite and chromite) are dominating along Cr_2O_3 . Although trevorite forms in the outer layer of the passive film, which would make it more exposed and thus of interest for radionuclide retention, this film could be discontinuous and therefore Cr_2O_3 in the passive film may also be of interest.

3.3 Corrosion under flowing conditions (in collaboration with SNL)

A set of experiments with identical steel types and brine composition was performed in Sandia National Laboratory (SNL) in New Mexico, USA under Charly Sisk-Scott with the aim to obtain the corrosion rates under saline anoxic flowing conditions (60 mL/day) at 90 °C and allow a comparison to stagnant conditions performed at INE. A more detailed description and obtained corrosion rates are shown in the *Annex*.

Comparing the results to outcomes of our stagnant condition experiments, comparable corrosion rates were obtained for the Cr-Ni steel considering the uncertainties after 26 weeks in the identical brines at 90 °C. Lower corrosion rates were expected under flowing conditions, as in case of stainless steels, it is the stagnant environment, accumulation and heterogeneities in the solution, which cause pitting and dissolution. However, this effect may not be observable as the corrosion rates have high uncertainty.

Considering the corrosion allowance material such as SGI, flowing conditions prohibit oxide formation on the surface, which would lead to inhibition of iron dissolution, due to convection of cations away from the surface. We have observed this mechanism as the corrosion rate has decreased with time in our stagnant samples. Therefore, it was expected to observe higher corrosion rates under flowing conditions. This was only fulfilled for the 5 M NaCl brine. In 3.4 M MgCl₂ and solution 3 we have observed 2-3 times higher corrosion rates under stagnant conditions, respectively. Furthermore, Raman analyses showed lack of silicate compounds on SGI corroded under flowing conditions in 5 M NaCl brine and presence of green rust chloride (not iron hydroxychloride) in 3.4 M MgCl₂ brine. This is likely due to different pH values and lack of saturation of Si in the solution. This comparative study has shown that the conditions (stagnant brine or flowing brine) in the repository play a role in the formation of corrosion products and affect the corrosion rate. This may have further effect on radionuclide retention as the different conditions would favour different phases serving as sinks.

4 Sorption studies

The formed corrosion phases may serve as a sink for the radionuclides upon canister breach. This chapter focuses on the sorption behaviour of the various corrosion phases, which have been identified in the corrosion experiments and considered relevant with regard to long-term stability under conditions relevant to repository in the salt rock. As a representative for a sorbing radionuclide, europium and americium were taken for sorption studies. As already mentioned previously, Eu(III) can be considered a chemical analogue to trivalent actinides such as Am/Cm/Pu(III).

In each evaluated system, the uptake of europium and $\log K_D$ values were determined as a function of pH_M under various ionic strengths in either NaCl or MgCl_2 brine. In case of certain solid phases, a surface complexation model of europium sorption was developed and complexation constants obtained at infinite dilution. For some studies Am(III) sorption was investigated by X-ray spectroscopy in order to identify the surface speciation of the radionuclide.

Figure 46 shows both steel types along with observed and/or long-term stable corrosion phases, which were examined for retention in this work, but also others, which may be of interest in future studies. The detailed description of the sorption experiments is presented in *Section 2.5*. All experiments in the sorption studies were performed at 25 °C, considering that the canister breach will potentially occur once the temperature of the canister surface decreased to low temperature. The pH_M in this part is therefore the measured pH_{EXP} corrected for ionic strength.

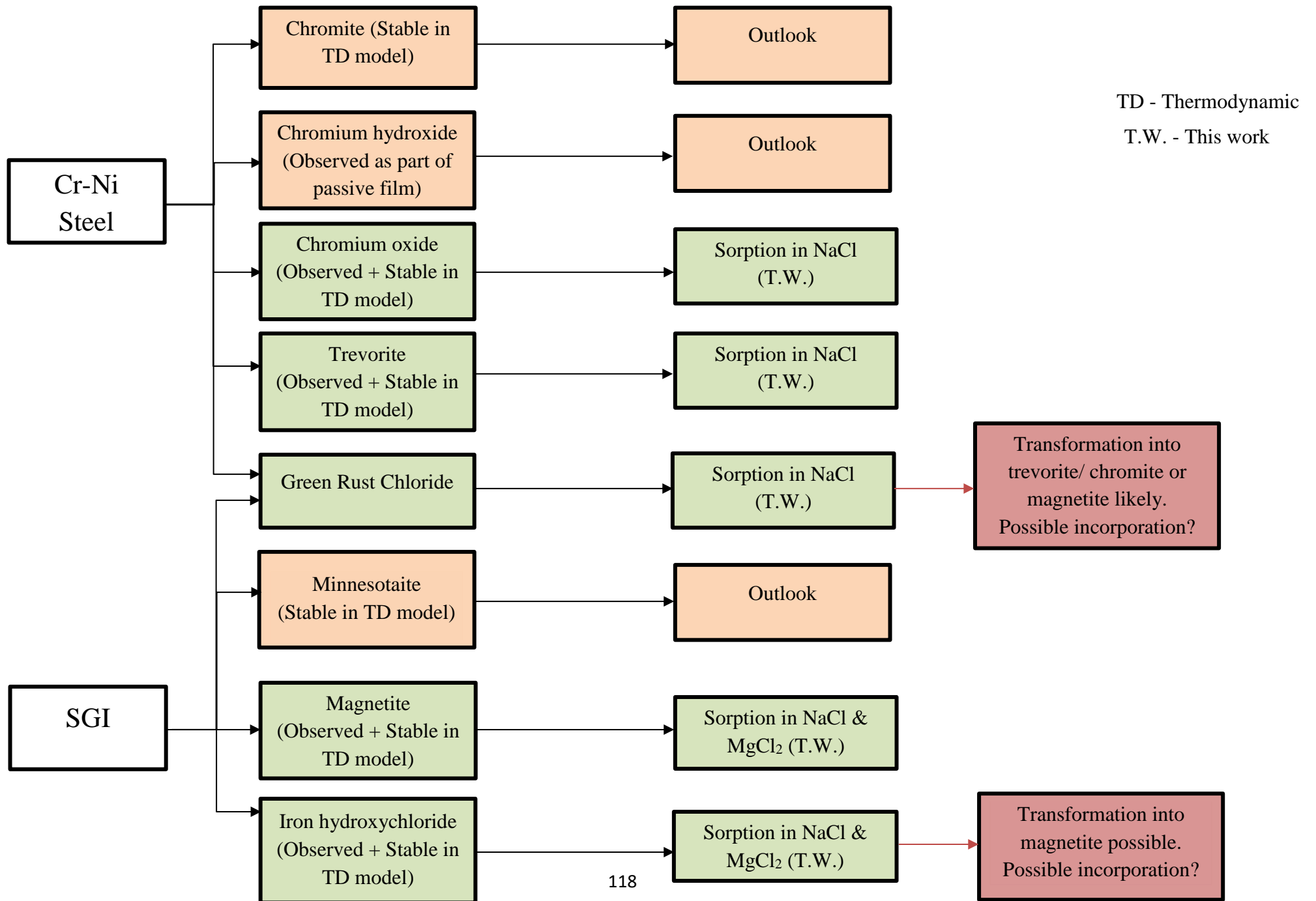


Figure 46: Scheme of the observed / stable corrosion phases and outline of which phases are examined in this work for europium / americium retention.

4.1 Solubility and speciation of europium and americium in dilute to concentrated NaCl and MgCl₂ solutions

4.1.1 Solubility

Prior to the experiments, it was crucial to assess the potential precipitation of any solid europium and americium phase under the studied conditions. The saturation indices of significant solid phases were plotted as a function of pH_M at various ionic strengths used in the experiments, for europium and americium. The saturation indices were calculated with the PhreeqC software using the SIT approach with [TC] at ionic strength of 0.1 M and 1 M NaCl, and additionally Pitzer approach with [TPA] database at ionic strength of 4.7 M and higher. These results set the upper limit for the pH_M range for the sorption studies and define the selected metal concentration ranges.

The solubility calculations were performed for various concentrations of Eu/Am in NaCl and MgCl₂ brine and the pH_M values of precipitation onset of relevant Eu/Am-solid phases or salts are shown in **Table 24**. The N.P. (No Precipitation) in the table signifies that the compound will not precipitate in the whole pH_M range (1-14). There is no europium available in the [TPA] database, thus the calculations were done with americium for high *I* instead. Furthermore, Am(OH)_{3,cr} is also not available in the [TPA] database, only Am(OH)_{3,am}. The saturation indices for one set of calculations, [Eu] = 5.1×10⁻¹⁰ M are shown in **Figure 47**. The graphs showing the saturation indices for the other sets of calculations are shown in **Annex Figures A58, A59 and A60**.

As a set of sorption experiments for XAS (EXAFS) measurements was performed with americium. These samples and XAS experiments aim at obtaining structural information at the molecular scale of the sorption species. The saturation indices of americium were thus evaluated for a concentration of 8.2×10⁻⁶ M for the two ionic strengths of 0.95 M and 4.7 M NaCl, which were used in the XAS experiments. (**Annex Figure A59**). According to the **Table 24**, no precipitation is taking place in samples prepared for XAS measurements where the pH_M was set to ~ 6.1 and ~ 7.0.

Table 24: The pH_M values of precipitation onset of Eu/Am-solid phases or salts.

[Eu/Am] and I (M)	Solid phase				
NaCl brine					
Europium	Eu(OH) _{3,cr}	Eu(OH) _{3,am}	Am(OH) _{3,am}	EuCl(OH) ₂	
5.1×10^{-10}, $I = 0.1$, SIT (Figure 57 A)	9.3	N.P.		N.P	
5.1×10^{-10}, $I = 0.96$, SIT	9.5	N.P		N.P	
5.1×10^{-10}, $I = 4.8$, SIT (Figure 57 B)	12	N.P		N.P	
1×10^{-7}, $I = 0.1$, SIT	7.9	9.1		N.P	
1×10^{-7}, $I = 0.96$, SIT	8.11	9.3		N.P	
1×10^{-7}, $I = 4.8$, SIT	9.6	11.6	Pitzer 11.1	N.P	
1×10^{-5}, $I = 0.1$, SIT	7.1	7.9		N.P	
1×10^{-5}, $I = 0.96$, SIT	7.4	8.1		8.1	
1×10^{-5}, $I = 4.8$, SIT	8.2	9.8	Pitzer 9.3	8.4	
Americium	Am(OH) _{3,cr}		Am(OH) _{3,am}		
8.2×10^{-6}, $I = 0.95$, SIT	7.5		7.9		
8.2×10^{-6}, $I = 4.7$, SIT	8.4		9.6 (9.2 Pitzer)		
MgCl₂ brine	Eu(OH) _{3,cr}	Eu(OH) _{3,am}	Am(OH) _{3,am}	EuCl(OH) ₂	Mg(OH) ₂
5.1×10^{-10}, $I = 0.1$, SIT	9.1	N.P		N.P	9.4
5.1×10^{-10}, $I = 9.77$, Pitzer			N.P		9.3
1×10^{-5}, $I = 0.1$, SIT	7	7.8		8.5	9.4
1×10^{-5}, $I = 9.77$, Pitzer			9.2		9.2

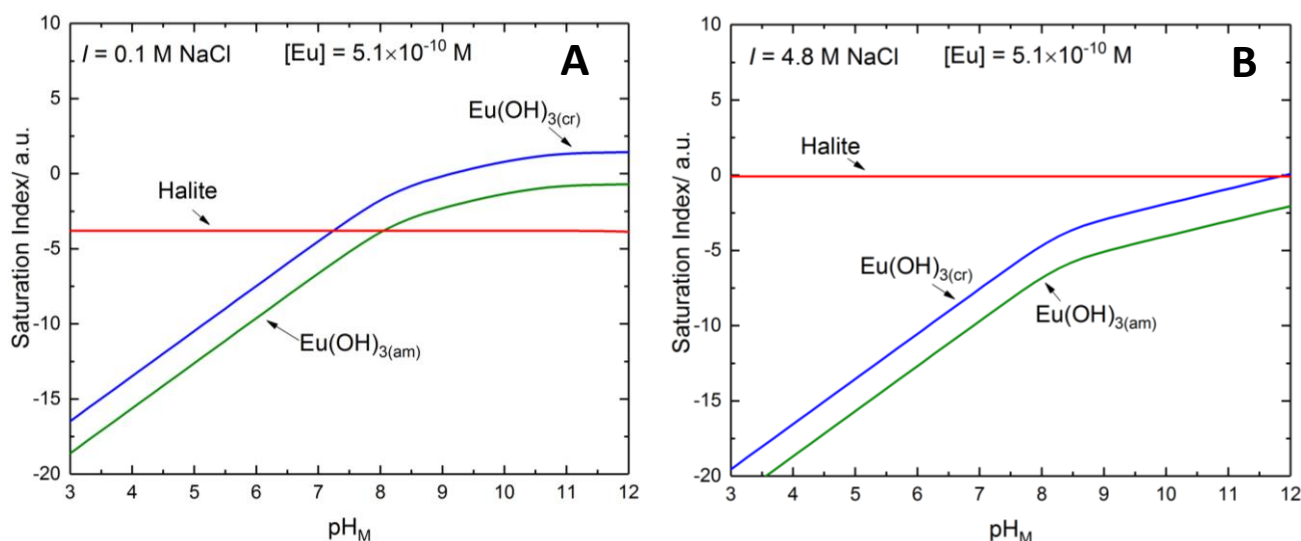


Figure 47: Saturation indices of europium solid phases vs. pH_M calculated using the SIT approach and [TC] database. $I = 0.1$ M NaCl (A) and $I = 4.8$ M NaCl (B), $[Eu] = 5.1 \times 10^{-10}$ M.

Overall, increasing the ionic strength shifts the precipitation threshold to the alkaline region. At $I = 4.7$ M (americium) and 4.8 M (europium), the halite line is also close to zero as the salt concentration is close to saturation point of NaCl. The upper pH_M limits for sorption were set such as to stay below

precipitation of phases for each system. Considering the Eu/Am(OH)₃, only the amorphous phase was taken into account for the limit setting, as crystalline phases are not expected to form under our experimental conditions. These pH_M limits are conservative, as they do not account for sorption, which would decrease the solute amount in the solution.

4.1.2 Speciation

Europium and Americium speciation in NaCl brines are plotted below (**Figures 48 and 49**). The speciation is the same, independent of the europium or americium concentration. Using the SIT approach and [TC] database, the predominant species in acidic-neutral pH_M range are Eu³⁺ for low ionic strength and Eu³⁺, EuCl₂²⁺ and EuCl₂⁺ for high ionic strength. In alkaline pH_M region, hydroxo species take over. Similar behaviour is observed in case of americium. Speciation curves for the MgCl₂ brines follow identical patterns as in the case of NaCl brines, as long as the ionic strength is the same.

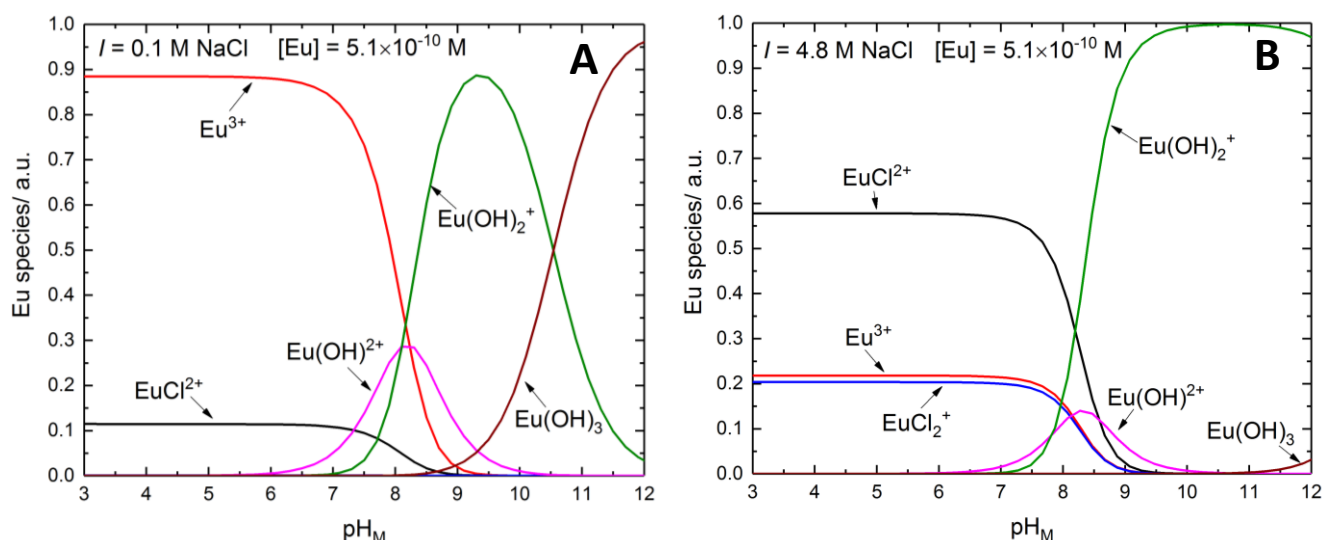


Figure 48: Aqueous speciation of europium vs. pH_M calculated using the SIT approach and [TC] database. $I = 0.1$ M NaCl (A) and $I = 4.8$ M NaCl (B), $[Eu] = 5.1 \times 10^{-10}$ M.

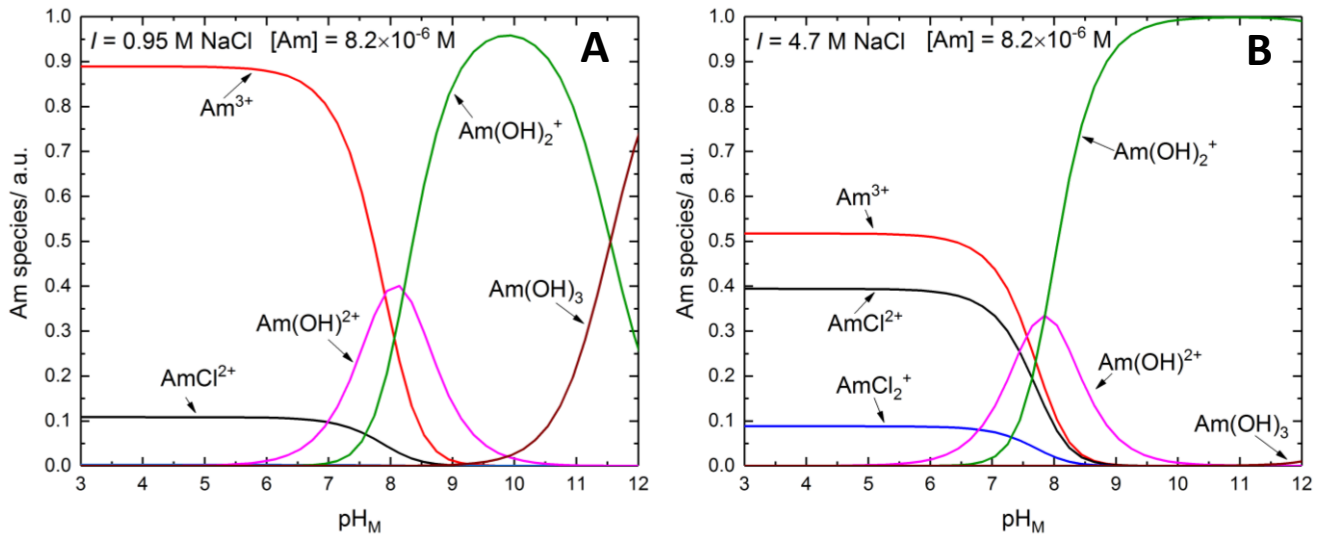


Figure 49: Aqueous speciation of americium vs. pH_M calculated using SIT approach and [TC] database. $I = 0.95 \text{ M NaCl}$ (A) and $I = 4.7 \text{ M NaCl}$ (B), $[\text{Am}] = 8.2 \times 10^{-6} \text{ M}$.

4.2 Uptake of europium/amerium by Fe (Ni, Cr) minerals

4.2.1 Magnetite (Fe_3O_4)

Magnetite was established as the dominant and thermodynamically long-term stable corrosion phase for SGI in dilute to concentrated NaCl brines at elevated temperature. The magnetite structure is shown in *Figure 50*.

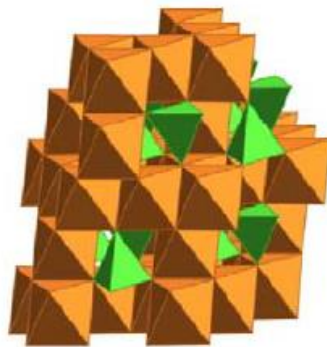


Figure 50: Structure of magnetite showing the tetrahedral (green) and octahedral (orange) sites [Jolivet et al., 2006].

Magnetite for sorption experiments was synthesised in house according to the procedure described by Cornell and Schwertmann [1996] in *Table 3*. Prior to the experiments, the solid phase was characterized using various methods to confirm its purity. Initial pH_M and E_h of the magnetite stock suspension kept under Ar atmosphere were $\text{pH}_M = 6.64$ and $E_h = -5 \text{ mV}$, respectively.

The SEM images of the solid in **Figure 51** show clear octahedral morphology and a size range of 50 to 300 nm with an average size of 100 nm. EDX confirmed a Fe/O ratio of $\frac{3}{4}$ consistent with magnetite. SEM images suggest the predominance of the (111) plane as being relevant for sorption.

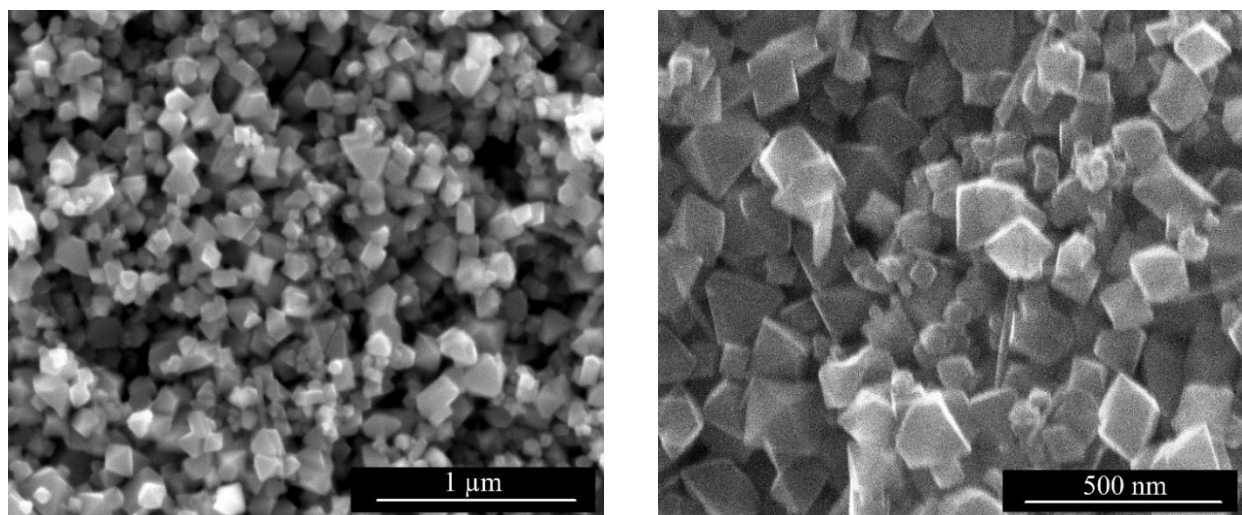


Figure 51: SEM images of dried magnetite, showing octahedral shaped structures.

The XRD analysis (**Figure 52**) was performed on the solid and compared to the database, showing an excellent match with PDF card 88-0315 (magnetite) and the absence of additional crystalline phases. The specific surface area of the same batch (42 g/L stock suspension) was previously determined by the BET method by Finck et al. [2016_b] to be 13.1 m²/g.

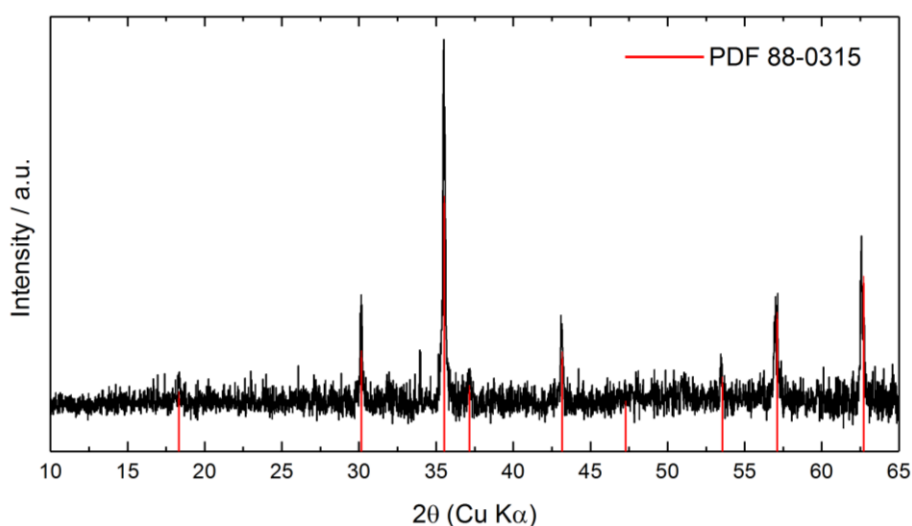


Figure 52: X-ray diffractogram of the dried magnetite, showing a perfect match of the sample diffraction pattern with PDF card of 88-0315 in the database - magnetite.

The Fe 2p XPS spectrum of the dried magnetite confirmed the presence of both Fe(II) and Fe(III) (**Figure 53**). The respective ratio of Fe(II)/Fe_(tot.) was found 0.25, while in the ideal magnetite structure

it should be 0.33. This result may hint at a slight increase in Fe(III) within the first few nm probed by XPS and likely originates from the long contact time between magnetite and traces of oxygen in the Ar-filled box.

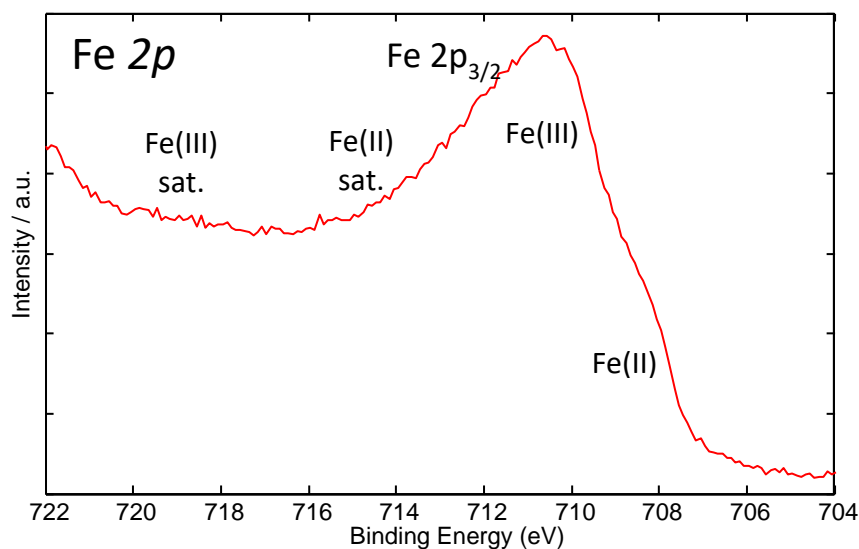


Figure 53: Fe 2p spectrum of dried magnetite obtained by XPS.

At last, prior to the sorption experiments, it was important to identify the stability of magnetite along the pH_M range to avoid mineral dissolution. *Pourbaix* diagram (not shown here) indicated low solubility for magnetite under reducing conditions in neutral and alkaline range. At $\text{pH}_M > 5.6$ (25 °C) the magnetite solubility is relatively low and unlikely to affect significantly the sorption experiments performed within a period of 24 h. This was shown by the study of Missana et al. [2003], who studied uranium sorption onto magnetite and found low dissolution above pH 5. In our corrosion experiments, this phase has been found being stable at pH_M 6.1 in 0.1 M NaCl at 90 °C. However, at higher ionic strength, the stability window of magnetite shifts to higher pH_M values and, therefore, dissolved iron in sorption samples was determined by ICP-MS to check for magnetite dissolution under given experimental conditions.

4.2.1.1 Solid phase titration in dilute to concentrated NaCl solutions

The magnetite solid phase was titrated according to the procedure described in *section 2.5.1* and the relative charge was calculated as a function of pH_M . The modelling was performed using a modified version of FITEQL 2 with activity coefficients obtained using the models and databases described in

section 1.3.5.2. Considering the complex structure of magnetite, containing tetrahedral and octahedral configurations exposed to the aqueous phase where Eu/Am can sorb, alongside different site densities for different crystal faces, the CD-MUSIC model was chosen to consider those different surfaces and to predict the proton binding constants for the several terminal oxygen sites. The absolute surface charge density data were fitted taking data from Vayssières [1995] into account, who reported the number of possible surface species along with formal charges and structural configuration for the (111) face of magnetite. The binding constants for Na⁺ and Cl⁻ to differently coordinated sites and the capacitance values were then obtained from the fit. In order to reduce the number of adjustable parameters, the constants for Cl⁻ and Na⁺ binding to non-charged surface hydroxyl groups were set equal. There are two different terminations in the (111) plane: oxygen atoms are either coordinated to iron atoms in mixed octahedral and tetrahedral sites or to iron atoms in octahedral sites only. In the mixed tetrahedral and octahedral termination, the oxygen atoms are doubly and singly coordinated, i.e. two and one metal ions are coordinated to the oxygen, while in the octahedral termination, they are doubly and triply coordinated. The pK values together with surface charges calculated from the bond valence for each coordination are summarised in *Table 25*.

Table 25: pK values for each coordination in two terminations of magnetite taken from Vayssières [1995].

Mixed octahedral and tetrahedral termination				
Coordination of oxo/hydroxo groups	Reaction	pK	Surface charge calculated from bond valence	
doubly	$Fe_2 - O^{-0.83} + H^+ \rightleftharpoons Fe_2 - OH^{0.17}$	9.3	-0.83	
doubly	$Fe_2 - OH^{0.17} + H^+ \rightleftharpoons Fe_2 - OH_2^{1.17}$	-5.1	0.17	
singly	$Fe_1 - O^{-1.25} + H^+ \rightleftharpoons Fe_1 - OH^{-0.25}$	17.5	-1.25	
singly	$Fe_1 - OH^{-0.25} + H^+ \rightleftharpoons Fe_1 - OH_2^{0.75}$	3.6	-0.25	
Octahedral termination				
Coordination of oxo/hydroxo groups	Reaction	pK	Surface charge calculated from bond valence	
doubly	$Fe_2 - O^{-1.16} + H^+ \rightleftharpoons Fe_2 - OH^{-0.16}$	16.4	-1.16	
doubly	$Fe_2 - OH^{-0.16} + H^+ \rightleftharpoons Fe_2 - OH_2^{0.84}$	2.5	-0.16	
triply	$Fe_3 - O^{-0.75} + H^+ \rightleftharpoons Fe_3 - OH^{0.25}$	7.6	-0.75	

The contributions from the two terminations in the model were adjusted in such a way that the experimental point of zero charge (pzc) was retrieved. This was done for low ionic strength (0.001 M) using a diffuse layer model.

After a satisfactory fit of the model to the experimentally determined pH dependent charge of the solid was obtained (*Figure 54*), the associated capacitance values and binding constants within the triple layer model were fixed. The solid to liquid ratio in pH titration experiments and europium sorption

experiments was 42 g/L and 0.5 g/L magnetite, respectively. Those different values were considered in model calculations. Suitable surface reactions with the radionuclide were defined and the model was modified to account for activity coefficients of europium species in solution. The dielectric constant of aqueous solutions was calculated for each ionic strength and used for the diffuse part of the triple layer model. The model was then run in various site configurations until a good fit with experimental uptake data was achieved.

Figure 54 shows the experimental titration data for two ionic strengths, 0.1 M and 1 M NaCl in the pH_M range of 5.3-8.8 and the associated modelled charges. The error bars for the surface charge are within the points. The point of zero charge was according to the titration curves at $\text{pH}_M = 6.4$. This is in agreement with literature data [Vidojkovic & Rakin, 2017].

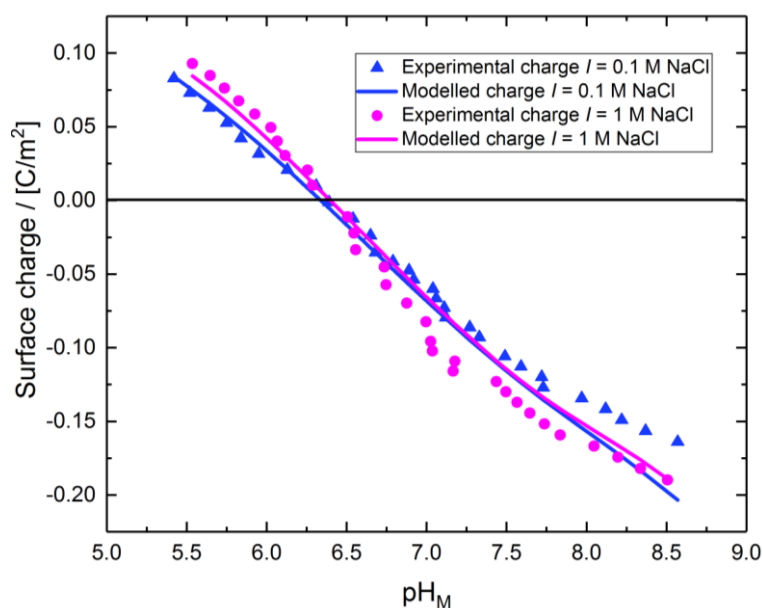


Figure 54: The experimental and modelled pH_M dependent surface charge of magnetite at two ionic strengths set by NaCl. The lines correspond to the calculated charges using the values summarized in **Table 26**.

The best model parameters are summarized in **Table 26**, showing the two capacitance values and ion binding constants (Na^+ , Cl^-) to differently coordinated hydroxyl sites. The ion binding constants for equally charged anions and cations on a given non-charged site were set to identical values. The simplest model in terms of numbers of adjustable parameters using equations in **Table 25** was obtained when enforcing identical intrinsic ion binding constants for singly and triply coordinated sites and a separate value for the doubly coordinated sites. The fitted value for the doubly coordinated sites is

negative, which indicates that ion binding on these sites is weak. It appears that ions are preferentially bound to singly/triply coordinated sites. The overall Stern capacitance value of 1.32 F/m² obtained in this work is within the range for overall capacitance for metal (hydr)oxides reported by Hiemstra & Van Riemsdijk [1991] for non-porous and well-ordered planar crystal faces ranging from 0.9 to 1.7 F/m².

Capacitance 1	3.22	F/m ²
Capacitance 2	2.25	F/m ²
Overall Stern capacitance	1.32	F/m ²
Constant for Cl⁻ and Na⁺ binding to doubly coordinated hydroxyl sites, log Ka	-5.01	-
Constant for Cl⁻ and Na⁺ binding to singly/triply coordinated hydroxyl sites, log Ke	2.45	-
Site densities used in optimization		
Doubly coordinated octahedral termination	6.68	sites/nm ²
Triplicly coordinated octahedral termination	2.23	sites/nm ²
Singly coordinated mixed termination	1.48	sites/nm ²
Doubly coordinated mixed termination	4.45	sites/nm ²

4.2.1.2 Uptake as a function of pH in dilute to concentrated NaCl and MgCl₂ solutions

The pH_M dependent dissolution of magnetite was evaluated and is shown for NaCl and MgCl₂ brines in *Figure 55*. The results showed an overall higher dissolution in MgCl₂ brine (*Figure 55 B*). Dissolution in this case refers to the preferential release of structural Fe²⁺, leaving behind Fe²⁺ - poor magnetite. The values for dissolved iron reached 1 % of the initial magnetite content at pH_M 5.4 in NaCl brine and 3 % at pH_M 5.4 in MgCl₂ brine. These dissolution values are unlikely to affect the sorption. For this reason the pH_M range for the study was set to pH_M > 5.5. The low dissolution in the used pH_M range is in agreement with the solubility study by Missana et al. [2003] and GWB modelling in this study.

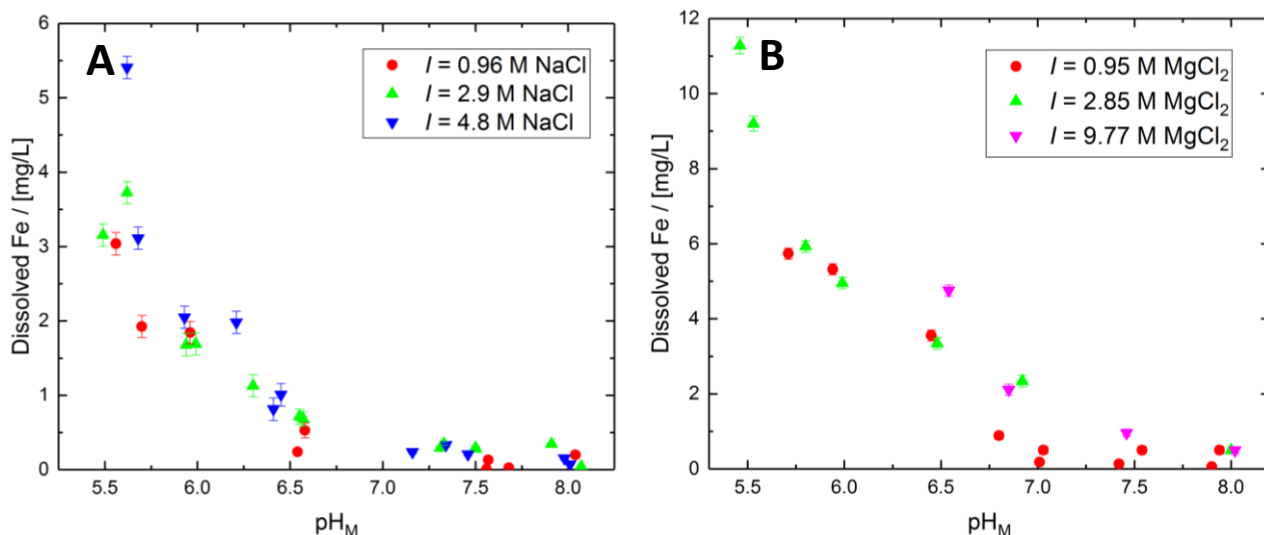


Figure 55: Dissolved iron concentration in aqueous solutions in contact with magnetite vs. pH_M at different ionic strengths of NaCl (A) and MgCl_2 (B).

The general pH_M dependent interaction of trivalent radionuclides (Eu) with iron oxides exhibits strong sorption above pH_M 5.5 (**Figure 56 A**). At such low europium concentration, for $\text{pH}_M > 6.2$ all the data points are in the shown grey detection limit area of the gamma counting method, which corresponds to 99.1 % sorption for magnetite. For $\text{pH}_M < 6.2$, the increase in salt content decreases the extent of sorption. The $\log K_D$ values range from 4.3 ± 0.2 to 7.1 ± 0.5 (**Figure 56 B**) with the $\log K_D$ value corresponding to the detection limit of 5.3.

Gamma counting of the used ^{152}Eu tracer yields only small analytical uncertainties. Errors due to pipetting, resuspension of solid particles after ultracentrifugation or wall sorption effects dominate the uncertainty of sorption data. The uncertainty of $\log K_D$ values by all these errors is around ± 0.5 , when the concentrations of dissolved Eu lie close to the detection limit, which is in agreement with data provided by Schnurr et al. [2015], who followed a very similar procedure examining the europium sorption onto clay.

Singh et al. [2009] investigated the sorption of europium onto magnetite (2 g/L) for a similar europium concentration of 2×10^{-9} M. The authors have observed a similar trend with quantitative sorption taking place at $\text{pH}_M > 5.5$ in background electrolyte with $I = 0.1$ M, using magnetite with higher specific surface area in comparison to the magnetite used in this study.

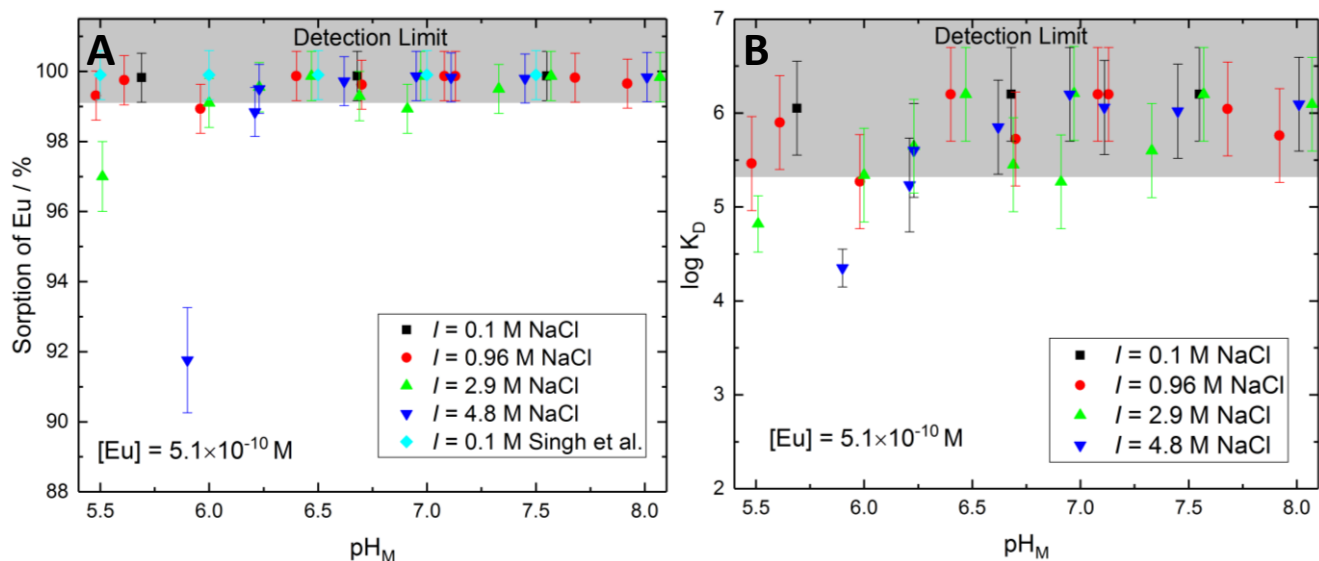


Figure 56: Sorption of europium $[Eu] = 5.1 \times 10^{-10}$ M as percentage uptake (A) and as logarithm of distribution ratio ($\log K_D$) (B) on magnetite (0.5 g/L) as a function of pH_M and at different ionic strengths of NaCl.

Sorption data were recorded at a higher Eu concentration of 1×10^{-5} M corresponding closely to the concentration of Am chosen for XAS experiments. The sorption exhibited a pH_M dependent behaviour (**Figure 57 A**). With this radionuclide concentration, the uptake was low at pH_M 5.5 and increased within 2 pH_M units, reaching quantitative sorption at $pH_M \geq 8.0$ for all ionic strength levels. The uncertainty regarding sorption was estimated in this case to ± 4 %, i.e. ± 0.2 for $\log K_D$. The $\log K_D$ values in this case vary from 2.7 ± 0.2 at 20 ± 4 % sorption to 4.6 ± 0.2 at 95 ± 4 % (**Figure 57 B**). A very small ionic strength effect on $\log K_D$ values can be observed considering the molar pH_M scale. These experimental data are in good agreement with the work of Catalette et al. [1998], who performed europium sorption onto magnetite at a Eu concentration of 2×10^{-4} M and observed > 99.99 % uptake at $pH_M > 7.0$ at $I = 0.1$ M.

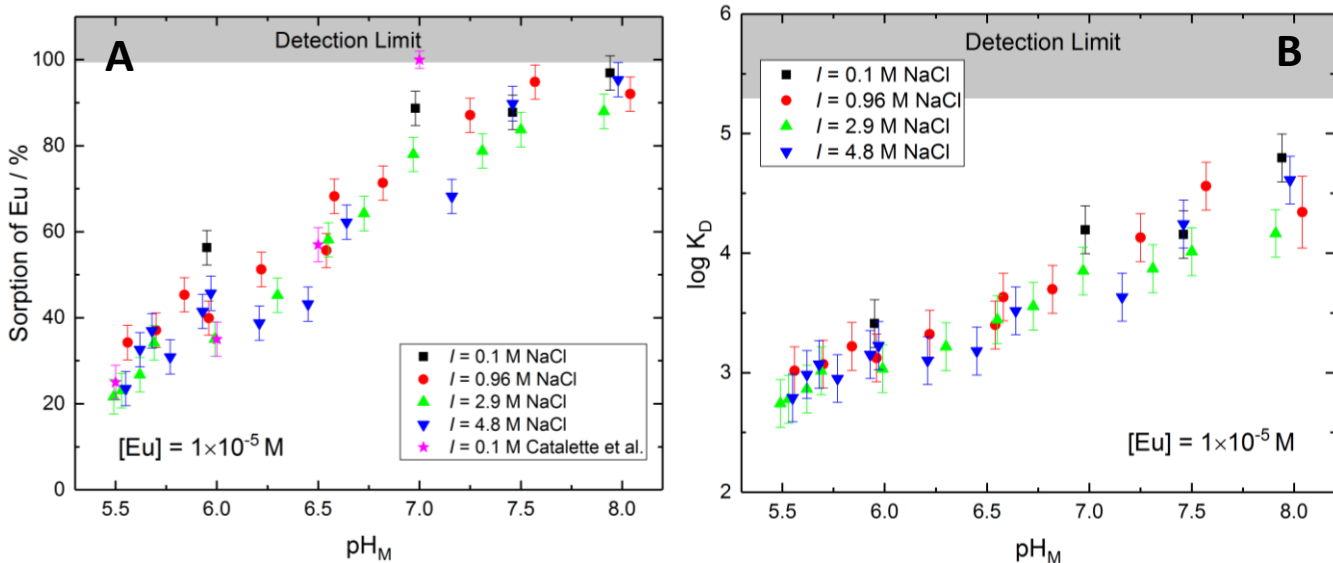


Figure 57: Sorption of europium $[Eu] = 1 \times 10^{-5} \text{ M}$ as percentage uptake (A) and as logarithm of distribution ratio ($\log K_D$) (B) on magnetite (0.5 g/L) as a function of pH_M and at different ionic strengths of NaCl.

Experiments in $MgCl_2$ brine with various ionic strength levels were performed following the same experimental procedure. At low europium concentration of $5.1 \times 10^{-10} \text{ M}$, the uptake was only performed for $I = 0.95 \text{ M}$. This data is comparable to data obtained at $I = 0.96 \text{ M NaCl}$, all the data for $pH_M \geq 5.6$ are below the detection limit (*Annex Figure A61*). Sorption data recorded for high europium concentration in $MgCl_2$ brine exhibited, as in the case of NaCl, a pH_M dependant behaviour (*Figure 58 A*). In this brine, the ionic strength effect is more evident. A clear decrease in sorption by $\sim 15 \%$ occurs between data of $I = 0.95 \text{ M MgCl}_2$ and $I = 2.85 \text{ M MgCl}_2$. The corresponding $\log K_D$ values are 2.7 ± 0.2 ($21 \pm 4 \%$) increasing to 4.0 ± 0.2 ($85 \pm 4 \%$) (*Figure 58 B*).

Increasing the ionic strength to a level, which may occur in Mg-brine solutions in rock salt formations ($I = 9.77 \text{ M MgCl}_2$), lowers the uptake significantly at slightly alkaline conditions due to competition of europium and magnesium for sorption. *Figure 59* shows the direct comparison of the uptake data between the two brines for identical ionic strength levels of 0.95-0.96 M (*Figure 59 A*) and 2.85-2.9 M (*Figure 59 B*). At $I = 0.95-0.96 \text{ M}$, the uptake is similar for the two brines until pH_M of 7.0, after which the uptake in $MgCl_2$ brine is slightly lower. The possible reason is Mg adsorption onto magnetite at alkaline pH_M . At $I = 2.85-2.9 \text{ M}$, there is a substantially lower Eu uptake in $MgCl_2$ for $pH_M \geq 6.2$ of about 15-20 % compared to the NaCl brine. In this case, it appears that the ionic strength is high enough not only for significant Mg adsorption but also for surface screening, which causes an overall lower sorption, also at neutral pH_M .

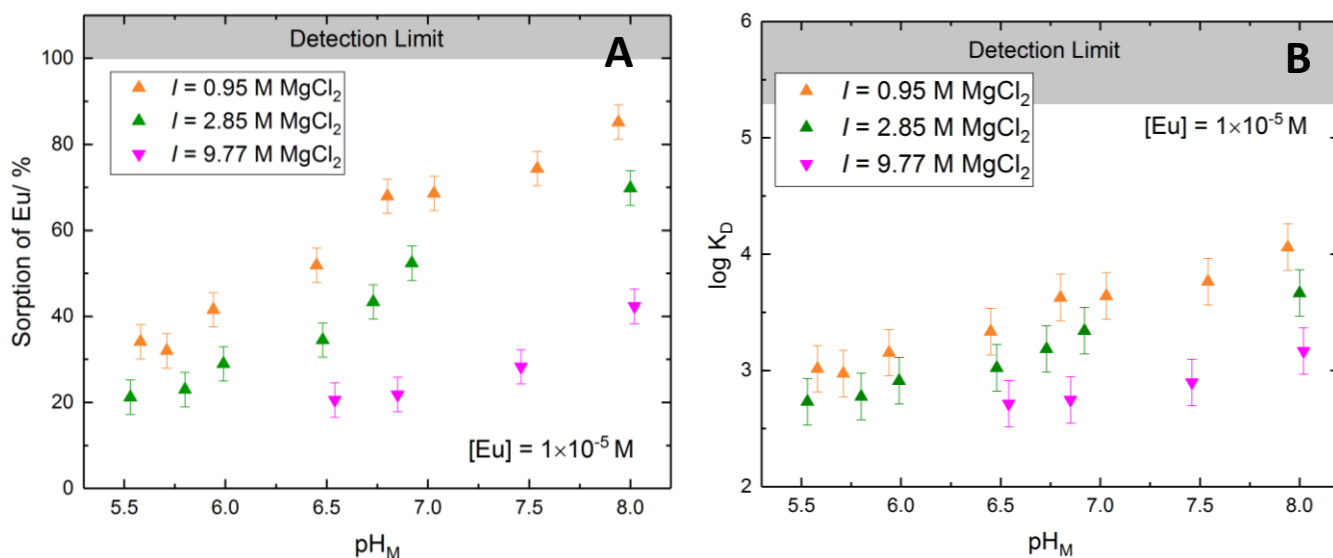


Figure 58: Sorption of europium $[Eu] = 1 \times 10^{-5} M$ as percentage uptake (A) and as logarithm of distribution ratio ($\log K_D$) (B) on magnetite (0.5 g/L) as a function of pH_M and at different ionic strengths of $MgCl_2$.

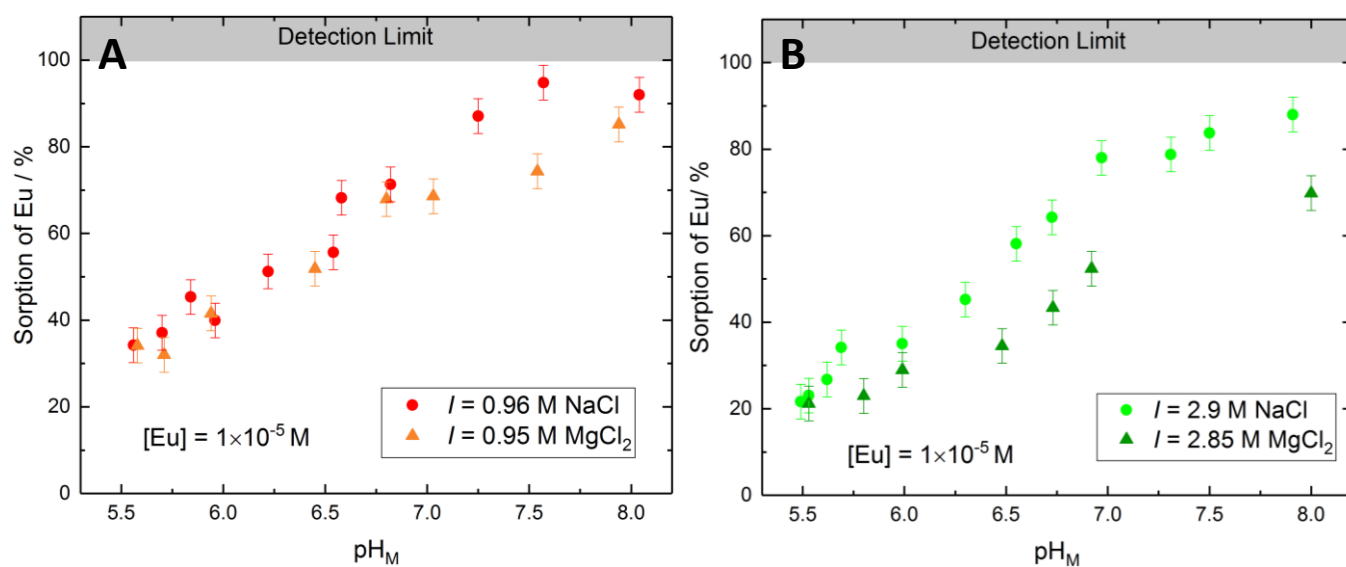


Figure 59: Sorption of europium $[Eu] = 1 \times 10^{-5} M$ as percentage uptake on magnetite (0.5 g/L) as a function of pH_M and at similar ionic strength levels of $NaCl$ and $MgCl_2$. $I = 0.95-0.96 M$ (A), $I = 2.85-2.9 M$ (B).

4.2.1.3 Uptake as a function of the Eu concentration in concentrated NaCl solutions

Sorption isotherms were performed at $\text{pH}_M \sim 6.0$ (**Figure 60 A**) and ~ 7.0 (**Figure 60 B**) for an europium concentration varying from 10^{-10} M to 10^{-4} M at various ionic strengths set by NaCl. The linear behaviour of the isotherms hints that magnetite exhibits only 1 strong sorption site group. Furthermore, the effect of ionic strength is not visible at all, as the points lay on top of each other until 10^{-5} M of Eu, where a slight deviation can be noted.

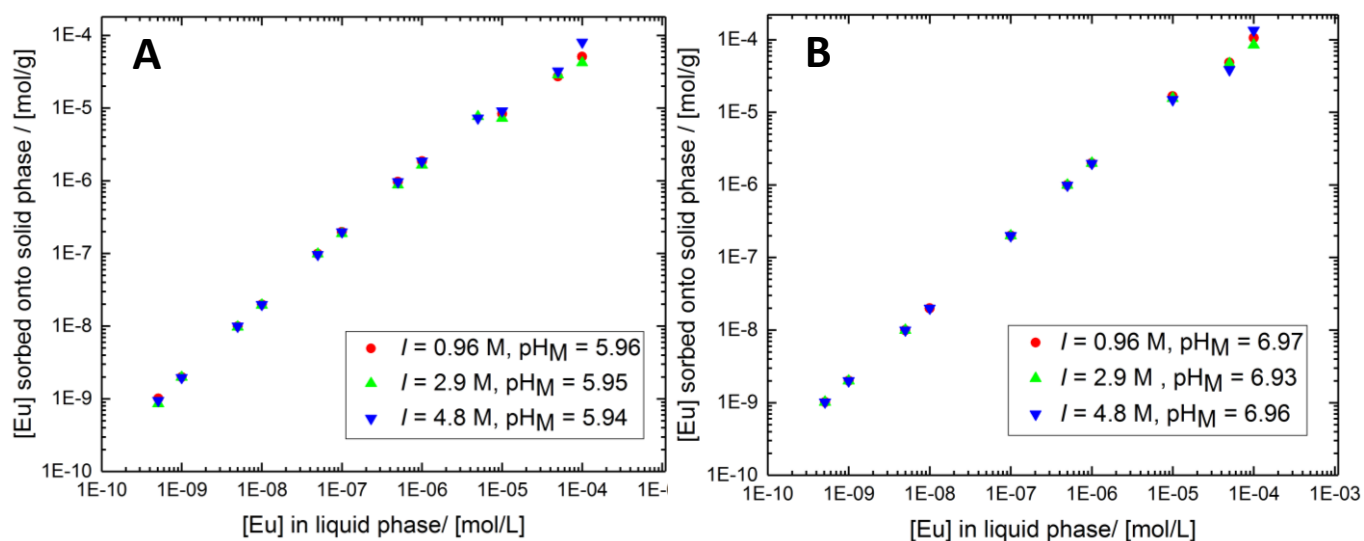


Figure 60: Sorption isotherms of europium onto magnetite (0.5 g/L) at $\text{pH}_M \sim 6.0$ (A) and ~ 7.0 (B) in mol/g at various ionic strengths of NaCl.

4.2.1.4 Structural interpretation of Am uptake: EXAFS

EXAFS measurements of Am L_3 -edge were performed on a set of sorption samples and the experimental procedure is described in detail in *section 2.6.1*. In order to obtain the amplitude reduction factor S_0^2 , reference Am^{3+} aquo ions were modelled, fitting the data with one O coordination shell containing 9 atoms ($\text{CN}_{\text{O1}} = 9.0$ atoms, set parameter) at a distance of $R(\text{Am-O1}) = 2.44$ Å. This is in agreement with literature data [Finck et al., 2015; Skerencak-Frech et al., 2014]. Samples containing magnetite showed different Fourier transforms at $R + \Delta R > 2.5$ Å in comparison to that of the aquo ions, highlighting the presence of an ordered shell at higher distances, likely iron. Nevertheless, the EXAFS spectra were very similar in all sorption samples, suggesting similar coordination environment for various pH_M and I . The aqueous speciation calculation confirmed that the dominant species do not significantly vary between pH_M 6.0 and 7.1 and thus a similar coordination

environment for various pH_M was expected. Experimental and modelled EXAFS spectra are shown in **Figure 61** with model parameters summarized in **Table 27**.

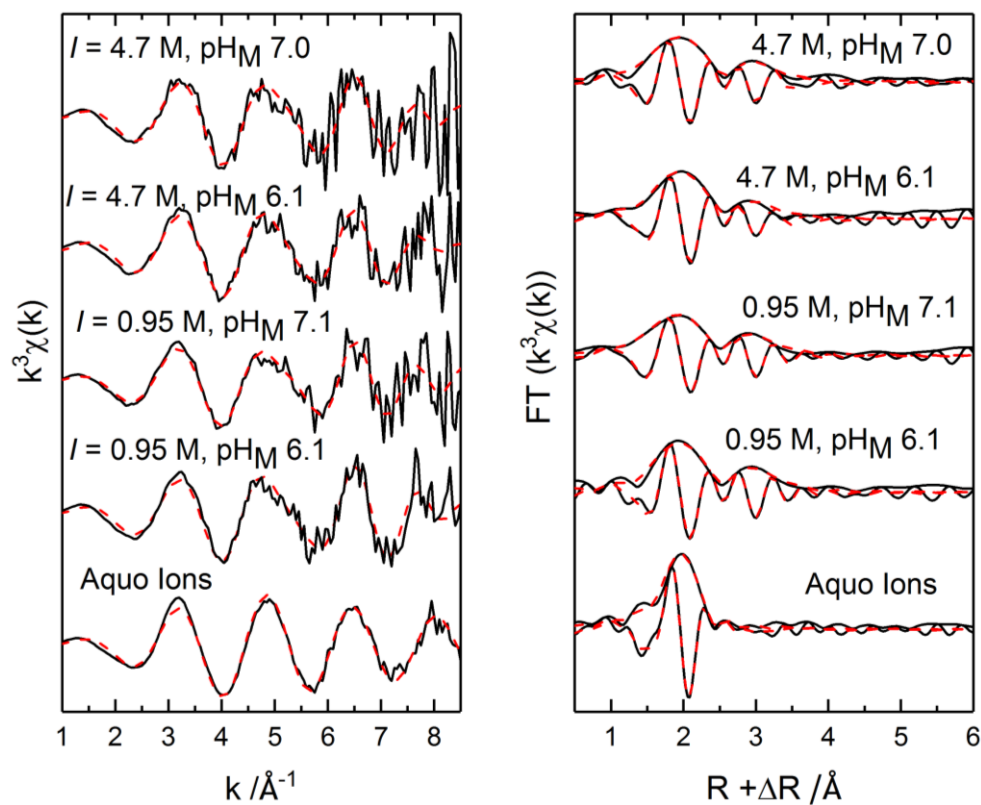


Figure 61: Experimental (black solid line) and modelled (red dashed line) EXAFS spectra in k space and Fourier transforms of the Am^{3+} aquo ions and sorption samples.

There is one contribution in the Fourier transformed (FT) spectra (**Figure 61**) originating from the aquo ions and two contributions from the sorption samples. The refinement of the first peak shows the similarity of the species to aquo ions having the same O coordination number. The refinement yields an Am-O path where the first peak corresponds to 9(1) oxygen atoms for all samples at a distance of 2.48-2.53 Å (**Table 27**). No neighbouring Am was detected excluding the presence of precipitates on the surface. The absence of precipitates is consistent with what is expected from PhreeqC modelling. In order to obtain further information about the structure of Am species on magnetite, the fit of the Fourier transform peak was extended beyond the oxygen coordination sphere. The refinement of the second shell in the FT data at $R + \Delta R = 3.35$ Å yields an Am-Fe interaction where the peak was fitted with 3(1) Fe atoms at a distance of 3.49-3.54 Å, suggesting a surface complex. This formation implies that an Am atom is linked via three oxygen atoms to three edge sharing FeO_6 octahedra, as shown in **Figure 62**, with six remaining oxygen atoms in the liquid phase. This is in agreement with the work of Kirsch et al. [2011], who examined Pu^{3+} sorption onto magnetite at low $I = 0.1$ M NaCl and with the data reported by Finck et al. [2016_{a,b}], who examined Am sorption onto magnetite at low I (0.1 M

NaCl). The latter authors observed the formation of the same monomeric tridentate inner sphere surface complex highlighting the similarity of the Am surface species structure for data obtained at low and high I , which confirms the negligible effect of I on the structure of surface complexes also observed in the uptake data.

Adding a Cl coordination shell, which might be expected because of Am-chloro complex formation at high Cl^- concentration, did not improve the fit. Thus, the presence of the chloride complex at the magnetite surface was considered insignificant under our experimental conditions.

Table 27: Best-fit EXAFS Model Parameters for americium sorbed onto magnetite and the reference compound (Am^{3+} in solution).

Sample	FT range [\AA^{-1}]	Fit range in R space [\AA]	Path	CN	R [\AA]	σ^2 [\AA^2]	ΔE_0 [eV]	F factor
Am^{3+} Aquo Ions	3.2-10.3	1.7-2.6	Am-O1	9.0	2.44	0.008	1.2(1.4)	0.0021
Am-Magnetite, pH_M 6.1, $I = 0.95$ M	3.2-8.2	1.5-3.5	Am-O1	8.9(6)	2.51	0.011	1.8(1.3)	0.0013
			Am-Fe1	3.1(5)	3.53	0.006		
Am-Magnetite, pH_M 7.1, $I = 0.95$ M	3.2-7.8	1.3-3.45	Am-O1	9.9(7)	2.48	0.016	0.1(1.1)	0.0019
			Am-Fe1	3(2)	3.49	0.006		
Am-Magnetite, pH_M 6.1, $I = 4.7$ M	3.3-8.0	1.35-3.3	Am-O1	9.6(9)	2.53	0.013	2.5(2.1)	0.0018
			Am-Fe1	2.5(9)	3.54	0.008		
Am-Magnetite, pH_M 7.0, $I = 4.7$ M	3.2-7.7	1.3-3.3	Am-O1	9.9(6)	2.49	0.015	1.9(0.5)	0.0019
			Am-Fe1	2.9(6)	3.54	0.007		

FT range: Fourier Transform range, CN: Coordination number, R: Interatomic distance, σ^2 : Debye - Waller factor, ΔE_0 : Shift in ionization energy where E_0 is the energy at the maxima of the first derivative, F factor: figure of merit of the fit representing the absolute misfit between the data and the model. Amplitude reduction factor $S_0^2 = 0.87$ for all samples. Estimated error for $R = \pm 0.03 \text{ \AA}$ and for $\sigma^2 = \pm 0.001 \text{ \AA}^2$. The numbers in parentheses indicate the uncertainty.

Literature data suggest that the americium presence during the formation of magnetite from corrosion of $\text{Fe}(0)$ would result in its substitution for Fe in early stages and once the magnetite phase is formed, it would be localized within its structure [Finck et al, 2016a]. The data obtained in the present study exclude Am incorporation under given experimental conditions.

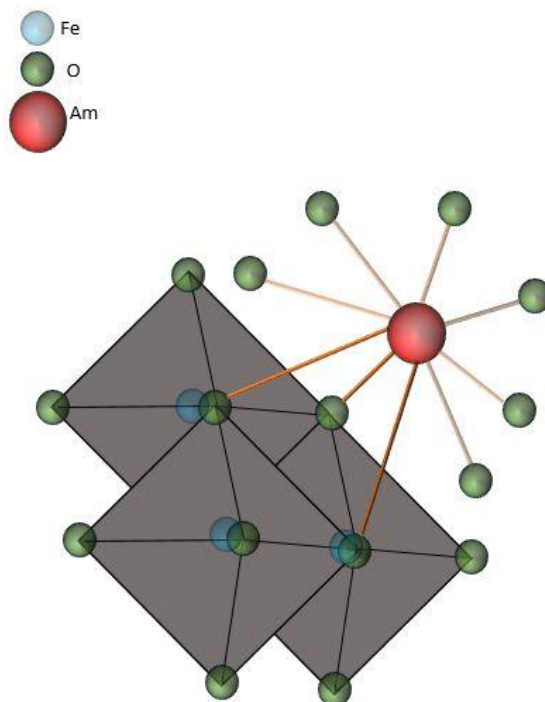


Figure 62: Sorption complex of Am^{3+} on the edge sharing octahedral (111) plane of magnetite.

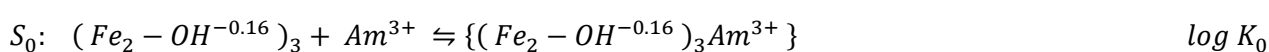
4.2.1.5 Surface complexation model

The developed surface complexation model is based on the aquatic speciation of europium/ americium as presented in *section 4.1.2*, the magnetite surface structural model in *Tables 25 and 26* and the EXAFS characterization of the surface complex structure obtained for americium, showing a tridentate binding mode. The model has been developed for americium complexes using europium uptake in NaCl solutions. As already mentioned before, europium sorption is well known to compare closely to that of americium. The surface of the Fe_3O_4 (111) plane was optimized with either octahedral termination or mixed octahedral and tetrahedral terminations to compare the two terminations as explained in *section 4.2.1.1*.

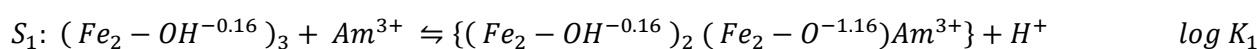
The charge distribution in the americium surface complex coordinated by nine oxygen atoms in the model was formulated such that three oxygen bonds would go to the surface and the remaining six were split such that three would be placed in the b plane and three equally divided between the 0 and the b plane to best represent the positioning of americium. This distribution is in agreement with the EXAFS data.

The model delivered a very poor fit when using only singly coordinated sites, which was unexpected as titration experiments showed these as the dominant sites for proton adsorption.

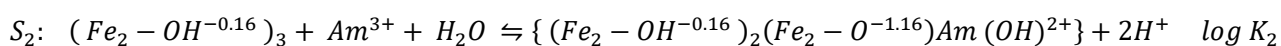
The fit was improving as the distribution of the sites in the model was moving more towards doubly coordinated sites. The best fit occurred if only doubly coordinated sites were used, with satisfactory fit for both terminating hydroxyl groups. The spectroscopic data suggest that the binding occurs at the octahedral termination. This configuration matches well with the structure of the octahedral termination given by Vayssières [1995] allowing Am to be located close to three Fe atoms with the same distances and three available O atoms, likewise at the same distances, which is not the case for the mixed termination. The result of fitting sorption data by assuming this surface species as relevant is shown in **Figure 63**. The model inherent surface complexes are shown below with the complexation constants at infinite dilution summarized in **Table 28**:



Transfer of charge: $\Delta z_0 = 1.5$, $\Delta z_\beta = 1.5$.



Transfer of charge: $\Delta z_0 = 0.5$, $\Delta z_\beta = 1.5$.



Transfer of charge: $\Delta z_0 = 0.5$, $\Delta z_\beta = 0.5$.

Table 28: The complexation constants at infinite dilution.

<i>log K₀</i>	6.9 ± 0.1
<i>log K₁</i>	0.2 ± 0.1
<i>log K₂</i>	-7.5 ± 0.1

The aquatic speciation of europium and americium showed significant contributions of AmCl²⁺/EuCl²⁺ species, however, these seem to be limited to the aqueous solution and do not contribute in significant manner to the surface complexation. The assumption is corroborated by the obtained satisfactory fit without the introduction of an Am-Cl surface complex $\{(Fe_2 - OH^{-0.16})_3 Am Cl\}$.

The model is able to describe the respective pH_M dependent trend of sorption (**Figure 63**) as well as experimental sorption data obtained at different Eu concentration and ionic strengths. The model fit for sorption isotherm data is shown in **Figure 64**.

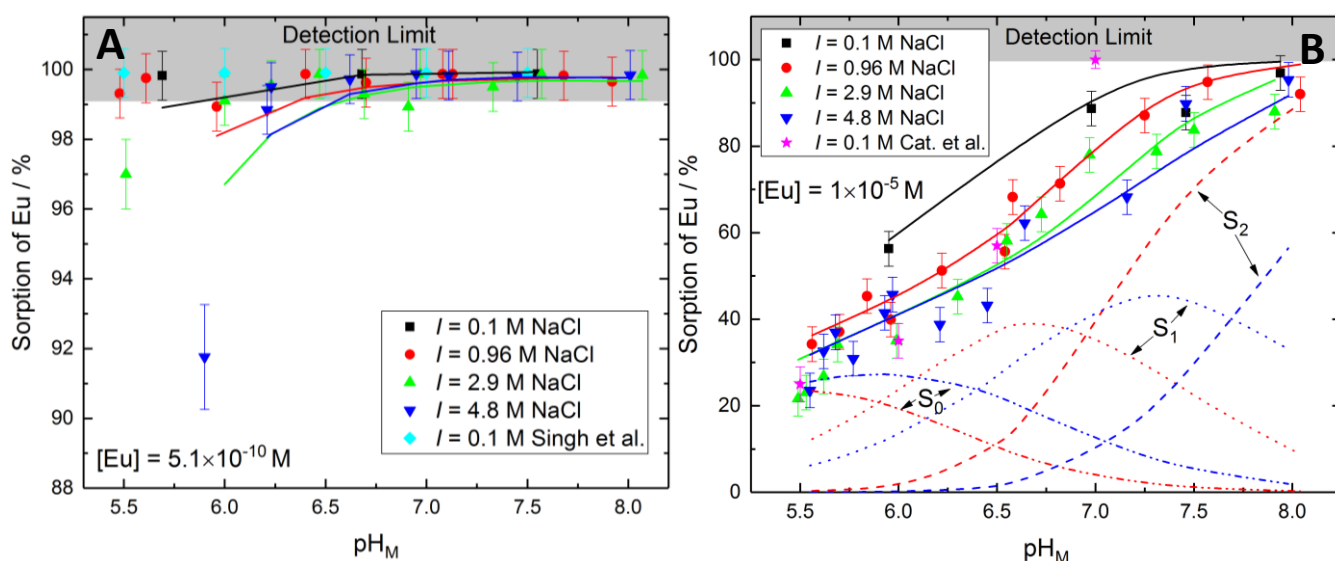


Figure 63: Sorption of europium $[Eu] = 5.1 \times 10^{-10}$ M (A) and 1×10^{-5} M (B) onto magnetite vs. pH_M . Experimental uptake (points) modelled (full lines) using surface complexation model in FITEQL with the Pitzer approach and [TPA] database for various ionic strengths (NaCl). The dashed lines represent the complex distribution for the three complexes for $I = 0.96$ M (red) and $I = 4.8$ M (blue), respectively. S_x represents the surface complexation reaction described in the text.

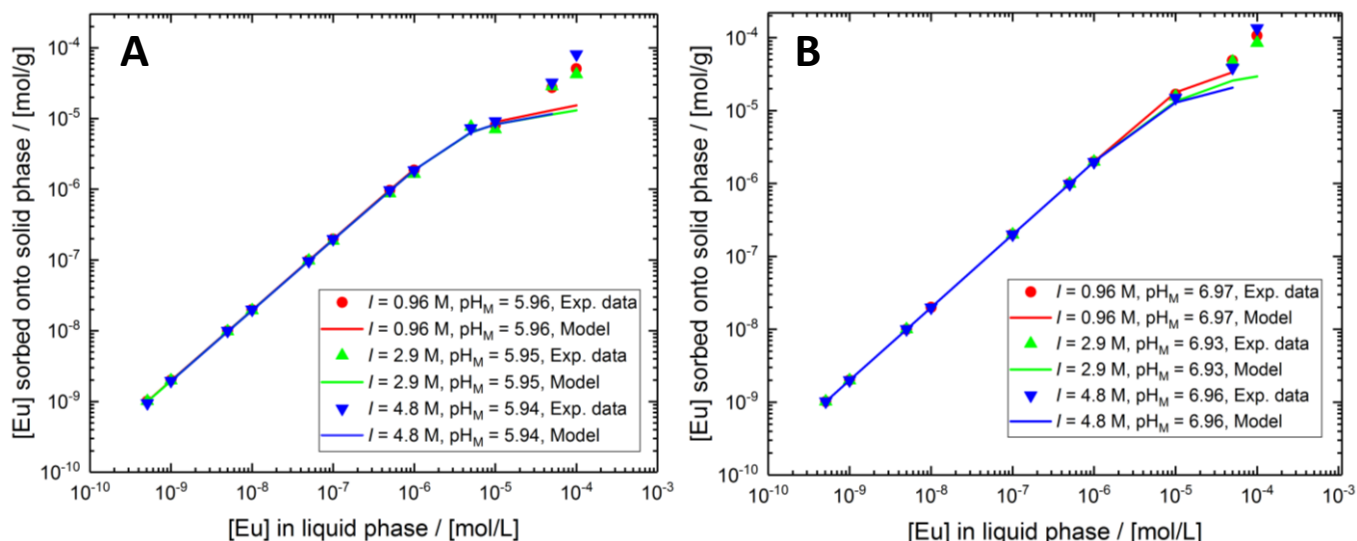


Figure 64: Sorption isotherm of europium onto magnetite (0.5 g/L) at $pH_M \sim 6.0$ (A) and ~ 7.0 (B). Experimental uptake (points) modelled (full lines) using surface complexation model in FITEQL with the Pitzer approach and [TPA] database for various ionic strengths (NaCl).

Subtracting $\log K_1$ from $\log K_2$ results in the constant for the hydrolysis reaction of the magnetite sorbed Am(III) surface complex. The difference is -7.7 and is close to $\log K$ for americium hydrolysis in solution (-7.2), showing that the obtained values are realistic.

Figure 63 B shows also the distribution of the different surface complexes as a function of pH_M for $[\text{Eu}] = 1 \times 10^{-5}$ M, where S_0 corresponds to the $\{(Fe_2 - OH^{-0.16})_3 Am^{3+}\}$ complex, S_1 to the $\{(Fe_2 - OH^{-0.16})_2 (Fe_2 - O^{-1.16}) Am^{3+}\}$ complex, and S_2 to the $\{(Fe_2 - OH^{-0.16})_2 (Fe_2 - O^{-1.16}) Am (OH)^{2+}\}$ complex. The dashed red lines correspond to surface complex distributions for $I = 0.96$ M, while the dashed blue lines correspond to surface complex distributions for $I = 4.8$ M. For $I = 0.96$ M, S_0 prevails at low pH_M up to 5.8, S_1 exists within the entire studied pH_M range and the hydrolysed S_2 is dominant at high pH_M (≥ 7.0). Upon increase of the I to 4.8 M, the distribution trend is the same, but the dominance of each complex is shifted to higher pH_M , with S_0 being dominant up to pH_M 6.4, and S_1 up to pH_M 7.7. For clarity, the distribution was not plotted for low europium concentrations of 5.1×10^{-10} M. In this case the distribution was different with complex S_0 dominating up to pH_M 7.6 for $I = 0.96$ M and in the whole investigated pH_M range for $I = 4.8$ M.

The reason for different ionic strength effects for the two Eu concentrations is the interplay of competition for sites and ionic strength effect on activities in solution. With higher ionic strength, the electrolyte interacts with surface sites and, thus, competes with Eu, and at higher concentration of this radionuclide, this effect becomes notable. With low Eu concentration, this competition is minor. It is worth noting that even at high Eu concentrations only about 59 % of the surface sites are occupied. This reflects the high sorption capacity of magnetite, rendering this corrosion phase a candidate for strong radionuclide retention in a nuclear waste repository near-field considering dilute to concentrated NaCl brine.

4.2.2 Iron hydroxychloride ($\text{Fe}_2(\text{OH})_3\text{Cl}$)

The iron hydroxychloride was also examined for its sorption capability as it has been observed in both brines in case of SGI corrosion, close to bulk steel in NaCl brine and as a dominant and long-term stable phase in MgCl_2 brine. A first batch of the solid has been synthesised by the project partners in GRS, while the second batch has been synthesised in house according to *Table 3*.

The SEM images of the two batches are shown in *Figure 65*. Batch 1 shows particles of approximately 200 nm in size. The batch 2 seems to have slightly smaller particle size; however the morphology of cube clusters is maintained. The shape is however different from the pyramid-trigonal morphology observed for this phase in the corrosion experiments. Furthermore, in corrosion experiments, Mg replaced part of Fe(II) in the structure (Fe^{2+},Mg) $_2(\text{OH})_3\text{Cl}$, but in the sorption experiments, pure $\text{Fe}_2(\text{OH})_3\text{Cl}$ was used.

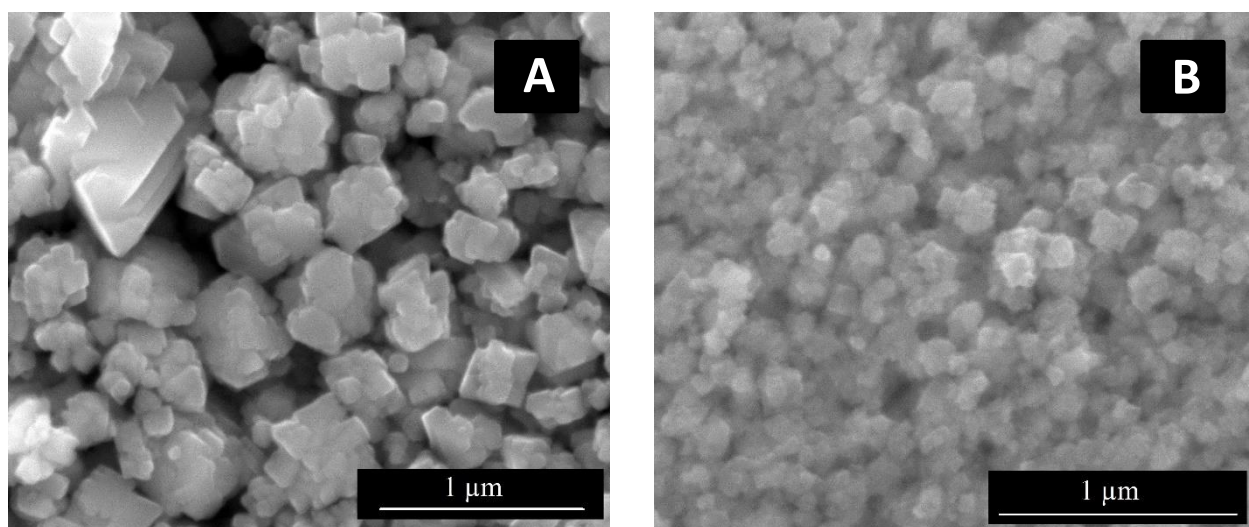


Figure 65: SEM images of iron hydroxychloride. Batch 1 synthesised at GRS (A) and batch 2 synthesised in house (B).

The EDX analysis was performed for both batches and the chemical compositions are shown in *Table 29*. The chemical composition of the two batches matches well and the Fe/Cl/O ratio matches iron hydroxychloride compound.

Table 29: The chemical composition of the two batches of iron hydroxychloride compound.			
Element/ Atomic %	O	Cl	Fe
Batch 1	52.05±1.01	16.59 ±0.32	31.36 ±0.72
Batch 2	50.4±1.6	16.2±0.4	33.3±0.7

XPS of batch 1 (*Figure 66*) shows the presence of Fe(II) only, highlighting that the surface of the phase is not oxidised.

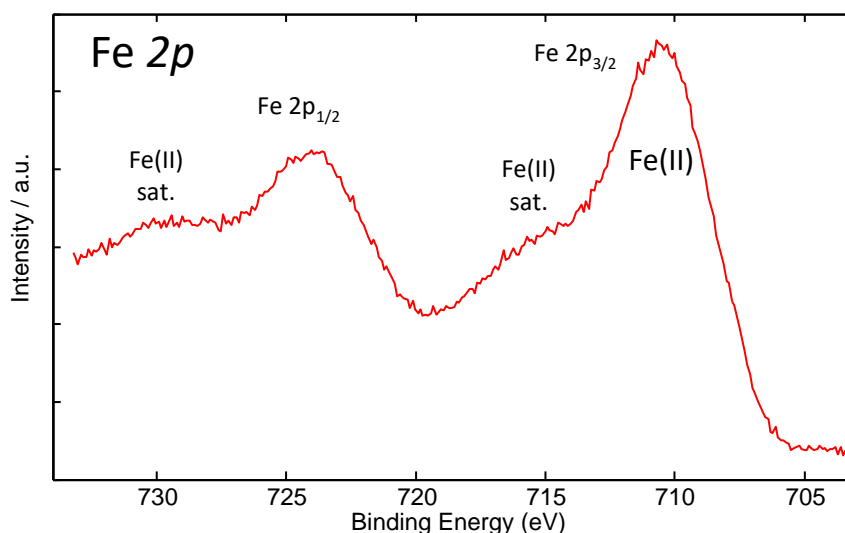


Figure 66: XPS narrow Fe 2p spectrum of the iron hydroxychloride compound from batch 1.

XRD analysis of batch 1 yielded high background and no clear peaks, thus Raman analysis was performed (not shown), obtaining peaks matching the iron hydroxychloride [Réguer et al., 2007]. XRD analysis of batch 2 (*Figure 67*) showed clear peaks matching iron hydroxychloride in the database. This could be attributed to the two different XRD machines used for the two respective batches with the first machine used for batch 1 having lower performance and tilting of samples leading to potential sample movement during measurement.

Choosing the correct pH_M range for sorption was challenging for this phase, as literature sources state stability only under neutral to mildly acidic conditions [Réguer et al, 2005]. In corrosion studies, the formation of this phase is observed in the pH_M range 5-7 at 90 °C and up to pH_M 8.5 at 25 °C. The selected pH_M range for sorption experiments was 6.7-9 to match the conditions of the corrosion experiments performed at room temperature.

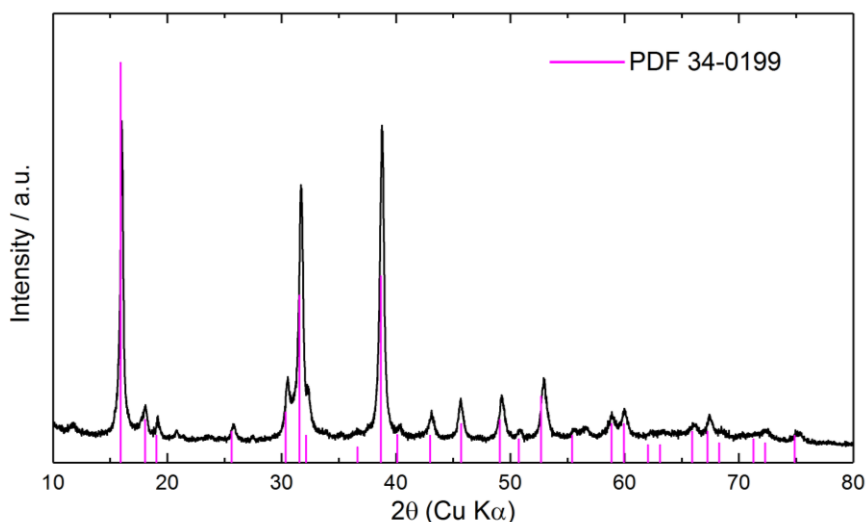


Figure 67: X-ray diffractogram of the synthesised iron hydroxychloride, batch 2. PDF card 34-0199 refers to $\text{Fe}_2(\text{OH})_3\text{Cl}$.

4.2.2.1 Uptake as a function of pH in dilute to concentrated NaCl and MgCl_2 solutions

ICP-MS analyses for dissolved iron for the experiments performed in NaCl and MgCl_2 brines (*Figure 68*) show significant dissolution in the pH_M range of 6.8-7.8 (almost half of introduced solid phase).

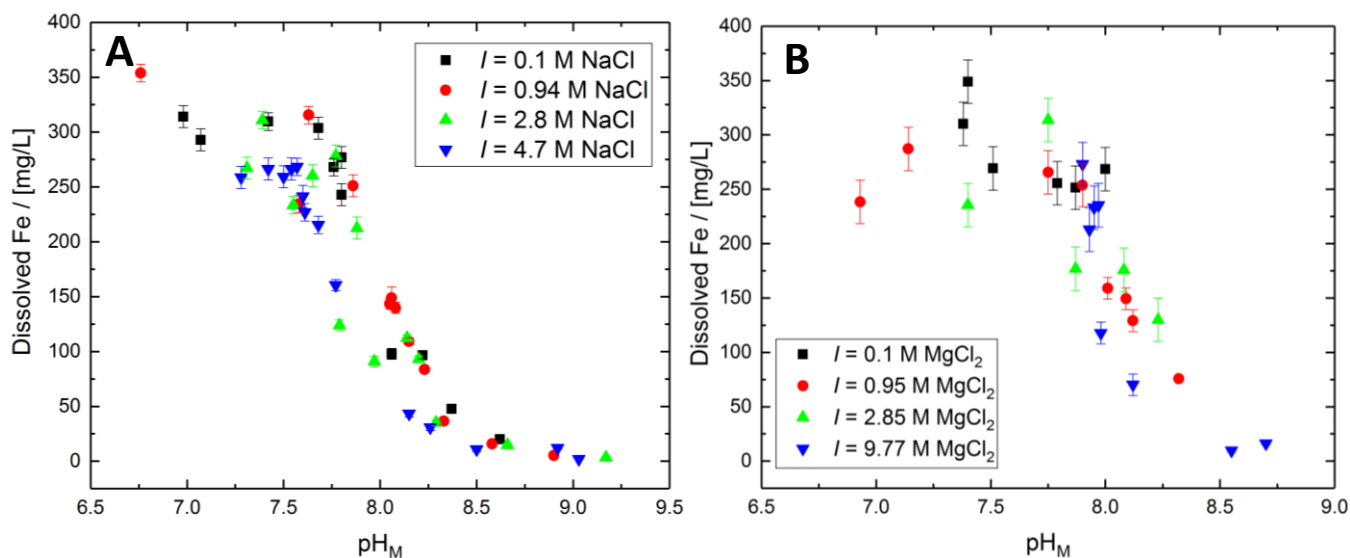


Figure 68: Dissolved iron concentration in aqueous solutions in contact with iron hydroxychloride vs. pH_M at different ionic strengths of NaCl (A) and MgCl_2 (B).

Geochemical calculations using PhreeqC software with the SIT approach and [TC] database showed that the 300 mg/L of dissolved iron under corresponding pH_M conditions give rise to precipitation of magnetite in the solution with an ionic strength of 0.1 M NaCl and 4.7 M NaCl. This finding therefore

questions the extent of uptake by only iron hydroxychloride and the contribution of the other precipitated solid phases in the pH_M region < 8 .

The retention of europium by iron hydroxychloride in dilute to concentrated NaCl brine is significant considering an europium concentration of 5.1×10^{-10} M, with an uptake above 96 % in the pH_M range of 6.2-9.2 with the majority of data points at the analytical detection limit (**Figure 69 A**). This limit corresponds to 99 % uptake and $\log K_D$ of 5.0-5.4. The range of $\log K_D$ values corresponding to the detection limit is shown in **Figure 69 B**. Due to significant loss of the solid phase, the $\log K_D$ values reported in this work were recalculated for each point to account for solid dissolution, leading also to the range of values corresponding to the detection limit. Considering that the remaining values lie close to the detection limit and their uncertainties, no ionic strength effect can be observed. The dissolution of the solid phase does not seem to affect the sorption in this case and the remaining solid (including potential magnetite precipitate) is sufficient to sorb the introduced europium.

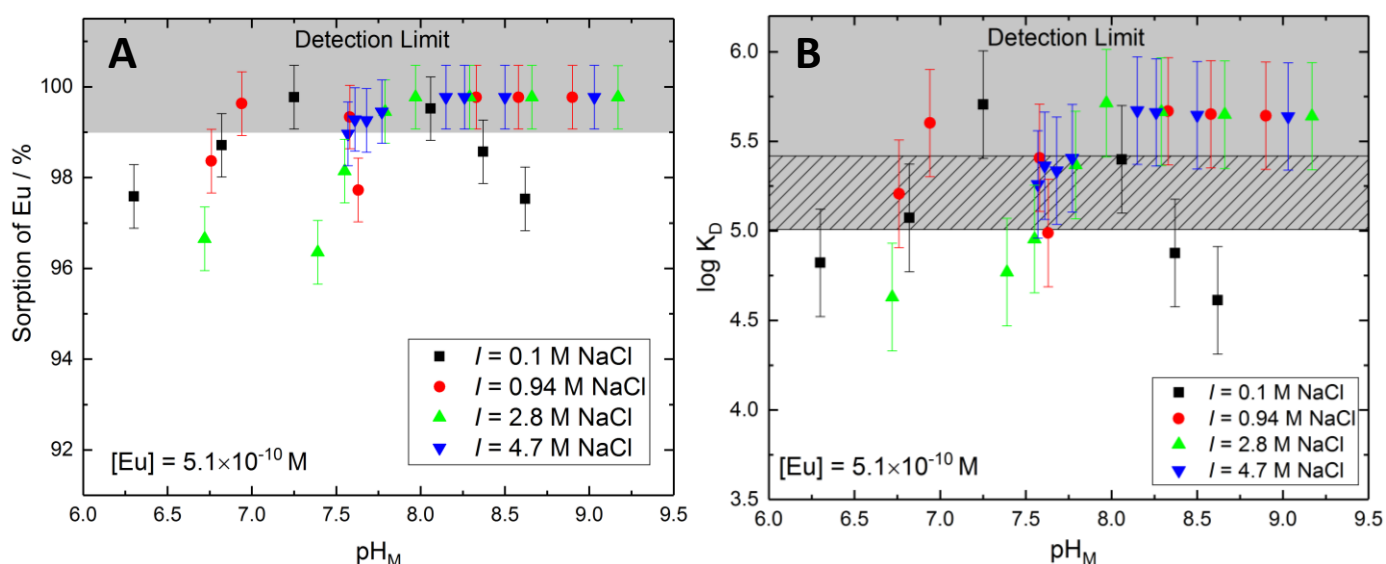


Figure 69: Sorption of europium $[\text{Eu}] = 5.1 \times 10^{-10}$ M as percentage uptake (A) and as logarithm of distribution ratio ($\log K_D$) (B) on iron hydroxychloride (1 g/L) as a function of pH_M and at different ionic strengths of NaCl.

Increasing the europium concentration to 1×10^{-7} M, the uptake seems to follow a stagnant to slightly decreasing trend with increasing pH_M until 7.7, after which the uptake increases for all ionic strength levels. There is no obvious ionic strength effect (**Figure 70 A**). The $\log K_D$ values range from 4.0 ± 0.1 to 4.7 ± 0.2 (**Figure 70 B**). It seems that the lower availability of the solid phase concurrent with sorption competition with dissolved Fe(II) affects the extent of sorption and thus an initial sorption decrease took place. Once the dissolution becomes less significant, europium uptake increases with increasing pH_M .

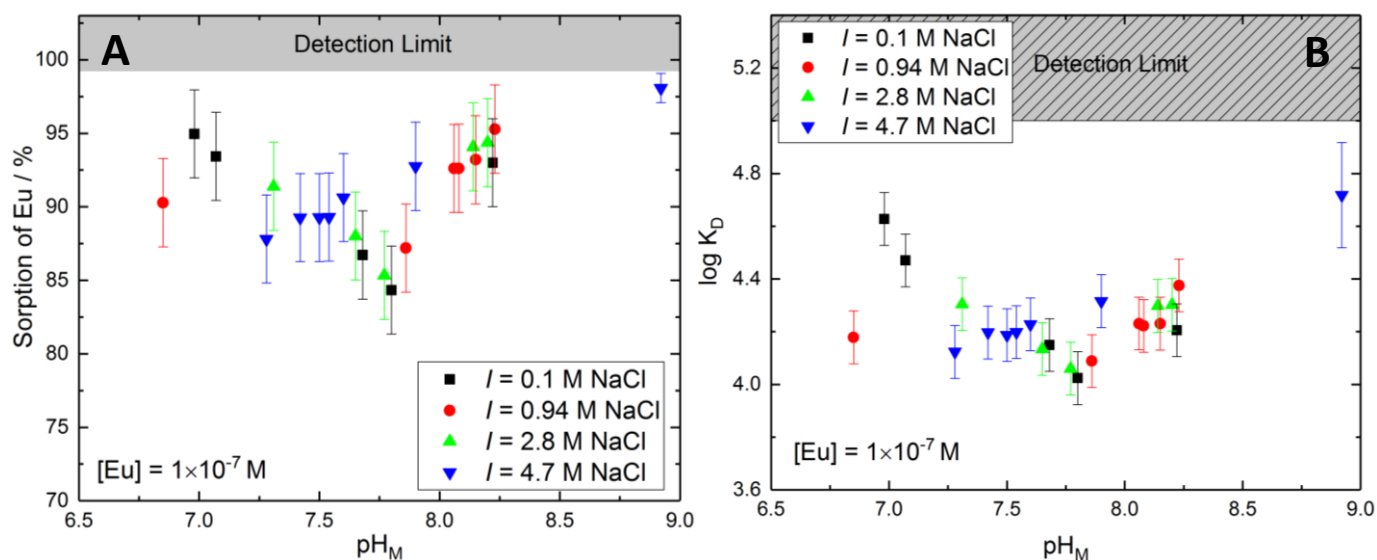


Figure 70: Sorption of europium $[Eu] = 1 \times 10^{-7} M$ as percentage uptake (A) and as logarithm of distribution ratio ($\log K_D$) (B) on iron hydroxychloride (1 g/L) as a function of pH_M and at different ionic strengths of NaCl.

Additional uptake experiments were performed in $MgCl_2$ brine with various ionic strength levels, one closely corresponding to the 3.4 M concentration used in the corrosion experiments. The sorption behaviour of iron hydroxychloride in $MgCl_2$ was of interest due to its formation mainly in those corrosion experiments performed in $MgCl_2$ brine.

For $[Eu] = 5.1 \times 10^{-10} M$ (Figure 71), the uptake data show a strong retention at an ionic strength of 0.1 M, comparable to data in the NaCl brine with identical ionic strength and $[Eu]$, with Eu(III) concentration values close to detection limit at the pH_M 7.6-7.8. However, with increasing ionic strength (0.95 M and 2.85 M), the uptake decreases with increasing pH_M . This effect was strongly enhanced for $I = 9.77 M MgCl_2$. This distinctly different behaviour in concentrated $MgCl_2$ brine was quite unexpected.

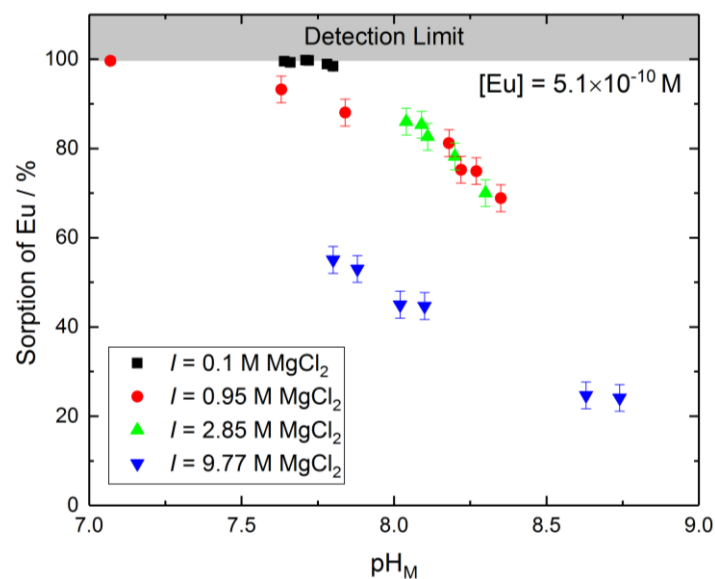


Figure 71: Sorption of europium $[Eu] = 5.1 \times 10^{-10}$ M as percentage uptake on iron hydroxychloride (1 g/L) as a function of pH_M and at different ionic strengths of $MgCl_2$.

Similar behaviour was observed in $MgCl_2$ solution for $[Eu] = 1 \times 10^{-7}$ M (**Figure 72 A**). At low ionic strength of 0.1 M $MgCl_2$, the uptake was close to the detection limit (pH_M 7.4 to 8.2). The corresponding $\log K_D$ values were $4.7-5.3 \pm 0.2$ (**Figure 72 B**). However, a clear, decreasing trend is observed with increasing ionic strength. For $I = 0.95$ M, the $\log K_D$ values decrease with increasing pH_M from 5.2 ± 0.2 to 2.9 ± 0.2 . Similarly, for $I = 9.77$ M $MgCl_2$, the $\log K_D$ values decrease from 3.4 ± 0.2 to 2.2 ± 0.2 .

Within the frame of the current thesis, a closer examination of a possible alteration of the solid phase was not performed. Additionally, other solid phases likely precipitated due to high amount of dissolved iron, hereby were expected to scavenge europium (**Figure 68**).

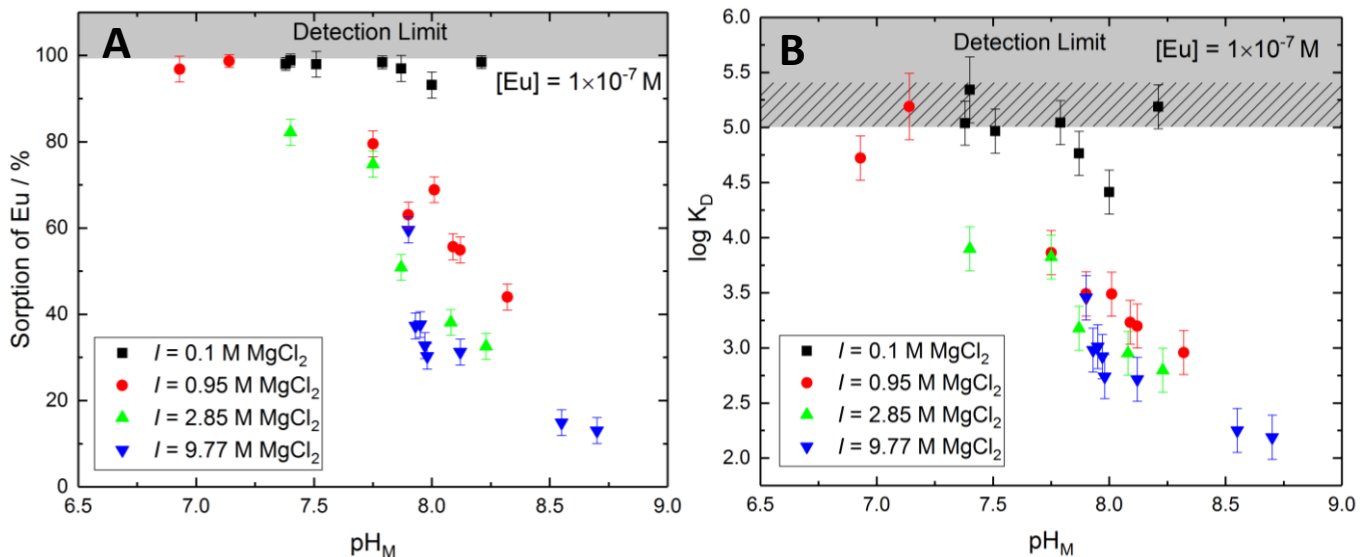


Figure 72: Sorption of europium $[Eu] = 1 \times 10^{-7} \text{ M}$ as percentage uptake (A) and as logarithm of distribution ratio ($\log K_D$) (B) on iron hydroxychloride (1 g/L) as a function of pH_M and at different ionic strengths of MgCl_2 .

One likely explanation for the observed behaviour could be a competing effect of divalent Mg ions on europium sorption onto iron hydroxychloride in the examined pH_M range. The sorption behaviour of Ca and Sr, also divalent ions, onto hydrous ferric oxide is described by Dzombak & Morel [1990], showing a high uptake already at comparably low concentrations (10^{-7} M). Considering the significantly higher amount of Mg compared to Eu, and stronger hydrolysis tendency of Mg as compared to Ca, this may justify the observed Eu- uptake trend with increasing MgCl_2 concentration in the brine. This would be an unfavourable behaviour for the repository scenario, where MgCl_2 rich brines with mildly alkaline pH_M intrude into the emplacement caverns. Due to the insufficient understanding of sorption data at present, a sorption model could not be developed within this thesis. As there are also no literature data describing sorption onto $\text{Fe}_2(\text{OH})_3\text{Cl}$, more experiments with this system could provide further clarifications.

4.2.3 Green rust chloride ($\text{Fe}_4(\text{OH})_8\text{Cl}$)· $n\text{H}_2\text{O}$ (GR-Cl)

Although the green rust chloride is a metastable phase, its presence was confirmed in corrosion experiments with SGI in 5 M NaCl at 25 °C, in solution 1 at 90 °C as a product of iron hydroxychloride oxidation and for Cr-Ni steel at the interface as the corrosion phase present upon start of pitting corrosion. In a scenario, where canister breach occurs when this phase is dominating the surface, its retention capability may be of interest. A brief sorption study in NaCl brine was performed with this solid phase. The green rust chloride solid phase was synthesised in house according to the procedure

described in *Table 3*. SEM images (*Figure 73*) show hexagonal particle morphology, typical for green rust, with particles of about 500 nm in size. Most of the platelets are laying flat.

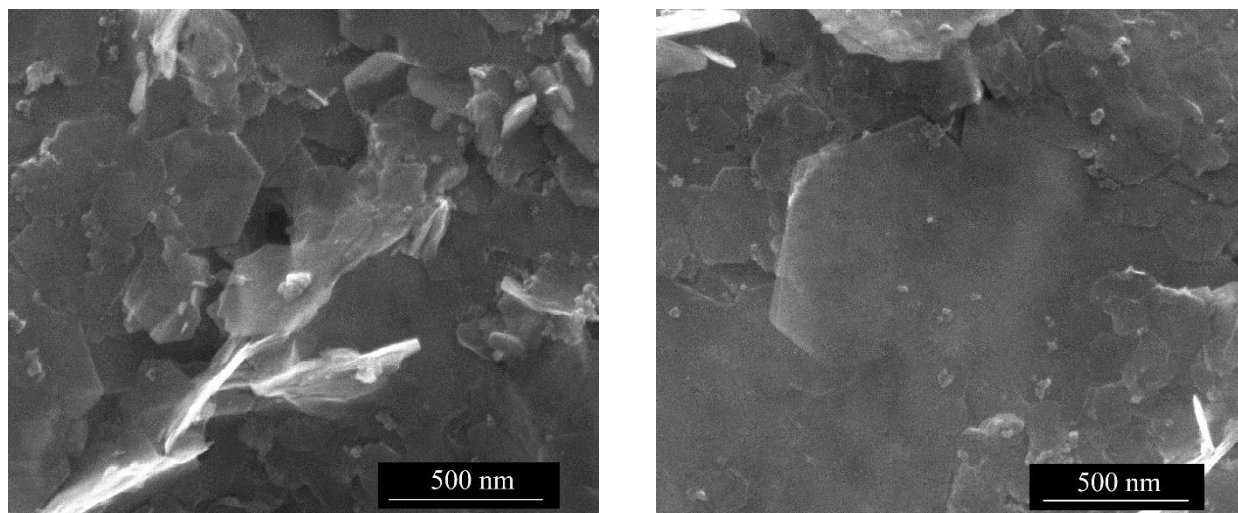


Figure 73: SEM images of the synthesised green rust chloride.

The EDX analysis on the phase showed a Cl/Fe ratio of 1/4, which is consistent with GR-Cl, but also a Cl/O ratio of 1/5 instead of 1/8. XPS analysis was not performed for this phase, but the presence of GR-Cl was confirmed by XRD analysis (*Figure 74*).

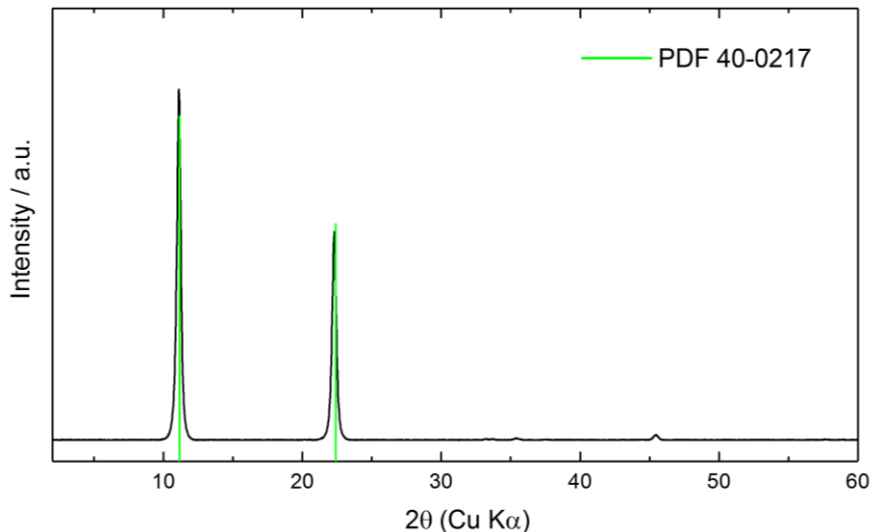


Figure 74: X-ray diffractogram of the synthesised green rust chloride. PDF card 40-0127 refers to green rust chloride in the database.

The green rust chloride is stable under neutral and reducing conditions [Refait et al., 1998]. In corrosion experiments, this phase has been found at pH_M 7.1, thus the investigated pH_M range for sorption studies was set to 7-9. The green rust chloride transforms into mixture of magnetite and $\text{Fe}(\text{OH})_2$ above pH 10 [Jolivet et al., 2004; Usman et al., 2018].

4.2.3.1 Uptake as a function of pH in dilute to concentrated NaCl solutions

The uptake of europium by green rust chloride considering 1 g/L solid phase shows quantitative uptake over the whole investigated pH_M range, considering both europium concentrations, 5.1×10^{-10} M (**Figure 75 A**) and 1×10^{-7} M (**Figure 75 B**). The $\log K_D$ values are all above 5.0 corresponding to the analytical detection limit of 99 % uptake.

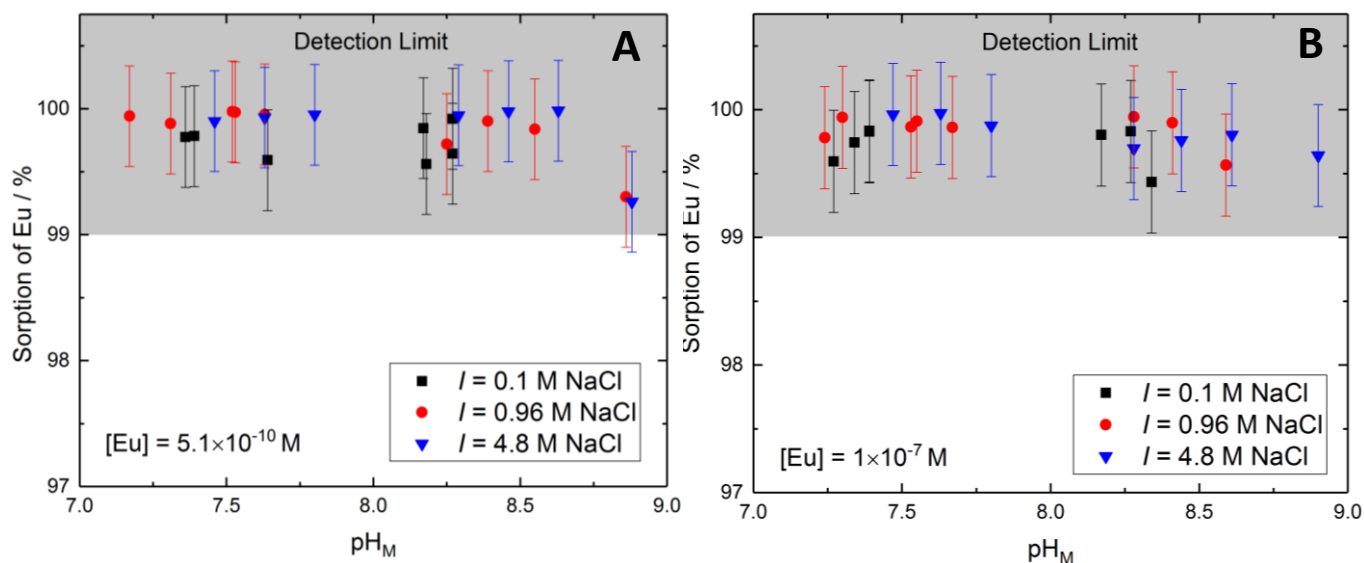


Figure 75: Sorption of europium as percentage uptake for $[\text{Eu}] = 5.1 \times 10^{-10}$ M (A) and $[\text{Eu}] = 1 \times 10^{-7}$ M (B) on green rust chloride (1 g/L) as a function of pH_M and at different ionic strengths of NaCl.

Figure 76 shows the pH dependent iron dissolution, with higher dissolved amounts at lower pH_M and higher I . Overall, the values of dissolved iron are in the mM range and could act as competitors to Eu(III) sorption. Using higher Eu concentration could lead to precipitation of $\text{Eu}(\text{OH})_3$ phase, but more experiments with lower solid amount, ideally with known specific surface area could reveal potential pH dependent uptake and/or effect of dissolved iron on sorption.

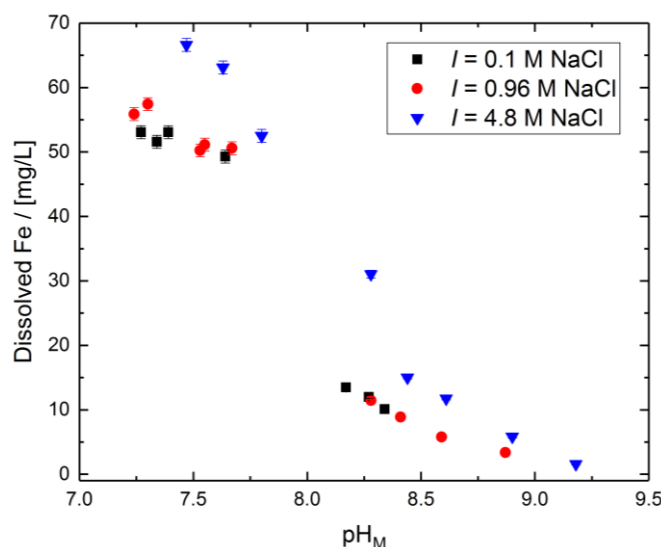


Figure 76: Dissolved iron concentration in aqueous solutions in contact with green rust chloride vs. pH_M at different ionic strengths of NaCl.

This uptake behaviour is in agreement with literature, which shows strong retention capability of green rust with respect to tetravalent [Latta et al., 2015; Römer et al., 2011] and trivalent [Jönsson & Sherman, 2008] radionuclides or pollutants in low ionic strength aqueous environment. The trivalent arsenic was found retained above pH 8 considering 1 g/L of solid and 1×10^{-3} M concentration at the green rust edge sites of the brucite layer by forming bidentate inner sphere surface complexes. One could, however, suspect that at an arsenic concentration of 1×10^{-3} M, precipitation could also contribute to the removal of arsenic from the liquid phase. Results obtained within this work are certainly not sufficient to derive a detailed atomistic model of the sorption reaction. However, they reveal the strong sorbent capability of GR-Cl solid in dilute to concentrated NaCl brines.

4.2.4 Trevorite (NiFe_2O_4)

Trevorite (Isostructural phase with magnetite, with Ni replacing for Fe(II) within the structure) has been established as the constituent of the oxide film layer formed on the Cr-Ni steel in saline brine environments at elevated temperature. Furthermore, in μXANES it has been confirmed as the phase on the outer layer of this oxide film. At last, thermodynamic calculations confirmed this phase as potentially long-term stable under conditions observed in corrosion experiments of Cr-Ni steel. Considering the possible breach scenario due to pitting corrosion, this phase will likely be the exposed phase, which could retain radionuclides. Trevorite is commercially available and has been purchased.

The purchased mineral has been characterized by SEM, shown in **Figure 77**, finding very fine agglomerated particles. BET analysis yields a large specific surface area of $82.39 \text{ m}^2/\text{g}$.

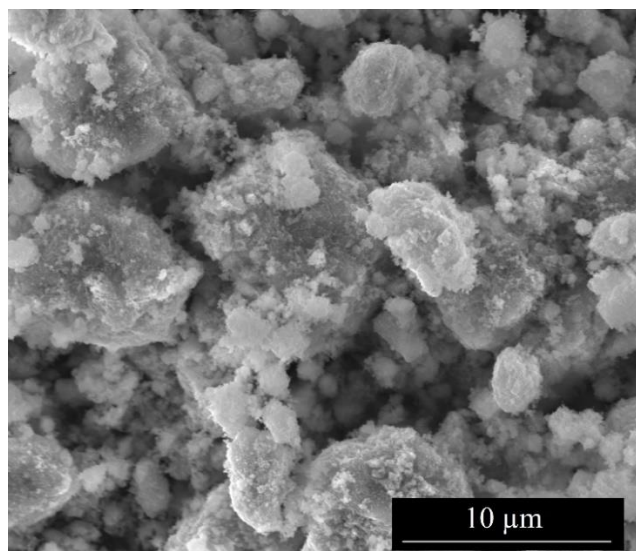


Figure 77: SEM image of the purchased trevorite compound.

XPS analysis of the purchased compound has shown the presence of Fe(III) (**Figure 78**) and Ni(II) along with small Na and Cl impurities. The extent of impurities was evaluated by EDX analysis shown in **Table 30**. Here the Ni/Fe/O ratios are matching well the stoichiometric composition of trevorite. In addition small impurities of Na, and negligible amounts of Cl and Al were found.

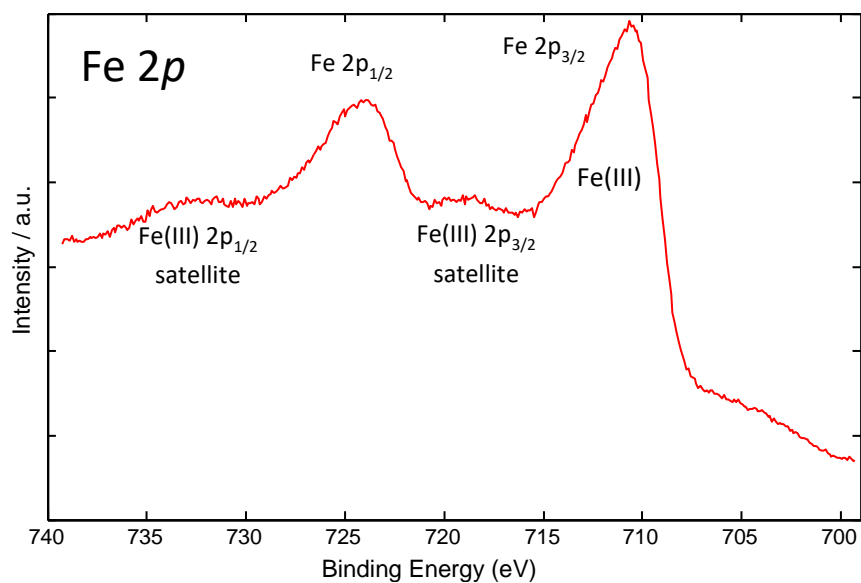


Figure 78: XPS narrow Fe 2p spectrum of the purchased trevorite compound.

Table 30: The chemical composition of the purchased trevorite compound.

Element	O	Na	Al	Cl	Fe	Ni
Atomic %	54.7±1.5	0.8±0.5	0.3±0.2	0.2±0.1	29.6±0.8	14.5±0.9

At last, the X-ray diffractogram (**Figure 79**) showed peaks matching those for trevorite in the database. The structure of trevorite is very similar to that of magnetite. Furthermore, the small peak at $2\theta = 33.2^\circ$ belongs to iron oxide (hematite).

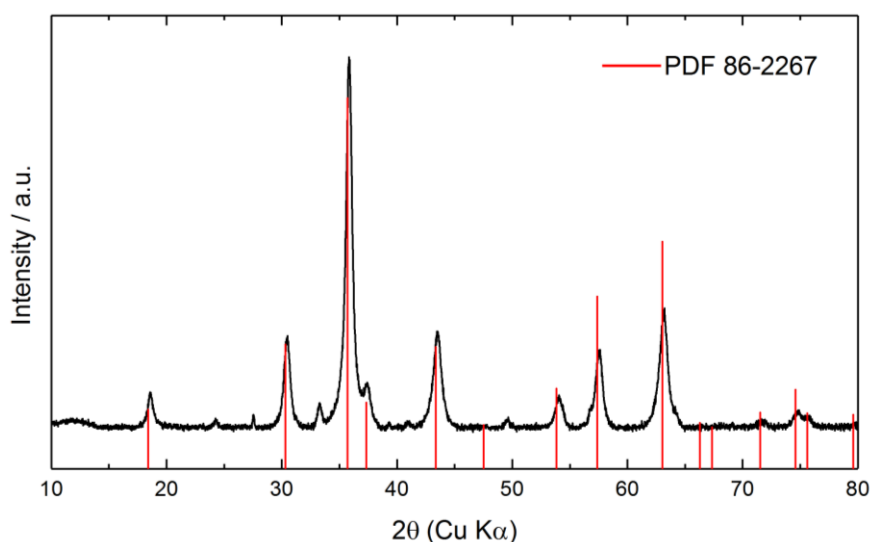


Figure 79: X-ray diffractogram of the purchased trevorite compound. PDF card 86-2267 refers to nickel iron oxide in the database.

The trevorite phase is stable under similar pH_M conditions as magnetite but has a wider stability range in the oxidizing E_h region, as Fe(III) and Ni(II) cannot oxidize further. The same pH_M range as for magnetite was selected for sorption studies to compare the two compounds and establish the effect of Ni on sorption.

4.2.4.1 Solid phase titration in dilute to concentrated NaCl solutions

No detailed structural information (morphology, exposed plane, charge distribution) was available for trevorite (compared to magnetite), and therefore a generic site for sorption was assumed to interpret titration data and to develop a sorption model. The generic site usually reflects the reactivity of singly coordinated site. The selected site density of 10 sites/ nm^2 is usually used in models with one generic site, as it is sufficiently high.

Trevorite was titrated as described in **section 2.5.1**. Modelling was performed as in case of magnetite using a modified version of FITEQL 2 with activity coefficients obtained using the models and databases described in **section 1.3.5.2**. **Figure 80** shows the experimental titration data for two ionic strengths, 0.1 M and 1 M NaCl in the pH_M range of 7.0-9.2 and the associated modelled charges. The error bars for the surface charge are within the points. The point of zero charge is shown at 8.3, matching the literature [Barale et al., 2008; Martin Cabañas et al., 2011]. The best fit model parameters

are summarized in **Table 31**, showing the two capacitance values and ion binding constants for cation (Na^+) and anion (Cl^-) to the singly coordinated generic sites. The linear shape of the titration curve in **Figure 80** is due to a one-step protonation process. The capacitance values are comparable to those for magnetite. The ion pair formation constants are similar, with a slightly weaker binding affinity for cations.

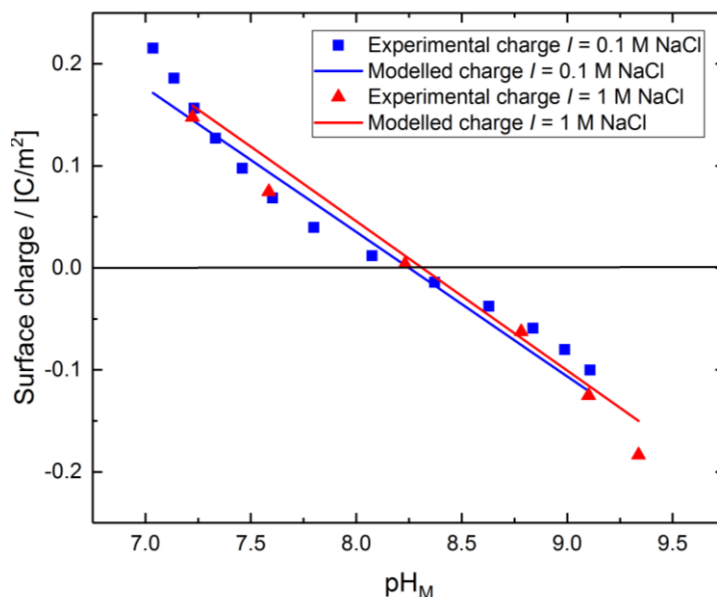


Figure 80: The experimental and modelled pH_M dependent charging behaviour of trevorite at two ionic strengths set by NaCl. The lines correspond to the calculated charges using the values summarized in **Table 31**.

Table 31. The CD-MUSIC model parameters for trevorite proton surface charge curves.		
Capacitance 1	3.07	F/m^2
Capacitance 2	2.34	F/m^2
Overall Stern capacitance	1.33	F/m^2
Constant for Cl^- binding, log Ka	0.63	-
Constant for Na^+ binding, log Kc	0.5	-

4.2.4.2 Europium uptake as a function of pH in dilute to concentrated NaCl solutions

The uptake of europium by trevorite was investigated following the same procedure as used for magnetite studies, to allow direct comparison of data, and, thus, to identify a potential nickel effect on sorption. Ionic strength levels in solution and the solid surface to solution volume were similar ($6.5 \text{ m}^2/\text{L}$). For $[\text{Eu}] = 5.1 \times 10^{-10} \text{ M}$, the uptake is high with values above the detection limit ($>99 \%$) for $\text{pH}_M \geq 6.2$ for all ionic strength levels (**Figure 81 A**). The corresponding $\log K_D$ values range from 4.7 ± 0.3 ($81 \pm 3 \%$ sorption) to above 6.1 corresponding to the analytical detection limit (**Figure 81 B**). An ionic strength effect on sorption can be observed at pH_M below 6.2, where uptake decreases notably at the highest investigated ionic strength of 4.8 M.

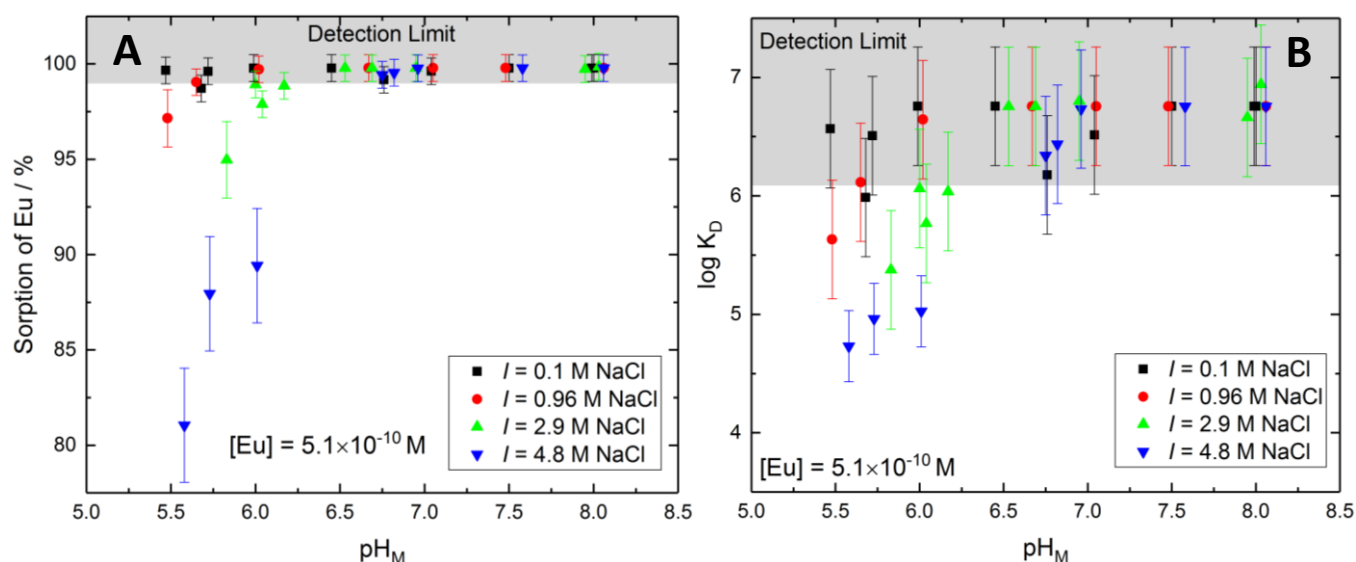


Figure 81: Sorption of europium $[\text{Eu}] = 5.1 \times 10^{-10} \text{ M}$ as percentage uptake (A) and as logarithm of distribution ratio ($\log K_D$) (B) on trevorite (0.08 g/L) as a function of pH_M and at different ionic strengths of NaCl.

For $\text{Eu} = 1 \times 10^{-5} \text{ M}$, the uptake showed a pH_M dependent behaviour, with low uptake of $30 \pm 4 \%$ at pH_M 5.4 for $I = 0.1 \text{ M}$, and $18 \pm 4 \%$ at pH_M 5.8 for $I = 4.8 \text{ M}$ (**Figure 82 A**). At these low pH_M values, a small ionic strength effect is observed. This effect decreases with uptake and no significant effect is observed at $\text{pH}_M > 7.0$. The uptake reaches above 90 % at pH_M 8.2 for all I levels. The $\log K_D$ values range from 3.4 ± 0.1 for $18 \pm 4 \%$ to 6.1 at 99 % uptake, with a $\log K_D$ of 5.0 ± 0.2 at 90 % uptake (**Figure 82 B**).

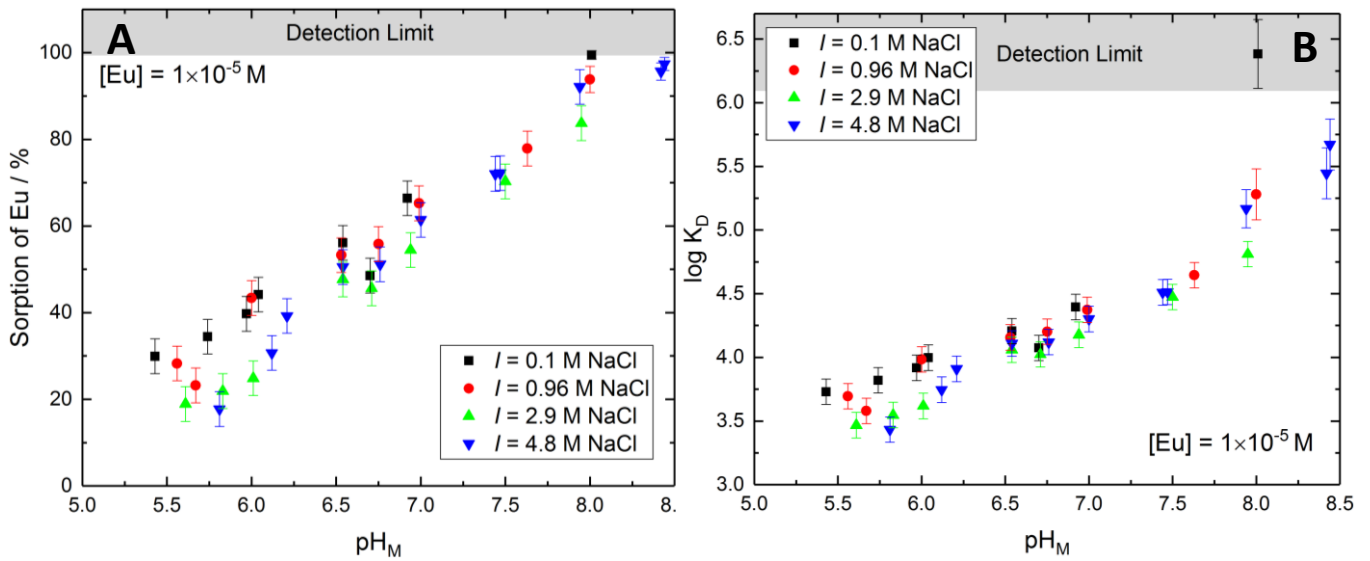


Figure 82: Sorption of europium $[Eu] = 1 \times 10^{-5} \text{ M}$ as percentage uptake (A) and as logarithm of distribution ratio ($\log K_D$) (B) on trevorite (0.08 g/L) as a function of pH_M and at different ionic strengths of NaCl.

The analyses of dissolved metals showed negligible dissolution of the trevorite (**Figure 83 A** and **Figure 83 B**), with a slightly decreasing trend with increasing pH_M for nickel and no evolution pattern in case of iron. Overall, nickel concentrations seems to be somewhat higher, pointing to an incongruent dissolution behaviour. These dissolved amounts will not affect the sorption process considering the loss of solid, however the values of dissolved iron and nickel are in the mM range where they could compete with the Eu(III) sorption.

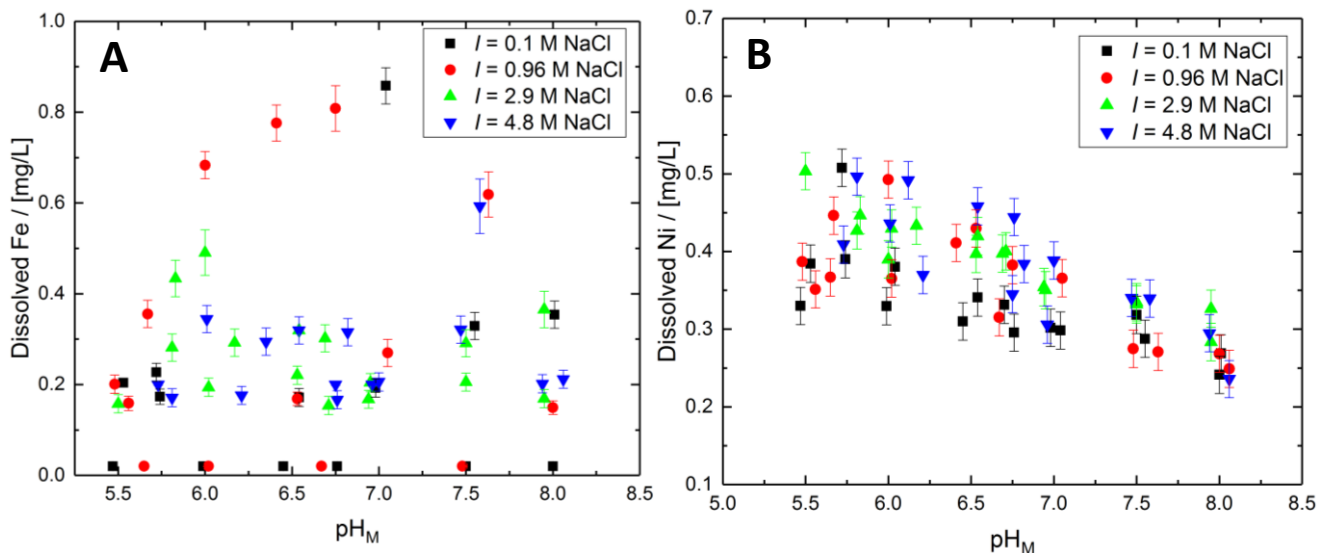


Figure 83: Dissolved iron and nickel concentrations in aqueous solutions in contact with trevorite vs. pH_M at different ionic strengths of NaCl.

The behaviour for the Eu(III) uptake by trevorite is somewhat similar to that for magnetite considering both Eu concentrations, highlighting the negligible effect of nickel in the trevorite structure and

suggesting similar surface reactivity of the two compounds. It can however be noticed that for trevorite the uptake is weaker than for magnetite for both studied Eu concentrations, which is attributed to the different point of zero charge (6.4 for magnetite and 8.3 for trevorite), with solids with lower point of zero charge exhibiting stronger sorption behaviour of cations due to electrostatics.

4.2.4.3 Surface complexation model

The developed surface complexation model is very similar to the one derived for europium/americium sorption to magnetite. Optimization of parameters was challenging for this solid phase as the lack of information on the correct charge distribution and site densities did not allow for obtaining a good fit of the model to experimental data. It is assumed that the binding mode for trevorite sorbed europium is tridentate like at the magnetite surface. This, however, was not experimentally confirmed. **Figure 84** shows the fitting results for sorption data at $[Eu] = 1 \times 10^{-5}$ M only. The model was not able to reproduce the measured sorption data at both investigated europium concentrations.

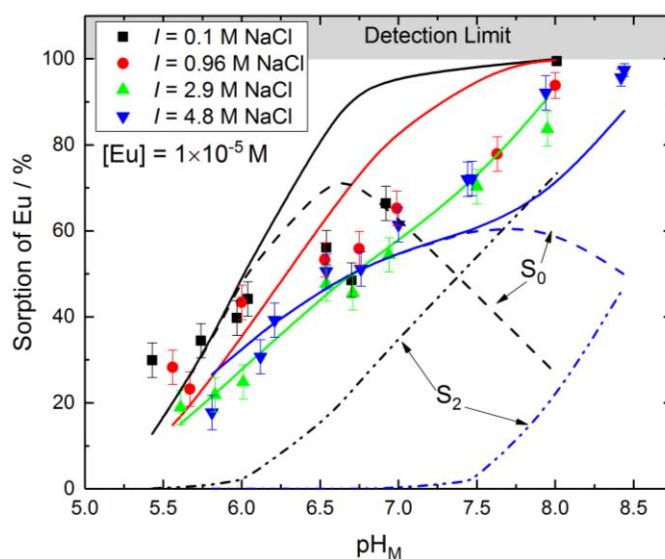
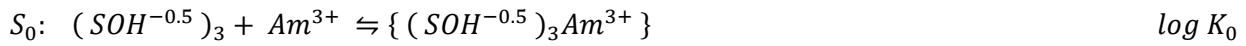


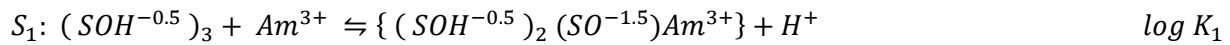
Figure 84: Sorption of $[Eu] = 1 \times 10^{-5}$ M onto trevorite vs. pH_M . Experimental uptake (points) modelled (full lines) using surface complexation model in FITEQL with the Pitzer approach and [TPA] database for various ionic strengths (NaCl). The dashed lines represent the complex distribution for the two complexes for $I = 0.1$ M (black) and $I = 4.8$ M (blue), respectively. S_x represents the surface complexation reaction described in the text. The contribution of S_1 is too low to be visible in the figure.

The model is overestimating the uptake at low ionic strength and slightly underestimating the uptake for high ionic strength conditions compared to the experimental data. More structural and electrostatic information on the trevorite phase would be needed to improve the model. Surface complexation

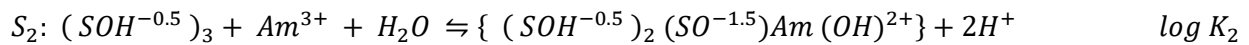
reactions and respective fitted complexation constants at infinite dilution are shown below and summarized in **Table 32**. The obtained complexation constants are significantly different from those obtained for magnetite, despite similarities in uptake data. This can be attributed to use of different models, lower uptake for trevorite and potential nickel and iron sorption onto trevorite, which competes with Eu(III) but is not included in the model, as its extent is not known. This factor could also contribute to the poor fit of the model.



Transfer of charge: $\Delta z_0 = 2.5$, $\Delta z_\beta = 1.0$.



Transfer of charge: $\Delta z_0 = 1.5$, $\Delta z_\beta = 1.0$.



Transfer of charge: $\Delta z_0 = 1.5$, $\Delta z_\beta = 0.0$.

Table 32: The complexation constants at infinite dilution.

$\log K_0$	10.0 ± 0.1
$\log K_1$	-2.2 ± 0.1
$\log K_2$	-6.6 ± 0.1

Figure 84 also shows the distribution of the different surface complexes as a function of pH_M . The dashed black lines correspond to surface complex distributions for $I = 0.1$ M, while the dashed blue lines correspond to surface complex distributions for $I = 4.8$ M. For $I = 0.1$ M, S_0 prevails up to pH_M 7.4, above which the hydrolysed S_2 is dominant. S_1 does not contribute in significant fractions within the whole studied pH_M range (close to 0), which is reflected in the low value of $\log K_1$. Increasing the ionic strength to 4.8 M, S_0 becomes dominant within the whole investigated pH_M range up to pH_M 8.4. A slight competition of europium and electrolyte ions for the surface sites may explain as for the case of magnetite the observed small ionic strength effect. Based on the experimental data, trevorite as the passive film constituent seems also to be a good candidate for strong radionuclide retention in a nuclear waste repository near-field in salt rock. To our knowledge, no other uptake data of trivalent pollutants onto trevorite have been reported so far. The proposed sorption model, however, has to be considered preliminary. A further development of the model requires the characterization of the trevorite surface structure in more detail.

4.2.5 Chromium oxide (Cr_2O_3)

The last phase investigated for its capability to sorb trivalent radionuclides is the chromium oxide. This phase is present as a passive film constituent in all stainless steel samples and we have confirmed its presence by μXANES and multiple other techniques. Although Ni and Fe dissolution from the steel at several spots aid in the formation of a passive layer where these elements are included, due to heterogeneity of this film, a large area of the canister may still be covered by a Cr_2O_3 passive film even if pitting corrosion causes a canister breach. Thus, its retention ability and the ionic strength effect on sorption are of interest. Chromium oxide powder has been commercially purchased and characterized in house. The SEM image of the compound (*Figure 85*) showed the presence of large crystals without specific morphology. The BET specific surface area of chromium oxide was at $1.15 \text{ m}^2/\text{g}$. EDX analysis further indicated a Cr/O ratio of 2/3 and the absence of additional elements.

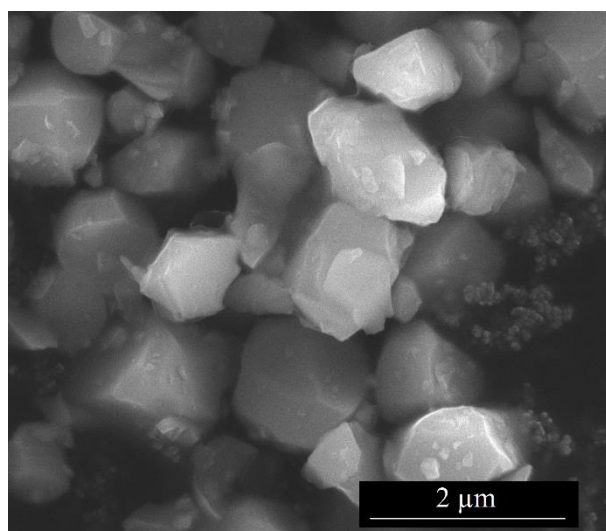


Figure 85: SEM image of the purchased chromium oxide.

At last, XRD analysis (*Figure 86*) showed peaks matching with the expected XRD pattern for crystalline Cr_2O_3 and confirmed the absence of additional crystalline phases. The chromium oxide compound is stable under a wide range of conditions and only soluble under very acidic conditions [Lide, 2004], thus a wide pH_M range of 3-9 was selected for sorption experiments.

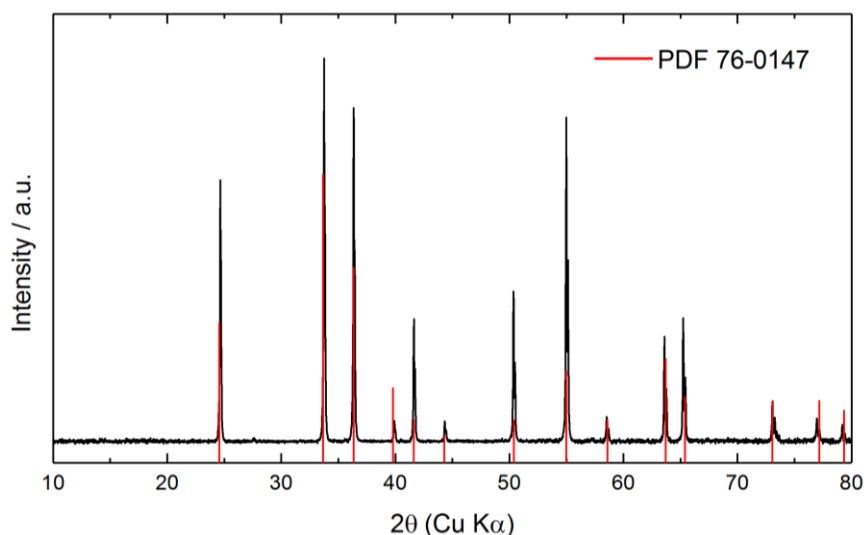


Figure 86: X-ray diffractogram of the purchased chromium oxide compound. PDF card 76-0147 refers to chromium oxide in the database.

4.2.5.1 Solid phase titration in dilute to concentrated NaCl solutions

Similarly to trevorite, also for chromium oxide no detailed structural information could be obtained and therefore the same model with a generic site with density of 10 sites/nm² was used to fit the titration experimental data and model uptake data. **Figure 87** shows the experimental titration data for two ionic strengths, 0.1 M and 1 M NaCl in the pH_M range of 5.2-8.7 and the associated modelled charges. The error bars for the surface charge are within the points. The point of zero charge is shown at 7.9, taken from the literature [Blesa et al., 2000; Wiśniewska & Szewczuk-Karpisz, 2013]. The best fit model parameters are summarized in **Table 33**, showing the two capacitance values and ion binding constants for Na⁺ and Cl⁻ to the singly coordinated generic sites. The inner layer capacitance (C1) has a higher value compared to magnetite and trevorite, while the low value of the outer layer capacitance (C2) causes a very low overall Stern capacitance for the chrome oxide. The binding constants for Na⁺ and Cl⁻ are similar.

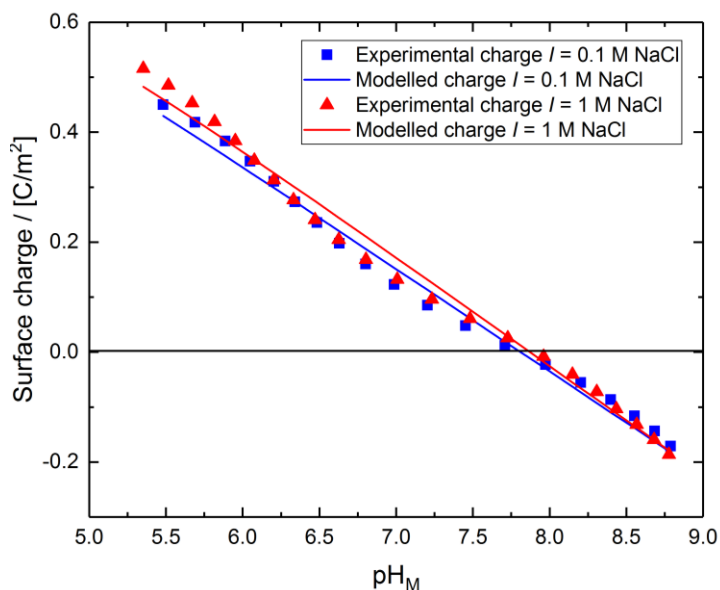


Figure 87: The experimental and modelled pH_M dependent charging behaviour of chromium oxide at two ionic strengths set by NaCl. The lines correspond to the calculated charges using the values summarized in *Table 33*.

Table 33. The CD-MUSIC model parameters for chromium oxide proton surface charge curves.

Capacitance 1	4.49	F/m^2
Capacitance 2	0.11	F/m^2
Overall Stern capacitance	0.11	F/m^2
Constant for Cl^- binding, $\log K_a$	0.57	-
Constant for Na^+ binding, $\log K_c$	0.53	-

4.2.5.2 Uptake as a function of pH in dilute to concentrated NaCl solutions

Two sets of sorption experiments with different solid to liquid ratios were performed. One set was done using 1 g/L of solid, and the other had 5.7 g/L, giving an exposed surface area to solution volume ratio of $6.5 \text{ m}^2/\text{L}$, directly comparable to the experiments with magnetite and trevorite.

For the lower solid content (1 g/L) and $[\text{Eu}] = 5.1 \times 10^{-10} \text{ M}$, the uptake showed a typical pH_M dependent sorption reaching $\geq 98\%$ sorption at $\text{pH} \geq 7.0$ for all ionic strength levels (*Figure 88 A*). The corresponding K_D values range from 2.3 ± 0.2 to 5.0 where the europium concentration in solution lies below the detection limit (*Figure 88 B*). No significant ionic strength effect is observable.

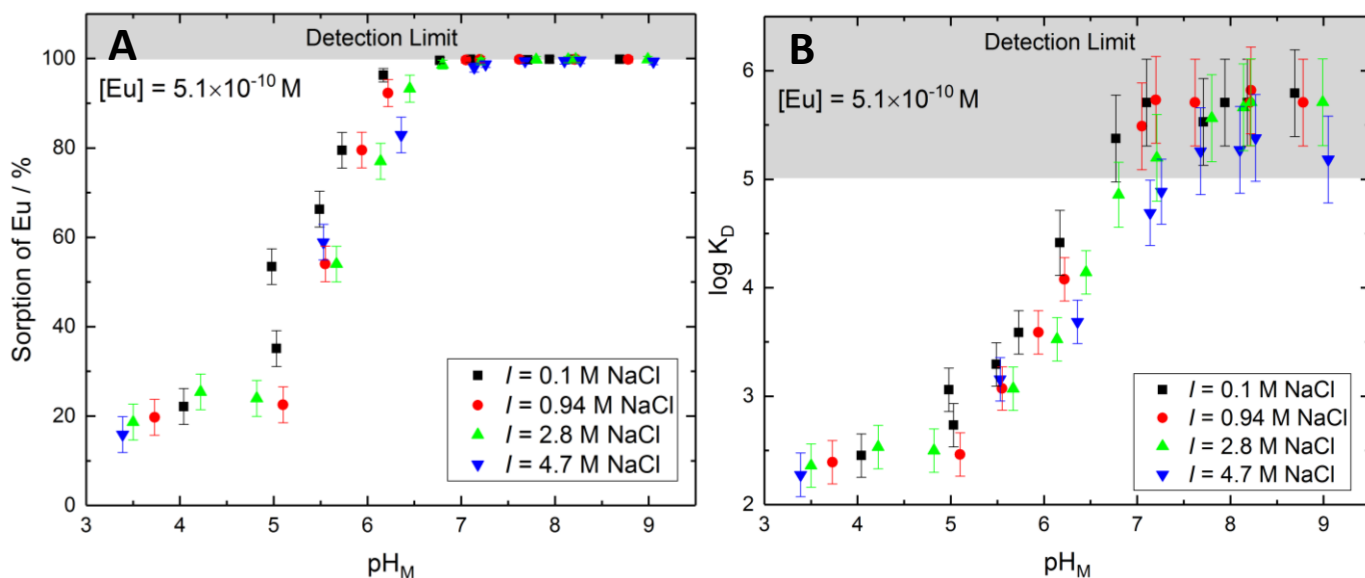


Figure 88: Sorption of europium $[Eu] = 5.1 \times 10^{-10} \text{ M}$ as percentage uptake (A) and as logarithm of distribution ratio ($\log K_D$) (B) on chromium oxide (1 g/L) as a function of pH_M and at different ionic strengths of NaCl.

Similar pH_M dependent behaviour is observed for $[Eu] = 1 \times 10^{-5} \text{ M}$, however in this case, the uptake only reaches $73 \pm 4 \%$ at $pH_M 8.4$, while for $pH_M < 4.0$ the uptake is below $\sim 10 \%$ (Figure 89 A). No significant ionic strength effect is observable. The $\log K_D$ values range from 1.9 ± 0.1 to 3.4 ± 0.1 at $73 \pm 4 \%$ uptake (Figure 89 B).

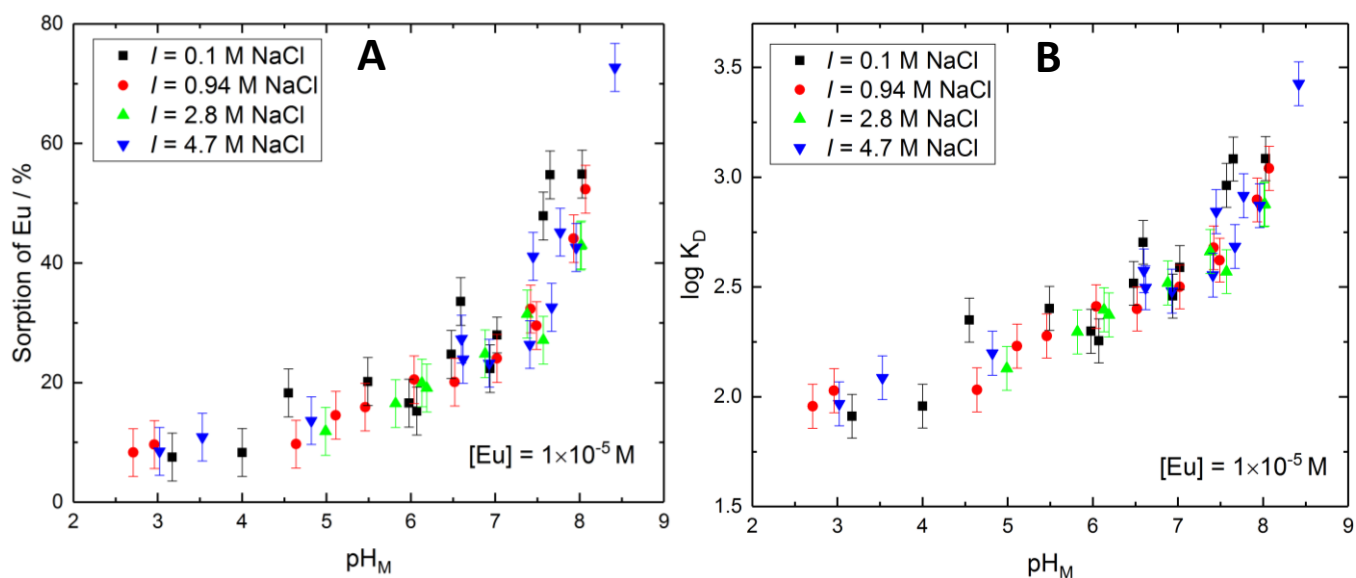


Figure 89: Sorption of europium $[Eu] = 1 \times 10^{-5} \text{ M}$ as percentage uptake (A) and as logarithm of distribution ratio ($\log K_D$) (B) on chromium oxide (1 g/L) as a function of pH_M and at different ionic strengths of NaCl.

The **Figure 90** shows the dissolved chromium amount from the compound as a function of pH_M . The amounts in the examined pH_M range are, as expected due to the low solubility of the compound, negligible.

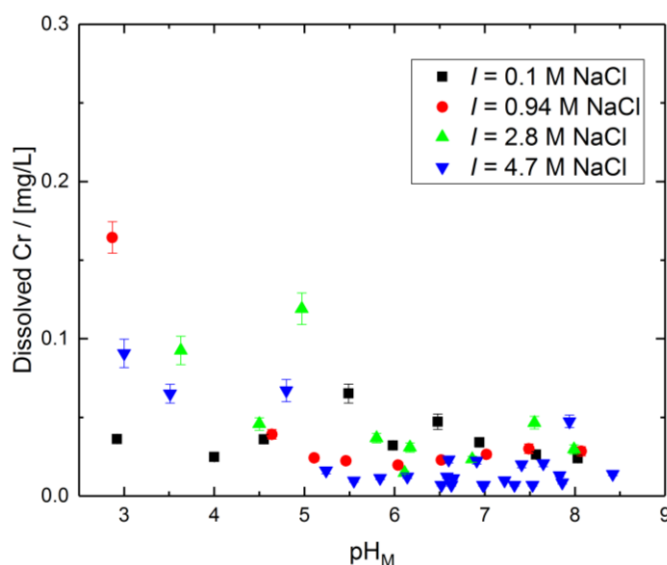


Figure 90: Dissolved chromium concentration in aqueous solutions in contact with chromium oxide vs. pH_M at different ionic strengths of NaCl.

The set of experiments with higher solid content performed at two ionic strength levels, show a behaviour comparable to that found for trevorite and magnetite. **Figure 91 A** shows the uptake in a similar pH_M range as studied for the other two compounds, for $[\text{Eu}] = 5.1 \times 10^{-10}$ M. For $\text{pH}_M > 6.3$, the data points are in the area corresponding to the analytical detection limit for both ionic strength levels. A small ionic strength effect is visible. The $\log K_D$ value corresponding to the detection limit of 99 % uptake is 4.2 (**Figure 91 B**).

Also at $[\text{Eu}] = 1 \times 10^{-5}$ M a pH_M dependant sorption is observed for both ionic strength levels (**Figure 92 A**). A small ionic strength effect (approximately 15 % decrease in sorption) is observed between the two examined ionic strength levels below $\text{pH}_M 7.0$. The $\log K_D$ values range from 1.4 ± 0.2 to 3.8 ± 0.3 (**Figure 92 B**).

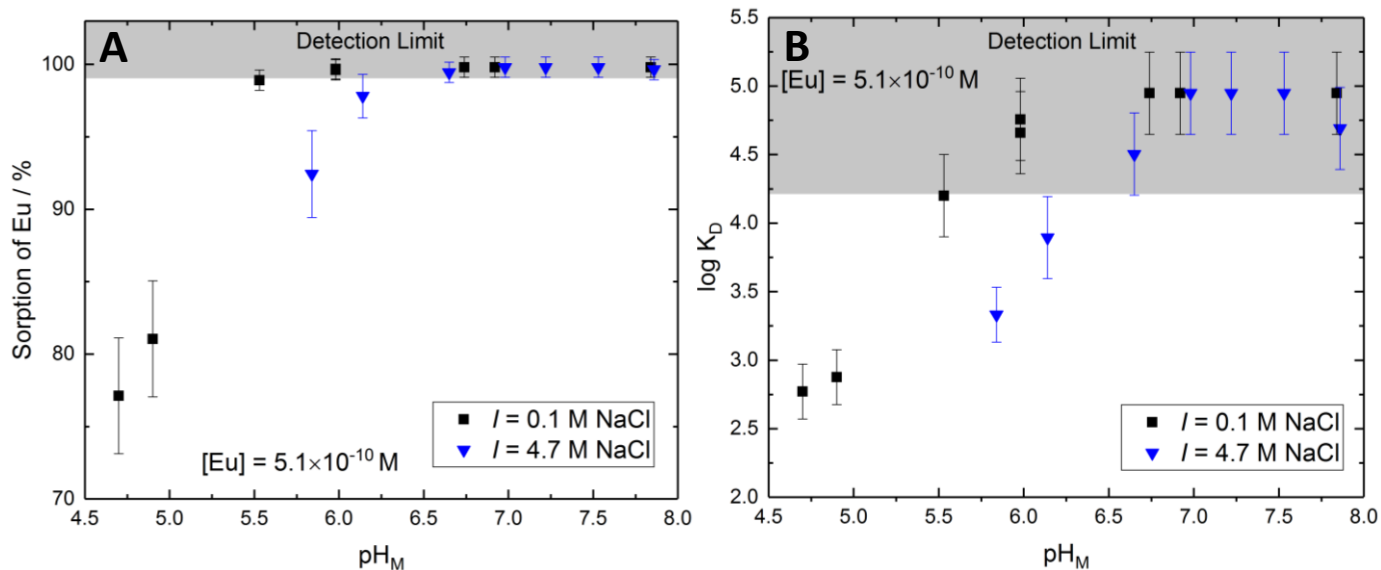


Figure 91: Sorption of europium $[Eu] = 5.1 \times 10^{-10} M$ as percentage uptake (A) and as logarithm of distribution ratio ($\log K_D$) (B) on chromium oxide (5.7 g/L) as a function of pH_M and at different ionic strengths of NaCl.

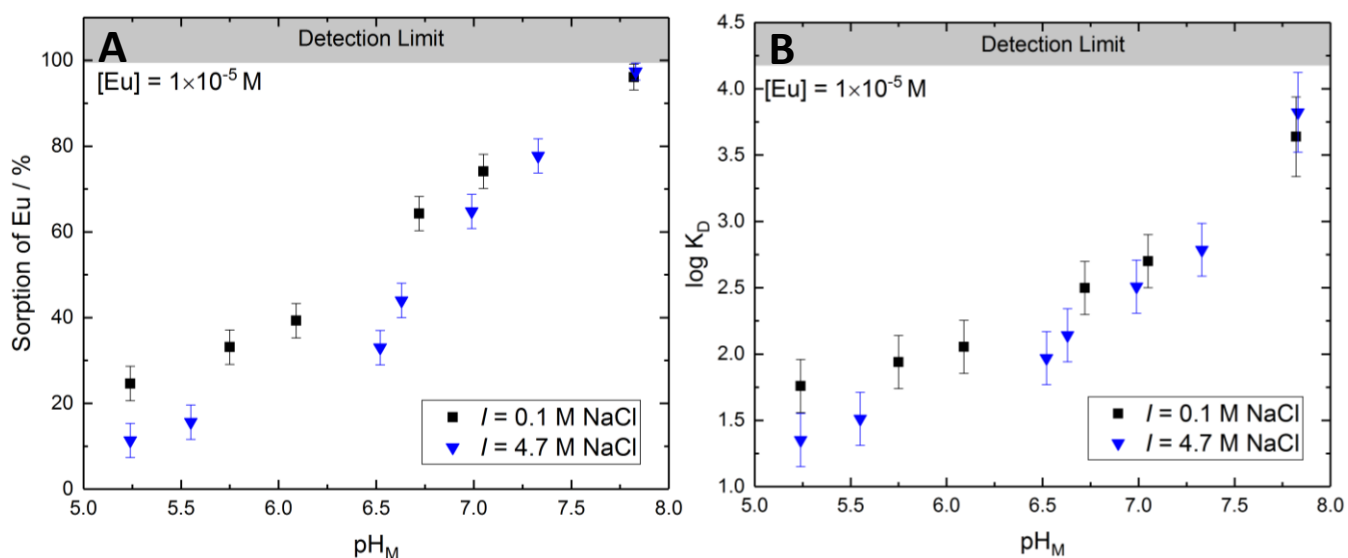


Figure 92: Sorption of europium $[Eu] = 1 \times 10^{-5} M$ as percentage uptake (A) and as logarithm of distribution ratio ($\log K_D$) (B) on chromium oxide (5.7 g/L) as a function of pH_M and at different ionic strengths of NaCl.

4.2.5.3 Surface complexation model

The same model as in the case of trevorite was used to obtain the complexation constants for europium sorption onto chromium oxide. Due to lack of structural information for this compound, it was not possible for the model to fit the uptake data for the two europium concentrations simultaneously. The proposed model as such can, thus, only be very preliminary. As the lower europium concentration of 5.1×10^{-10} M showed a pH_M dependent uptake up to complete retention at high pH_M , this set of data was chosen for a first model version. Due to the lack of experimental data in the low pH_M range, the data set for $I = 4.7$ M had been removed to allow model convergence. Furthermore, tridentate binding mode of europium was assumed for this model as well. **Figure 93** shows the fitting results for the $[\text{Eu}] = 5.1 \times 10^{-10}$ M with the model inherent surface complexes shown below and the complexation constants at infinite dilution summarized in **Table 34**. The model produced a satisfactory fit to the experimental data and managed to reproduce the ionic strength effect. Underestimation of the uptake is observed below pH_M 4.5. More structural and electrostatic information on the solid phase would allow further improvement of the model.

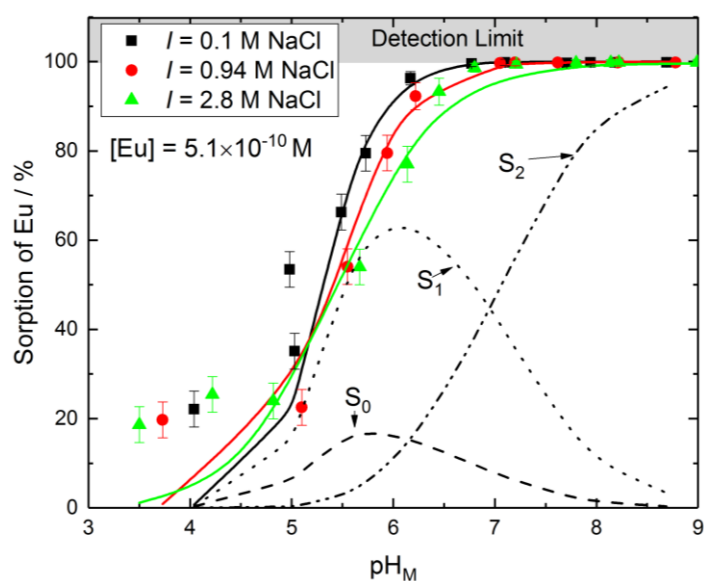
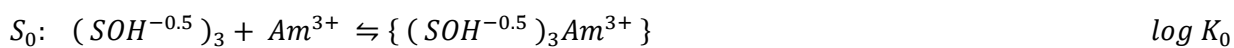
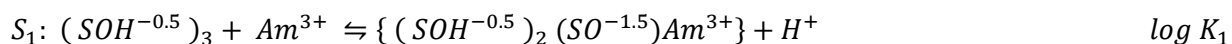


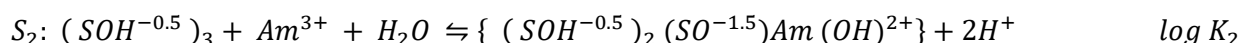
Figure 93: Sorption of $[\text{Eu}] = 5.1 \times 10^{-10}$ M onto chromium oxide vs. pH_M . Experimental uptake (points) modelled (full lines) using surface complexation model in FITEQL with the Pitzer approach and [TPA] database for various ionic strengths (NaCl). The dashed lines represent the complex distribution for the three complexes for $I = 0.1$ M. S_x represents the surface complexation reaction described in the text.



Transfer of charge: $\Delta z_0 = 2.0$, $\Delta z_\beta = 1.5$.



Transfer of charge: $\Delta z_0 = 1.0$, $\Delta z_\beta = 1.5$.



Transfer of charge: $\Delta z_0 = 1.0$, $\Delta z_\beta = 0.5$.

Table 34: The complexation constants at infinite dilution.

$\log K_0$	9.6 ± 0.1
$\log K_1$	2.5 ± 0.1
$\log K_2$	-5.2 ± 0.1

As the data for the ionic strength of 4.7 M was not modelled, **Figure 93** shows the distribution of the different surface complexes as a function of pH_M only for $I = 0.1$ M. The S_0 is present in low contribution within the whole studied pH_M range, while S_1 prevails up to pH_M 7.0, above which the hydrolysed S_2 is dominant. Further experimental and structural data are needed to accurately describe the retention mechanism. However, based on our obtained data, the chromium oxide has similar reactivity towards europium as magnetite and trevorite, making the passive oxide film on the canister surface a good sink for the radionuclides considering a salt rock repository. Furthermore, to our knowledge, no other uptake data of trivalent pollutants onto chromium oxide have been reported.

Conclusions and Outlook

This PhD thesis addresses the corrosion behaviour of steels used for construction of spent fuel containers and vitrified waste containers, and the subsequent uptake behaviour of some of the identified corrosion phases with respect to trivalent radionuclides in brine solutions. These processes have been systematically evaluated in dilute to concentrated NaCl and MgCl₂ brines. A special attention is given to saline systems due to lack of studies concerning uptake behaviour and in order to gain better insight into formation of corrosion products from steel corrosion under saline conditions relevant for scenarios to be considered for a repository for radioactive waste in rock salt

The corrosion of spheroidal graphite iron, SGI (GGG40.3), foreseen as a material for the POLLUX container for heat generating high-level radioactive waste in Germany, and Cr-Ni steel (309S), used as material to construct coquilles for vitrified waste, was systematically investigated in dilute (0.1 M NaCl, 0.033 M MgCl₂) to concentrated (5 M NaCl, 3.4 M MgCl₂) brines at room and elevated temperature (90 °C) under anoxic conditions in airtight autoclaves for exposure times in the range of 13 to 49 weeks. The corrosion evolution with time was followed in the case of 5 M NaCl at 90 °C and 3.4 M MgCl₂ at 90 °C, and concentrated solutions containing accessory components (e.g. K⁺, Ca²⁺, SO₄²⁻) representing realistic brine compositions (solution 1 and solution 3) at room temperature. The corrosion in dilute systems at 90 °C, concentrated NaCl and MgCl₂ systems at room temperature and the concentrated NaCl and MgCl₂ dominated solutions 3 and 1 at 90 °C were evaluated only after specific exposure time, no evolution with time was followed for these systems. The steel specimen surface area to brine volume ratio was 1:5 for all systems. Measured pH_M and E_h values along with the quantified amounts of the dissolved metals in the aqueous phase were used to calculate predominance fields for solution species and solid phases. The experimental solid phase characterization using various analytical techniques showed a strong influence of the composition of the contacting brine on the nature of the formed corrosion phases for the SGI and the Cr-Ni steel. At last, corrosion rates were determined for all systems, an important parameter for the estimation of the container integrity time frame.

The results for SGI show that the pH_M is an important driver for iron corrosion, with lower pH_M values resulting in higher corrosion rates. The pH_M variation in different systems can be attributed to the brine/steel impurities, water reduction associated to iron oxidation, precipitated solids buffering the systems and water dissociation constant dependence on temperature.

An initial formation of the (mixed Fe(II), Fe(III)) silicate phase cronstedtite due to silica dissolution from the steel was observed after 13 weeks in 5 M NaCl at 90 °C system, while upon longer exposure, the precipitated compounds (cronstedtite and magnetite) seem to decrease the steel dissolution rate. After 42 weeks, given geochemical conditions favour the predominant formation of magnetite as this phase has been identified in significant amounts. Cronstedtite was also present, but a significantly smaller surface area was covered by this phase. Calculations show that the stability window of these two solids are overlapping (under the identical alkaline/reducing conditions), however another phase, minnesotaite (purely Fe(II) silicate phase) is the long-term stable phase when the silica activity (dissolved silica amount) is high. Although the thermodynamic calculations do not reflect the experimental findings, possibly due to locally different conditions or kinetic effects on solid phase formation, suggesting the long-term stability of hematite under experimental conditions, magnetite appears as the long-term thermodynamically stable phase under strongly reducing conditions, taking into account uncertainty concerning silica activity. The corrosion rate for this system was found to be decreasing with time, from $2.89 \pm 0.05 \mu\text{m/a}$ after 13 weeks to $1.22 \pm 0.05 \mu\text{m/a}$ after 42 weeks. The presence of cronstedtite and magnetite was identified also in the dilute systems (0.1 M NaCl and 0.033 M MgCl₂) exposed for 28 weeks, regardless of the nature of the brine. In agreement with experimental results, geochemical calculations result in magnetite as the long-term stable phase under those conditions. The corrosion rate for the two dilute systems was the same, $10.0 \pm 1.0 \mu\text{m/a}$ after 28 weeks. Results show that at an ionic strength of 0.1 M, the brine composition does not play a role and that at an ionic strength of 5 M NaCl, the nature of the formed phases is identical to dilute systems.

For the SGI corroded in 5 M NaCl at 90 °C, the characterization of the crosscut sample by μ -XAS at the synchrotron light source evidenced the presence of iron(II) hydroxychloride at the steel/corrosion product interface. This finding shows that despite magnetite being the dominant phase on the outer side of the corrosion layer and being the long-term stable phase considering the conditions in the aqueous phase, the interface conditions favour the formation of Cl⁻ bearing compounds. This finding also evidenced the formation of a double corrosion layer at the SGI surface in saline brines, a property described in literature for low alloyed steels in dilute brines.

In the 5 M NaCl brine corroded for 49 weeks at room temperature, a different phase was formed, green rust chloride, which was established as the likely precursor of magnetite. The aqueous conditions of pH_M 7.10 ± 0.05 and E_h of -160 ± 50 mV were favouring this phase. The corrosion rate for the 5 M NaCl room temperature system was found to be $1.11 \pm 0.05 \mu\text{m/a}$ given the exposure of 49 weeks.

For the SGI corroded in NaCl rich solution 3 at 90 °C, results show the presence of cronstedtite only after 26 weeks at pH_M 5.2 ± 0.3 and E_h of -200 ± 50 mV, but in low coverage. The corrosion rate for this system was higher than in pure NaCl solution at 9.6 ± 1.0 $\mu\text{m/a}$, which likely is due to the low pH_M establishing in this solution (5.2 ± 0.3 in solution 3 as compared to 8.5 ± 0.3 in 5 M NaCl solution). It is not clear whether the formed cronstedtite will remain as part of the internal corrosion layer, as was the case of iron hydroxychloride in the 5 M NaCl brine or whether it will transform into magnetite (upon pH_M increase) or pyrite, possible long-term stable phases under very reducing conditions. The same system run at room temperature showed mainly iron dissolution, pH_M increase from 6.70 ± 0.05 to 9.0 ± 0.05 after 26 weeks, and a precipitation of $\text{Fe}(\text{OH})_2$ in very low amounts, likely a precursor of one of the more stable compounds: magnetite or cronstedtite. The corrosion rate was obtained as 0.79 ± 0.05 $\mu\text{m/a}$ after 26 weeks.

The corrosion in MgCl_2 brines is in general faster than in NaCl solutions. For SGI corroding in 3.4 M MgCl_2 brine, the iron(II) hydroxychloride appears as the single dominant formed secondary phase at room and elevated (90 °C) temperature after 49 and after 13 to 42 weeks, respectively. In these experiments, pH_M values of 8.60 ± 0.05 at room and 6.6 ± 0.3 at elevated temperature were obtained, with E_h of -300 ± 50 mV for room and -210 ± 50 mV for elevated temperature. The corrosion rate for the system at 90 °C is initially relatively high due to the low pH_M establishing in this experiment and decreased from 38.1 ± 2.0 $\mu\text{m/a}$ after 13 weeks to 16.9 ± 1.5 $\mu\text{m/a}$ after 42 weeks, due to formation of the iron(II) hydroxychloride layer. The corrosion rate of the same system run at room temperature was obtained as 1.22 ± 0.05 $\mu\text{m/a}$ after 49 weeks, comparable to the 5 M NaCl room temperature system. Under given experimental conditions, no solid phase has been found stable in the thermodynamic model. Iron(II) hydroxychloride was however found thermodynamically stable under reducing, acidic-neutral conditions, similar to the experimental conditions, given higher aqueous iron concentration, suggesting its stability and its relevance under very high ionic strength conditions, provided sufficient iron oxidation.

The formation of this phase appears to be initiated with FeO at the bulk steel, transforming into mixed $(\text{Mg,Fe})(\text{OH})_2$, which in the presence of FeCl_2 in the aqueous phase leads to the Mg doped iron(II) hydroxychloride formation. The presence of FeO at the bulk steel surface has been identified by the μ -XAS at the synchrotron for the 3.4 M MgCl_2 , 90 °C system. In all cases, Mg was found to substitute for iron in the $\text{Fe}_2(\text{OH})_3\text{Cl}$ structure accounting for about 20 %.

In the MgCl_2 rich solution 1 at 90 °C, the same phase is forming at pH_M of 6.7 ± 0.3 and E_h of -81 ± 50 mV, but additionally particles of green rust chloride were found, hinting at a slow anaerobic oxidation

of iron(II) hydroxychloride into green rust chloride under these pH_M / E_h conditions. The corrosion rate for this system was obtained as $26.3 \pm 1.5 \mu\text{m/a}$ considering an exposure time of 26 weeks, a similar rate as found in the pure MgCl_2 solution considering the same exposure.

At room temperature in solution 1, the corrosion rate was measured as $3.65 \pm 0.05 \mu\text{m/a}$ after 26 weeks, 3 times higher than the corrosion rate of the room temperature 3.4 M MgCl_2 system with sulfate after 49 weeks. As the corrosion rate decreases with time, this is likely the reason for the difference, as the pH_M values for both systems are similar. Lack of corrosion products was observed in this case. The MgCl_2 brines proved to represent a significantly more corrosive environment at elevated temperature, impact of the extremely high chloride concentration. For the MgCl_2 based brines, the long-term stable phase under conditions in this work, was identified as iron(II) hydroxychloride.

The corrosion of Cr-Ni steel was investigated in the same systems, but the available analytical techniques could not confirm with certainty the nature of the formed phases due to the thin precipitated films. In dilute to concentrated NaCl brine at 90 °C and in the 5 M NaCl system with presence of sulfate (solution 3) at 90 °C, the results hint at the presence of a very thin layer of trevorite (NiFe_2O_4) and/or chromite (FeCr_2O_4) along chromium oxide and hydroxide. In the concentrated (3.4 M) MgCl_2 brine at 90 °C, the analysis of samples for increased contact time up to 42 weeks showed the presence of a chromium oxide film only. In the concentrated MgCl_2 brine with sulfate (solution 1) run at 90 °C a pit initiation was observed, with Cr and Ni doped green rust chloride forming in the vicinity of the pit. This is in agreement with the findings reported in the literature, where for this steel type, 30 μm deep pit is reported in the laboratory studies after 2 years at 150 °C in brine identical to solution 1 [Kienzler, 2017_b].

All systems run at room temperature showed a lack of significant corrosion damage and only the presence of a chromium oxide film, present already prior to the experiments. A small pH_M increase is associated with dissolved nickel and iron from the steel in all systems. All final pH_M values were in the neutral region (5.6-7.7), while E_h values were in the range of $-80 \pm 50 \text{ mV}$ to $+210 \pm 50 \text{ mV}$, which cannot be anymore considered as reducing conditions. The corrosion rates are below $0.1 \mu\text{m/a}$ for all but two systems: in solution 3 at 90 °C the corrosion rate was at $0.49 \pm 0.05 \mu\text{m/a}$ and in solution 1 at 90 °C, where the pit initiation was observed, the corrosion rate was at $0.44 \pm 0.05 \mu\text{m/a}$, given the exposure time of 26 weeks. The thermodynamic model showed stability of chromite and trevorite along with Cr_2O_3 as the long-term stable phases for all NaCl systems, considering the experimental conditions in this work. The thermodynamic model was not obtained for MgCl_2 brine systems, where only Cr_2O_3 was experimentally confirmed. Upon pH_M increase in MgCl_2 systems, the conditions will

likely favour the same phases, trevorite and chromite. Overall, a combination of Cr_2O_3 and $\text{Cr}(\text{OH})_3$ was confirmed as part of the passive film by μ -XAS at the synchrotron. At elevated temperature, trevorite and chromite were found contributing to the passive film, with trevorite, likely part of the external passive film, confirmed experimentally in this work. Upon this passive film penetration, the local Cl^- accumulation at the metal/oxide interface favours the formation of green rust chloride. The long-term stable phases of interest for this steel type were identified as trevorite, chromite and chromium oxide.

The experiments in this work were performed using defined conditions in the laboratory, thus these systems are simplified as compared to those expected in the repository. The few aspects, which could influence the corrosion behaviour in the repository, are: gamma rays, roughness of the steel, presence of welding seams, different surface area to brine volume ratios, temperature treatment for Cr-Ni steel to simulate molten glass pouring and different contact brine composition such as e.g. carbonate presence in the solution. In addition, the waste components such as spent nuclear fuel or high-level waste glass in contact with container materials could have an impact. Further corrosion experiments involving these settings are required to verify or reject formation of identical compounds as found in this work. Furthermore, in-situ measurements of pH_M and E_h evolution in the autoclaves during the experiments, dedicated hydrogen production follow up and longer contact times could help provide more complete picture of the corrosion processes under saline conditions.

The uptake of europium by the relevant phases identified in the corrosion part was investigated in dilute to concentrated NaCl and MgCl₂ brines at room temperature under anoxic conditions considering different Eu concentrations (5.1×10^{-10} M, 1×10^{-7} M, 1×10^{-5} M). The titration of solids was performed for magnetite, trevorite and chromium oxide to obtain information about the behaviour of the solid phase in contact with the solution/brine. This information was further used in the modelling of the radionuclide uptake data.

The uptake data and the spectroscopic characterization of the sorbed species show a strong europium retention by magnetite with the formation of a tridentate surface complexes at pH_M of 8.0, with no significant ionic strength effect in dilute to concentrated NaCl brines independent of the Eu concentration (5.1×10^{-10} M and 1×10^{-5} M) considering a solid to liquid ratio of 0.5 g/L. Sorption data in dilute to concentrated MgCl_2 showed a small reduction in uptake due to Mg and Eu competition for the surface sites compared to NaCl brine with identical ionic strength. Strong reduction of europium uptake by iron(II) hydroxychloride is observed in MgCl_2 brines, notably at increased pH_M . Uptake

above 90 % was observed for $\text{pH}_M \geq 8.0$ in dilute to concentrated NaCl brines, with Eu concentration of 1×10^{-7} M and at a solid to liquid ratio of 1 g/L. For the identical Eu concentration and solid to liquid ratio, the uptake in dilute MgCl_2 brine was also above 90 % for $\text{pH}_M \geq 8.0$, but in concentrated (3.26 M) MgCl_2 brine, the uptake was only at 30 % for $\text{pH}_M = 8.0$. The reason for this sorption reduction is not clear. A possible conversion of the iron(II) hydroxychloride solid to mixed phases in MgCl_2 brines with different sorption properties along with Mg competition for surface sites can be speculated.

For trevorite and chromium oxide in dilute to concentrated NaCl brines, data showed comparable retention capability to magnetite when identical surface area were exposed, with a pH_M dependent uptake behaviour at Eu concentration of 1×10^{-5} M and a lack of significant ionic strength effect independent of Eu concentration. Finally, the Eu sorption by green rust chloride at a solid to liquid ratio of 1 g/L is quantitative in the investigated pH_M range (7.0-9.0) in dilute to concentrated NaCl brine with no ionic strength effect independent of the Eu concentration.

The magnetite sorption data were modelled using a charge distribution multi-site complexation model incorporating the tridentate binding mode and detailed structural information obtained from the literature coupled with parameters obtained from the titration of the solid. The complexation constants were obtained for three surface complexes. No chloride containing surface complexes could be found. In a similar manner, preliminary complexation constants were obtained for trevorite and chromium oxide using a simplified generic site model and information obtained from the solid titrations. Despite similar sorption behaviour for the three solid phases and presence of identical surface complexes, the obtained complexations constants ($\log K_D$ values) varied probably due to incomplete information on solid surface structures.

Further uptake experiments with chromite and potentially minnesotaite and chromium hydroxide are needed, as these phases have been confirmed as relevant corrosion layer/passive film constituents and the effect of ionic strength on the sorption needs to be evaluated. Additionally, more adequate model with in depth solid crystallographic information alongside spectroscopic information on the radionuclide interaction with the solid would allow obtaining more accurate complexation constants for trevorite and chromium oxide. At last, the investigation of the complex composition of the repository near-field environment including the presence of e.g. spent nuclear fuel and high-level waste glass being in contact with the container material could provide more accurate insight into the radionuclide behaviour within given repository scenarios.

References

- Ahmed, F., Elraies, A., Mohammed, A. and Gaafar, R. (2015). An Investigation Study on the Effect of Brine Composition on Silica Dissolution. *Advances in Environmental and Geological Science and Engineering*.
- Altmaier, M., Metz, V., Neck, V., Müller, R. and Fanghänel, T. (2003). Solid-liquid equilibria of $\text{Mg}(\text{OH})_2(\text{cr})$ and $\text{Mg}_2(\text{OH})_3\text{Cl}\cdot 4\text{H}_2\text{O}(\text{cr})$ in the system Mg-Na-H-OH-Cl- H_2O at 25°C. *Geochimica et Cosmochimica Acta*, 67(19), pp.3595-3601. [https://doi.org/10.1016/S0016-7037\(03\)00165-0](https://doi.org/10.1016/S0016-7037(03)00165-0)
- Altmaier, M., Neck, V., & Fanghänel, T. (2008). Solubility of Zr(IV), Th(IV) and Pu(IV) hydrous oxides in CaCl_2 solutions and the formation of ternary Ca-M(IV)-OH complexes. *Radiochimica Acta*, 96(9-11), pp. 541-550. DOI: [10.1524/ract.2008.1535](https://doi.org/10.1524/ract.2008.1535)
- Ams, D., Swanson, J., Szymanowski, J., Fein, J., Richmann, M. and Reed, D. (2013). The effect of high ionic strength on neptunium (V) adsorption to a halophilic bacterium. *Geochimica et Cosmochimica Acta*, 110, pp. 45-57. <http://dx.doi.org/10.1016/j.gca.2013.01.024>
- Anantatmula, R., & Fish, R. (1986). Corrosion Behavior of Container Materials in Grande Ronde Basalt Groundwater. *MRS Proceedings*, 84, 295. DOI: [10.1557/PROC-84-295](https://doi.org/10.1557/PROC-84-295)
- Appelo, C.A.J. (2015). Principles, caveats and improvements in databases for calculating hydrogeochemical reactions in saline waters from 0 to 200 °C and 1 to 1000 atm. *Applied Geochemistry*, 55, pp. 62-71. <https://doi.org/10.1016/j.apgeochem.2014.11.007>
- ASTM International. (2003). *G1-03 Standard Practice for Preparing, Cleaning, and Evaluating Corrosion Test Specimens*. West Conshohocken, PA; ASTM International, doi: <https://doi.org/10.1520/G0001-03>
- Bach, D., Christiansen, B., Schild, D. and Geckeis, H. (2014). TEM study of Green Rust Sodium Sulphate (GRNa_2SO_4) Interacted with Neptunyl Ions (NpO_2^+). *Radiochimica Acta*, 102(4), pp. 279-289. <https://doi.org/10.1515/ract-2013-2105>
- Banik, N., Marsac, R., Lützenkirchen, J., Marquardt, C., Dardenne, K., & Rothe, J., Bender, K. and Geckeis, H. (2017). Neptunium sorption and redox speciation at the illite surface under highly saline conditions. *Geochimica Et Cosmochimica Acta*, 215, pp. 421-431. DOI: [10.1016/j.gca.2017.08.008](https://doi.org/10.1016/j.gca.2017.08.008)

- Barale, M., Mansour, C., Carrette, F., Pavageau, E., Catalette, H., Lefèvre, G., Fedoroff, M. and Cote, G. (2008). Characterization of the surface charge of oxide particles of PWR primary water circuits from 5 to 320°C. *Journal of Nuclear Materials*, 381(3), pp. 302-308. <https://doi.org/10.1016/j.jnucmat.2008.09.003>
- Barry, P. (1994). JPCalc, a software package for calculating liquid junction potential corrections in patch-clamp, intracellular, epithelial and bilayer measurements and for correcting junction potential measurements. *Journal of Neuroscience Methods*, 51(1), pp. 107-116. [https://doi.org/10.1016/0165-0270\(94\)90031-0](https://doi.org/10.1016/0165-0270(94)90031-0)
- Bates, R. and Macaskill, J. (1978). Standard Potential of the Silver-Silver Chloride Electrode. *Pure and Applied Chemistry*, 50(11-12), pp.1701-1706. <https://doi.org/10.1351/pac197850111701>
- Bayol, E., Kayakırılmaz, K. and Erbil, M. (2007). The inhibitive effect of hexamethylenetetramine on the acid corrosion of steel. *Materials Chemistry and Physics*, 104(1), pp. 74-82. <https://doi.org/10.1016/j.matchemphys.2007.02.073>
- Bauer, A., Rabung, T., Claret, F., Schäfer, T., Buckau, G. and Fanghänel, T. (2005). Influence of temperature on sorption of europium onto smectite: The role of organic contaminants. *Applied Clay Science*, 30(1), pp. 1-10. <https://doi.org/10.1016/j.clay.2005.02.001>
- Bethke, C.M. (1996). Geochemical reaction modeling. New York: *Oxford University Press*, pp.111.
- Bethke, C.M. and Yeakel, S. (2018). The Geochemists' Workbench User's guides, Version 11 Aqueous Solutions LLC, Champaign.
- Beverskog, B. and Puigdomenech, I. (1999). Pourbaix Diagrams for the Ternary System of Iron-Chromium-Nickel. *CORROSION*, 55(11), pp. 1077-1087. <https://doi.org/10.5006/1.3283945>
- BGR- Bundesanstalt für Geowissenschaften und Rohstoffe (2007). Investigation and evaluation of regions with potentially suitable host rock formations for a geologic nuclear repository. Bericht. https://www.bgr.bund.de/EN/Themen/Endlagerung/Downloads/Schriften/3_Wirtsgesteine_Salz_Ton_Granit/WasteDisposal_HostRockFormations_en.pdf?__blob=publicationFile&v=2
- BGR- Bundesanstalt für Geowissenschaften und Rohstoffe (2019). https://www.bgr.bund.de/EN/Themen/Endlagerung/Standortauswahl/standortauswahl_node_en.html
- Blesa, M., Weisz, A., Morando, P., Salfity, J., Magaz, G. and Regazzoni, A. (2000). The interaction of metal oxide surfaces with complexing agents dissolved in water. *Coordination Chemistry Reviews*, 196(1), pp. 31-63. [https://doi.org/10.1016/S0010-8545\(99\)00005-3](https://doi.org/10.1016/S0010-8545(99)00005-3)

- Bojinov, M. & Beverskog, B. (2006). Interaction of Oxide Layers on Structural Materials with Light Water Reactor Coolant – its influence on the mechanism of oxide growth and restructuring. *Passivation of Metals and Semiconductors and Properties of Thin Oxide Layers*. pp. 431-436. <https://doi.org/10.1016/B978-044452224-5/50068-8>
- Borello, E., Cerruti, L., Ghiotti, G., and Guglielminotti, E. (1972). Surface complexes of nitrous oxide adsorbed on α -Cr₂O₃. *Inorganica Chimica Acta*, 6, pp. 45-48. [https://doi.org/10.1016/S0020-1693\(00\)91756-0](https://doi.org/10.1016/S0020-1693(00)91756-0)
- Bradbury, M., & Baeyens, B. (2006). Modelling sorption data for the actinides Am(III), Np(V) and Pa(V) on montmorillonite. *Radiochimica Acta*, 94(9-11). <https://doi.org/10.1524/ract.2006.94.9-11.619>
- Brady, P., Arnold, B., Altman, S. and Vaughn, P. (2012). Deep Borehole Disposal of Nuclear Waste: Final Report. *Sandia National Laboratories*, SAND2012-7789.
- Bratsch, S. G. (1989). Standard Electrode Potentials and Temperature Coefficients in Water at 298.15 K. *Journal of Physical and Chemical Reference Data*, 18(1), pp.1-21. <https://doi.org/10.1063/1.555839>
- Bretti, C., Foti, C. and Sammartano, S. (2004). A new approach in the use of SIT in determining the dependence on ionic strength of activity coefficients. Application to some chloride salts of interest in the speciation of natural fluids. *Chemical Speciation & Bioavailability*, 16(3), pp.105-110. <https://doi.org/10.3184/095422904782775036>
- Brewitz, W. (1980) Zusammenfassender Zwischenbericht GSF T 114.
- Brönsted, J. (1922). STUDIES ON SOLUBILITY. IV. THE PRINCIPLE OF THE SPECIFIC INTERACTION OF IONS. *Journal of the American Chemical Society*, 44(5), pp.877-898. <https://doi.org/10.1021/ja01426a001>
- Buck, R., Rondinini, S., Covington, A., Baucke, F., Brett, C., Camoes, M., Milton, M., Mussini, T., Naumann, R., Pratt, K., Spitzer, P. and Wilson, G. (2002). Measurement of pH. Definition, standards, and procedures (IUPAC Recommendations 2002). *Pure and Applied Chemistry*, 74(11), pp.2169-2200. DOI: [10.1351/pac200274112169](https://doi.org/10.1351/pac200274112169)
- Catalette, H., Dumonceau, J. and Ollar, P. (1998). Sorption of cesium, barium and europium on magnetite. *Journal of Contaminant Hydrology*, 35(1-3), pp.151-159. [https://doi.org/10.1016/S0169-7722\(98\)00123-5](https://doi.org/10.1016/S0169-7722(98)00123-5)
- Chaturvedi, T. (2009). An overview of the corrosion aspect of dental implants (titanium and its alloys). *Indian Journal of Dental Research*, 20(1), pp. 91. DOI: [10.4103/0970-9290.49068](https://doi.org/10.4103/0970-9290.49068)

- Chen, C., Britt, H., Boston, J. and Evans, L. (1979). Extension and application of the pitzer equation for vapor-liquid equilibrium of aqueous electrolyte systems with molecular solutes. *AIChE Journal*, 25(5), pp.820-831. <https://doi.org/10.1002/aic.690250510>
- Chen, Z., Tang, C., Shen, Z., Liu, Y. and Shi, B. (2017). The geotechnical properties of GMZ buffer/backfill material used in high-level radioactive nuclear waste geological repository: a review. *Environmental Earth Sciences*, 76 (270). <https://doi.org/10.1007/s12665-017-6580-2>
- Chesworth, W., Perez-Alberti, A., Arnaud, E., Morel-Seytoux, H.J., Schwertmann, U. (2008) Iron oxides. Encyclopedia of Soil Science. Encyclopedia of Earth Sciences Series. Springer, Dordrecht <https://doi.org/10.1007/978-1-4020-3995-9>
- Christiansen, B., Geckeis, H., Marquardt, C., Bauer, A., Römer, J., Wiss, T., Schild, D. and Stipp, S. (2011). Neptunyl (Np) interaction with green rust. *Geochimica et Cosmochimica Acta*, 75(5), pp.1216-1226. <https://doi.org/10.1016/j.gca.2010.12.003>
- Colombo, U., Gazzarrini, F., Lanzavecchia, G., and Sironi, G. (1965). Magnetite Oxidation: A Proposed Mechanism. *Science*, 147(3661), 1033-1033. DOI: [10.1126/science.147.3661.1033](https://doi.org/10.1126/science.147.3661.1033)
- Coppin, F., Berger, G., Bauer, A., Castet, S. and Loubet, M. (2002). Sorption of lanthanides on smectite and kaolinite. *Chemical Geology*, 182(1), pp.57-68. DOI: [10.1016/S0009-2541\(01\)00283-2](https://doi.org/10.1016/S0009-2541(01)00283-2)
- Cornell R. M. and Schwertmann U. (1996). The Iron Oxides. VCH, New York.
- Covington, A., Bates, R. and Durst, R. (1985). Definition of pH scales, standard reference values, measurement of pH and related terminology. *Pure and Applied Chemistry*, 57(3), pp.531-542.
- Davies, C.W. (1962). Ion Association, Butterworth's, pp. 37-53.
- Davis, J., James, R. and Leckie, J. (1978). Surface ionization and complexation at the oxide/water interface. *Journal of Colloid and Interface Science*, 63(3), pp.480-499. [https://doi.org/10.1016/S0021-9797\(78\)80009-5](https://doi.org/10.1016/S0021-9797(78)80009-5)
- de Pablo, L., Lourdes Chavez, M., Abatal, M. (2011). Adsorption of heavy metals in acid to alkaline environments by montmorillonite and Ca-montmorillonite. *Chemical Engineering Journal*, 171(3), pp. 1276-1286. DOI: [10.1016/j.cej.2011.05.055](https://doi.org/10.1016/j.cej.2011.05.055)
- Diomidis, N. (2014). Scientific basis for the production of gas due to corrosion in a deep geological repository. Arbeitsbericht NAB 14-21. NAGRA.
- Duan, Z., Arjmand, F., Zhang, L. and Abe, H. (2015). Investigation of the corrosion behavior of 304L and 316L stainless steels at high-temperature borated and lithiated water. *Journal of Nuclear Science and Technology*, 53(9), pp.1435-1446. <https://doi.org/10.1080/00223131.2015.1125311>

- Dumas, T., Fellhauer, D., Schild, D., Gaona, X., Altmaier, M., & Scheinost, A. (2019). Plutonium Retention Mechanisms by Magnetite under Anoxic Conditions: Entrapment versus Sorption. *ACS Earth and Space Chemistry*, 3(10), 2197-2206. DOI: [10.1021/acsearthspacechem.9b00147](https://doi.org/10.1021/acsearthspacechem.9b00147)
- Dzombak, D. and Morel, F. (1990). Surface complexation modeling. *Hydrous Ferric Oxide*. New York: Wiley.
- El Mendili, Y., Abdelouas, A., Ait Chaou, A., Bardeau, J. and Schlegel, M. (2014). Carbon steel corrosion in clay-rich environment. *Corrosion Science*, 88, pp.56-65. <https://doi.org/10.1016/j.corsci.2014.07.020>
- Estes, S., Arai, Y., Becker, U., Fernando, S., Yuan, K., Ewing, R., Zhang, J., Shibata, T. and Powell, B. (2013). A self-consistent model describing the thermodynamics of Eu(III) adsorption onto hematite. *Geochimica et Cosmochimica Acta*, 122, pp.430-447. <https://doi.org/10.1016/j.gca.2013.08.023>
- Filbert, W., Tholen, M., Engelhardt, H.-J., Graf, R., Brammer, K.-J. (2011). Disposal of Spent Fuel from German Nuclear Power Plants: The Third Option - Disposal of Transport and Storage Casks (Status) – 11517 WM2011 Conference, Phoenix, AZ ** *DBE TECHNOLOGY GmbH, Peine, Germany **GNS - Gesellschaft für Nuklear-Service mbH, Essen, Germany.
- Finck, N., Dardenne, K. and Geckeis, H. (2015). Am(III) coprecipitation with and adsorption on the smectite hectorite. *Chemical Geology*, 409, pp.12-19. <https://doi.org/10.1016/j.chemgeo.2015.04.020>
- Finck, N., Nedel, S., Dideriksen, K. and Schlegel, M. (2016_a). Trivalent Actinide Uptake by Iron (Hydr)oxides. *Environmental Science & Technology*, 50(19), pp.10428-10436. <https://doi.org/10.1021/acs.est.6b02599>
- Finck, N., Radulescu, L., Schild, D., Rothmeier, M., Huber, F., Lützenkirchen, J., Rabung, T., Heberling, F., Schlegel, M., Dideriksen, K., Nedel, S. and Geckeis, H. (2016_b). XAS signatures of Am(III) adsorbed onto magnetite and maghemite. *Journal of Physics: Conference Series*, 712, pp.012085. [doi:10.1088/1742-6596/712/1/012085](https://doi.org/10.1088/1742-6596/712/1/012085)
- Finck, N., Bouby, M., Dardenne, K. and Yokosawa, T. (2017). Yttrium co-precipitation with smectite: A polarized XAS and AsFIFFF study. *Applied Clay Science*, 137, pp.11-21. <https://doi.org/10.1016/j.clay.2016.11.029>
- Franco, F., Benitez-Guerrero, M., Gonzalez-Trivino, I., Perez-Recuerda, R., Assiego, C., Cifuentes-Melchor, J. (2016) Low-cost aluminum and iron oxides supported on dioctahedral and trioctahedral smectites: A comparative study of the effectiveness on the heavy metal adsorption from water. *Applied Clay Science*, 119, pp. 321-332. <https://doi.org/10.1016/j.clay.2015.10.035>

- Frankel, G. (1998). Pitting Corrosion of Metals. A Review of the Critical Factors. *Journal of The Electrochemical Society*, 145(6), pp.2186 - 2198. DOI:[10.1149/1.1838615](https://doi.org/10.1149/1.1838615)
- Friis, E., Andersen, J., Madsen, L., Bonander, N., Møller, P. and Ulstrup, J. (1997). Dynamics of *Pseudomonas aeruginosa* azurin and its Cys3Ser mutant at single-crystal gold surfaces investigated by cyclic voltammetry and atomic force microscopy. *Electrochimica Acta*, 42(19), pp.2889-2897. [https://doi.org/10.1016/S0013-4686\(97\)00109-6](https://doi.org/10.1016/S0013-4686(97)00109-6)
- Gallagher, K., Feitknecht, W. and Mannweiler, U. (1968). Mechanism of Oxidation of Magnetite to γ -Fe₂O₃. *Nature*, 217, pp.1118-1121.
- García, D., Lützenkirchen, J., Petrov, V., Siebentritt, M., Schild, D., Lefèvre, G., Rabung, T., Altmaier, M., Kalmykov, S., Duro, L. and Geckeis, H. (2019). Sorption of Eu(III) on quartz at high salt concentrations. *Colloids and Surfaces A: Physicochemical and Engineering Aspects*, 578, p.123610. <https://doi.org/10.1016/j.colsurfa.2019.123610>
- Gaudin, A., Gaboreau, S., Tinseau, E., Bartier, D., Petit, S., Grauby, O., Foct, F. and Beaufort, D. (2009). Mineralogical reactions in the Tournemire argillite after in-situ interaction with steels. *Applied Clay Science*, 43(2), pp.196-207. <https://doi.org/10.1016/j.clay.2008.08.007>
- Geckeis, H., Lützenkirchen, J., Polly, R., Rabung, T., & Schmidt, M. (2013). Mineral–Water Interface Reactions of Actinides. *Chemical Reviews*, 113(2), pp. 1016-1062. <https://doi.org/10.1021/cr300370h>
- Génin, J., Bourrié, G., Trolard, F., Abdelmoula, M., Jaffrezic, A., Refait, P., Maitre, V., Humbert, B. and Herbillon, A. (1998). Thermodynamic Equilibria in Aqueous Suspensions of Synthetic and Natural Fe(II)–Fe(III) Green Rusts: Occurrences of the Mineral in Hydromorphic Soils. *Environmental Science & Technology*, 32(8), pp.1058-1068. <https://doi.org/10.1021/es970547m>
- Grambow, B., Smailos, E., Geckeis, H., Müller, R. and Hentschel, H. (1996). Sorption and Reduction of Uranium(VI) on Iron Corrosion Products under Reducing Saline Conditions. *Radiochimica Acta*, 74, pp.149–154. <https://doi.org/10.1524/ract.1996.74.special-issue.149>
- Grenthe, I., Mompean, F., Spahiu, K. and Wanner, H. (2013). Guidelines for the extrapolation to zero ionic strength. *Nuclear Energy Agency, OECD*. Available at: <https://www.oecd-neo.org/dbtdb/guidelines/tdb2.pdf>
- Grivé, M., Duro, L., Colàs, E., Giffaut, E. (2015). Thermodynamic data selection applied to radionuclides and chemotoxic elements: an overview of the ThermoChimie-TDB. *Applied Geochemistry*, 55, pp.85-94. <https://doi.org/10.1016/j.apgeochem.2014.12.017>
- Guilbaud, R., White, M. and Poulton, S. (2013). Surface charge and growth of sulphate and carbonate green rust in aqueous media. *Geochimica et Cosmochimica Acta*, 108, pp.141-153. <https://doi.org/10.1016/j.gca.2013.01.017>

- GNS - Gesellschaft für Nuklear Behälter. (2020) <https://www.gns.de/language=de/24376/pollux>
- Guo, X., Gin, S., Lei, P., Yao, T., Liu, H., Schreiber, D., Ngo, D., Viswanathan, G., Li, T., Kim, S., Vienna, J., Ryan, J., Du, J., Lian, J. and Frankel, G. (2020). Self-accelerated corrosion of nuclear waste forms at material interfaces. *Nature Materials*, 19(3), pp.310-316. <https://doi.org/10.1038/s41563-019-0579-x>
- Guillaumont, R., Mompean, F., Fanghangel, T., Neck, V., Fuger, J., Palmer, D., Grenthe, I., Rand, M., Illemassene, M., Domenech-Orti, C. and Ben-Said, K. (2003). Update on the chemical thermodynamics of uranium, neptunium, plutonium, americium and technetium. Amsterdam: Nuclear energy agency organisation for economic co-operation and development. <https://www.oecd-nea.org/dbtdb/pubs/vol5-update-combo.pdf>
- Hall, D. S., Lockwood, D. J., Bock, C. and MacDougall, B. R. (2015). Nickel hydroxides and related materials: a review of their structures, synthesis and properties. *Proceedings of the Royal Society A: Mathematical, Physical and Engineering Sciences*, 471 (2174), 20140792. <https://doi.org/10.1098/rspa.2014.0792>
- Harvie, C., Møller, N. and Weare, J. (1984). The prediction of mineral solubilities in natural waters: The Na-K-Mg-Ca-H-Cl-SO₄-OH-HCO₃-CO₃-CO₂-H₂O system to high ionic strengths at 25°C. *Geochimica et Cosmochimica Acta*, 48(4), pp.723-751. [https://doi.org/10.1016/0016-7037\(84\)90098-X](https://doi.org/10.1016/0016-7037(84)90098-X)
- Hartmann, E., Geckeis, H., Rabung, T., Lützenkirchen, J. and Fanghänel, T. (2008). Sorption of radionuclides onto natural clay rocks. *Radiochimica Acta*, 96(9-11), pp. 699-707. <https://doi.org/10.1524/ract.2008.1556>
- Hazan, E., Sadia, Y., & Gelbstein, Y. (2013). Characterization of AISI 4340 corrosion products using Raman spectroscopy. *Corrosion Science*, 74, pp. 414-418. <https://doi.org/10.1016/j.corsci.2013.05.002>
- Helmholtz, H. (1853). Über einige Gesetze der Vertheilung elektrischer Ströme in körperlichen Leitern mit Anwendung auf die thierisch-elektrischen Versuche. <https://doi.org/10.1002/andp.18531650603>
- Hiemstra, T. and Van Riemsdijk, W. H. (1991). Physical chemical interpretation of primary charging behaviour of metal (hydr)oxides. *Colloids and Surfaces*, 59, pp.7-25. [https://doi.org/10.1016/0166-6622\(91\)80233-E](https://doi.org/10.1016/0166-6622(91)80233-E)
- Hiemstra, T. and Van Riemsdijk, W. H. (1996). A Surface Structural Approach to Ion Adsorption: The Charge Distribution (CD) Model. *Journal of Colloid and Interface Science*, 179(2), pp.488-508. <https://doi.org/10.1006/jcis.1996.0242>

- Hixon, A. E. and Powell, B. A. (2018). Plutonium environmental chemistry: mechanisms for the surface-mediated reduction of Pu(v/vi). *Environmental Science: Processes & Impacts*, 20(10), pp.1306-1322. <https://doi.org/10.1039/C7EM00369B>
- Hsu, C. H. and Chen, M. L. (2010). Corrosion behavior of nickel alloyed and austempered ductile irons in 3.5% sodium chloride. *Corrosion Science*, 52(9), pp.2945-2949. <https://doi.org/10.1016/j.corsci.2010.05.006>
- Huber, F., Schild, D., Vitova, T., Rothe, J., Kirsch, R. and Schäfer, T. (2012). U(VI) removal kinetics in presence of synthetic magnetite nanoparticles. *Geochimica et Cosmochimica Acta*, 96, pp.154-173. <https://doi.org/10.1016/j.gca.2012.07.019>
- Hummel, W., Berner, U., Curti, E., Pearson, F., Thoenen, T. (2002). Nagra/PSI Chemical Thermodynamic Data Base 01/01. *Radiochimica Acta*, 90(9-11). DOI:[10.1524/ract.2002.90.9-11_2002.805](https://doi.org/10.1524/ract.2002.90.9-11_2002.805)
- Hung, C. C., Wu, Y. C. and King, F. (2017). Corrosion assessment of canister for the disposal of spent nuclear fuel in crystalline rock in Taiwan. *Corrosion Engineering, Science and Technology*, 52(sup1), pp.194-199. <https://doi.org/10.1080/1478422X.2017.1285855>
- HZDR (2018). RES³T - Rossendorf Expert System for Surface and Sorption Thermodynamics - Helmholtz-Zentrum Dresden-Rossendorf, HZDR. <https://www.hzdr.de/db/RES3T.DATAASSEMBLY>
- IAEA – International Atomic Energy Agency. (1997). Experience in selection and characterization of sites for geological disposal of radioactive waste. IAEA TECDOC-991. https://www-pub.iaea.org/MTCD/Publications/PDF/te_991_prn.pdf
- IAEA – International Atomic Energy Agency. (2009). Nuclear Energy Series, Geological Disposal of Radioactive Waste: Technological Implications for Retrievability. No. NW-T-1.19. https://www-pub.iaea.org/MTCD/Publications/PDF/Pub1378_web.pdf
- Ilton, E., Boily, J., Buck, E., Skomurski, F., Rosso, K., Cahill, C., Bargar, J. and Felmy, A. (2010). Influence of Dynamical Conditions on the Reduction of U(VI) at the Magnetite–Solution Interface. *Environmental Science & Technology*, 44(1), pp.170-176. <https://doi.org/10.1021/es9014597>
- Jobmann, M., Bebiolka, A., Burlaka, V., Herold, P., Jahn, S., Lommerzheim, A., Maßmann, J., Meleshyn, A., Mrugalla, S., Reinhold, K., Rübél, A., Stark, L., Ziefle, G. (2017): Safety assessment methodology for a German high-level waste repository in clay formations, *Journal of Rock Mechanics and Geotechnical Engineering*, 9(5), pp. 856-876. <https://doi.org/10.1016/j.jrmge.2017.05.007>
- JOINT COMMITTEE ON POWDER DIFFRACTION STANDARDS. (1970). *Analytical Chemistry*, 42(11), pp. 81A-81A. <https://doi.org/10.1021/ac60293a779>

- Jolivet, J., Chanéac, C., & Tronc, E. (2004). Iron oxide chemistry. From molecular clusters to extended solid networks. *Chemical Communications*, (5), pp. 481-487. <https://doi.org/10.1039/B304532N>
- Jolivet, J., Tronc, E. and Chanéac, C. (2006). Iron oxides: From molecular clusters to solid. A nice example of chemical versatility. *Comptes Rendus Geoscience*, 338(6-7), pp. 488-497. <https://doi.org/10.1016/j.crte.2006.04.014>
- Jönsson, J. and Sherman, D. M. (2008). Sorption of As(III) and As(V) to siderite, green rust (fougerite) and magnetite: Implications for arsenic release in anoxic groundwaters. *Chemical Geology*, 255(1-2), pp.173-181. <https://doi.org/10.1016/j.chemgeo.2008.06.036>
- Jung, J., Lee, J. K. and Hahn, P. S. (2001). Development and application of a sorption data base for the performance assessment of a radwaste repository. *Waste Management*, 21(4), pp.363-369. DOI: [10.1016/S0956-053X\(00\)00083-0](https://doi.org/10.1016/S0956-053X(00)00083-0)
- Kaufhold, S., Hassel, A. W., Sanders, D. and Dohrmann, R. (2015). Corrosion of high-level radioactive waste iron-canisters in contact with bentonite. *Journal of Hazardous Materials*, 285, pp.464-473. <https://doi.org/10.1016/j.jhazmat.2014.10.056>
- Kienzler, B. and Loida, A. (2001). Endlagerrelevante Eigenschaften von hochradioaktiven Abfallprodukten. Charakterisierung und Bewertung. Empfehlung des Arbeitskreises HAW Produkte. INE, Kernforschungszentrum Karlsruhe. Wissenschaftliche Berichte FZKA 6651.
- Kienzler, B. (2017_a). Corrosion of Canister Materials for Radioactive Waste Disposal. *Decommissioning and waste management, ATW*, 62 (8/9), pp. 542-549. https://inis.iaea.org/search/search.aspx?orig_q=RN:48083936
- Kienzler, B. (2017_b). Investigations of Corrosion Processes of Alloyed Steels in Salt Solutions. INE, Kernforschungszentrum Karlsruhe. Wissenschaftliche Berichte.
- Kim, J. I. and Grambow, B. (1999). Geochemical assessment of actinide isolation in a German salt repository environment. *Engineering Geology*, 52(3-4), pp.221-230. [https://doi.org/10.1016/S0013-7952\(99\)00007-1](https://doi.org/10.1016/S0013-7952(99)00007-1)
- King, F. (2008). Corrosion of carbon steel under anaerobic conditions in a repository for SF and HLW in Opalinus Clay. Technical Report 08-12. NAGRA. Integrity Corrosion Consulting Ltd. https://inis.iaea.org/collection/NCLCollectionStore/_Public/41/030/41030156.pdf?r=1
- King, F. and Lilja, C. (2011). Scientific basis for corrosion of copper in water and implications for canister lifetimes. *Corrosion Engineering, Science and Technology*, 46(2), pp. 153–158. <https://doi.org/10.1179/1743278210Y.0000000002>

- King, F. (2012). General corrosion in nuclear reactor components and nuclear waste disposal systems. Nuclear Corrosion Science and Engineering. Woodhead Publishing Limited. https://cds.cern.ch/record/1629271/files/9781845697655_TOC.pdf
- King, F., Sanderson, D. and Watson, Sarah. (2016). Durability of High Level Waste and Spent Fuel Disposal Containers – an overview of the combined effect of chemical and mechanical degradation mechanisms, including Appendix B2, B3 and B4. Nuclear Decommissioning Authority- Radioactive Waste Management Limited. <https://rwm.nda.gov.uk/publication/durability-of-high-level-waste-and-spent-fuel-disposal-containers/>
- Kirchheim, R., Heine, B., Fischmeister, H., Hofmann, S., Knotte, H. and Stolz, U. (1989). The passivity of iron-chromium alloys. *Corrosion Science*, 29(7), pp.899-917. [https://doi.org/10.1016/0010-938X\(89\)90060-7](https://doi.org/10.1016/0010-938X(89)90060-7)
- Kirsch, R., Fellhauer, D., Altmaier, M., Neck, V., Rossberg, A., Fanghänel, T., Charlet, L. and Scheinost, A. (2011). Oxidation State and Local Structure of Plutonium Reacted with Magnetite, Mackinawite, and Chukanovite. *Environmental Science & Technology*, 45(17), pp.7267-7274. <https://doi.org/10.1021/es200645a>
- Koh, D., Khoo, K. and Chan, C. (1985). The application of the pitzer equations to 1-1 electrolytes in mixed solvents. *Journal of Solution Chemistry*, 14(9), pp.635-651. <https://doi.org/10.1007/BF00646056>
- Kommission Lagerung hoch radioaktiver Abfallstoffe (2016). "ABSCHLUSSBERICHT: Verantwortung für die Zukunft: Ein faires und transparentes Verfahren für die Auswahl eines nationalen Endlagerstandortes." Geschäftsstelle der Kommission Lagerung hoch radioaktiver Abfallstoffe https://www.bundestag.de/resource/blob/434430/bb37b21b8e1e7e049ace5db6b2f949b2/drs_268-data.pdf
- Kowal-Fouchard, A., Drot, R., Simoni, E., Marmier, N., Fromage, F., Ehrhardt, J. J. (2004). Structural identification of europium (III) adsorption complexes on montmorillonite. *New Journal of Chemistry*. 28(7), pp. 864-869. <https://doi.org/10.1039/B400306C>
- Kühlenbeck, H., Xu, C., Dillmann, B., Haßel, M., Adam, B., Ehrlich, D., Wohlrab, S., Freund, H. J., Ditzinger, U.A., Neddermeyer, H., Neumann, M. and Neuber, M. (1992), Adsorption and Reaction on Oxide Surfaces: CO and CO₂ on Cr₂O₃(111). *Berichte der Bunsengesellschaft für physikalische Chemie*, 96(1), pp. 15-27. <https://doi.org/10.1002/bbpc.19920960104>
- Kursten B., Smailos, E., Azkarate, I., Werme, L., Smart, N. and Santarini G. (2004). State of the art document on the corrosion behavior of container materials. Contract n° fikw-ct-20014-20138.

- Latta, D., Gorski, C., Boyanov, M., O'Loughlin, E., Kemner, K. and Scherer, M. (2011). Influence of Magnetite Stoichiometry on UVI Reduction. *Environmental Science & Technology*, 46(2), pp.778-786. <https://doi.org/10.1021/es2024912>
- Latta, D., Boyanov, M., Kemner, K. M., O'Loughlin, E. J., Scherer, M. Reaction of uranium(VI) with green rusts: Effect of interlayer anion. (2015). *Current Inorganic Chemistry*, 5(3), pp. 156-168. DOI: [10.2174/1877944105666150420235350](https://doi.org/10.2174/1877944105666150420235350)
- Lee, J. K., Baik, M. H. and Jeong, J. T. (2013). Development of Sorption Database (KAERI-SDB) for the Safety Assessment of Radioactive Waste Disposal. *Journal of Nuclear Fuel Cycle and Waste Technology*, 11(1), pp.41-54. <https://doi.org/10.7733/jkrws.2012.11.1.41>
- Lemire, R. J., Berner, U., Musikas, C., Palmer, D.A., Taylor, P., Tochiyama, O., Perrone, J., (2013) Chemical Thermodynamics of Iron, Part 1. Chemical thermodynamics Volume 13a. Nuclear energy agency organisation for economic co-operation and development. <https://www.oecd-neo.org/dbtdb/pubs/6355-vol13a-iron.pdf>
- Lemire, R. J., Palmer, D.A., Taylor, P., Schlenz, H., Ragoussi, M.-E., Costa, D., Martinez, J. (2020) Chemical Thermodynamics of Iron, Part 2. Chemical thermodynamics Volume 13b. Nuclear energy agency organisation for economic co-operation and development. <http://www.oecd-neo.org/dbtdb/pubs/7499-vol13b-iron.pdf>
- Li, D. and Kaplan, D. (2012). Sorption coefficients and molecular mechanisms of Pu, U, Np, Am and Tc to Fe (hydr)oxides: A review. *Journal of Hazardous Materials*, 243, pp.1-18. <https://doi.org/10.1016/j.jhazmat.2012.09.011>
- Li, Z., Chanéac, C., Berger, G., Delaunay, S., Graff, A. and Lefèvre, G. (2019). Mechanism and kinetics of magnetite oxidation under hydrothermal conditions. *RSC Advances*, 9(58), pp.33633-33642. <https://doi.org/10.1039/C9RA03234G>
- Lide, D. (2004). CRC handbook of chemistry and physics, 84th edition, 2003-2004. Boca Raton: CRC Press.
- Lujanienė, G., Beneš, P., Štamberg, K., Šapolaitė, J., Vopalka, D., Radžiūtė, E. and Ščiglo, T. (2010). Effect of natural clay components on sorption of Cs, Pu and Am by the clay. *Journal of Radioanalytical and Nuclear Chemistry*, 286(2), pp.353-359. <https://doi.org/10.1007/s10967-010-0726-y>
- Lützenkirchen, J. (2006). Surface Complexation Modelling, Volume 11. Burlington: Elsevier.
- Lützenkirchen, J., Preočanin, T., Kovačević, D., Tomišić, V., Lövgren, L. and Kallay, N. (2012). Potentiometric Titrations as a Tool for Surface Charge Determination. *Croatica Chemica Acta*, 85(4), pp. 391-417. <http://dx.doi.org/10.5562/cca2062>

- Lyon, S. (2012). Overview of corrosion engineering, science and technology. *Nuclear Corrosion Science and Engineering*. Woodhead Publishing Limited, pp. 3-30. DOI: [10.1533/9780857095343.1.3](https://doi.org/10.1533/9780857095343.1.3)
- Mahoney, J. and Langmuir, D. (1991). Adsorption of Sr on Kaolinite, Illite and Montmorillonite at High Ionic Strengths. *Radiochimica Acta*, 54(3), pp. 139-144. <https://doi.org/10.1524/ract.1991.54.3.139>
- Marcus, P. (2011). *Corrosion Mechanisms in Theory and Practice*, Third Edition. CRC Press.
- Marsac, R., Banik, N., Lützenkirchen, J., Diascorn, A., Bender, K., Marquardt, C., & Geckeis, H. (2017). Sorption and redox speciation of plutonium at the illite surface under highly saline conditions. *Journal of Colloid and Interface Science*, 485, pp. 59-64. <https://doi.org/10.1016/j.jcis.2016.09.013>
- Marsh, G.P., Bland, I., Desport, J.A., Naish, C., Wescott, C. and Taylor K.J. (1983). Corrosion assessment of metal overpacks for radioactive waste disposal. *Nuclear Science and Technology*, 5, pp. 223-252.
- Marsh, G. P., Taylor, K. J., Bland, I., Westcott, C., Tasker, P., & Sharland, S. (1986). Evaluation of the Localised Corrosion of Carbon Steel Overpacks for Nuclear Waste Disposal in Granite Environments. *Proceedings of Scientific Basis for Nuclear Waste Management IX* 50, 421. DOI:[10.1557/PROC-50-421](https://doi.org/10.1557/PROC-50-421)
- Martin Cabañas, B., Leclercq, S., Barboux, P., Fédoroff, M. and Lefèvre, G. (2011). Sorption of nickel and cobalt ions onto cobalt and nickel ferrites. *Journal of Colloid and Interface Science*, 360(2), pp.695-700. <https://doi.org/10.1016/j.jcis.2011.04.082>
- McCafferty, E. (2010). *Introduction to corrosion science*. Alexandria, VA: Springer, pp.15-31, 47, 66-68, 95-160, 209-297. DOI: [10.1007/978-1-4419-0455-3](https://doi.org/10.1007/978-1-4419-0455-3)
- Millero, F.J.; Yao, W.; and Aicher, J.(1995). The Speciation of Fe(II) and Fe(III) in Natural Waters. *Marine Chemistry*, 50(1-4), pp. 21-39. [https://doi.org/10.1016/0304-4203\(95\)00024-L](https://doi.org/10.1016/0304-4203(95)00024-L)
- Missana, T., García-Gutiérrez, M. and Fernández, V. (2003). Uranium (VI) sorption on colloidal magnetite under anoxic environment: experimental study and surface complexation modelling. *Geochimica et Cosmochimica Acta*, 67(14), pp. 2543-2550. [https://doi.org/10.1016/S0016-7037\(02\)01350-9](https://doi.org/10.1016/S0016-7037(02)01350-9)
- Moog, H. C., Bok, F., Marquardt, C. and Brendler, V. (2015). Disposal of nuclear waste in host rock formations featuring high-saline solutions – Implementation of a thermodynamic reference database (THEREDA). *Applied Geochemistry*, 55, pp.72-84. <https://doi.org/10.1016/j.apgeochem.2014.12.016>

- Nagies, F. and Heusler, K. (1998). Corrosion of metallic materials in hot salt brines. *Electrochimica Acta*, 43(1-2), pp.41-51. [https://doi.org/10.1016/S0013-4686\(97\)00233-8](https://doi.org/10.1016/S0013-4686(97)00233-8)
- Nakata, K., Nagasaki, S., Tanaka, S., Sakamoto, Y., Tanaka, T. and Ogawa, H. (2002). Sorption and reduction of neptunium(V) on the surface of iron oxides. *Radiochimica Acta*, 90(9-11), pp. 655-669. https://doi.org/10.1524/ract.2002.90.9-11_2002.665
- Naveau, A., Monteil-Rivera, F., Dumonceau, J. and Boudesocque, S. (2005). Sorption of europium on a goethite surface: influence of background electrolyte. *Journal of Contaminant Hydrology*, 77(1-2), pp.1-16. <https://doi.org/10.1016/j.jconhyd.2004.10.002>
- Necib, S., Linard, Y., Crusset, D., Michau, N., Daumas, S., Burger, E., Romaine, A. and Schlegel, M. (2016). Corrosion at the carbon steel-clay borehole water and gas interfaces at 85 °C under anoxic and transient acidic conditions. *Corrosion Science*, 111, pp.242-258. <https://doi.org/10.1016/j.corsci.2016.04.039>
- Necib, S., Linard, Y., Crusset, D., Schlegel, M., Daumas, S. and Michau, N. (2017). Corrosion processes of C-steel in long-term repository conditions. *Corrosion Engineering, Science and Technology*, 52(sup1), pp.127-130. <https://doi.org/10.1080/1478422X.2017.1320155>
- Neck, V., Altmaier, M., Rabung, T., Lützenkirchen, J. and Fanghänel, T. (2009). Thermodynamics of trivalent actinides and neodymium in NaCl, MgCl₂, and CaCl₂ solutions: Solubility, hydrolysis, and ternary Ca-M(III)-OH complexes. *Pure and Applied Chemistry*, 81(9), pp.1555-1568. <https://doi.org/10.1351/PAC-CON-08-09-05>
- Nemer, M.B., Xiong, Y., Ismail, A. E. and Jang, J. H. (2011). Solubility of Fe₂(OH)₃Cl (pure-iron end-member of hibbingite) in NaCl and Na₂SO₄ brines. *Chemical Geology*, 280(1-2), pp.26-32. <https://doi.org/10.1016/j.chemgeo.2010.10.003>
- Oecd-nea.org. (2012). Destruction of long-lived radioactive waste. Nuclear Energy Agency <https://www.oecd-nea.org/trw/intro/ens.html>
- Parkhurst, D.L. and Appelo, C.A.J., 1999. User's guide to PHREEQC (version 2) - A computer program for speciation, batch-reaction, one-dimensional transport, and inverse geochemical calculations: U.S. Geological Survey, Water-Resources Investigations Report 99-4259. <https://pubs.usgs.gov/wri/1999/4259/report.pdf>
- Payne, T. E., Brendler, V., Ochs, M., Baeyens, B., Brown, P. L., Davis, J. A., Ekberg, C., Kulik, D. A., Lützenkirchen, J., Missana, T., Tachi, Y., Van Loon, L. R. and Altmann, S. (2013). Guidelines for thermodynamic sorption modelling in the context of radioactive waste disposal. *Environmental Modelling & Software*, 42, pp.143-156. <https://doi.org/10.1016/j.envsoft.2013.01.002>

- Pepper, S. E., Bunker, D. J., Bryan, N. D., Livens, F. R., Charnock, J. M., Patrick, R., & Collison, D. (2003). Treatment of radioactive wastes: An X-ray absorption spectroscopy study of the reaction of technetium with green rust. *Journal of Colloid And Interface Science*, 268(2), pp. 408-412. <https://doi.org/10.1016/j.jcis.2003.08.024>
- Pérez, F. J., Pedraza, F., Sanz, C., Hierro, M. P. and Gómez, C. (2002). Effect of thermal cycling on the high temperature oxidation resistance of austenitic AISI 309S stainless steel. *Materials and Corrosion*, 53(4), pp.231-238.
- Pidchenko, I., Kvashnina, K. O., Yokosawa, T., Finck, N., Bahl, S., Schild, D., Polly, R., Bohnert, E., Rossberg, A., Göttlicher, J., Dardenne, K., Rothe, J., Schäfer, T., Geckeis, H. and Vitova, T. (2017). Uranium Redox Transformations after U(VI) Coprecipitation with Magnetite Nanoparticles. *Environmental Science & Technology*, 51(4), pp. 2217-2225. <https://doi.org/10.1021/acs.est.6b04035>
- Pitzer, K. S. (1973). Thermodynamics of electrolytes. I. Theoretical basis and general equations. *The Journal of Physical Chemistry*, 77(2), pp.268-277. <https://doi.org/10.1021/j100621a026>
- Pitzer, K. S. and Mayorga, G. (1973). Thermodynamics of electrolytes. II. Activity and osmotic coefficients for strong electrolytes with one or both ions univalent. *The Journal of Physical Chemistry*, 77(19), pp.2300-2308. <https://doi.org/10.1021/j100638a009>
- Pitzer, K. S. and Kim, J. J. (1974). Thermodynamics of electrolytes. IV. Activity and osmotic coefficients for mixed electrolytes. *Journal of the American Chemical Society*, 96(18), pp.5701-5707. <https://doi.org/10.1021/ja00825a004>
- Plummer, L. N., Parkhurst, D. L., Fleming, G. W., Dunkle, S. A. (1988). PHRQPITZ - A Computer Program Incorporating Pitzer's Equations for Calculation of Geochemical Reactions in Brines. U.S. Geological Survey, Water-Resources Investigations Report 884153. <https://pubs.usgs.gov/wri/1988/4153/report.pdf>
- Popov, B. N. (2015). Corrosion Engineering: *Principles and Solved Problems*. (pp. 181-237). Elsevier Science. <https://doi.org/10.1016/C2012-0-03070-0>
- Pourbaix, M. (1974). Atlas of Electrochemical Equilibria in Aqueous Solutions. 2nd Edition. National Association of Corrosion Engineers. <http://sunlight.caltech.edu/aic/pourbaix.pdf>
- Powell, B. A., Fjeld, R. A., Kaplan, D. I., Coates, J. T. and Serkiz, S. M. (2004). Pu(V)O₂⁺ Adsorption and Reduction by Synthetic Magnetite (Fe₃O₄). *Environmental Science & Technology*, 38(22), pp. 6016-6024. <https://doi.org/10.1021/es049386u>

- Rabung, T., Geckeis, H., Kim, J., & Beck, H. P. (1998). Sorption of Eu(III) on a Natural Hematite: Application of a Surface Complexation Model. *Journal of Colloid and Interface Science*, 208(1), pp. 153-161. <https://doi.org/10.1006/jcis.1998.5788>
- Rabung, T., Pierret, M. C., Bauer, A., Geckeis, H., Bradbury, M. H. and Baeyens, B. (2005). Sorption of Eu(III)/Cm(III) on Ca-montmorillonite and Na-illite. Part 1: Batch sorption and time-resolved laser fluorescence spectroscopy experiments. *Geochimica et Cosmochimica Acta*, 69(23), pp.5393-5402. <https://doi.org/10.1016/j.gca.2005.06.030>
- Ramya, S., Anita, T., Shaikh, H. and Dayal, R. K. (2010). Laser Raman microscopic studies of passive films formed on type 316LN stainless steels during pitting in chloride solution. *Corrosion Science*, 52(6), pp.2114-2121. <https://doi.org/10.1016/j.corsci.2010.02.028>
- Ravel, B. (2000). EXAFS analysis with FEFF and FEFFIT. Part 2: Commentary. Version 0.04.
- Ravel, B. and Newville, M. (2005). ATHENA, ARTEMIS, HEPHAESTUS: data analysis for X-ray absorption spectroscopy using IFEFFIT. *Journal of Synchrotron Radiation*, 12(4), pp.537-541. <https://doi.org/10.1107/S0909049505012719>
- Refait, P., & Génin, J. (1993). The oxidation of ferrous hydroxide in chloride-containing aqueous media and pourbaix diagrams of green rust one. *Corrosion Science*, 34(5), pp. 797-819. [https://doi.org/10.1016/0010-938X\(93\)90101-L](https://doi.org/10.1016/0010-938X(93)90101-L)
- Refait, P., Drissi, S., Pytkiewicz, J. and Génin, J. (1997). The anionic species competition in iron aqueous corrosion: Role of various green rust compounds. *Corrosion Science*, 39(9), pp.1699-1710. [https://doi.org/10.1016/S0010-938X\(97\)00076-0](https://doi.org/10.1016/S0010-938X(97)00076-0)
- Refait, P., Abdelmoula, M., & Génin, J. (1998). Mechanisms of formation and structure of green rust one in aqueous corrosion of iron in the presence of chloride ions. *Corrosion Science*, 40(9), pp. 1547-1560. [https://doi.org/10.1016/S0010-938X\(98\)00066-3](https://doi.org/10.1016/S0010-938X(98)00066-3)
- Refait, P., Memet, J., Bon, C., Sabot, R. and Génin, J., (2003). Formation of the Fe(II)–Fe(III) hydroxysulphate green rust during marine corrosion of steel. *Corrosion Science*, 45(4), pp.833-845. [https://doi.org/10.1016/S0010-938X\(02\)00184-1](https://doi.org/10.1016/S0010-938X(02)00184-1)
- Refait, P., Sabot, R. and Jeannin, M. (2017). Role of Al(III) and Cr(III) on the formation and oxidation of the Fe(II-III) hydroxysulfate Green Rust. *Colloids and Surfaces A: Physicochemical and Engineering Aspects*, 531, pp.203-212. <https://doi.org/10.1016/j.colsurfa.2017.08.006>
- Réguer, S., Dillmann, P., Mirambet, F. and Bellot-Gurlet L. (2005). Local and structural characterisation of chlorinated phases formed on ferrous archaeological artefacts by μ XRD and μ XANES. *Nuclear Instruments & Methods in Physics Research Section B-Beam Interactions with Materials and Atoms* 240(1-2): pp. 500-504. DOI: [10.1016/j.nimb.2005.06.217](https://doi.org/10.1016/j.nimb.2005.06.217)

- Réguer, S., Neff, D., Bellot-Gurlet, L. and Dillmann, P. (2007). Deterioration of iron archaeological artefacts: micro-Raman investigation on Cl-containing corrosion products. *Journal of Raman Spectroscopy*, 38(4), pp.389-397. <https://doi.org/10.1002/jrs.1659>
- Réguer, S., Mirambet, F., Rémazeilles, C., Vantelon, D., Kergourlay, F., Neff, D. and Dillmann, P. (2015). Iron corrosion in archaeological context: Structural refinement of the ferrous hydroxychloride $\beta\text{-Fe}_2(\text{OH})_3\text{Cl}$. *Corrosion Science*, 100, pp.589-598. <https://doi.org/10.1016/j.corsci.2015.08.035>
- Rémazeilles, C. and Refait, P. (2008). Formation, fast oxidation and thermodynamic data of Fe(II) hydroxychlorides. *Corrosion Science*, 50(3), pp.856-864. <https://doi.org/10.1016/j.corsci.2007.08.017>
- Revie, R. W. and Uhlig, H. (2011). Uhlig's corrosion handbook. 3rd Edition. John Wiley & Sons, Inc., Hoboken, New Jersey.
- Roberts, H. E., Morris, K., Mosselmans, J., Law, G. and Shaw, S. (2019). Neptunium Reactivity During Co-Precipitation and Oxidation of Fe(II)/Fe(III) (Oxyhydr)oxides. *Geosciences*, 9(1), pp.27. <https://doi.org/10.3390/geosciences9010027>
- Rojo, I., Seco, F., Rovira, M., Giménez, J., Cervantes, G., Martí, V. and de Pablo, J. (2009). Thorium sorption onto magnetite and ferrihydrite in acidic conditions. *Journal of Nuclear Materials*, 385(2), pp.474-478. <https://doi.org/10.1016/j.jnucmat.2008.12.014>
- Rothe, J., Butorin, S., Dardenne, K., Denecke, M. A., Kienzler, B., Löble, M., Metz, V., Seibert, A., Steppert, M., Vitova, T., Walther, C. and Geckeis, H. (2012). The INE-Beamline for actinide science at ANKA. *Review of Scientific Instruments*, 83, 043105. <https://doi.org/10.1063/1.3700813>
- Rovira, M., El Aamrani, S., Duro, L., Giménez, J., de Pablo, J. and Bruno, J. (2007). Interaction of uranium with in situ anoxically generated magnetite on steel. *Journal of Hazardous Materials*, 147(3), pp.726-731. <https://doi.org/10.1016/j.jhazmat.2007.01.067>
- Ruby, C., Usman, M., Naille, S., Hanna, K., Carteret, C., Mullet, M., François, M. and Abdelmoula, M. (2009). Synthesis and transformation of iron-based layered double hydroxides. *Applied Clay Science*, 48(1-2), pp.195-202. <https://doi.org/10.1016/j.clay.2009.11.017>
- Sagoe-Crentsil, K. K. and Glasser, F. P. (1993). "Green rust", iron solubility and the role of chloride in the corrosion of steel at high pH. *Cement and Concrete Research*, 23(4), pp.785-791. [https://doi.org/10.1016/0008-8846\(93\)90032-5](https://doi.org/10.1016/0008-8846(93)90032-5)
- Sato, N. (2012). Basics of Corrosion Chemistry. Green Corrosion Chemistry and Engineering, Wiley-VCH, pp.1-32. <https://doi.org/10.1002/9783527641789.ch1>

- Scatchard, G. (1936). Concentrated Solutions of Strong Electrolytes. *Chemical Reviews*, 19(3), pp.309-327. <https://doi.org/10.1021/cr60064a008>
- Schlegel, M., Bataillon, C., Benhamida, K., Blanc, C., Menut, D. and Lacour, J. (2008). Metal corrosion and argillite transformation at the water-saturated, high-temperature iron–clay interface: A microscopic-scale study. *Applied Geochemistry*, 23(9), pp.2619-2633. <https://doi.org/10.1016/j.apgeochem.2008.05.019>
- Schlegel, M., Bataillon, C., Brucker, F., Blanc, C., Prêt, D., Foy, E. and Chorro, M. (2014). Corrosion of metal iron in contact with anoxic clay at 90 °C: Characterization of the corrosion products after two years of interaction. *Applied Geochemistry*, 51, pp.1-14. <https://doi.org/10.1016/j.apgeochem.2014.09.002>
- Schlegel, M., Necib, S., Daumas, S., Blanc, C., Foy, E., Trcera, N. and Romaine, A. (2016). Microstructural characterization of carbon steel corrosion in clay borehole water under anoxic and transient acidic conditions. *Corrosion Science*, 109, pp.126-144 <https://doi.org/10.1016/j.corsci.2016.03.022>
- Schlegel, M., Necib, S., Daumas, S., Labat, M., Blanc, C., Foy, E. and Linard, Y. (2018). Corrosion at the carbon steel-clay borehole water interface under anoxic alkaline and fluctuating temperature conditions. *Corrosion Science*, 136, pp.70-90. <https://doi.org/10.1016/j.corsci.2018.02.052>
- Schnurr, A., Marsac, R., Rabung, T., Lützenkirchen, J. and Geckeis, H. (2015). Sorption of Cm(III) and Eu(III) onto clay minerals under saline conditions: Batch adsorption, laser-fluorescence spectroscopy and modeling. *Geochimica et Cosmochimica Acta*, 151, pp.192-202. <https://doi.org/10.1016/j.gca.2014.11.011>
- Scholze, R., Amayri, S. and Reich, T. (2019). Modeling the sorption of Np(V) on Namontmorillonite – effects of pH, ionic strength and CO₂. *Radiochimica Acta*, 107(7), pp. 615-622. <https://doi.org/10.1515/ract-2019-3109>
- Scott, T. B., Allen, G. C., Heard, P. J. and Randell, M. G. (2005). Reduction of U(VI) to U(IV) on the surface of magnetite. *Geochimica et Cosmochimica Acta*, 69(24), pp.5639-5646. <https://doi.org/10.1016/j.gca.2005.07.003>
- Shannon, R. D. (1976). Revised effective ionic radii and systematic studies of interatomic distances in halides and chalcogenides. *Acta Crystallographica Section A*, 32(5), pp. 751-767. <https://doi.org/10.1107/S0567739476001551>
- Shoesmith, D.W. (2006). Assessing the Corrosion Performance of High-Level Nuclear Waste Containers. *CORROSION*, 62(8), pp.703-722. <https://doi.org/10.5006/1.3278296>

- Shoesmith, D.W. and King, F. (1999). The effects of gamma radiation on the corrosion of candidate materials for the fabrication of nuclear waste packages. Atomic Energy of Canada Limited, Technical Report, AECL-11999. <https://www.osti.gov/etdeweb/servlets/purl/20070844>
- Silva, R. J., Bidoglio, G., Rand, M. H., Robouch, P. B., Wanner, H., Puigdomenech, I. (1995). Chemical Thermodynamic of Americium. Nuclear energy agency organisation for economic co-operation and development. <https://www.oecd-nea.org/dbtdb/pubs/amnew-ocr.pdf>
- Silvester, L. F. and Pitzer, K. S. (1976). Thermodynamics of Geothermal Brines, I. Thermodynamic Properties of Vapor-Saturated NaCl(aq) Solutions From 0-300°C. LBL-4456, Berkeley, California 94702. <https://digital.library.unt.edu/ark:/67531/metadc1448443/m1/>
- Singh, B., Kar, A., Kumar, S., Tomar, B., Tomar, R., Manchanda, V. and Ramanathan, S. (2009). Role of magnetite and humic acid in radionuclide migration in the environment. *Journal of Contaminant Hydrology*, 106(3-4), pp.144-149. DOI:[10.1016/j.jconhyd.2009.02.004](https://doi.org/10.1016/j.jconhyd.2009.02.004)
- Skerencak-Frech, A., Fröhlich, D., Rothe, J., Dardenne, K. and Panak, P. (2014). Combined Time-Resolved Laser Fluorescence Spectroscopy and Extended X-ray Absorption Fine Structure Spectroscopy Study on the Complexation of Trivalent Actinides with Chloride at T = 25–200 °C. *Inorganic Chemistry*, 53(2), pp.1062-1069. <https://doi.org/10.1021/ic4025603>
- Smailos, E. (1985). Korrosionsuntersuchungen an ausgewählten metallischsten Werkstoffen als Behälter Materialien für die Endlagerung von hochradioaktiven Abfallprodukten in Steinsalzformationen. INE, Kernforschungszentrum Karlsruhe. Wissenschaftliche Berichte FZKA 3953.
- Smailos, E., Schwarzkopf, W., Köster, R., (1987). Corrosion behavior of container materials for the disposal of high level waste forms in rock salt formation. INE, Kernforschungszentrum Karlsruhe. Wissenschaftliche Berichte FZKA 4265.
- Smailos, E. and Fiehn, B. (1995). In-situ Corrosion Testing of Selected HLW Container Materials under the Conditions of the HLW Test Disposal in the Asse Salt Mine. INE, Kernforschungszentrum Karlsruhe. Wissenschaftliche Berichte FZKA 5508.
- Smailos, E., Schwarzkopf, W., Köster, R., Fiehn, B. and Halm, G. Corrosion testing of selected packaging materials for disposal of high-level waste glass in rock salt formations. INE, Kernforschungszentrum Karlsruhe. Wissenschaftliche Berichte.
- Solé, V.A., Papillon, E., Cotte, M., Walter, P., Susini, J. (2007). A multiplatform code for the analysis of energy-dispersive X-ray fluorescence spectra. *Spectrochimica Acta Part B: Atomic spectroscopy*, 62(1), pp. 63-68. <https://doi.org/10.1016/j.sab.2006.12.002>

- Stumpf, S., Stumpf, T., Dardenne, K., Hennig, C., Foerstendorf, H., Klenze, R. and Fanghänel, T. (2006). Sorption of Am(III) onto 6-Line-Ferrihydrite and Its Alteration Products: Investigations by EXAFS. *Environmental Science & Technology*, 40(11), pp. 3522-3528. <https://doi.org/10.1021/es052518e>
- Stumpf, T., Curtius, H., Walther, C., Dardenne, K., Ufer, K. and Fanghänel, T. (2007). Incorporation of Eu(III) into Hydrotalcite: A TRLFS and EXAFS Study. *Environmental Science & Technology*, 41(9), pp.3186-3191. <https://doi.org/10.1021/es0624873>
- Swaddle, T. W., & Oltmann, P. (1980). Kinetics of the magnetite–maghemite–hematite transformation, with special reference to hydrothermal systems. *Canadian Journal of Chemistry*, 58(17), pp. 1763-1772. DOI: [10.1139/v80-279](https://doi.org/10.1139/v80-279)
- Tanei, H. and Kondo, Y. (2017). Strain Development in Oxide Scale during Phase Transformation of FeO. *ISIJ International*, 57(3), pp.506-510. <https://doi.org/10.2355/isijinternational.ISIJINT-2016-552>
- Terachi, T., Yamada, T., Miyamoto, T., Arioka, K. and Fukuya, K. (2008). Corrosion Behavior of Stainless Steels in Simulated PWR Primary Water—Effect of Chromium Content in Alloys and Dissolved Hydrogen—. *Journal of Nuclear Science and Technology*, 45(10), pp.975-984. <https://doi.org/10.1080/18811248.2008.9711883>
- Tosca, N. J., Ahmed, I. A. M., Tutolo, B. M., Ashpittel, A. and Hurowitz, J. A. (2018). Magnetite authigenesis and the warming of early Mars. *Nature Geoscience*, 11(9), pp.635-639. DOI: [10.1038/s41561-018-0203-8](https://doi.org/10.1038/s41561-018-0203-8)
- Usman, M., Byrne, J. M., Chaudhary, A., Orsetti, S., Hanna, K., Ruby, C., Kappler, A. and Haderlein, S. B. (2018). Magnetite and Green Rust: Synthesis, Properties, and Environmental Applications of Mixed-Valent Iron Minerals. *Chemical Reviews*. 118(7), pp. 3251-3304. <https://doi.org/10.1021/acs.chemrev.7b00224>
- Vacher, L. G., Truche, L., Faure, F., Tissandier, L., Mosser-Ruck, R. and Marrocchi, Y. (2019), Deciphering the conditions of tochilinite and cronstedtite formation in CM chondrites from low temperature hydrothermal experiments. *Meteoritics & Planetary Science*, 54(8), pp. 1870-1889. <https://doi.org/10.1111/maps.13317>
- Van Iseghem, P. (2012). Corrosion issues of radioactive waste packages in geological disposal systems. *Nuclear Corrosion Science and Engineering*, pp. 939–987. Institutional Repository of the Belgian Nuclear Research Centre (SCK-CEN). Woodhead Publishing Series in Energy. <https://doi.org/10.1533/9780857095343.6.939>
- Vayssières, L., (1995). Thèse de doctorat. Université P. et M. Curie, Paris.

- Vidojkovic, S. M. and Rakin, M. P. (2017). Surface properties of magnetite in high temperature aqueous electrolyte solutions: A review. *Advances in Colloid and Interface Science*, 245, pp.108-129. <https://doi.org/10.1016/j.cis.2016.08.008>
- Vilks, P., & Yang, T. (2018). Sorption of Selected Radionuclides on Sedimentary Rocks in Saline Conditions- Updated Sorption Values. Atomic Energy of Canada Limited & Nuclear Waste Management Organisation. NWMO TR-2018-03.
- Wang, Z., Moore, R. C., Felmy, A. R., Mason, M. J. and Kukkadapu, R. K., (2000). A study of the corrosion products of mild steel in high ionic strength brines. *Waste management*, 21(4), pp. 335-341. [https://doi.org/10.1016/S0956-053X\(00\)00058-1](https://doi.org/10.1016/S0956-053X(00)00058-1)
- Wang, G., Um, W., Kim, D., & Kruger, A. A. (2019). ⁹⁹Tc immobilization from off-gas waste streams using nickel-doped iron spinel. *Journal of Hazardous Materials*, 364, pp. 69-77. <https://doi.org/10.1016/j.jhazmat.2018.09.064>
- Westall, J. C., (1982). FITEQL: A Computer Program for Determination of Chemical Equilibrium Constants from Experimental Data, Version 2.0. Report 82-02, Department of Chemistry, Oregon State University, Corvallis.
- Westerman, R. E. and Pitman, S. G. (1984). Corrosion of Candidate Iron-Base Waste Package Structural Barrier Materials in Moist Salt Environments. *Materials Research Society Symposium Proceedings 44*, 279, pp. 279–285. <https://doi.org/10.1557/PROC-44-279>
- Winterle, J., Ofoegbu, G., Pabalan, R., Manepally, C., Mintz, T., Percy, E., Smart, K., McMurry, J., Pauline, R., Fedors, R. (2012). *GEOLOGIC DISPOSAL OF HIGH-LEVEL RADIOACTIVE WASTE IN SALT FORMATIONS*. U.S. Nuclear Regulatory Commission Washington, DC. <https://www.nrc.gov/docs/ML1206/ML12068A057.pdf>
- WIPP, Waste isolation pilot plant. (2019). <https://www.wipp.energy.gov/>
- Wiśniewska, M. and Szewczuk-Karpisz, K. (2013). Removal possibilities of colloidal chromium (III) oxide from water using polyacrylic acid. *Environmental Science and Pollution Research*, 20, pp. 3657-3669. <https://doi.org/10.1007/s11356-012-1273-6>
- WNA, World nuclear association. (2019_a) nuclear power in the world today. <https://www.world-nuclear.org/information-library/current-and-future-generation/nuclear-power-in-the-world-today.aspx>
- WNA, World nuclear association. (2019_b) Storage and disposal of radioactive waste. <https://www.world-nuclear.org/information-library/nuclear-fuel-cycle/nuclear-waste/storage-and-disposal-of-radioactive-waste.aspx>

- WNA, World nuclear association. (2019_c) nuclear fuel cycle, fuel recycling, plutonium. <https://www.world-nuclear.org/information-library/nuclear-fuel-cycle/fuel-recycling/plutonium.aspx>
- Yalçıntaş, E., Gaona, X., Scheinost, A. C., Kobayashi, T., Altmaier, M., & Geckeis, H. (2015). Redox chemistry of Tc(VII)/Tc(IV) in dilute to concentrated NaCl and MgCl₂ solutions. *Radiochimica Acta*, 103(1), pp. 57-72. <https://doi.org/10.1515/ract-2014-2272>
- Yuan, K., Renock, D., Ewing, R. C. and Becker, U. (2015). Uranium reduction on magnetite: Probing for pentavalent uranium using electrochemical methods. *Geochimica et Cosmochimica Acta*, 156, pp.194-206. <https://doi.org/10.1016/j.gca.2015.02.014>
- Zarrouk, S. J., & Purnanto, M. H. (2015). Geothermal steam-water separators: Design overview. *Geothermics*, 53, pp. 236-254. <https://doi.org/10.1016/j.geothermics.2014.05.009>
- Zhang, B., Hao, S., Wu, J., Li, X., Li, C., Di, X. and Huang, Y. (2017). Direct evidence of passive film growth on 316 stainless steel in alkaline solution. *Materials Characterization*, 131, pp.168-174. <https://doi.org/10.1016/j.matchar.2017.05.013>
- Zhou, Q., Ling, Y., Lu, Z., Zhang, M., Zhang, Z., Xiao, T., & Wang, R. (2019). Effect of helium implantation on the hydrogen retention of Cr₂O₃ films formed in an ultra-low oxygen environment. *International Journal of Hydrogen Energy*, 44(48), pp. 26685-26697. <https://doi.org/10.1016/j.ijhydene.2019.08.122>
- Zhu, J., Xu, L., Lu, M., Zhang, L. and Chang, W. (2015). Interaction effect between Cr(OH)₃ passive layer formation and inhibitor adsorption on 3Cr steel surface. *RSC Advances*, 5(24), pp.18518-18522. <https://doi.org/10.1039/C4RA15519J>

Annex

Table A1: Aqueous species of elements of interest in each used database.

		TC		TPA	PI
Am(OH) ₂ ⁺	Cr(OH) ₄ ⁻	Fe(HS) ₂	FeCl ₃ ⁻	Am ⁺³	Fe ⁺²
Am(OH) ₂ ⁺	Cr(OH)Cl ₂	Fe(HSO ₄) ⁺	FeCl ₄ ⁻	Am(OH) ₂ ⁺	Fe ⁺³
Am(OH) ₃	Cr ₂ (OH) ₂₊₄	Fe ⁺²	FeCrO ₄ ⁺	Am(OH) ₃	FeCl ₂ ⁺
Am(OH) ₄ ⁻	Cr ₂ O ₇ ⁻²	Fe ⁺³	FeHSO ₄ ⁺²	Am(OH) ₄ ⁻	FeCl ⁺
AmCl ₂ ⁺	Cr ₃ (OH) ₄₊₅	Fe(OH) ⁺	FeS ₂ O ₃ ⁺	Am(OH) ₂ ⁺	FeCl ₂
AmCl ₂ ⁺	CrCl ⁺	Fe(OH) ₂ ⁺	Ni ⁺²	AmCl ₂ ⁺	FeCl ₂ ⁺
AmO ₂ (OH) ₂ ⁻	CrCl ₂ ⁺	Fe(OH) ₂	Ni(HS) ₂	AmCl ₂ ⁺	FeCl ₃
AmO ₂ OH	CrCl ₂ ⁺	Fe(OH) ₃	Ni(OH) ⁺		FeCl ₄ ⁻
Am ⁺²	CrO ₃ Cl ⁻	Fe(OH) ₃ ⁻	Ni(OH) ₂		Fe(OH) ⁺
Am ⁺³	CrSO ₄ ⁺	Fe(OH) ₄ ⁻	Ni(OH) ₃ ⁻		Fe(OH) ₂
Am ⁺⁴	H ₂ CrO ₄	Fe(OH) ₄ ⁻²	Ni(S ₂ O ₃)		Fe(OH) ₂ ⁺
AmO ₂ ⁺	HCrO ₄ ⁻	Fe(SO ₄)	Ni(SO ₄)		Fe(OH) ₂ ⁺
AmO ₂ ⁺²	Eu ⁺³	Fe(SO ₄) ⁺	Ni(SO ₄) ₂₋₂		Fe(OH) ₃
Cr ⁺²	Eu(OH) ₂ ⁺	Fe(SO ₄) ₂ ⁻	Ni ₂ (OH) ₃		Fe(OH) ₃ ⁻
Cr ⁺³	Eu(OH) ₂ ⁺	Fe ₂ (OH) ₂₊₄	Ni ₄ (OH) ₄₊₄		Fe(OH) ₄ ⁻
CaCrO ₄	Eu(OH) ₃	Fe ₃ (OH) ₄₊₅	NiCl ⁺		Fe ₃ (OH) ₄₍₅₊₎
ClO ₄ ⁻	Eu(OH) ₄ ⁻	FeCl ⁺	NiHS ⁺		Fe ₂ (OH) ₂₊₄
Cr(OH) ⁺	EuCl ₂ ⁺	FeCl ₂ ⁺			Fe(SO ₄) ₂ ⁻
Cr(OH) ₂ ⁺	EuCl ₂ ⁺	FeCl ₂			FeSO ₄
Cr(OH) ₂ ⁺	Fe(H ₃ SiO ₄) ₂ ⁺	FeCl ₂ ⁺			FeSO ₄ ⁺
Cr(OH) ₃	Fe(HS) ⁺	FeCl ₃			FeHSO ₄ ⁺²

Table A2: Overview of chemicals used in this work.

Name	Chemical Formula	Molar mass (g/mol)	Producer/ Supplier
2-(N-morpholino)ethanesulfonic acid (MES)	C ₆ H ₁₃ NO ₄ S	195.24	Sigma-Aldrich, ≥99.5 %
2-Amino-2-(hydroxymethyl)-1,3-propanediol (TRIS)	C ₄ H ₁₁ NO ₃	121.14	Sigma-Aldrich, ≥99.8 %
2-Propanol	C ₃ H ₈ O	60.1	Carl Roth, ≥99.5 %
3-(N-Morpholino)propanesulfonic acid (MOPS)	C ₇ H ₁₅ NO ₄ S	209.26	Sigma-Aldrich, ≥99.5 %
Calcium Chloride dihydrate	CaCl ₂ ·2H ₂ O	147.02	Merck (p.a.)
Chromium Chloride	CrCl ₃	158.35	Merck, ≥98 %
Chromium Hydroxide	Cr(OH) ₃	103	Combi-Blocks, 95 %
Chromium Oxide	Cr ₂ O ₃	151.99	Alfa Aesar, 99.6 %
Epoxy Resin/ Hardener	-	-	Buehler
Ethanol	C ₂ H ₅ OH	46.07	Merck (p.a.)
Hexamethylenetetramine	C ₆ H ₁₂ N ₄	140.19	Sigma-Aldrich, ≥99 %
Hydrochloric acid 37 %	HCl	36.4	Merck (p.a.)
Iron (II) Chloride tetrahydrate	FeCl ₂ ·4H ₂ O	198.81	Acros, ≥99 %
Iron (III) Chloride	FeCl ₃	162.2	Merck, >98 %
Iron (III) Oxide-Hematite	Fe ₂ O ₃	159.69	Alfa Aesar, 99.99 %
Iron Granules	Fe	55.85	Alfa Aesar, 99.98 %
Iron Nickel Oxide-Trevorite	NiFe ₂ O ₄	234.39	Alfa Aesar, ≥99 %
Magnesium Chloride hexahydrate	MgCl ₂ ·6H ₂ O	203.3	Merck (p.a.)
Magnesium Sulfate heptahydrate	MgSO ₄ ·7H ₂ O	246.48	Merck (p.a.)
Nickel (II) Chloride hexahydrate	NiCl ₂ ·6H ₂ O	237.69	Sigma-Aldrich, 99.9 %
Nickel Chromium Oxide	NiCr ₂ O ₄	226.7	Alfa Aesar, ≥99 %
Nickel Oxide	NiO	74.71	Alfa Aesar, 99.99 %
Potassium Chloride	KCl	74.55	Merck (p.a.)
Sodium Chloride	NaCl	58.44	Merck (p.a.)
Sodium Hydroxide	NaOH	40	Merck (p.a.)
Sodium Sulfate	Na ₂ SO ₄	142.04	Merck (p.a.)

Iron granules corrosion in concentrated NaCl and MgCl₂ solutions

In a first series of experiments, zero valent iron (granules) was corroded in concentrated NaCl or MgCl₂ brines at elevated temperature of 60 °C for periods ranging from 2 to 18 weeks. Those experiments were considered as pretests for the following studies on materials foreseen as container wall materials in Germany. It turned out that the setup could not be operated under complete exclusion of air (and oxygen). Note that the outcome of the studies described in this section is, therefore, not entirely applicable to the anaerobic and strongly reducing conditions expected in deep geological repository. Results are nevertheless reported here.

The pH and E_h values were measured, then the liquid was analysed for dissolved iron concentration and the iron granules were examined for formed secondary phases.

Dissolved metals evolution

Exposure/ weeks	$I = 1 \text{ M NaCl}$	$I = 1 \text{ M MgCl}_2$	$I = 3 \text{ M NaCl}$	$I = 9 \text{ M MgCl}_2$
0	0	0	0	0
2	-	-	<0.09	8.76 (0.73)
6	0.137 (5.88)	28.33 (2.03)	0.169 (3.52)	33.6 (0.72)
12	<0.09	60.64 (0.56)	1.017 (11.55)	67.88 (3.31)
18	<0.09	82.47 (1.30)	-	-

From **Table A3** it is clear that the MgCl₂ brine represents an aggressive medium resulting in significantly higher and steadily rising dissolution of iron as compared to NaCl brine. The dissolved amounts of iron in NaCl brines were below or close to the detection limit of 0.09 mg/L all cases. At lower pH_M, the dissolution is higher considering the general iron *Pourbaix* diagram (**Figure 6**), where in the acidic range the oxidation of Fe and the presence of Fe²⁺ dominate in the system, while at higher pH values (neutral and alkaline), iron phases start to precipitate suppressing the dissolution due to passivation of the surface. Overall, the absolute values (max. 82.47 mg/L) are very low considering the initial amount of iron in the system.

pH/ E_h evolution with time

The pH_M values shown in the **Figure A1 A** are the recalculated in-situ pH_M values of the systems at 60 °C using the PhreeqC software, [PI] database with Pitzer approach and the dissolved iron concentrations shown in **Table A3**. There is a clear trend considering the pH_M evolution of the two brines. In case of $MgCl_2$ brine, the pH_M decreases from initial values of 6.5 ± 0.1 and plateaus after about 12 weeks at $pH_M \sim 5.4$. An additional increase is observed for $I = 1$ $MgCl_2$ after 18 weeks to $pH_M 5.9 \pm 0.1$. The pH_M for NaCl increases slightly for $I = 1$ M NaCl from $pH_M 6.0 \pm 0.1$ to 6.3 ± 0.1 , while the value decreases for $I = 3$ M NaCl from 6.6 ± 0.1 to 6.0 ± 0.1 after 6 weeks and further increases to 6.2 ± 0.1 after 12 weeks. The final pH_M values in NaCl brine are all higher than in $MgCl_2$. All the observed variations are within ~ 1 pH_M unit. The use of SIT approach and [TC] database resulted in similar recalculated pH_M values, except for $I = 9$ $MgCl_2$, thus this system has larger uncertainty.

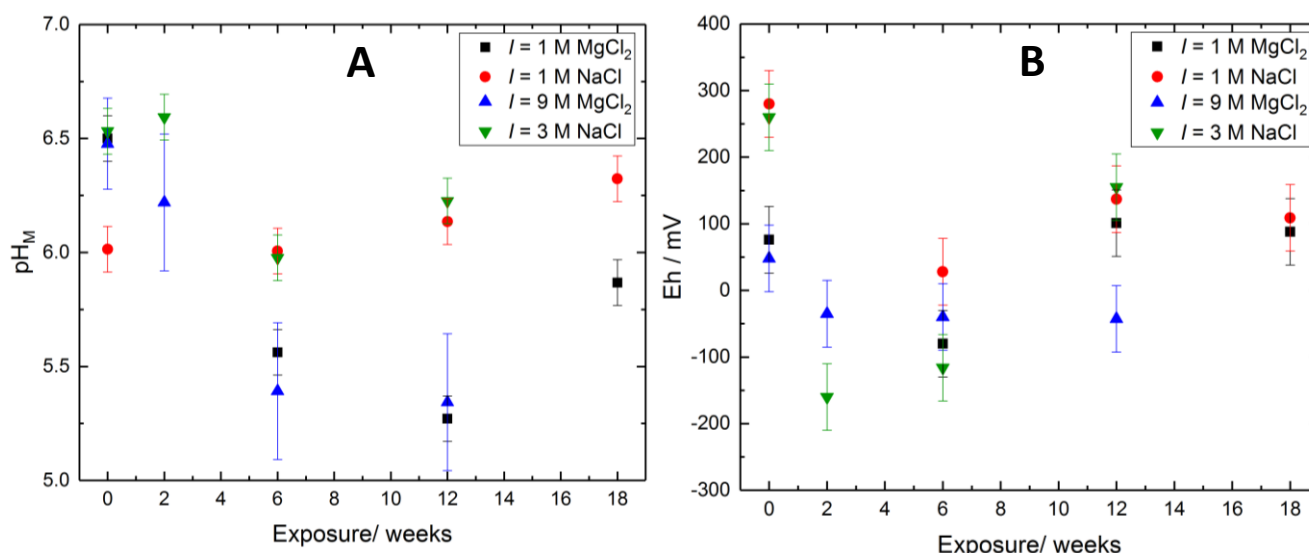


Figure A1: The pH_M (A) and E_h (B) evolution of the zero valent iron experiments. The pH_M is recalculated for 60 °C using the PhreeqC software, [PI] database with Pitzer approach.

The E_h evolution shown in **Figure A1 B** has an initial decreasing trend for all salt levels, and further increase for $I = 1$ M NaCl, $I = 3$ M NaCl and $I = 1$ M $MgCl_2$, confirming the tightness of the setup in the beginning but eventual oxygen intrusion in some cases perhaps due to repeated heating and cooling. The biggest decrease was observed for the $I = 3$ M NaCl, where the value dropped from 260 ± 50 mV to -120 ± 50 mV after which it increased to 155 ± 50 mV after 12 weeks. The decrease in E_h was steady for $I = 9$ M $MgCl_2$, from 48 ± 50 mV to -43 ± 50 mV, where it remained.

Secondary phase characterization and evolution

SEM analyses for solid phase in $I = 1 \text{ M MgCl}_2$ brine showed presence of small octahedral crystals typical for magnetite and occasionally platy crystallites of morphology typical to either green rust chloride or $\text{Fe}(\text{OH})_2$ [Ruby et al., 2009] after 6 and 12 weeks (**Figure A2 A**). However EDX analyses exclude the presence of chloride in the platy structures and the ratio of O/Fe of 2 hints at the presence of $\text{Fe}(\text{OH})_2$, while the composition of the octahedral structures matches magnetite. Interestingly, a small amount of Mg is present in the platy structure, likely replacing part of Fe(II) after 6 and 12 weeks. The magnetite formation seems to be proceeding via the Schikorr reaction where $\text{Fe}(\text{OH})_2$ is transforming into magnetite. The formed presumably magnetite is free of magnesium indicating that it is released upon magnetite formation. The XPS Fe 2*p* analyses (**Figure A3 A**) show presence mainly of Fe(0) (706.5 eV) with small contributions of Fe(II) (709.7 eV) and Fe(III) (710.3 eV) after 6 and 12 weeks. The Fe(II) shoulder is very close to Fe(III) peak in the narrow Fe 2*p* spectrum, hence its intensity is difficult to distinguish. XRD analysis of the precipitate after 6 weeks is too noisy and inconclusive. The XRD pattern of the precipitate after 12 weeks (**Figure A4**) shows peaks matching with magnetite in the database (PDF card 88-0315). This is in agreement with the colour of the precipitate, which was black. Although the pH_M and E_h should not favour the stability of magnetite, it appears that transformation is kinetically slow.

After 18 weeks, the morphology of the secondary phases changed from octahedral to mainly platy crystals, however, not anymore clearly of hexagonal shape (**Figure A2 A**). It could be considered as green rust chloride due to its stability in the pH_M and E_h region [Refait et al., 1998], but the chloride presence was not detected by EDX. Furthermore, magnetite dissolution into $\text{Fe}(\text{OH})_2$ could also be a possibility, however, the XPS Fe 2*p* spectrum showed presence of Fe(III) as dominant species thus likely oxidation occurred on the surface (**Figure A3 A**). Fe/O ratio deduced from EDX is a match with hematite ($\alpha\text{-Fe}_2\text{O}_3$) or maghemite ($\gamma\text{-Fe}_2\text{O}_3$). Both are pure Fe(III) phases. Hematite is known to crystalize in the hexagonal crystallographic system and can be of platy morphology having a sheet like structure, while maghemite crystalizes in the cubic system, being isostructural with magnetite. Hematite is thermodynamically more stable compared to maghemite, although a route of oxidation of magnetite to maghemite and further to hematite is also possible and is a kinetically controlled process [Li et al., 2019].

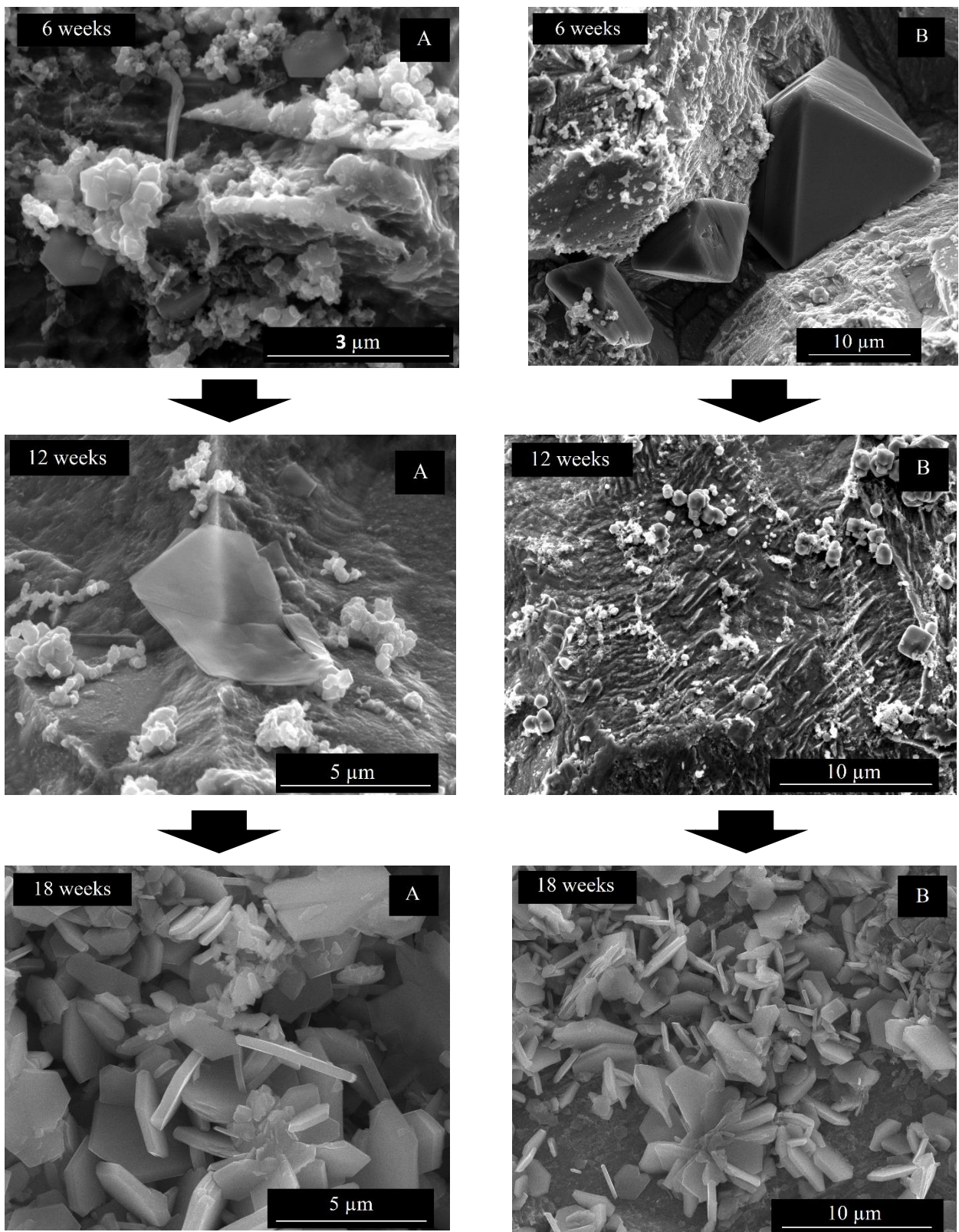


Figure A2: SEM images of the evolution of the solid phase morphology in the $I = 1 \text{ M MgCl}_2$ brine (A) and $I = 1 \text{ M NaCl}$ brine (B) from 6 weeks (top) to 18 weeks (bottom), $T = 60 \text{ }^\circ\text{C}$.

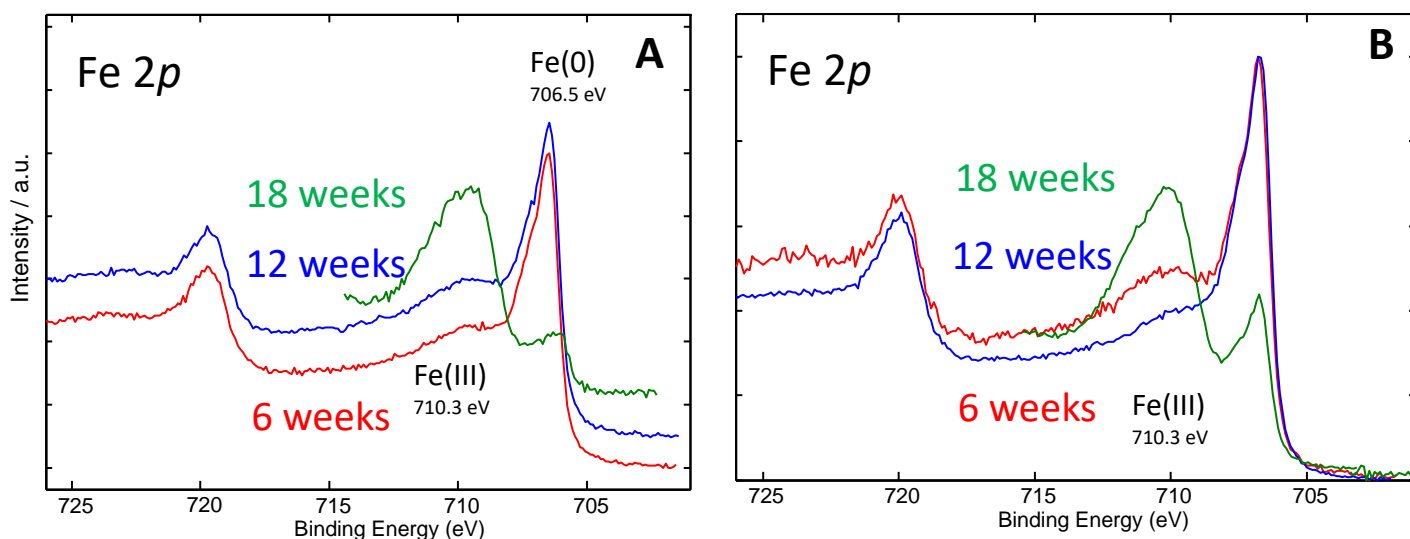


Figure A3: XPS Fe 2p spectra of the solid phase in the $I = 1$ M MgCl_2 brine (A) and $I = 1$ M NaCl brine (B) after 6 weeks (bottom), 12 weeks and 18 weeks (top), $T = 60$ °C.

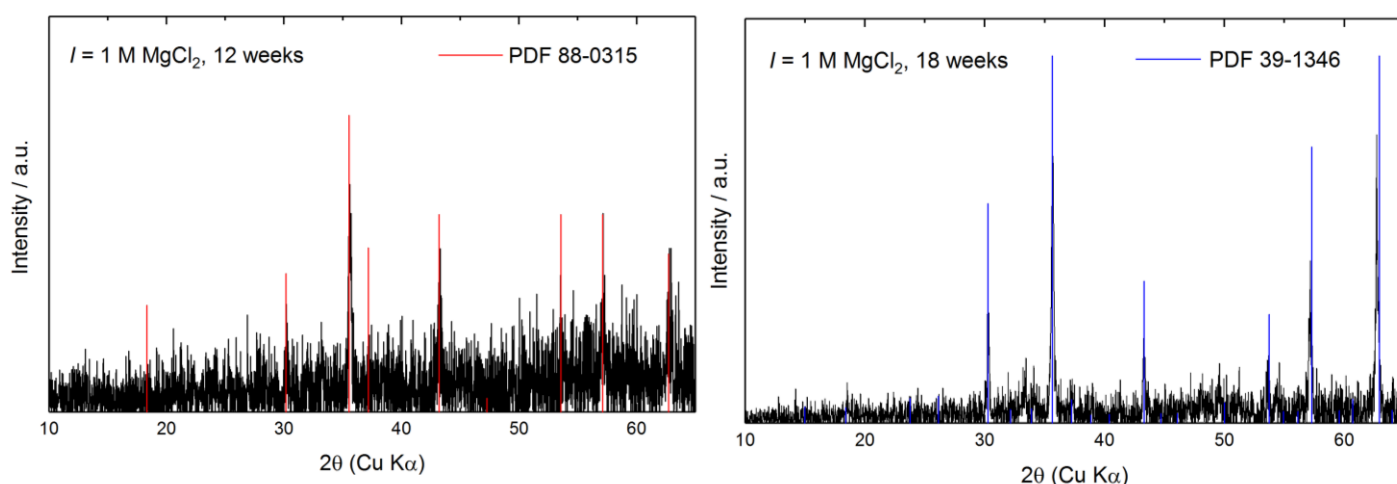


Figure A4: The X-ray diffractogram of the precipitate in $I = 1$ M MgCl_2 brine after 12 and 18 weeks exposure. PDF card 88-0315 refers to magnetite in the database, while the PDF card 39-1346 refers to maghemite.

XRD pattern of the precipitate after 18 weeks (**Figure A4**) shows a match with maghemite (PDF card 39-1346). However, magnetite and maghemite are both cubic and have very similar unit cell parameter. Given the noise level, it cannot be discriminated with certainty, based on XRD only. The colour of the precipitate at this point turned dark red/brown. Hematite is known for its red colour while maghemite has brown colour. It can be concluded that in the MgCl_2 brine with $I = 1$ M, the magnetite was formed via Schikorr reaction from $\text{Fe}(\text{OH})_2$ and (partly) oxidized to hematite. The increase in E_h is a consequence of oxidation, and oxidation may very likely be due to oxygen intrusion through leakages.

In summary, experimental data indicate initial formation of Fe(II) phase, which transforms to magnetite and finally oxidizes to maghemite and/or hematite.

Already in the 1960s, the studies reported various routes of magnetite oxidation. At higher temperatures, greater than 600 °C, the oxidation proceeds directly to hematite, while at lower temperature, the oxidation steps depend on the origin and nature of the starting magnetite [Colombo et al., 1965; Swaddle & Oltmann, 1980]. The final formation of Fe(III) solid phases is in agreement with the outcome of geochemical calculations for the measured pH_M/E_h conditions as shown in the *Pourbaix* diagram (**Figure A5 A**).

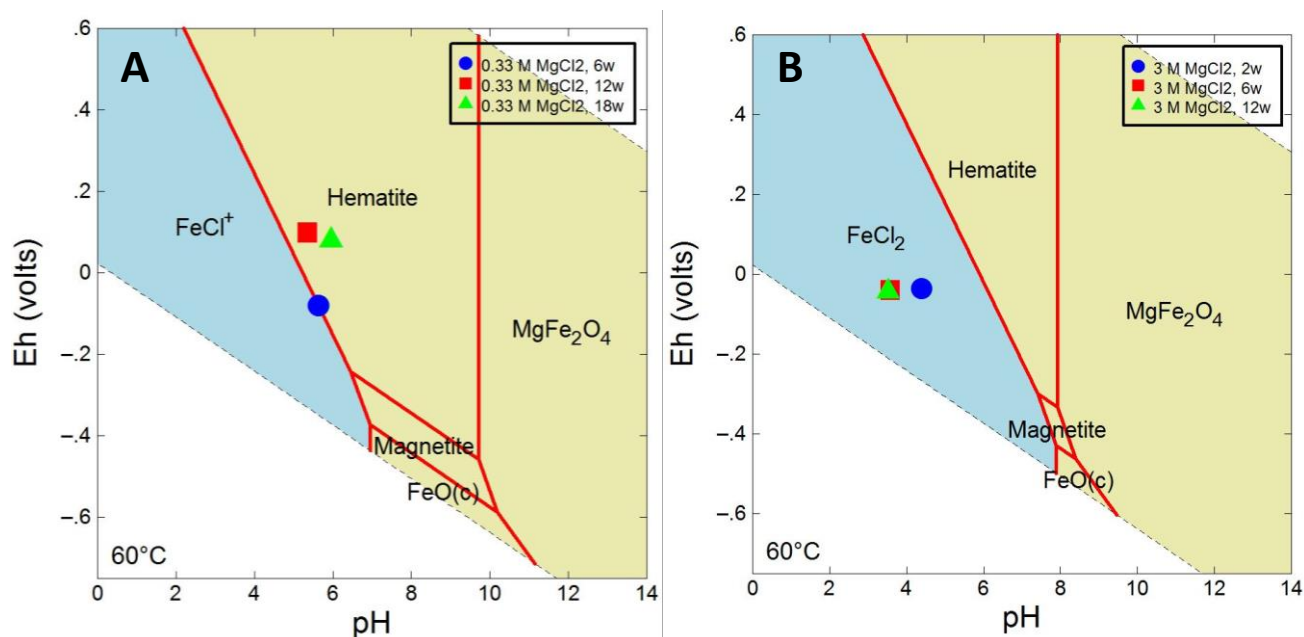


Figure A5: *Pourbaix* diagram for 0.33 M MgCl₂ ($I = 1$ M) (A) and 3 M MgCl₂ ($I = 9$ M) systems at 60 °C using the dissolved metals amounts after 18 and 12 weeks, respectively, Pitzer approach and [PI] database.

The sample in the NaCl brine with the identical ionic strength of 1 M followed very similar evolution. After 6 weeks, the morphology resembled small octahedral crystals, with occasional large crystals in diameter of 10-20 μm (**Figure A2 B**). No platy morphology was observed. The EDX analyses of the small and big crystals showed the absence of chloride and a Fe/O ratio matching that of magnetite. Likewise, the XPS Fe 2*p* spectra show the presence of Fe(II) and Fe(III) after 6 and 12 weeks (**Figure A3 B**). After 12 weeks, once the E_h has increased, the SEM shows small crystallites, but the large ones disappeared.

After 18 weeks, the SEM shows the same platy morphology of the solids (**Figure A2 B**) as in the case of MgCl₂ brine with the identical ionic strength. XPS and EDX analyses follow the same pattern, showing only presence of Fe(III) (**Figure A3 B**) and Fe/O ratio of 2/3 indicating presence of an

oxidized phase like hematite or maghemite. XRD showed a low amount of crystalline precipitates and the presence of salt. The colour of the precipitate was black after 6 weeks and turned red/brown after 18 weeks.

Although the corrosion evolution is similar for the two brines, the concentration of dissolved iron show higher corrosion and dissolution rates for MgCl₂ brine. The presence of the large crystals in NaCl solution may be due to lack of Mg interfering with the Fe(OH)₂ transformation into magnetite and as well due to the higher pH_M, which is favouring the formation of magnetite.

Increasing the ionic strength to $I = 9$ M in MgCl₂ brine, the SEM analyses revealed the absence of corrosion phases after 2 weeks and formation of very few platy crystals after 6 and 12 weeks with no sign of octahedral structure resembling magnetite (**Figure A6 A**). The Fe 2p XPS spectra show only presence of Fe(0) after 2 weeks and an additional peak of Fe(III) after 6 and 12 weeks (**Figure A7 A**). The predominant Fe(0) peak and the otherwise noisy spectrum highlight the lack of a corrosion phase. The EDX could not provide information about the platy morphology of the crystals as they were too thin and too few. The XRD analyses showed only presence of precipitated MgCl₂ after 2, 6 and 12 weeks. This is not surprising as 3 M is a high concentration close to precipitation limit for MgCl₂. In the presence of such high chloride concentration, it was expected that chloride bearing phases would occur. Dissolved Fe concentration of ~ 1 mM can be explained by the solubility of a Fe(III) solid phase with the dissolved iron being Fe(II). The saturation indices calculations for this system using [PI] database showed lack of precipitation of any solid phases, in agreement with the *Pourbaix* diagram generated for this system in **Figure A5 B**, which shows only presence of aqueous FeCl₂ under corresponding experimental conditions.

Similarly, increasing the ionic strength in the NaCl brine to 3 M, the SEM analyses show lack of secondary phases after 2 weeks, presence of octahedral structures of 20-30 μm in diameter and platy structures after 6 weeks, and presence of platy morphology only after 12 weeks (**Figure A6 B**). This behaviour is very similar to the one in NaCl brine with relatively low ionic strength of 1 M. Fe 2p XPS spectra show an increase in Fe(III) with time (**Figure A7 B**), as in the previous cases suggesting oxidation of formed magnetite into pure Fe(III) phase. The EDX analyses of the octahedral and platy structures confirm a Fe/O ratio comparable to that of magnetite and hematite (maghemite) respectively. The X-ray diffractogram of the precipitate shows only salt (halite) after 2 and 6 weeks and presence of maghemite alongside halite after 12 weeks. The colour of the precipitate was brown indicative for the presence of maghemite after 12 weeks. It seems that the precipitated magnetite from the early stages oxidized to maghemite and partially further to hematite. The pH_M and E_h conditions like in the case

of NaCl brine with lower ionic strength favour the initial formation of magnetite transforming with time to the thermodynamically stable Fe(III) phases.

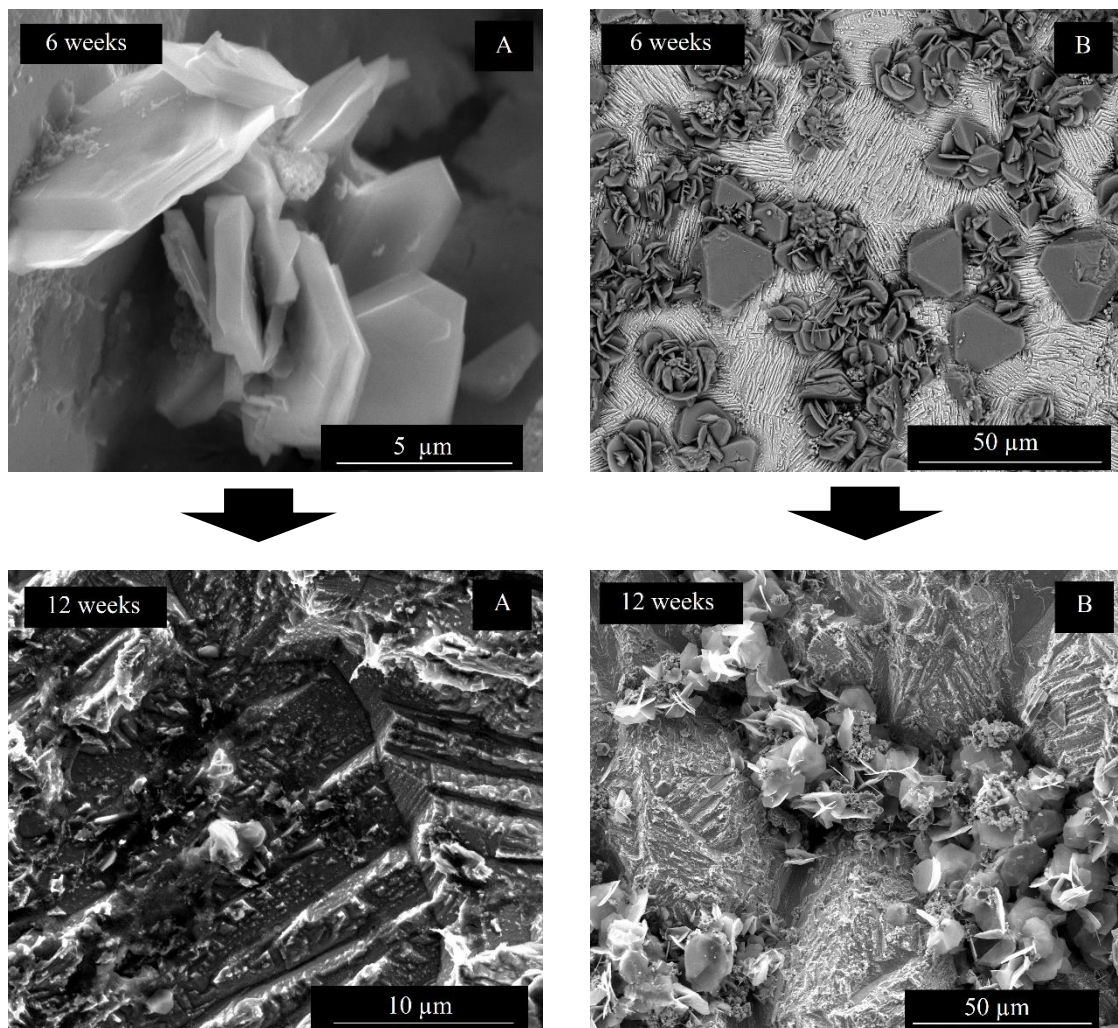


Figure A6: SEM images of the solid phase morphology in the $I = 9 \text{ M MgCl}_2$ brine (A) and $I = 3 \text{ M NaCl}$ brine (B) after 6 weeks (top) and after 12 weeks (bottom), $T = 60 \text{ }^\circ\text{C}$.

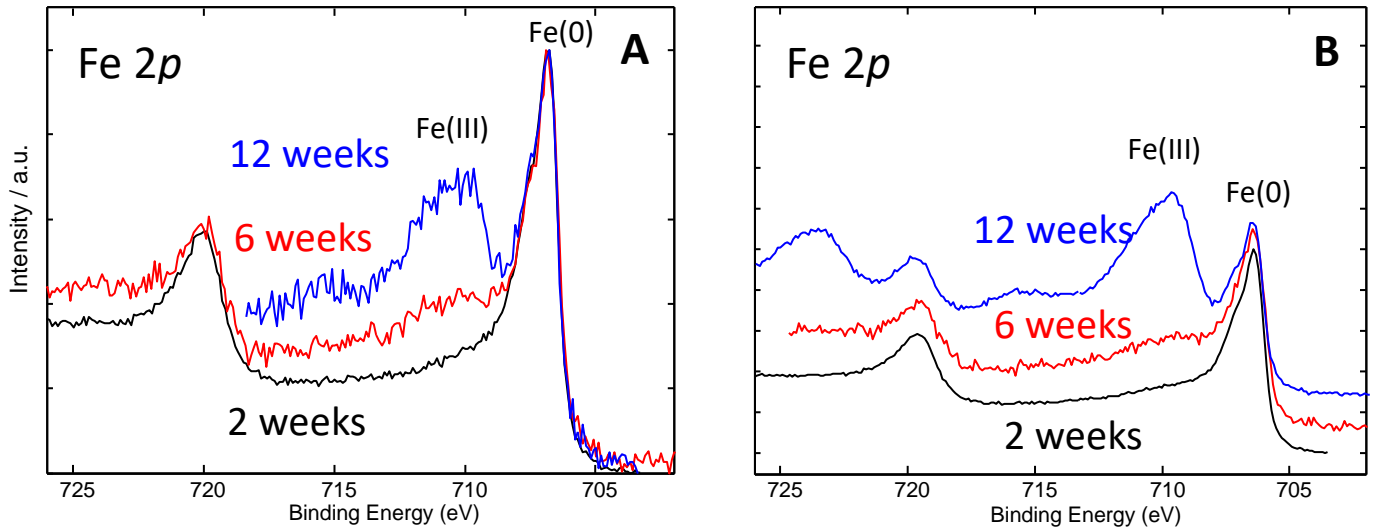
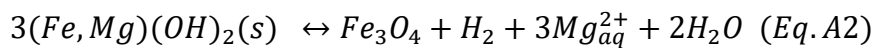
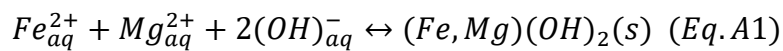
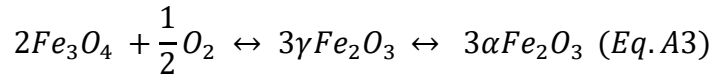


Figure A7: XPS Fe 2p spectra of the solid phase in the $I = 9$ M MgCl₂ brine (A) and $I = 3$ M NaCl brine (B) after 2 weeks (bottom) and after 12 weeks (top), $T = 60$ °C.

Corrosion mechanism

Corrosion rate and type of corrosion cannot be concluded from these experiments due to the nature of the specimen. Under the experimental conditions which are: pure iron specimen corroded in brines with ionic strength up to 9 M under initial anoxic conditions at 60 °C, the corrosion mechanism appears to be proceeding as follows: The zero valent iron oxidizes to aqueous divalent iron which forms the Fe(OH)₂. In case of MgCl₂ brine with $I = 1$ M, a mixed (Mg,Fe)(OH)₂ phase forms (**Eq. 1**) with Mg fraction of up to 10 at. %. Fe(OH)₂ transforms into magnetite, as long as the pH_M is above 5.2 and E_h below 30 mV. Upon transformation, the Mg is released back into solution and no Mg appears to substitute for iron in magnetite (**Eq. A2**). Upon the oxidation to maghemite and to hematite (**Eq. A3**), the E_h proceeds to increase. These mechanisms are well known [Gallagher et al., 1968; Li et al., 2019]. The initial iron oxidation and concomitant water reduction are responsible for the initial E_h decrease in all samples. The formation of Fe(OH)₂ and magnetite (**Eq. 3** and **5**) should not cause any pH_M variation, which corresponds to the experimental observation of only negligible pH_M variation in NaCl brines. However in MgCl₂, HCl is produced by hydrolysis (**Eq. A4**), which could explain the observed initial decrease in pH_M in MgCl₂ brines. Upon further oxidation into maghemite/hematite, minimal pH_M variation is observed.





At $I = 1$ M, both, Mg- and Na- rich brines have shown similar behaviour regarding the development of secondary phases at elevated temperature. This shows that the nature of the cation does not play a role as long as identical ionic strength is achieved. It appears that under the ionic strength in these systems (up to 3 M), the favoured corrosion phase in case of pure iron corrosion is magnetite under reducing conditions and not Cl⁻ bearing phases. Furthermore, under the given experimental conditions, which include presence of oxygen, the final solid phases are Fe(III) phases. These results cannot be transferred to “real” conditions because the setup was clearly not tight and reducing conditions were not maintained.

Table A4: Various configurations of the batch corrosion experiments.

Steel type	Brine type-concentration	T/°C	Exposure	Environment	Fittings for gas sampling	Note
Cr-Ni steel	5 M NaCl	90	13 weeks	heating plate - no box	Yes	O ₂ intrusion
Cr-Ni steel	5 M NaCl	90	13 weeks	heating plate - no box -batch 2	Yes	Crosscut
Cr-Ni steel	5 M NaCl	90	26 weeks	heating plate - nitrogen box	Yes	
Cr-Ni steel	5 M NaCl	90	31 weeks	oven	No	Synchrotron
Cr-Ni steel	5 M NaCl	90	42 weeks	heating plate - nitrogen box	Yes	
Cr-Ni steel	5 M NaCl	25	26 weeks	argon box	Yes	
Cr-Ni steel	5 M NaCl	25	49 weeks	nitrogen box	Yes	
Cr-Ni steel	Brine 3	25	20 weeks	nitrogen box	Yes	
Cr-Ni steel	Brine 3	90	26 weeks	heating plate - no box	Yes	
Cr-Ni steel	0.1 M NaCl	90	28 weeks	oven	No	
Cr-Ni steel	3.4 M MgCl ₂	90	13 weeks	heating plate - no box	Yes	
Cr-Ni steel	3.4 M MgCl ₂	90	13 weeks	heating plate - no box -batch 2	Yes	
Cr-Ni steel	3.4 M MgCl ₂	90	26 weeks	heating plate - nitrogen box	Yes	
Cr-Ni steel	3.4 M MgCl ₂	90	31 weeks	oven	No	Synchrotron
Cr Ni steel	3.4 M MgCl ₂	90	42 weeks	heating plate - nitrogen box	Yes	
Cr-Ni steel	3.4 M MgCl ₂	25	26 weeks	argon box	Yes	
Cr-Ni steel	3.4 M MgCl ₂	25	49 weeks	nitrogen box	Yes	
Cr-Ni steel	Brine 1	25	20 weeks	nitrogen box	Yes	
Cr-Ni steel	Brine 1	90	26 weeks	heating plate - no box	Yes	Crosscut
Cr-Ni steel	0.033 M MgCl ₂	90	28 weeks	oven	No	
SGI	5 M NaCl	90	13 weeks	heating plate - no box	Yes	

SGI	5 M NaCl	90	13 weeks	heating plate - no box -batch 2	Yes	
SGI	5 M NaCl	90	26 weeks	heating plate - nitrogen box	Yes	
SGI	5 M NaCl	90	31 weeks	oven	No	Synchrotron
SGI	5 M NaCl	90	42 weeks	heating plate - nitrogen box	Yes	
SGI	5 M NaCl	25	26 weeks	argon box	Yes	
SGI	5 M NaCl	25	49 weeks	nitrogen box	Yes	
SGI	Brine 3	25	20 weeks	nitrogen box	Yes	
SGI	Brine 3	90	26 weeks	heating plate - no box	Yes	Crosscut
SGI	0.1 M NaCl	90	28 weeks	oven	No	
SGI	3.4 M MgCl ₂	90	13 weeks	heating plate - no box	Yes	
SGI	3.4 M MgCl ₂	90	13 weeks	heating plate - no box -batch 2	Yes	Crosscut
SGI	3.4 M MgCl ₂	90	26 weeks	heating plate - nitrogen box	Yes	
SGI	3.4 M MgCl ₂	90	31 weeks	oven	No	Synchrotron
SGI	3.4 M MgCl ₂	90	42 weeks	heating plate - nitrogen box	Yes	
SGI	3.4 M MgCl ₂	25	26 weeks	argon box	Yes	
SGI	3.4 M MgCl ₂	25	49 weeks	nitrogen box	Yes	
SGI	Brine 1	25	20 weeks	nitrogen box	Yes	
SGI	Brine 1	90	26 weeks	heating plate - no box	Yes	Crosscut
SGI	0.033 M MgCl ₂	90	28 weeks	oven	No	

Table A5: Experimental conditions for the europium sorption.

Solid phase	Background electrolyte (<i>I</i>)	Solid to liquid ratio (g/L)	Investigated pH _M range	Eu concentration
Magnetite	0.1 M NaCl	0.5	5.7-7.6	5.1×10 ⁻¹⁰ M
Magnetite	0.96 M NaCl	0.5	5.5-8.0	5.1×10 ⁻¹⁰ M
Magnetite	2.9 M NaCl	0.5	6.0-8.1	5.1×10 ⁻¹⁰ M
Magnetite	4.8 M NaCl	0.5	6.2-8.1	5.1×10 ⁻¹⁰ M
Magnetite	0.1 M NaCl	0.5	6.0-8.0	1×10 ⁻⁵ M
Magnetite	0.96 M NaCl	0.5	5.5-8.1	1×10 ⁻⁵ M
Magnetite	2.9 M NaCl	0.5	5.5-8.0	1×10 ⁻⁵ M
Magnetite	4.8 M NaCl	0.5	5.5-8.0	1×10 ⁻⁵ M
Magnetite	0.95 M MgCl ₂	0.5	5.5-7.9	5.1×10 ⁻¹⁰ M
Magnetite	0.95 M MgCl ₂	0.5	5.5-8.0	1×10 ⁻⁵ M
Magnetite	2.85 M MgCl ₂	0.5	5.5-8.0	1×10 ⁻⁵ M
Magnetite	9.77 M MgCl ₂	0.5	6.5-8.0	1×10 ⁻⁵ M
Magnetite	0.96 M NaCl	0.5	~ 6	5.1×10 ⁻¹⁰ M–1×10 ⁻⁴ M
Magnetite	2.9 M NaCl	0.5	~ 6	5.1×10 ⁻¹⁰ M–1×10 ⁻⁴ M
Magnetite	4.8 M NaCl	0.5	~ 6	5.1×10 ⁻¹⁰ M–1×10 ⁻⁴ M
Magnetite	0.96 M NaCl	0.5	~ 7	5.1×10 ⁻¹⁰ M–1×10 ⁻⁴ M
Magnetite	2.9 M NaCl	0.5	~ 7	5.1×10 ⁻¹⁰ M–1×10 ⁻⁴ M
Magnetite	4.8 M NaCl	0.5	~ 7	5.1×10 ⁻¹⁰ M–1×10 ⁻⁴ M
Trevorite	0.1 M NaCl	0.08	5.5-8.0	5.1×10 ⁻¹⁰ M
Trevorite	0.96 M NaCl	0.08	5.5-8.1	5.1×10 ⁻¹⁰ M
Trevorite	2.9 M NaCl	0.08	5.8-8.0	5.1×10 ⁻¹⁰ M
Trevorite	4.8 M NaCl	0.08	5.5-8.1	5.1×10 ⁻¹⁰ M
Trevorite	0.1 M NaCl	0.08	5.4-8.0	1×10 ⁻⁵ M
Trevorite	0.96 M NaCl	0.08	5.5-8.0	1×10 ⁻⁵ M
Trevorite	2.9 M NaCl	0.08	5.6-8.0	1×10 ⁻⁵ M
Trevorite	4.8 M NaCl	0.08	5.8-8.5	1×10 ⁻⁵ M
Chromium oxide	0.1 M NaCl	1	4.0-8.7	5.1×10 ⁻¹⁰ M
Chromium oxide	0.94 M NaCl	1	3.7-8.8	5.1×10 ⁻¹⁰ M
Chromium oxide	2.8 M NaCl	1	3.5-9.0	5.1×10 ⁻¹⁰ M
Chromium oxide	4.7 M NaCl	1	3.5-9.0	5.1×10 ⁻¹⁰ M
Chromium oxide	0.1 M NaCl	1	3.0-8.0	1×10 ⁻⁵ M
Chromium oxide	0.94 M NaCl	1	2.7-8.1	1×10 ⁻⁵ M
Chromium oxide	2.8 M NaCl	1	2.7-8.0	1×10 ⁻⁵ M
Chromium oxide	4.7 M NaCl	1	2.7-8.4	1×10 ⁻⁵ M
Chromium oxide	0.1 M NaCl	5.7	4.7-7.9	5.1×10 ⁻¹⁰ M
Chromium oxide	4.7 M NaCl	5.7	5.8-7.9	5.1×10 ⁻¹⁰ M
Chromium oxide	0.1 M NaCl	5.7	4.3-7.8	1×10 ⁻⁵ M
Chromium oxide	4.7 M NaCl	5.7	5.2-7.8	1×10 ⁻⁵ M
Green rust chloride	0.1 M NaCl	1	7.2-8.3	5.1×10 ⁻¹⁰ M
Green rust chloride	0.96 M NaCl	1	7.2-8.9	5.1×10 ⁻¹⁰ M
Green rust chloride	4.8 M NaCl	1	7.4-8.9	5.1×10 ⁻¹⁰ M
Green rust chloride	0.1 M NaCl	1	7.2-8.4	1×10 ⁻⁷ M

Green rust chloride	0.96 M NaCl	1	7.2-8.9	1×10^{-7} M
Green rust chloride	4.8 M NaCl	1	7.4-8.9	1×10^{-7} M
Iron hydroxychloride	0.1 M NaCl	1	6.8-8.6	5.1×10^{-10} M
Iron hydroxychloride	0.94 M NaCl	1	6.7-8.9	5.1×10^{-10} M
Iron hydroxychloride	2.8 M NaCl	1	6.7-9.2	5.1×10^{-10} M
Iron hydroxychloride	4.7 M NaCl	1	7.6-9.0	5.1×10^{-10} M
Iron hydroxychloride	0.1 M NaCl	1	7.0-8.2	1×10^{-7} M
Iron hydroxychloride	0.94 M NaCl	1	6.9-8.2	1×10^{-7} M
Iron hydroxychloride	2.8 M NaCl	1	7.3-8.2	1×10^{-7} M
Iron hydroxychloride	4.7 M NaCl	1	7.3-8.9	1×10^{-7} M
Iron hydroxychloride	0.1 M MgCl ₂	1	7.6-7.8	5.1×10^{-10} M
Iron hydroxychloride	0.95 M MgCl ₂	1	7.1-8.4	5.1×10^{-10} M
Iron hydroxychloride	2.85 M MgCl ₂	1	8.0-8.3	5.1×10^{-10} M
Iron hydroxychloride	9.77 M MgCl ₂	1	7.8-8.7	5.1×10^{-10} M
Iron hydroxychloride	0.1 M MgCl ₂	1	7.4-8.2	1×10^{-7} M
Iron hydroxychloride	0.95 M MgCl ₂	1	6.9-8.3	1×10^{-7} M
Iron hydroxychloride	2.85 M MgCl ₂	1	7.4-8.2	1×10^{-7} M
Iron hydroxychloride	9.77 M MgCl ₂	1	7.9-8.7	1×10^{-7} M

Table A6: Reference samples used for XANES fingerprinting.

Maghemite (γ -Fe ₂ O ₃)	Iron hydroxychloride (Fe ₂ (OH) ₃ Cl)
Akaganeite (β -FeOOH)	Magnetite (Fe ₃ O ₄)
Iron II chloride (FeCl ₂ ·4H ₂ O)	Green rust chloride pure (Fe ₄ (OH) ₈ Cl·nH ₂ O)
Hematite (α -Fe ₂ O ₃)	GR chloride doped ((Ni,Cr,Fe) ₄ (OH) ₈ Cl·nH ₂ O)
Iron III chloride (FeCl ₃)	Chromium oxide (Cr ₂ O ₃)
Trevorite (NiFe ₂ O ₄)	Chromium hydroxide (Cr(OH) ₃)
Iron oxide (FeO)	Nickel hydroxide (Ni(OH) ₂)
Chromite (FeCr ₂ O ₄)	Greenalite (Fe ₂₋₃ Si ₂ O ₅ (OH) ₄)
Cronstedtite (Fe ₃ (Si,Fe)O ₅ (OH) ₄)	

Spheroidal graphite iron corrosion in dilute to concentrated NaCl and MgCl₂ solutions

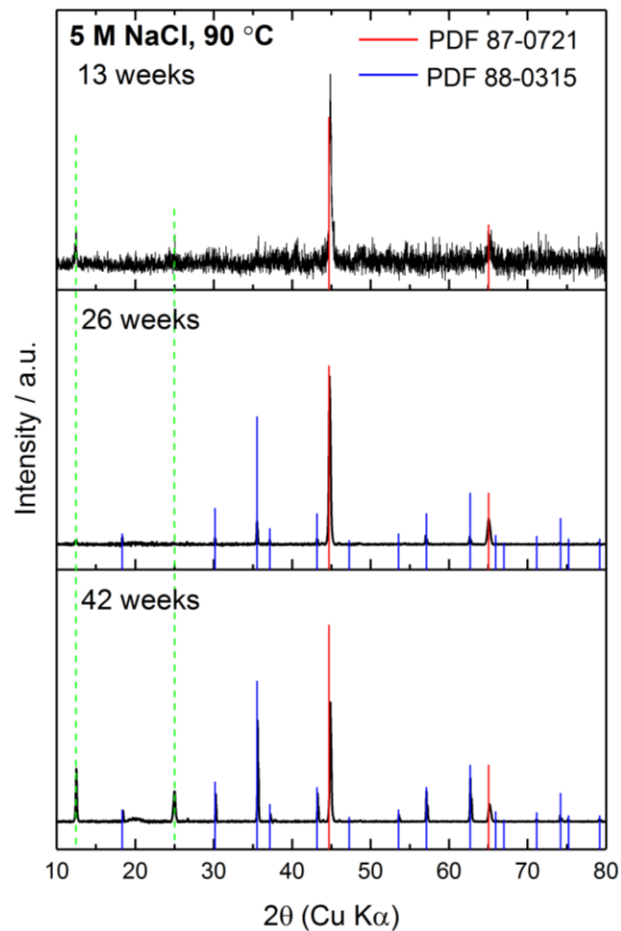


Figure A8: X-ray diffractograms of the spheroidal graphite iron corroded in 5 M NaCl for 13 (top), 26 and 42 weeks (bottom). PDF card 88-0315 refers to magnetite and PDF card 87-0721 refers to initial non-corroded surface - cubic iron.

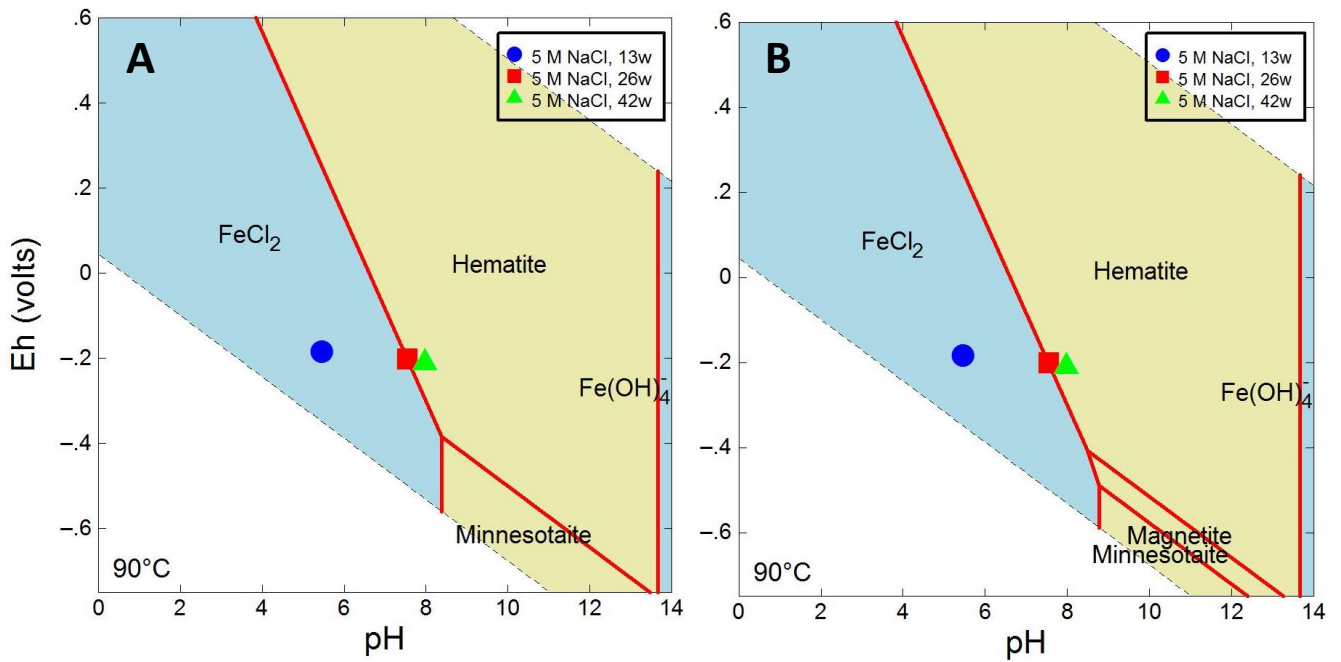


Figure A9: *Pourbaix* diagrams for experiments with SGI in 5 M NaCl system at 90 °C calculated with [PI] database and Pitzer approach. SiO_{2,aq} activity obtained from weight loss, log $a = -2.9$ (A) and reduced SiO_{2,aq} activity log $a = -3.5$ (B).

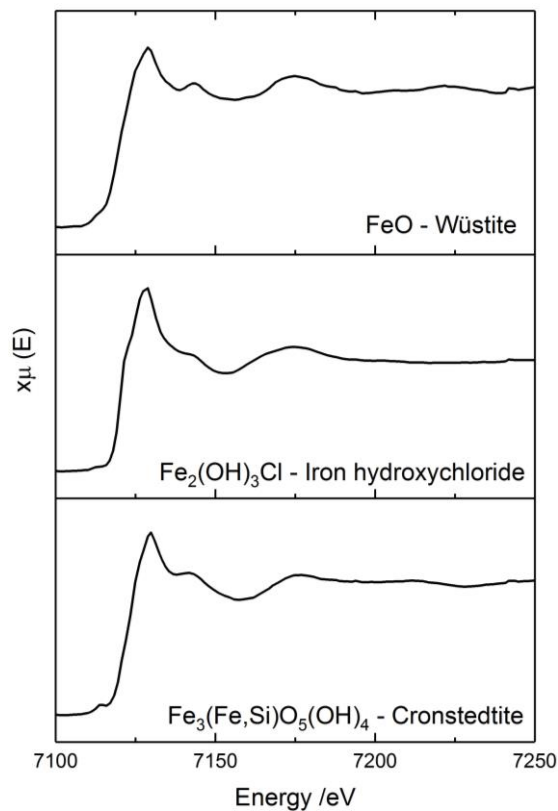


Figure A10: The μ XANES spectra of the reference compounds used for linear combination fitting of the spectra collected for the SGI crosscut samples corroded in 5 M NaCl (Cronstedtite, Iron hydroxychloride I.H.C.) and 3.4 M MgCl₂ (Iron hydroxychloride, Wüstite), examined at the synchrotron.

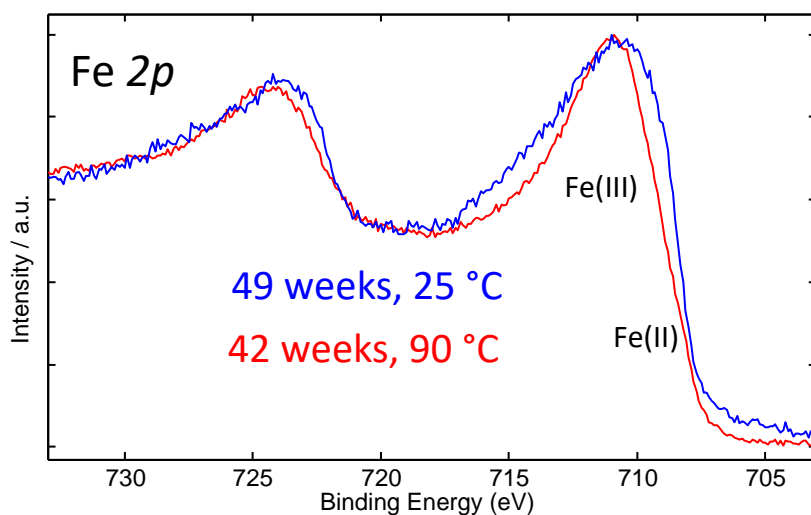


Figure A11: XPS Fe 2p narrow spectra showing evolution as a function of temperature for systems in 5 M NaCl for 42 and 49 weeks at 90 °C and 25 °C, respectively.

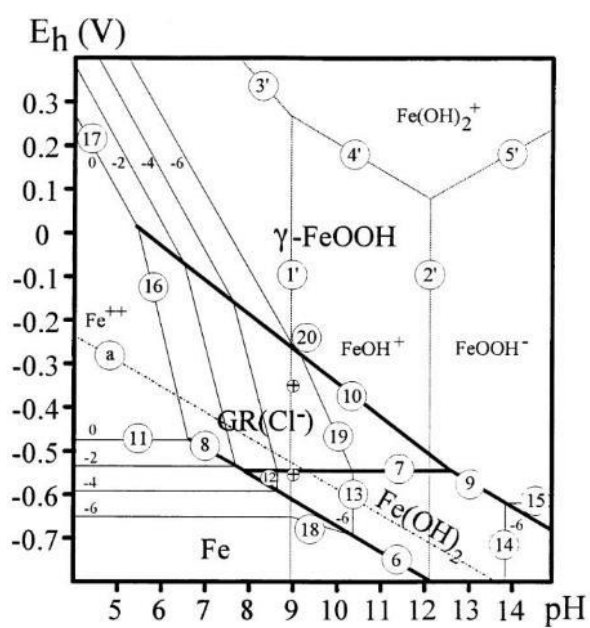


Figure A12: Pourbaix diagram showing the stability window of green rust chloride by Refait et al. [1998].

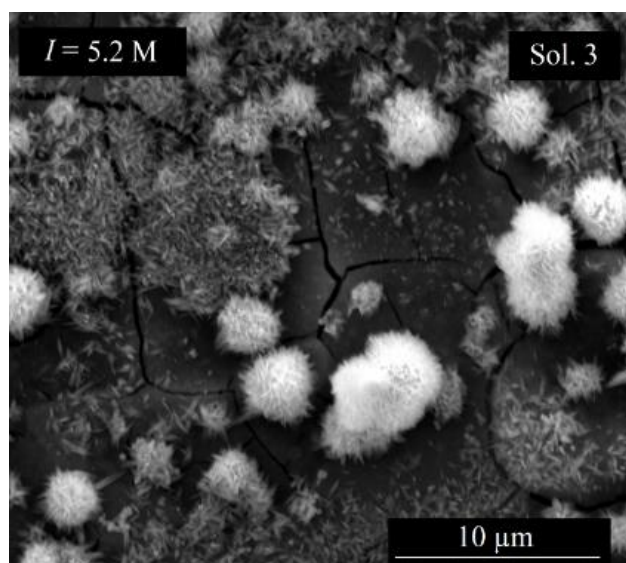


Figure A13: SEM image of the solid phase morphology for $I = 5.2$ M Solution 3, $T = 90$ °C with exposure time of 26 weeks.

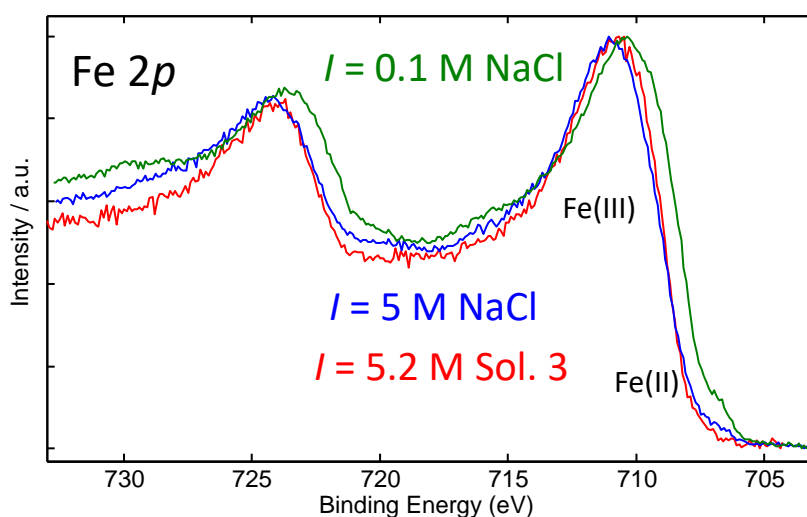


Figure A14: XPS Fe $2p$ spectra of the NaCl based systems with respect to ionic strength and sulfate presence. $T = 90$ °C with exposure time of 26-28 weeks.

XPS analysis of the sample corroded in solution with $I = 0.1$ M NaCl shows similar narrow Fe $2p$ spectra with the presence of Fe(II) and Fe(III) as in solution 3 and in 5 M NaCl, with higher iron (II) content in $I = 0.1$ M NaCl due to slight shift to lower energies.

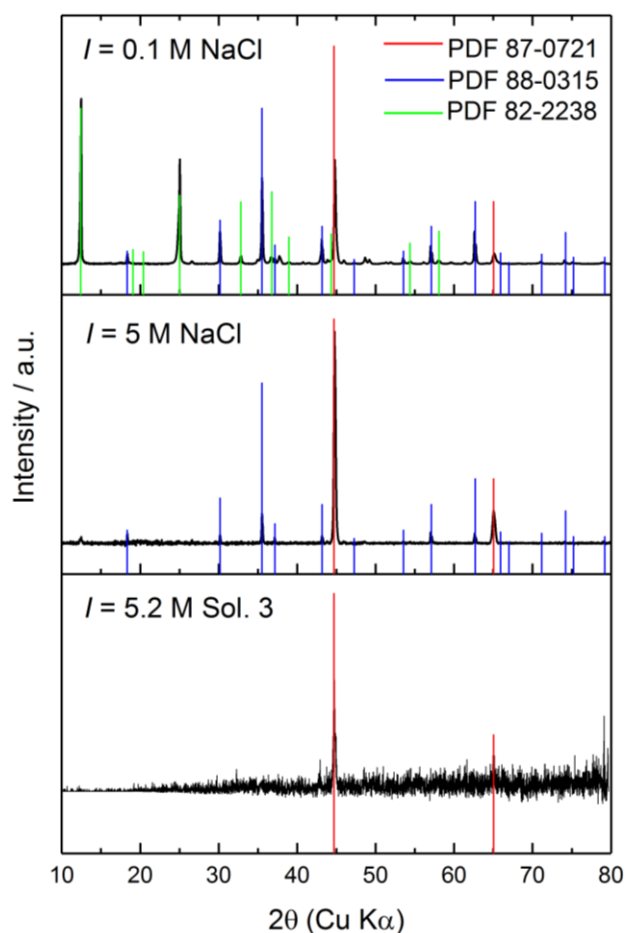


Figure A15: X-ray diffractograms of the spheroidal graphite iron corroded in various brines, $I = 0.1$ M NaCl (top), $I = 5$ M NaCl and $I = 5.2$ M Solution 3 (bottom). PDF card 87-0721 to initial SGI, 88-0315 to magnetite and 82-2238 to silicate phase cronstedtite.

Table A7: The chemical composition of the observed corrosion products according to the morphology in solution 3 at 90 °C.

Element / Atomic %	Si	Fe	O	Mg
Solution 3 - Hexagonal structure, Spot 1	7.54±0.12	25.74±0.36	61.6±0.65	5.12±0.14
Solution 3 - Hexagonal structure, Spot 2	7.67±0.18	22.77±0.5	64.21±0.84	5.36±0.2

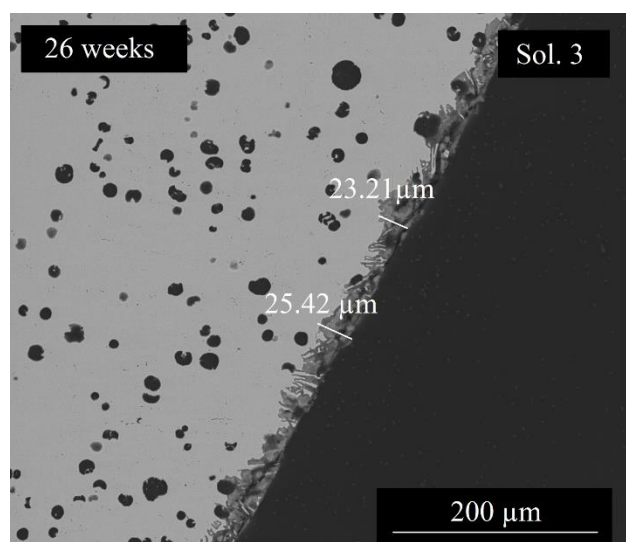


Figure A16: SEM image of the crosscut SGI corroded in solution 3 for 26 weeks at 90 °C.

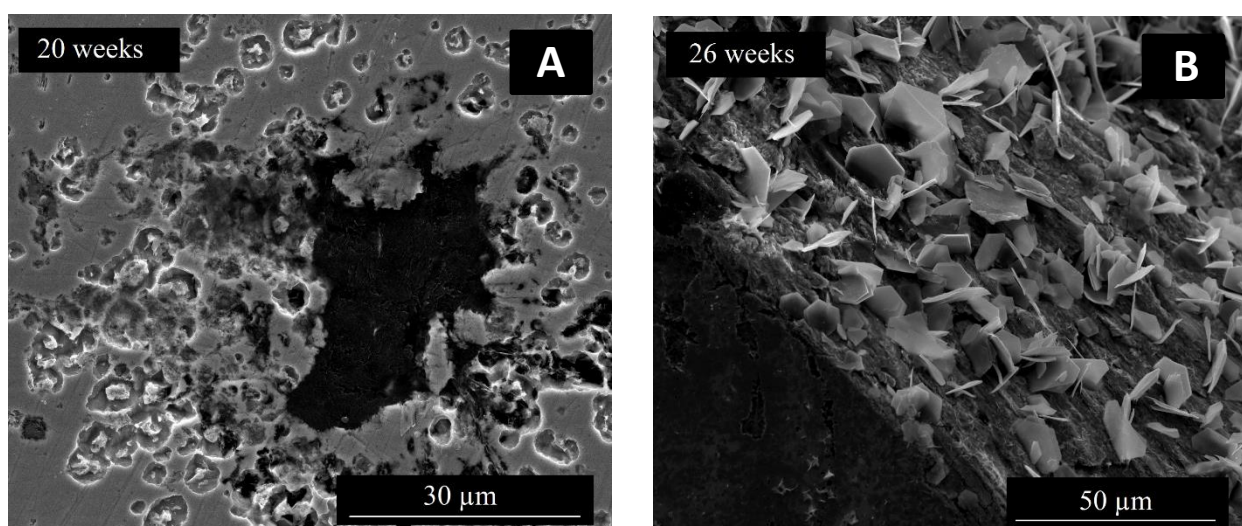


Figure A17: SEM images of the evolution of the solid phase/surface morphology in the solution 3, $I = 5.2$ M, $T = 25$ °C (A - close to graphite inclusion; B - inside the hole).

Table A8: The chemical composition of the observed corrosion products according to the morphology in solution 3 at 25 °C.

Element / Atomic %	Na	Fe	O	S
26 weeks - Hexagonal structure, Spot 1	13.33±0.77	19.62±0.80	60.2±1.27	6.85±0.31
26 weeks - Hexagonal structure, Spot 2	14.88±0.47	20.76±0.47	57.51±0.82	6.86±0.18
26 weeks - Hexagonal structure, Spot 3	11.66±0.74	26.81±0.79	55.97±1.12	5.56±0.26

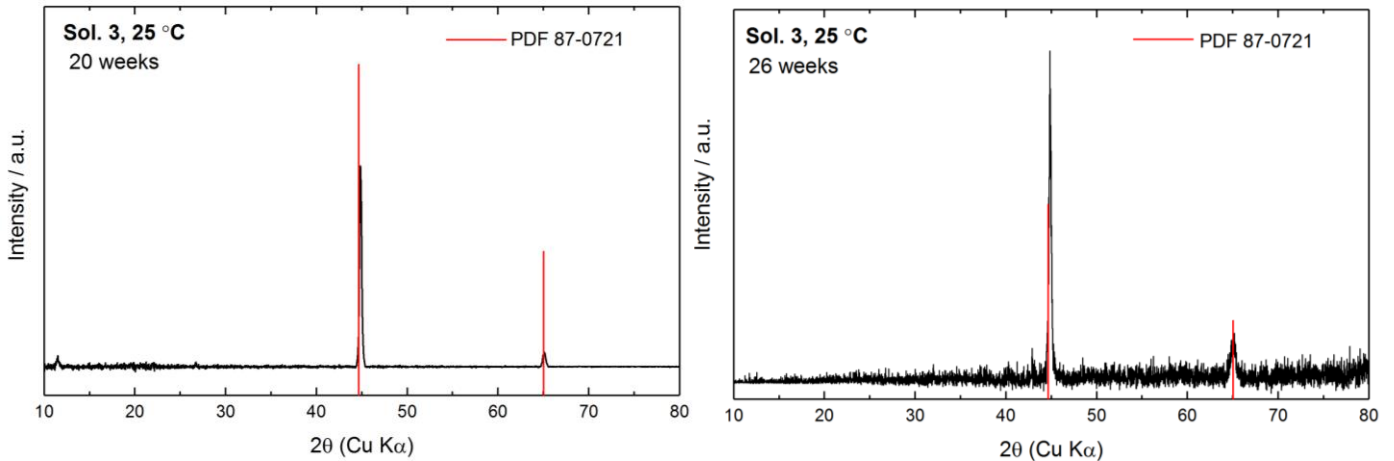


Figure A18: X-ray diffractograms of the spheroidal graphite iron corroded in solution 3 ($I = 5.2$ M) for 20 and 26 at 25 °C. PDF card 87-0721 refers non-corroded steel surface, cubic iron.

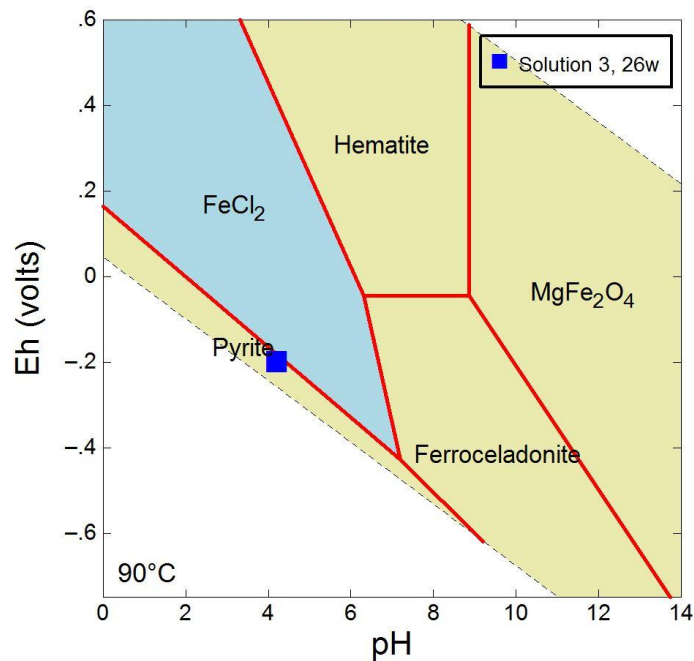


Figure A19: *Pourbaix* diagram for the solution 3 system at 90 °C after 26 weeks calculated using Pitzer approach for activity coefficients calculations and [PI] database.

The mineral ferroceldonite ($K_2Fe_2(Si_8O_{20})(OH)_4$) is another silicate mineral, including potassium, which is part of the solution 3.

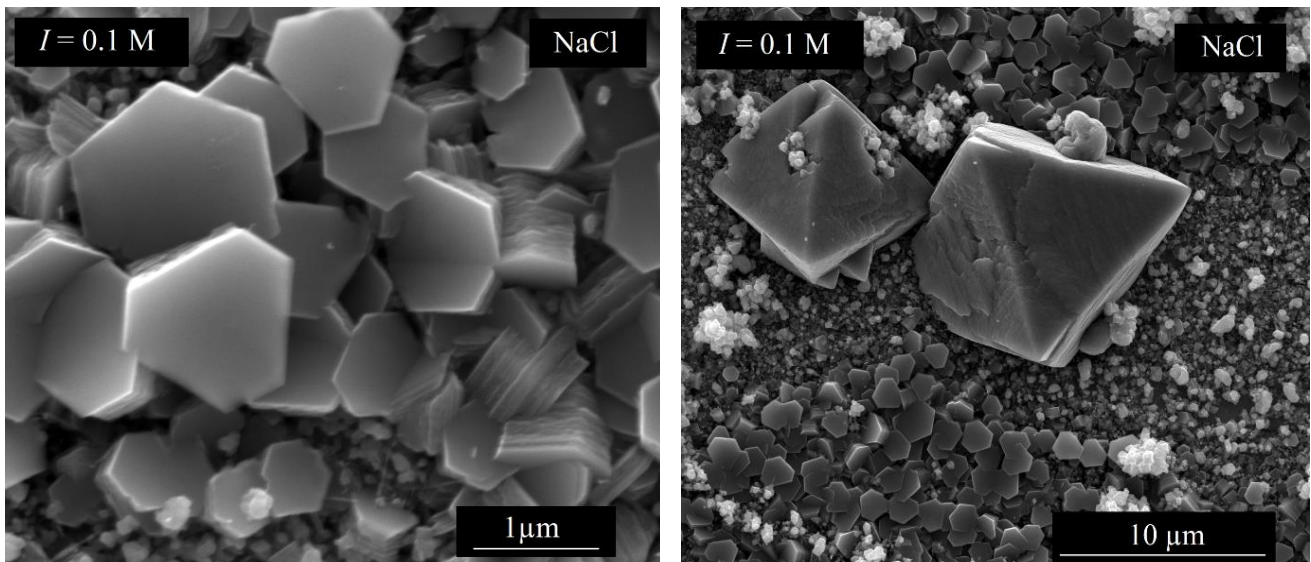


Figure A20: SEM images of the solid phase morphology for $I = 0.1$ M NaCl, $T = 90$ °C with exposure time of 28 weeks applying two microscope magnifications.

The EDX analyses of the samples in the dilute systems (*Table A9*) showed similar composition for the bright small crystallites, similar to the composition of the octahedral structure, matching the Fe/O ratio of magnetite. The small crystallites are likely small magnetite structures, which grow into the large ones, similarly as in the process observed in 5 M NaCl brine after 23 and 42 weeks.

Table A9: The chemical composition of the observed corrosion products according to the morphology in $I = 0.1$ M NaCl.

Element / Atomic %	Si	Fe	O
$I = 0.1$ M NaCl - Octahedral structure	2.00±0.26	39.47±1.30	58.53±1.45
$I = 0.1$ M NaCl - Small bright crystallites, Spot 1	2.95±0.38	40.25±1.84	56.81±1.87
$I = 0.1$ M NaCl - Small bright crystallites, Spot 2	3.17±0.26	41.17±1.23	55.66±1.34
$I = 0.1$ M NaCl - Small bright crystallites, Spot 3	3.38±0.34	37.46±1.58	59.16±1.77
$I = 0.1$ M NaCl - Small bright crystallites, Spot 4	2.81±0.30	39.08±1.48	58.11±1.61
$I = 0.1$ M NaCl - Hexagonal structure, Spot 1	9.14±0.32	27.40±1.04	63.22±1.42
$I = 0.1$ M NaCl - Hexagonal structure, Spot 2	8.00±0.39	30.12±1.36	61.08±1.60
$I = 0.1$ M NaCl - Hexagonal structure, Spot 3	8.26±0.31	30.08±1.12	61.65±1.40

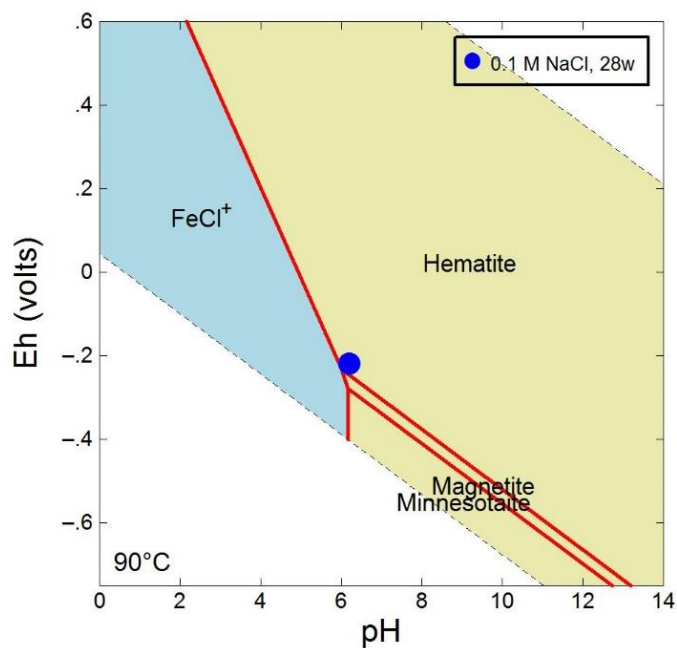


Figure A21: *Pourbaix* diagram for the 0.1 M NaCl system at 90 °C after 28 weeks calculated using SIT approach and [TC] database.

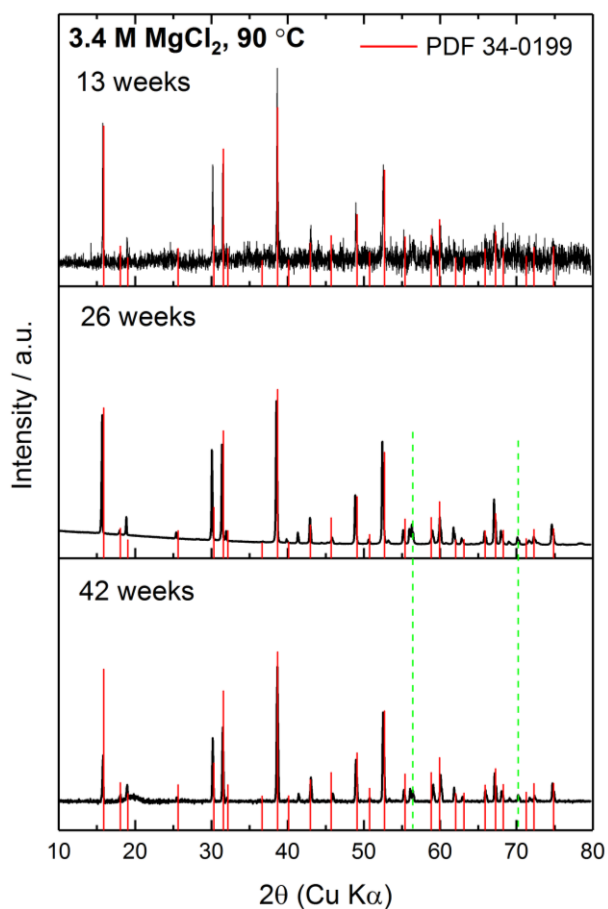


Figure A22: X-ray diffractograms of the spheroidal graphite iron corroded in 3.4 M MgCl₂ ($I = 10.2$ M) for 13 (top), 26 and 42 weeks (bottom). PDF card 34-0199 refers to iron hydroxychloride. The dotted green lines match the amakinite, (Mg,Fe)(OH)₂ phase (PDF card 15-0125).

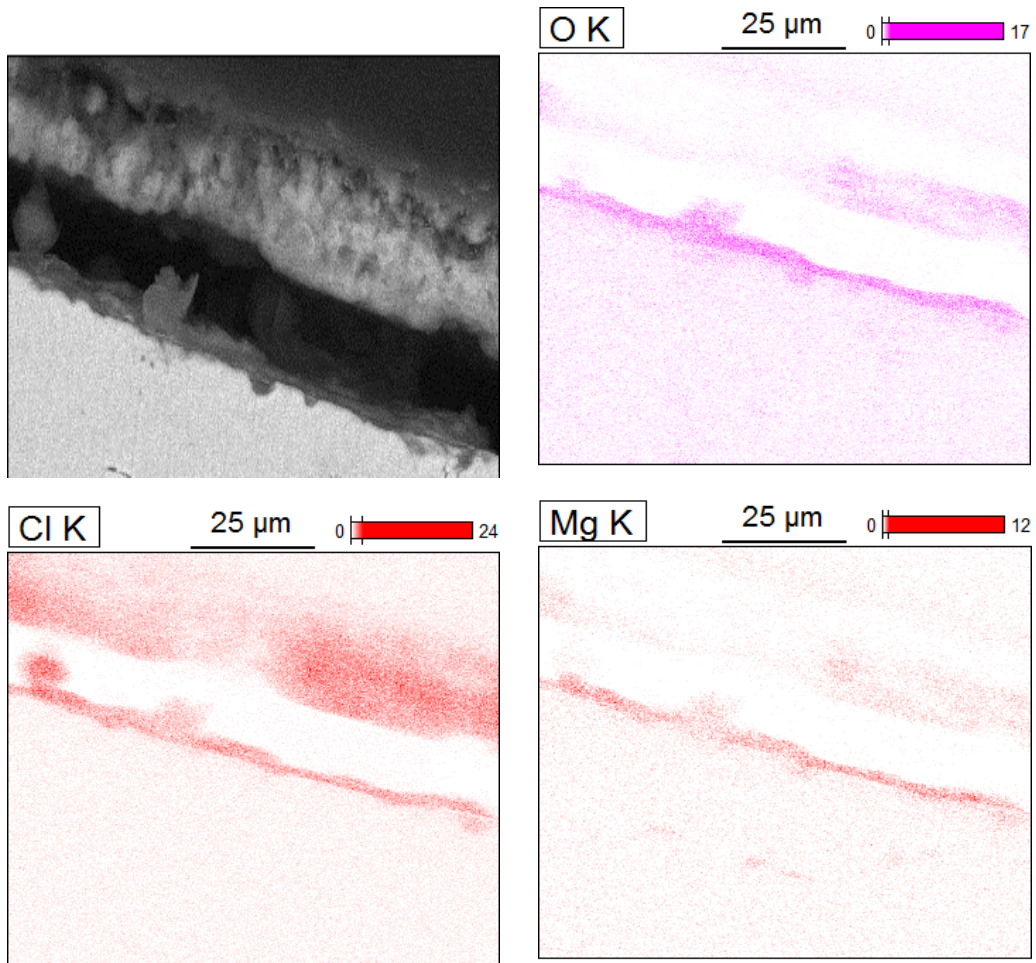


Figure A23: Elemental distribution obtained by EDX analysis of SGI crosscut corroded in 3.4 M MgCl_2 for 13 weeks at 90 °C.

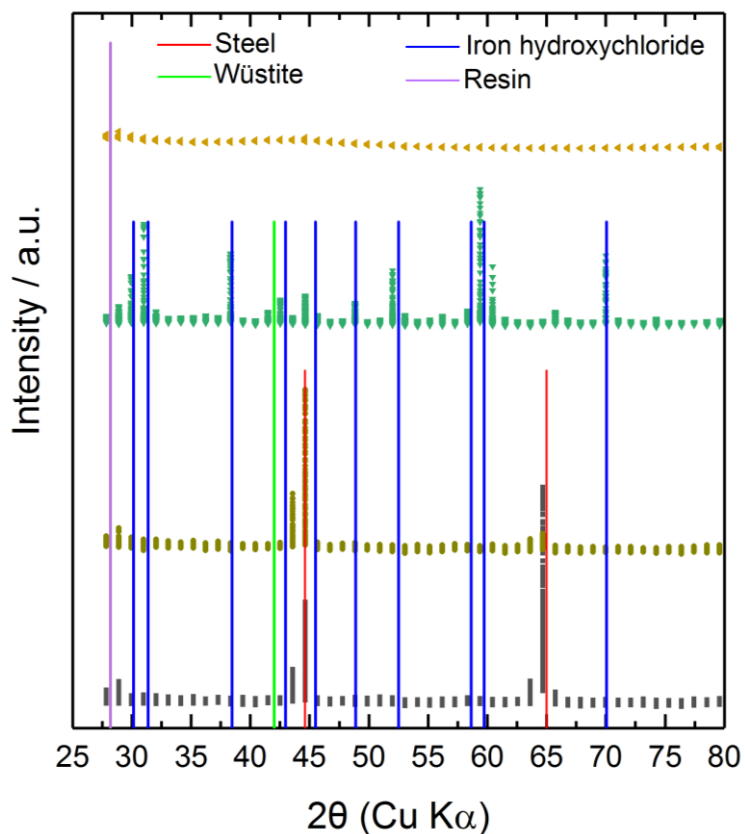


Figure A24: μ XRD line scan through the interface steel-corrosion layer-resin of the 3.4 M MgCl_2 SGI crosscut sample.

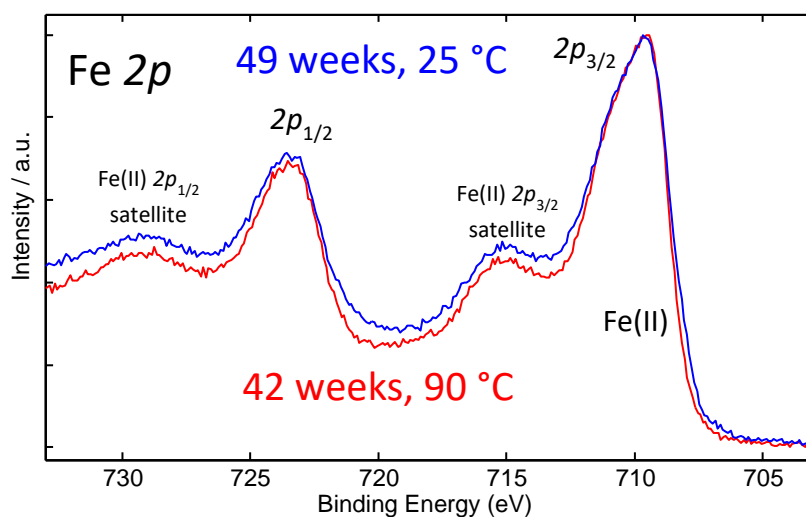


Figure A25: XPS Fe 2p narrow spectra for SGI in 3.4 M MgCl_2 corroded for 42 and 49 weeks at 90 °C and 25 °C respectively.

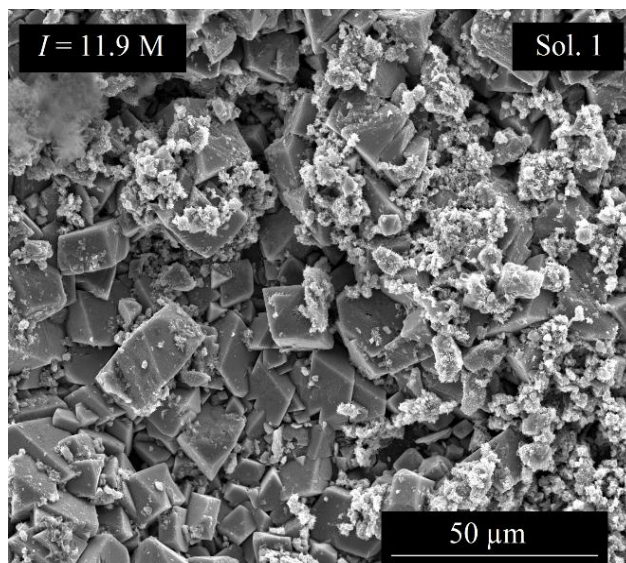


Figure A26: SEM image of the solid phase morphology for $I = 11.9$ M Solution 1, $T = 90$ °C with exposure time of 26 weeks.

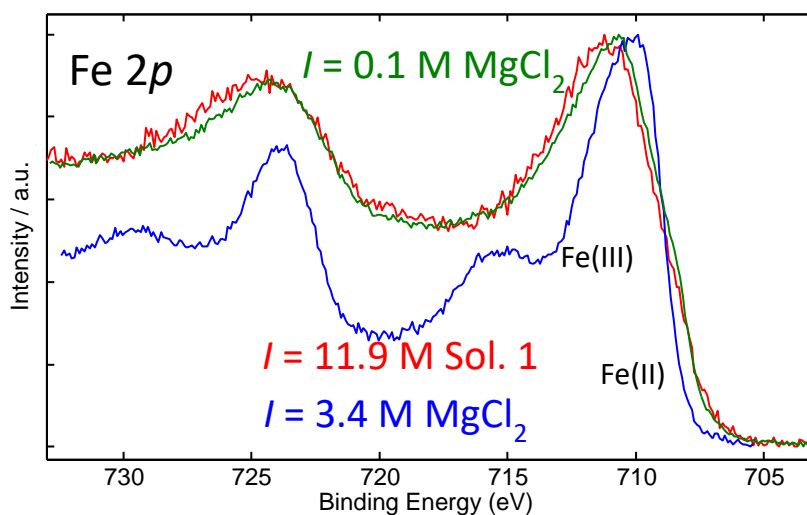


Figure A27: XPS Fe $2p$ spectra of the $MgCl_2$ based systems with respect to different brines. $T = 90$ °C with exposure time of 26-28 weeks.

Table A10: The chemical composition of the observed corrosion products according to morphology in solution 1.

Element / Atomic %	Fe	O	Mg	Cl
Solution 1- Pyramid structure	23.20±0.68	54.07±1.14	8.23±0.29	14.5±0.32
Solution 1 - Additional phase	19.24 ±0.63	57.44±1.06	13.8±0.33	9.51±0.28

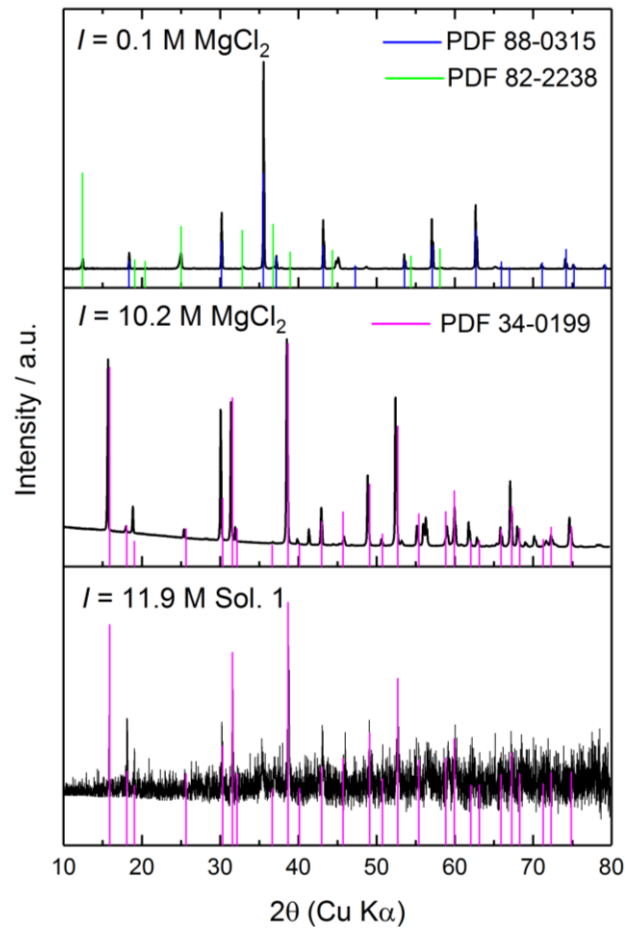


Figure A28: X-ray diffractogram of the spheroidal graphite iron corroded in various brines, $I = 0.1$ M MgCl_2 (top), $I = 3.4$ M MgCl_2 and $I = 11.9$ M Solution 1 (bottom). PDF 34-0199 refers to iron hydroxychloride, 88-0315 to magnetite and 82-2238 to silicate phase cronstedtite.

X-ray diffractogram for 0.033 M MgCl_2 ($I = 0.1$ M) shows similar pattern as in the case of $I = 0.1$ M NaCl with peaks matching magnetite and cronstedtite. The peak corresponding to the initial steel is in this case very small.

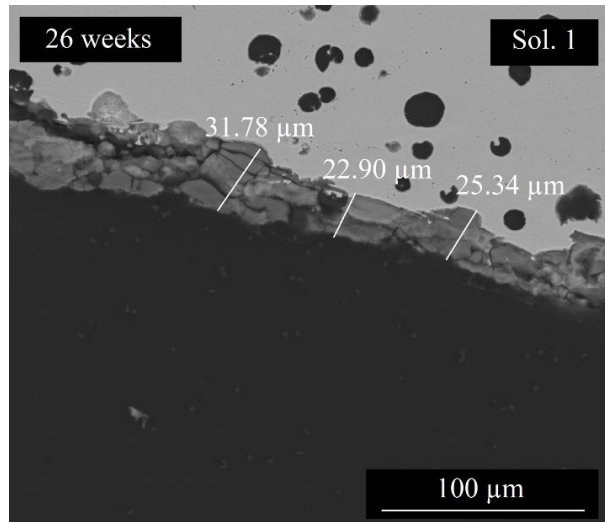


Figure A29: SEM image of the SGI crosscut corroded in solution 1 for 26 weeks at 90 °C.

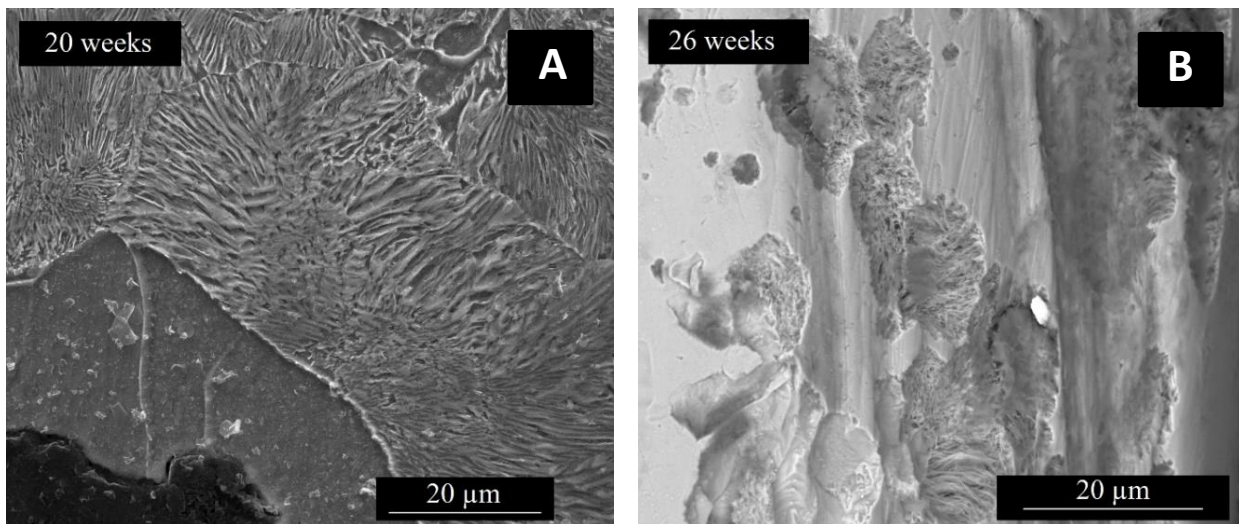


Figure A30: SEM images of the evolution of the solid phase/surface morphology in the solution 1, $I = 11.9 \text{ M}$ after 20 weeks in the proximity of graphite inclusion (A) and after 26 weeks at the edge of the sample (B), $T = 25 \text{ }^\circ\text{C}$.

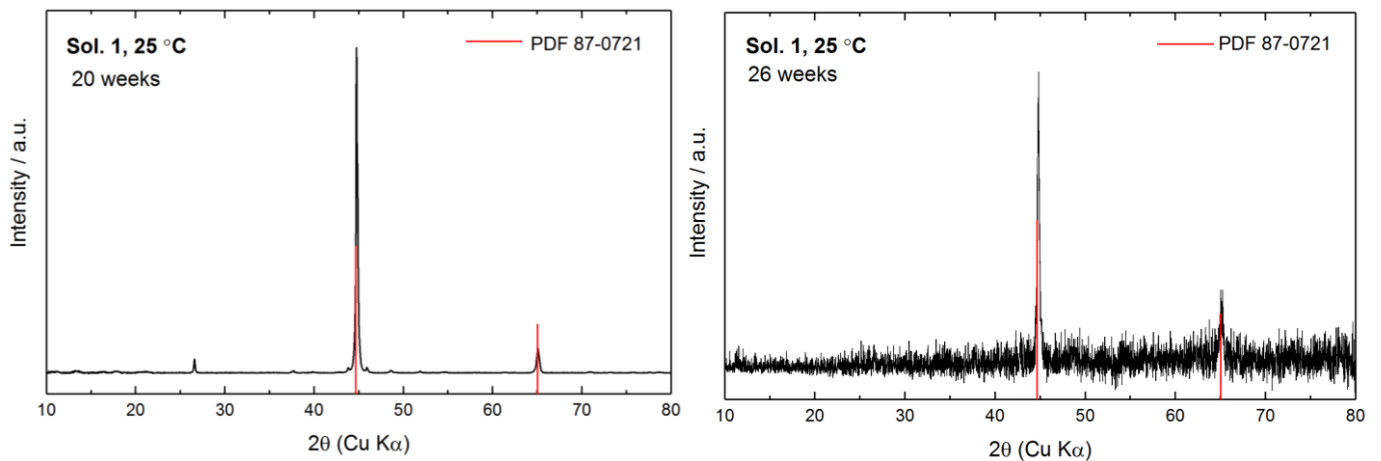


Figure A31: X-ray diffractograms of the spheroidal graphite iron corroded in solution 1 ($I = 11.9$ M) for 20 and 26 weeks at 25 °C. PDF card 87-0721 refers non-corroded steel surface, cubic iron.

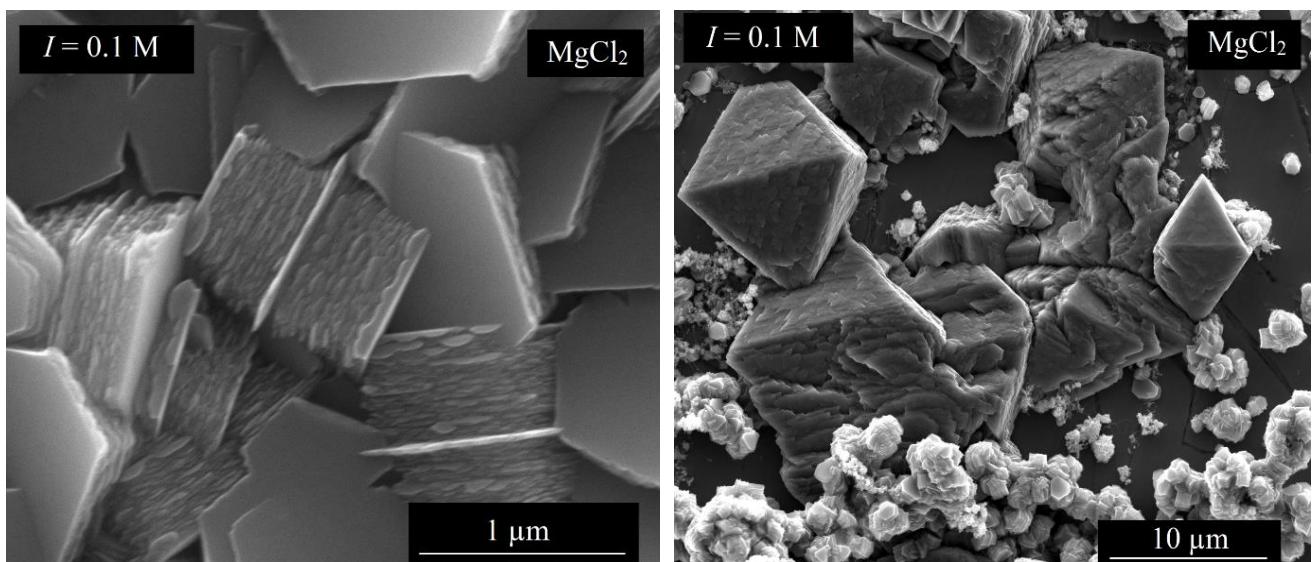


Figure A32: SEM image of the solid phase morphology for $I = 0.1$ M MgCl_2 , $T = 90$ °C with exposure time of 28 weeks applying two microscope magnifications.

Table A11: The chemical composition of the observed corrosion products according to morphology in $I = 0.1$ M MgCl_2 .

Element / Atomic %	Si	Fe	O	Mg
$I = 0.1$ M MgCl_2 - Octahedral structure, Spot 1	2.57 ± 0.29	37.42 ± 1.45	60.01 ± 1.64	-
$I = 0.1$ M MgCl_2 - Octahedral structure, Spot 2	2.25 ± 0.19	39.02 ± 0.72	58.74 ± 1.05	-
$I = 0.1$ M MgCl_2 - Small bright crystallites	3.11 ± 0.24	41.66 ± 1.00	55.23 ± 1.16	-
$I = 0.1$ M MgCl_2 - Hexagonal structure, Spot 1	9.22 ± 0.82	23.11 ± 2.65	64.8 ± 3.22	2.87 ± 0.55
$I = 0.1$ M MgCl_2 - Hexagonal structure, Spot 2	9.68 ± 0.31	21.39 ± 0.92	65.7 ± 1.46	3.23 ± 0.30
$I = 0.1$ M MgCl_2 - Hexagonal structure, Spot 3	9.22 ± 0.23	21.36 ± 0.66	66.39 ± 1.32	3.02 ± 0.21

Cr-Ni steel corrosion in dilute to concentrated NaCl and MgCl₂ solutions

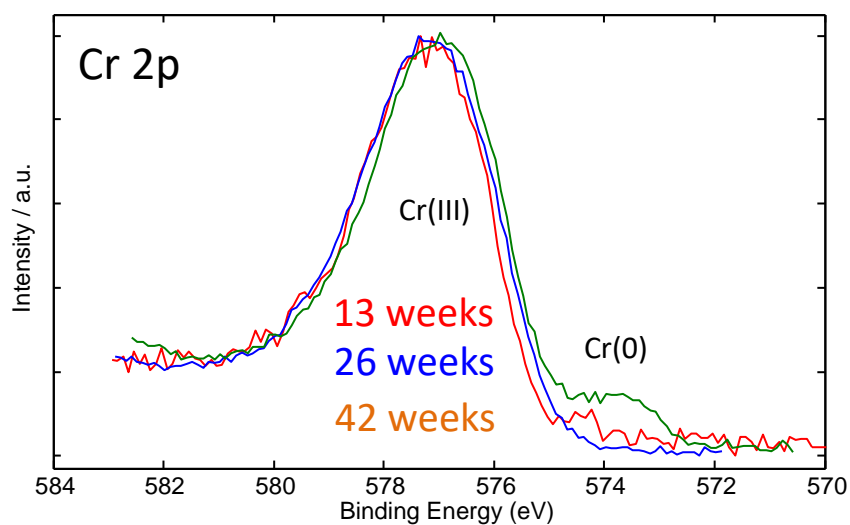


Figure A33: The XPS Cr 2p spectra with respect to time evolution of the corrosion products/ surface in 5 M NaCl sample.

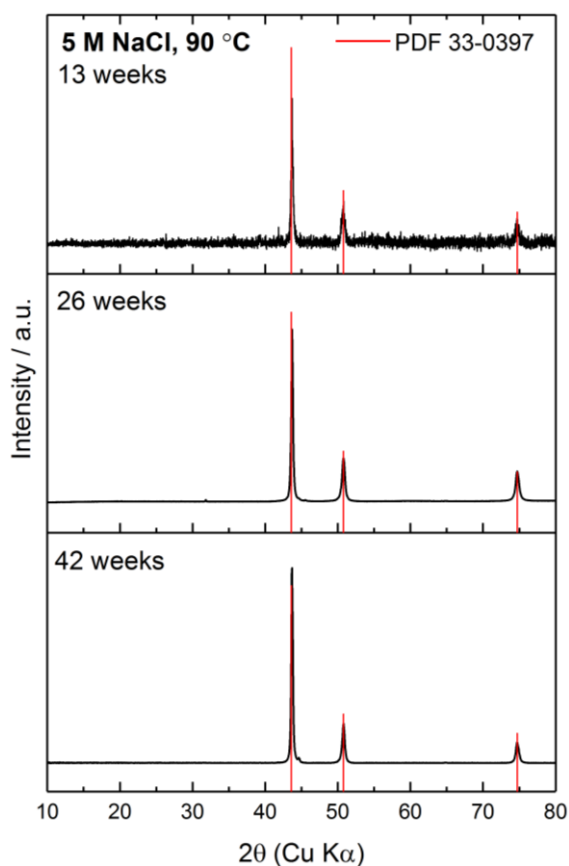


Figure A34: X-ray diffractograms of the Cr-Ni steel corroded in 5 M NaCl for 13 (top), 26 and 42 weeks (bottom). PDF card 33-0397 refers initial non-corroded Cr-Ni steel.

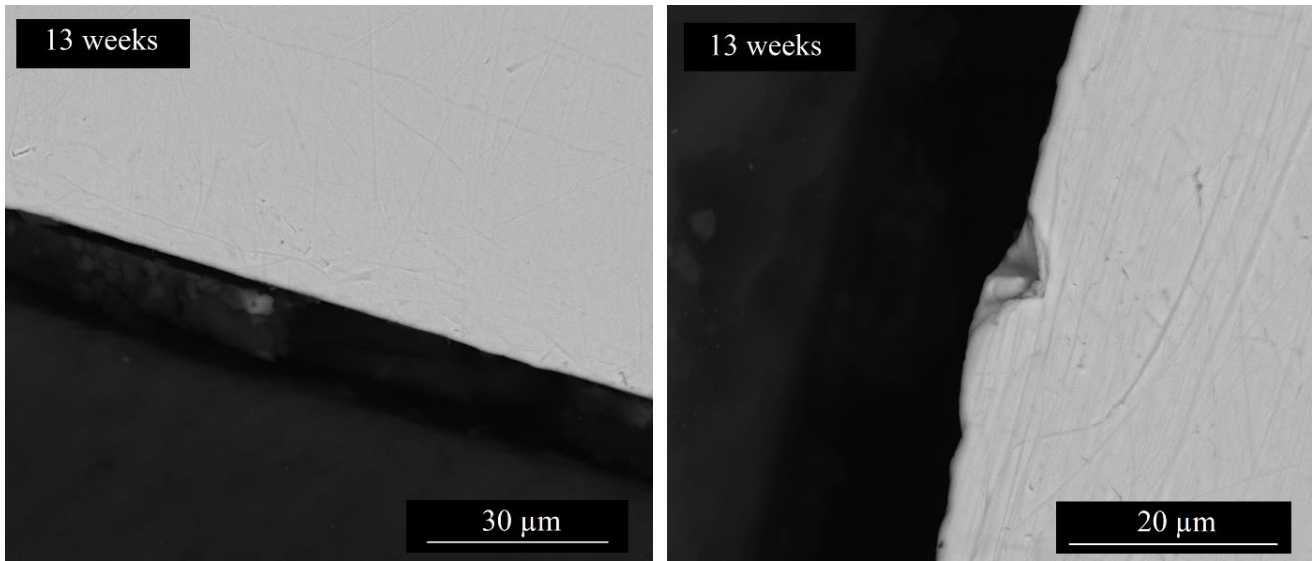


Figure A35: SEM images of the embedded and crosscut Cr-Ni steel corroded in 5 M NaCl for 13 weeks at 90 °C.

The *Figure A35* shows the steel coupon (light) and surrounding resin (black). No corrosion layer and no corrosion damage except of a single shallow hole of about 5 µm, likely detached during cutting, can be observed. This hole was not detected during the surface analysis.

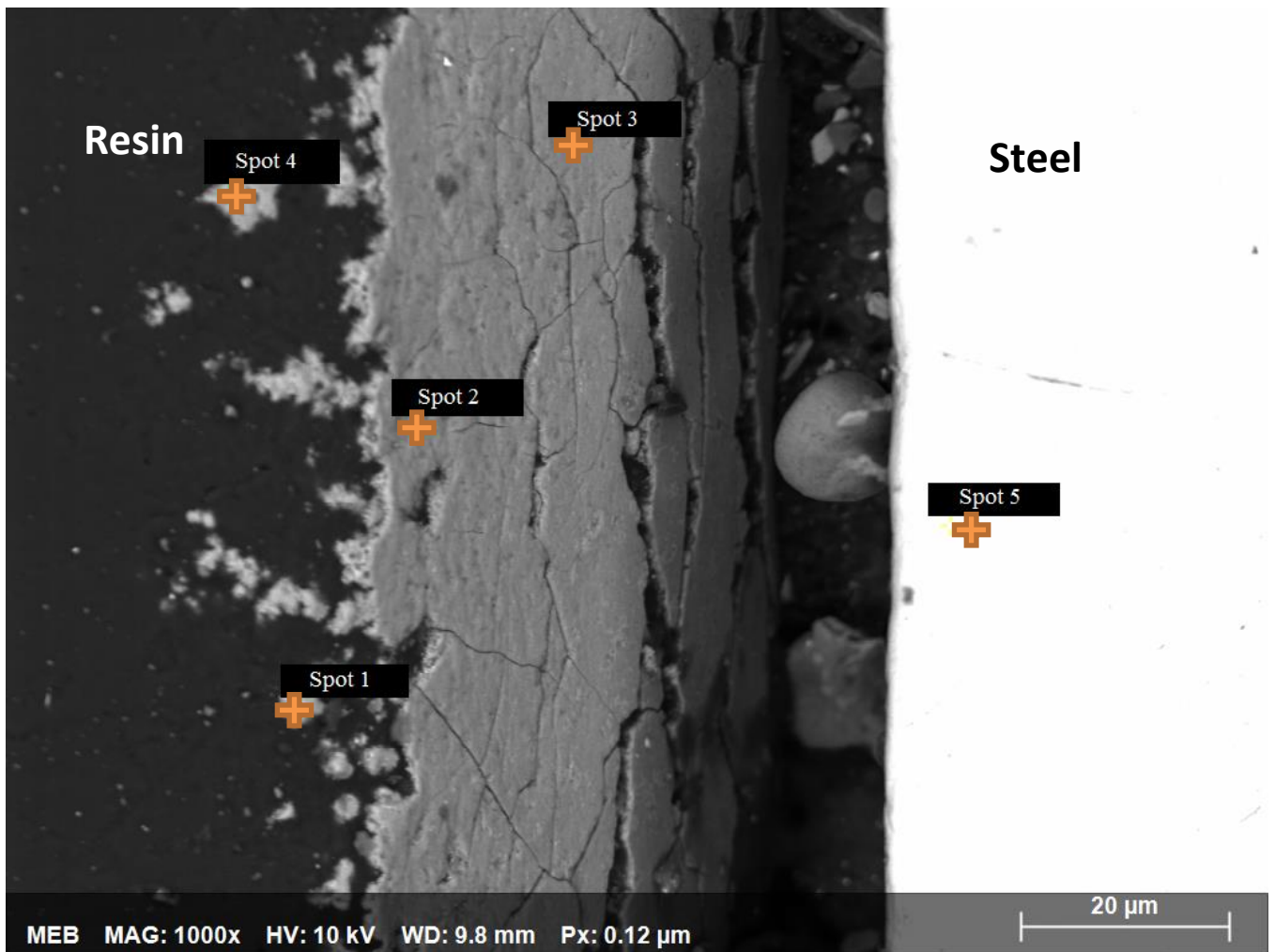


Figure A36: SEM image of the crosscut of the Cr-Ni steel sample corroded in 5 M NaCl for 31 weeks at 90 °C. The detached corrosion layer/passive film can be seen close to resin. The spots shown in the figure correspond to the spots in the *Table A12*.

Table A12: The chemical composition of the phases in the corrosion layer/passive film observed for Cr-Ni steel crosscut corroded in 5 M NaCl.

Element / Atomic %	O	Cr	Fe	Ni
Spot 1	58.10±3.21	28.64±2.44	10.66±1.48	2.58±0.82
Spot 2	3.16±0.88	69.83±3.75	25.53±2.51	1.46±0.80
Spot 3	3.59±0.88	63.51±3.52	28.22±2.44	4.68±0.96
Spot 4	61.22±3.44	22.43±2.12	11.13±1.50	5.19±0.98
Spot 5	3.86±0.91	22.66±2.12	61.18±3.45	12.28±1.80

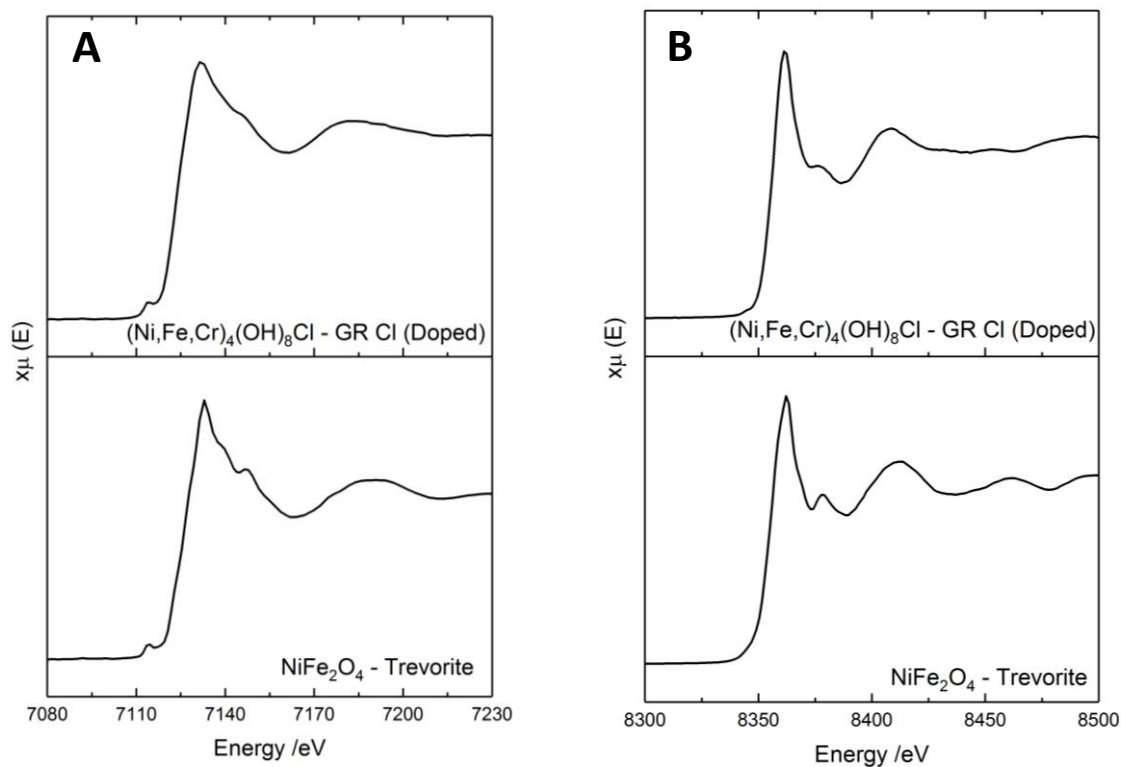


Figure A37: The μ XANES spectra of iron (A) and nickel (B) of the reference compounds used for linear combination fitting of the spectra collected for the Cr-Ni steel crosscut sample corroded in 5 M NaCl brine, examined at the synchrotron.

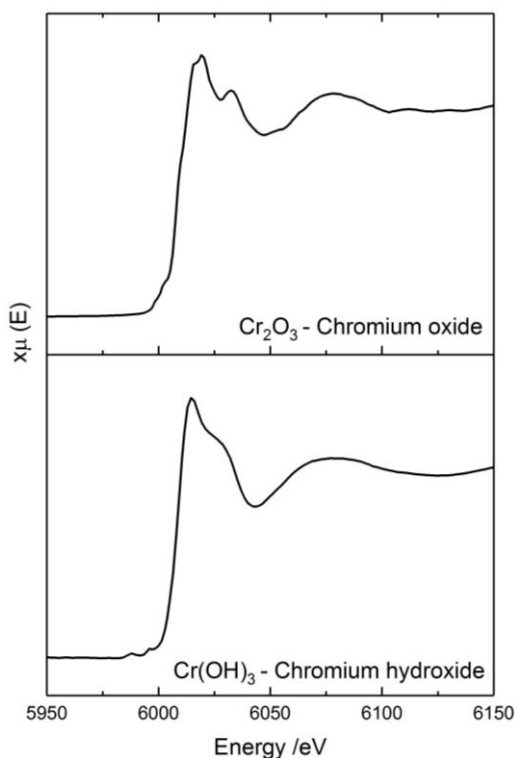


Figure A38: The μ XANES spectra of chromium of the reference compounds used for linear combination fitting of the spectra collected for the Cr-Ni steel crosscut sample corroded in 5 M NaCl brine, examined at the synchrotron.

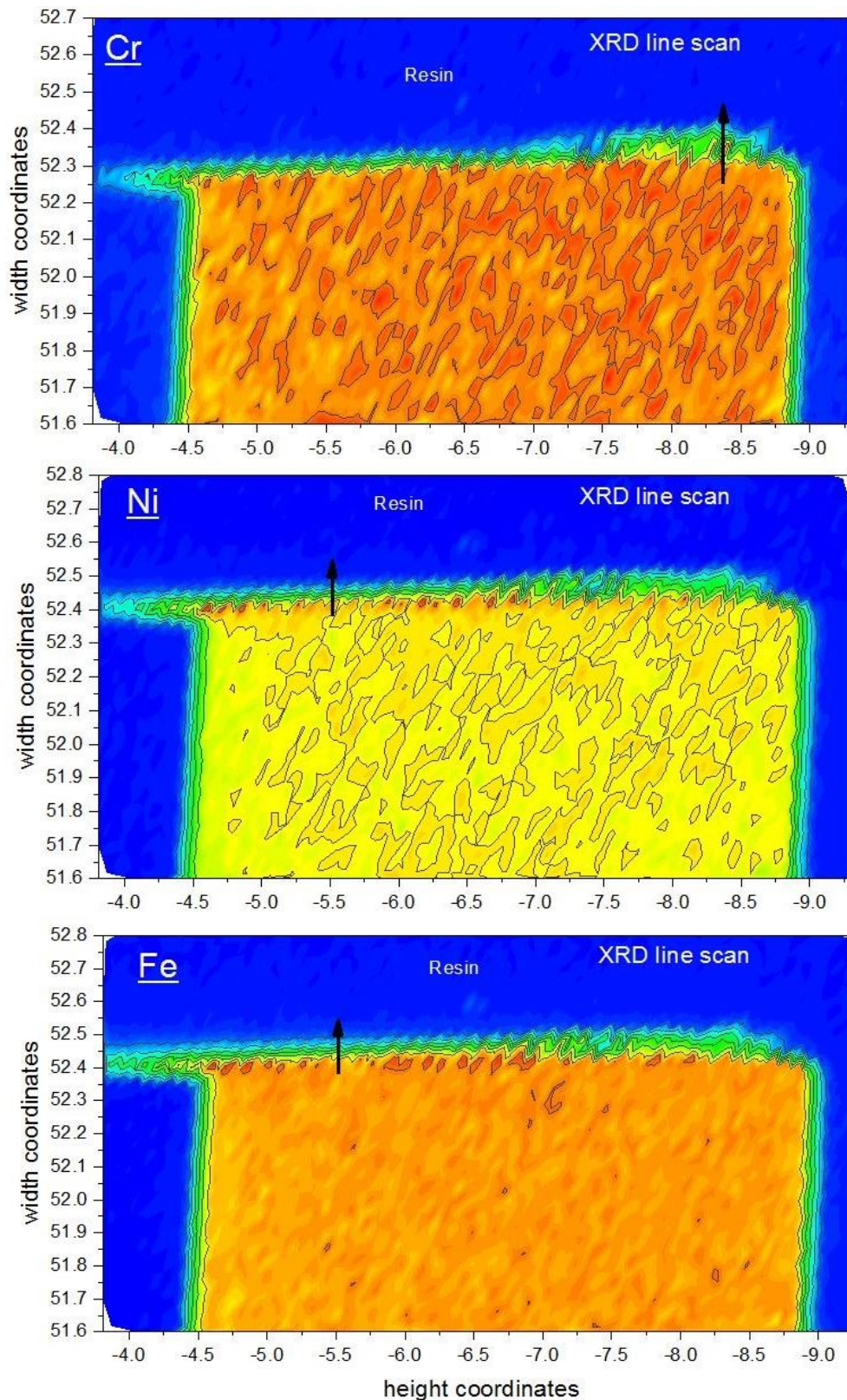


Figure A39: The μ XRF maps of the three elements with the corresponding locations of the μ XRD line scan through the interface steel-corrosion layer-resin of the Cr-Ni steel crosscut sample corroded in 5 M NaCl at 90 °C.

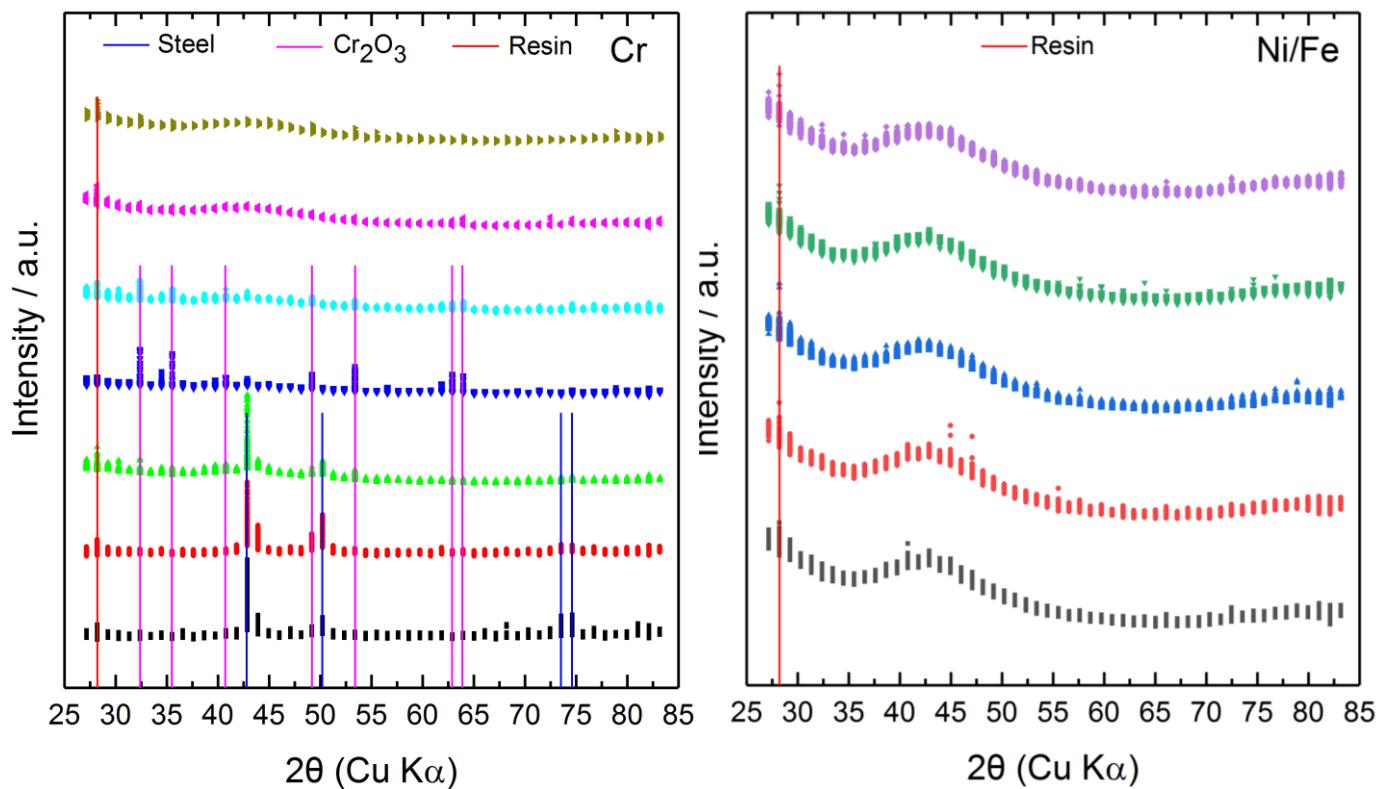


Figure A40: Diffractograms (μ XRD) of the line scan through the interface at different locations shown in *Figure A39*. Step size = 20 μ m.

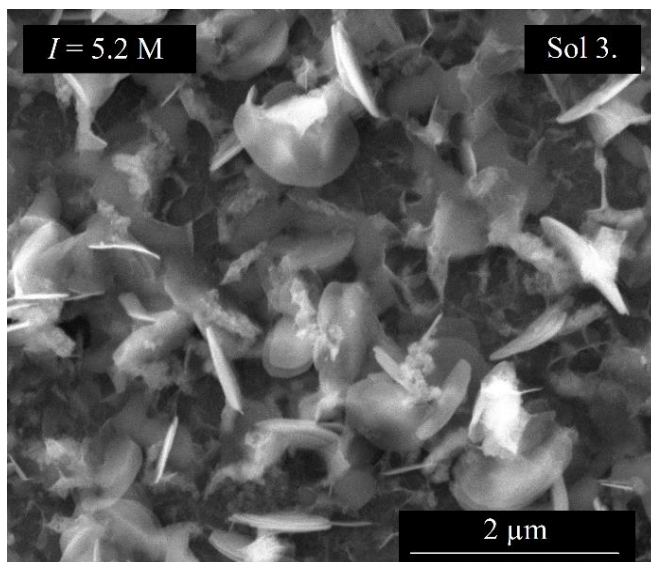


Figure A41: SEM image of the solid phase morphology for solution 3. $T = 90$ $^{\circ}C$ with exposure of 26 weeks.

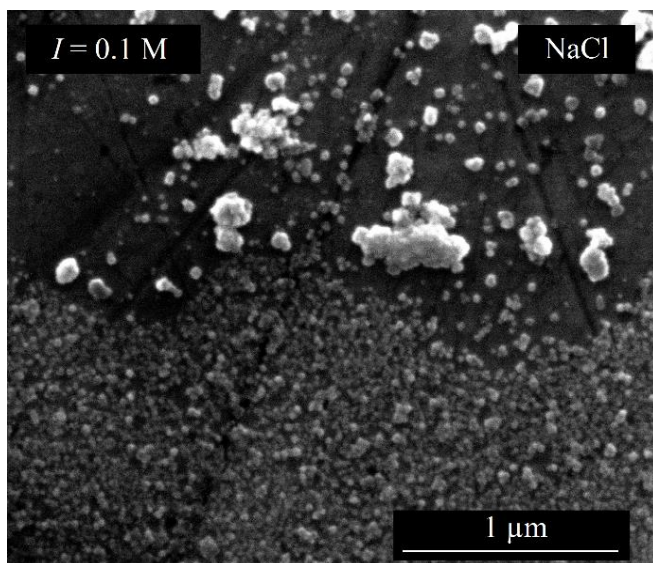


Figure A42: SEM image of the solid phase morphology for $I = 0.1 \text{ M}$ NaCl. $T = 90 \text{ }^\circ\text{C}$ with exposure of 28 weeks.

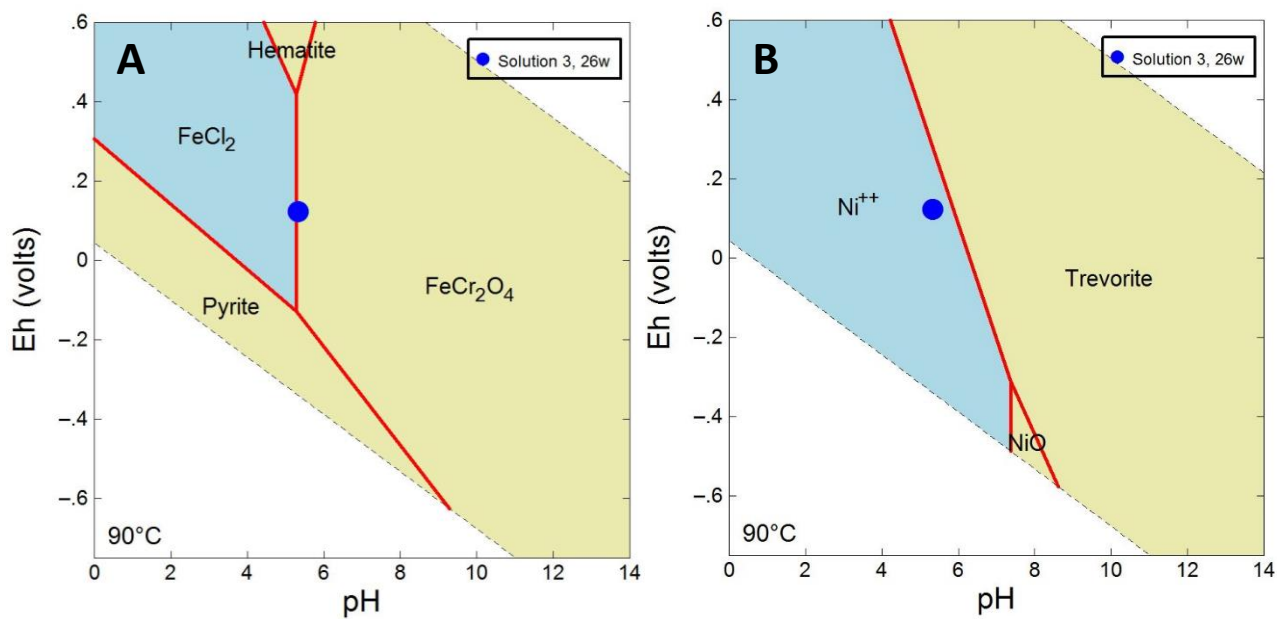


Figure A43: *Pourbaix* diagram for the solution 3 system at $90 \text{ }^\circ\text{C}$ drawn with respect to Fe (A) and with respect to Ni (B) using dissolved amounts after 26 weeks, SIT approach and [TC] database.

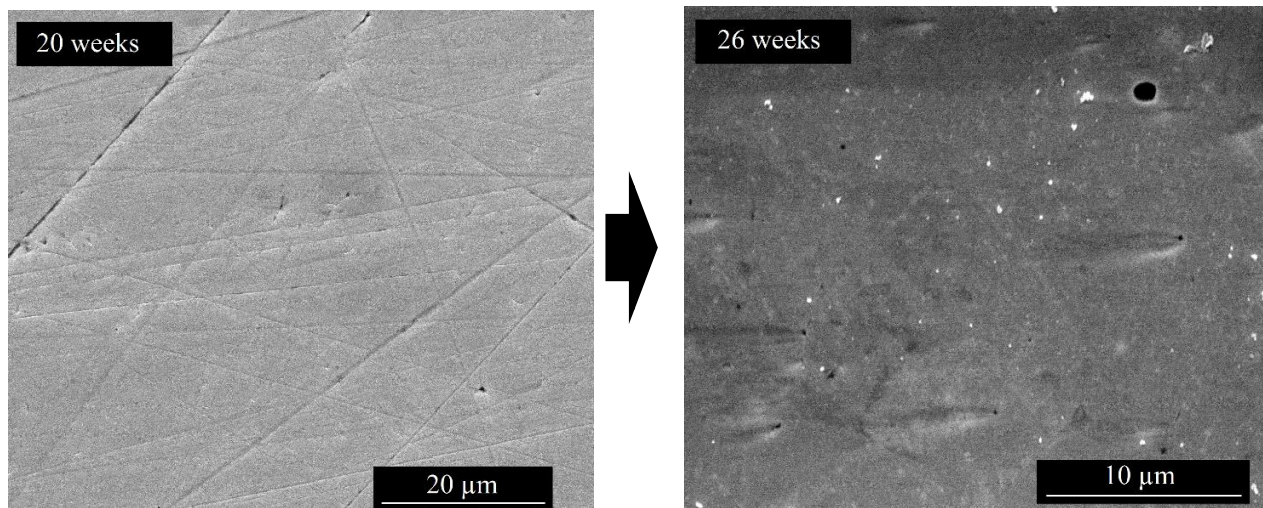


Figure A44: SEM images of the evolution of the solid phase/surface morphology in the solution 3, $I = 5.2$ M from 20 weeks to 26 weeks, $T = 25$ °C.

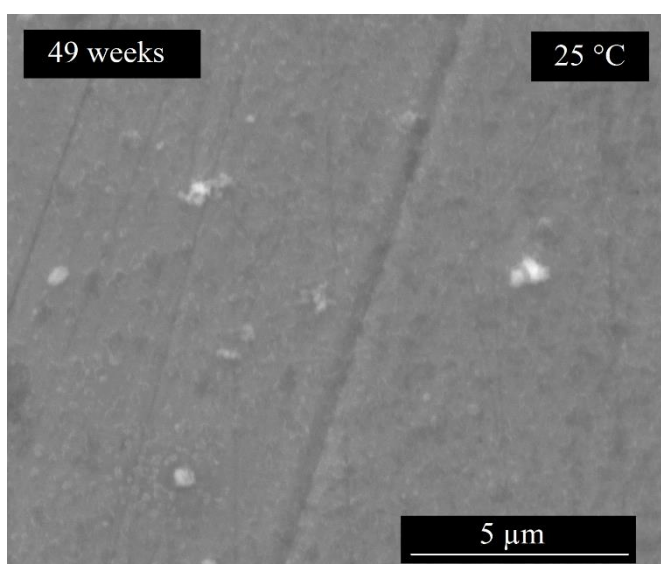


Figure A45: SEM image of the solid phase/surface morphology for 5 M NaCl brine. $T = 25$ °C with exposure of 49 weeks.

The scratches in the images in *Figures A44* and *A45* originate from the polishing of the steel.

Table A13: The chemical composition of the observed phases in solution 3 at 25 °C.

Element / Atomic %	Si	Cr	Mn	Fe	Ni
20 weeks - Overall surface	1.01±0.69	24.27±1.45	1.47±0.8	60.48±2.74	12.77±1.35
26 weeks - Overall surface	0.86±0.18	25.25±0.74	1.16±0.43	61.1±1.46	11.63±1.3
Exposure / Atomic %	S	Na	O		
26 weeks – Snowflake particle	14.88±0.22	33.83±0.53	51.29±0.79		

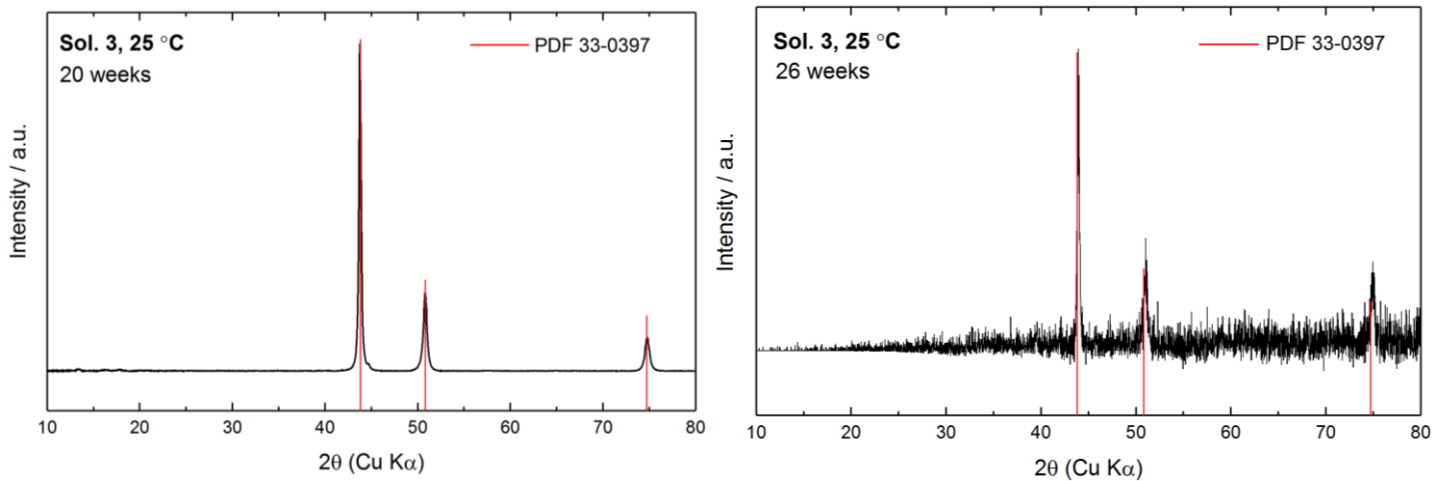


Figure A46: X-ray diffractograms of the Cr-Ni steel corroded in solution 3 ($I = 5.2$ M) for 20 and 26 weeks at 25 °C. PDF card 33-0397 refers non-corroded steel surface.

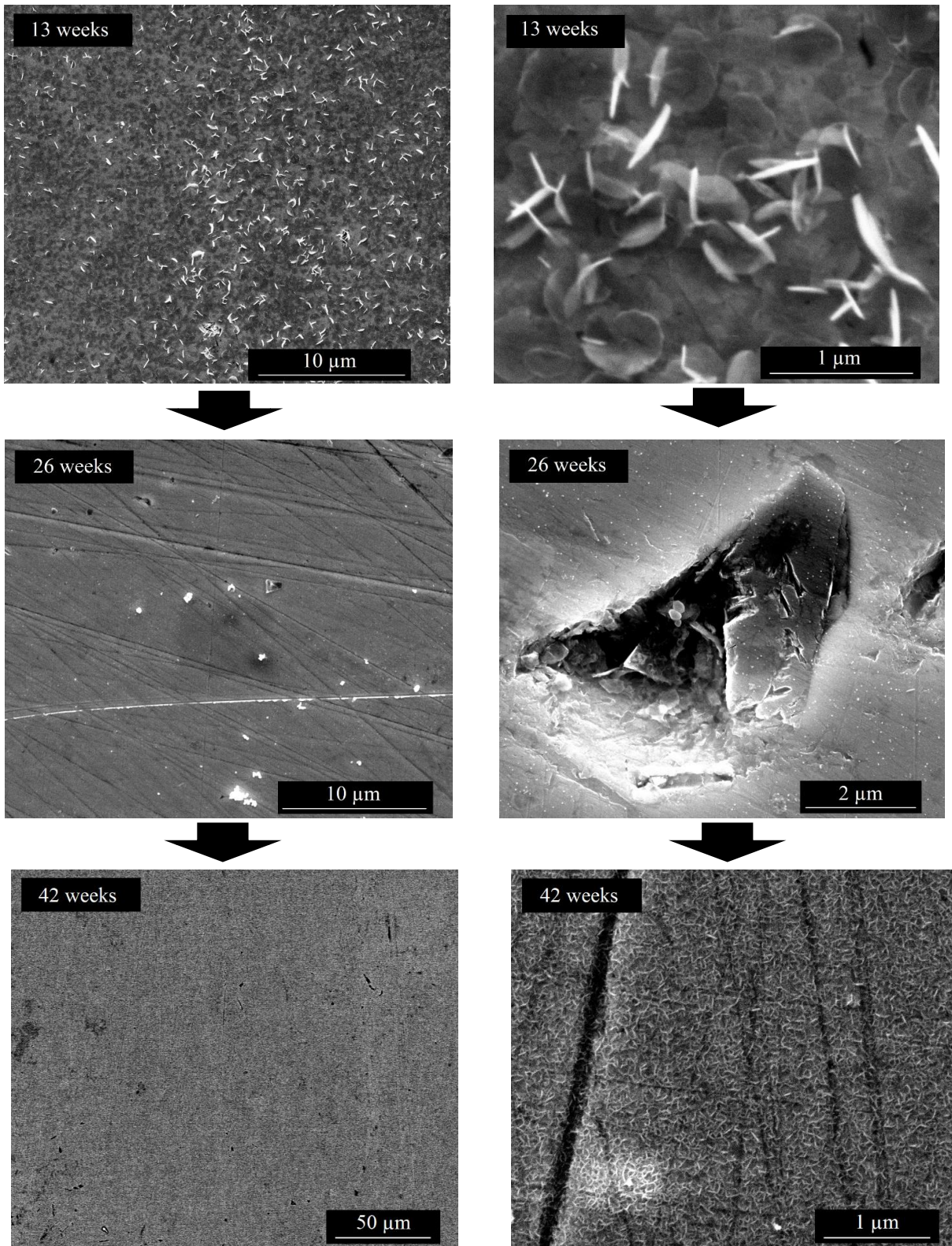


Figure A47: SEM images of the evolution of the solid phase/surface morphology in the 3.4 M ($I = 10.2$ M) MgCl_2 brine from 13 weeks (top) to 42 weeks (bottom), $T = 90$ °C, applying two microscope magnifications.

After 26 weeks, a hole damage of about $2 \mu\text{m} \times 4 \mu\text{m}$ is visible on the surface, which may rather originate from the steel production.

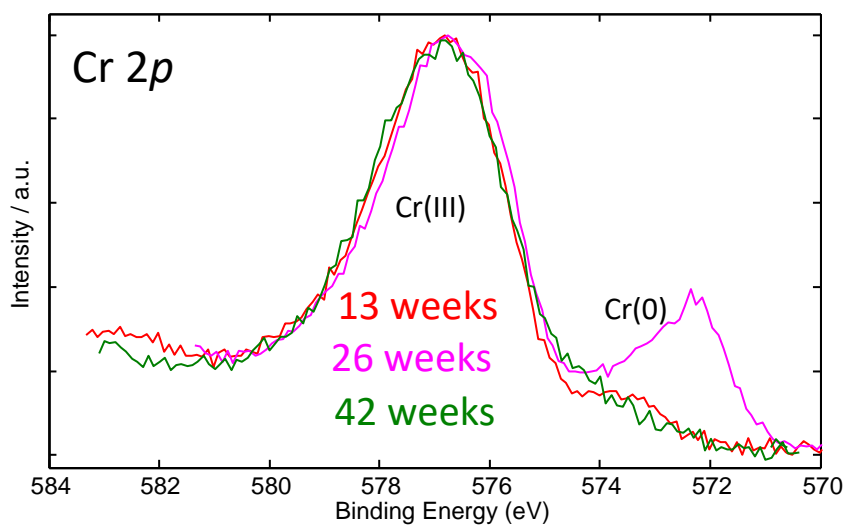


Figure A48: The XPS Cr 2p spectra with respect to time evolution of the corrosion products/surface in 3.4 M MgCl₂ sample.

Table A14: The chemical composition of the surface in the 3.4 M MgCl₂ brine.

Element / Atomic %	Si	Cr	Mn	Fe	Ni
Overall surface - 13 weeks	0.84±0.16	24.63±0.65	1.21±0.37	61.57±1.3	11.75±1.14
Overall surface - 26 weeks	1.02±0.1	25.18±0.23	1.16±0.19	60.93±0.45	11.72±0.28
Overall surface - 42 weeks	0.84±0.18	24.51±0.56	1.23±0.48	61.04±1.62	12.38±1.45

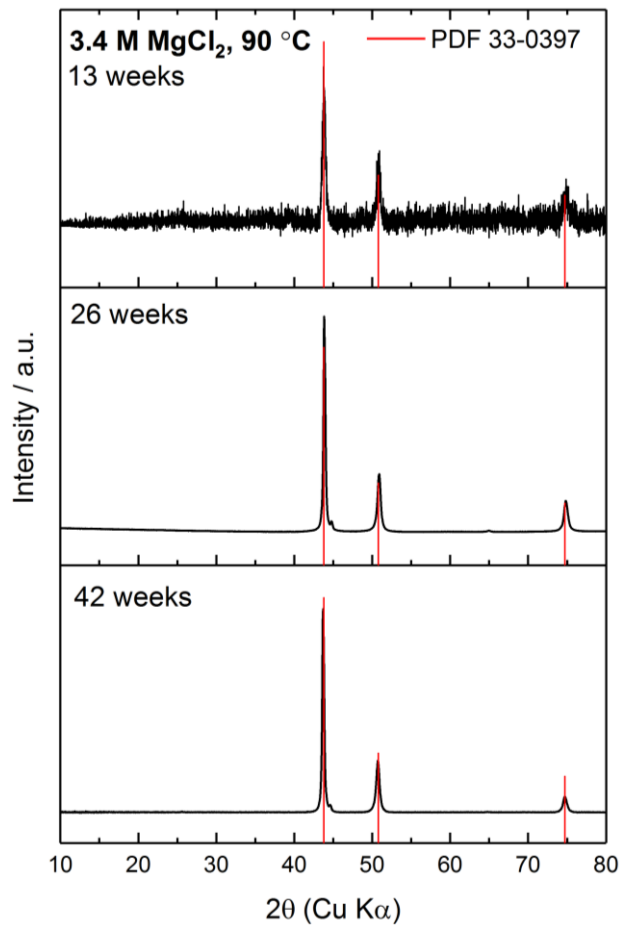


Figure A49: X-ray diffractograms of the Cr-Ni steel corroded in 3.4 M MgCl₂ for 13 (top), 26 and 42 weeks (bottom). PDF card 33-0397 refers initial non-corroded Cr-Ni steel.

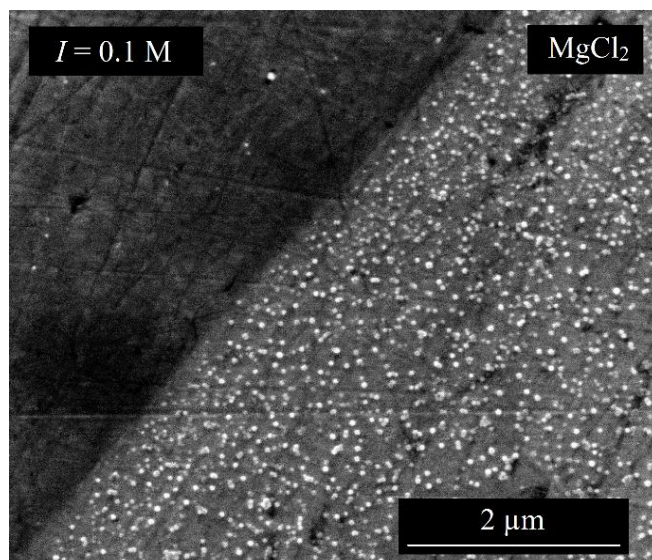


Figure A50: SEM image of the solid phase/surface morphology for $I = 0.1$ M MgCl₂ system, $T = 90$ °C with exposure time of 28 weeks.

The XPS analysis of the dilute solution, 0.033 M MgCl₂ ($I = 0.1$ M MgCl₂) showed the presence of Cr(III) but no narrow Ni and Fe spectra were measured, thus it was not possible to identify the precipitate.

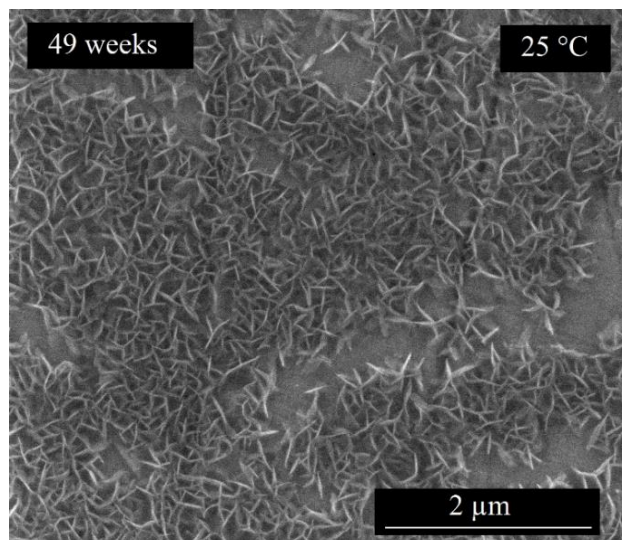


Figure A51: SEM image of the solid phase morphology for $I = 3.4$ M MgCl₂ system, $T = 25$ °C with exposure time of 49 weeks.

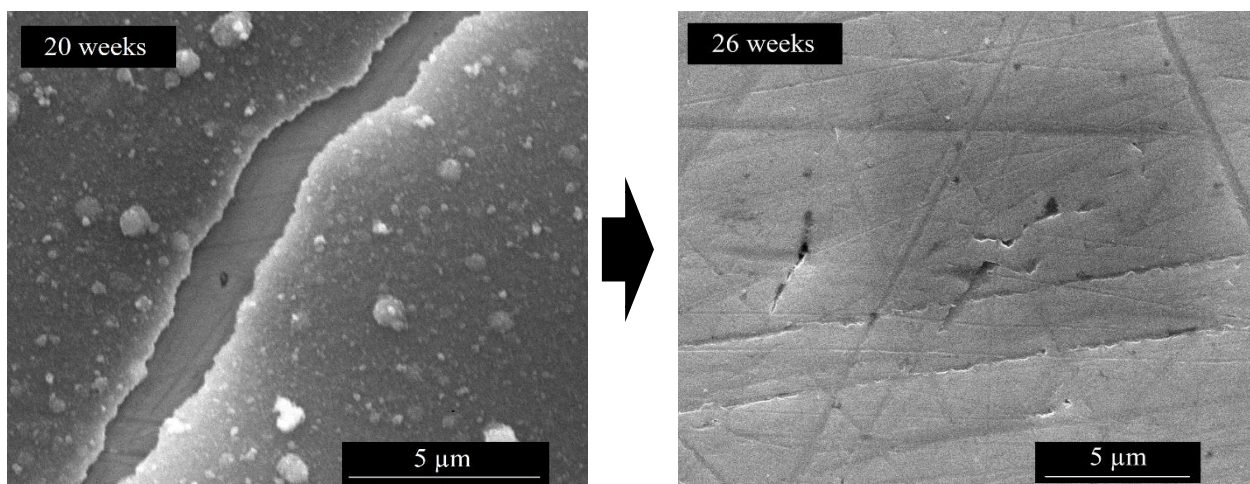


Figure A52: SEM images of the evolution of the solid phase/surface morphology in the solution 1, $I = 11.9$ M system from 20 weeks to 26 weeks, $T = 25$ °C.

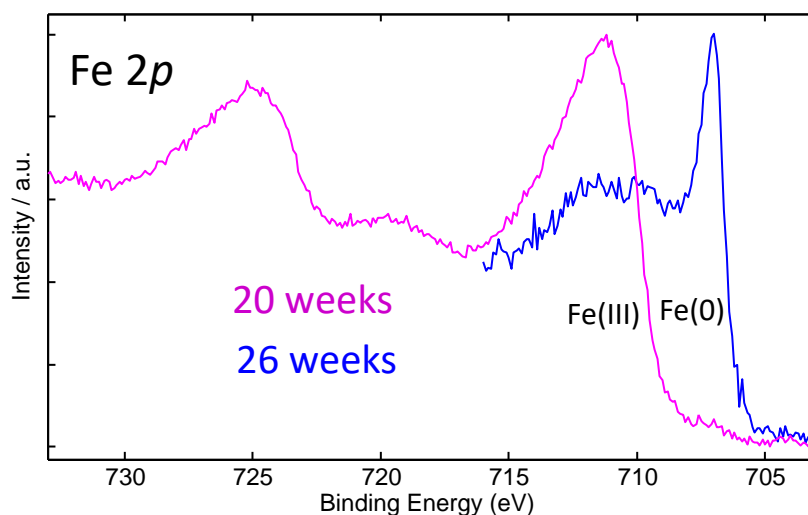


Figure A53: The XPS Fe 2p narrow spectra of the surface/corrosion phase in the solution 1, $I = 11.9$ M system after 20 weeks and 26 weeks, $T = 25$ °C.

Table A15: The chemical composition of the observed phases in solution 1 at 25 °C.

Element / Atomic %	Si	Cr	Mn	Fe	Ni		
20 weeks – Overall surface	0.87±0.68	24.71±1.43	1.32±0.80	61.17±2.75	11.93±2.10		
26 weeks – Overall surface	0.9±0.18	25.62±0.74	1.45±0.43	60.4±1.46	11.62±1.28		
Element / Atomic %	Mg	Cr	Mn	Fe	O	Cl	Ni
20 weeks - Layer	7.64±1.19	18.5±10	0.93±0.54	43.31±1.84	20.53±4.39	1.07±0.53	8.02±1.38

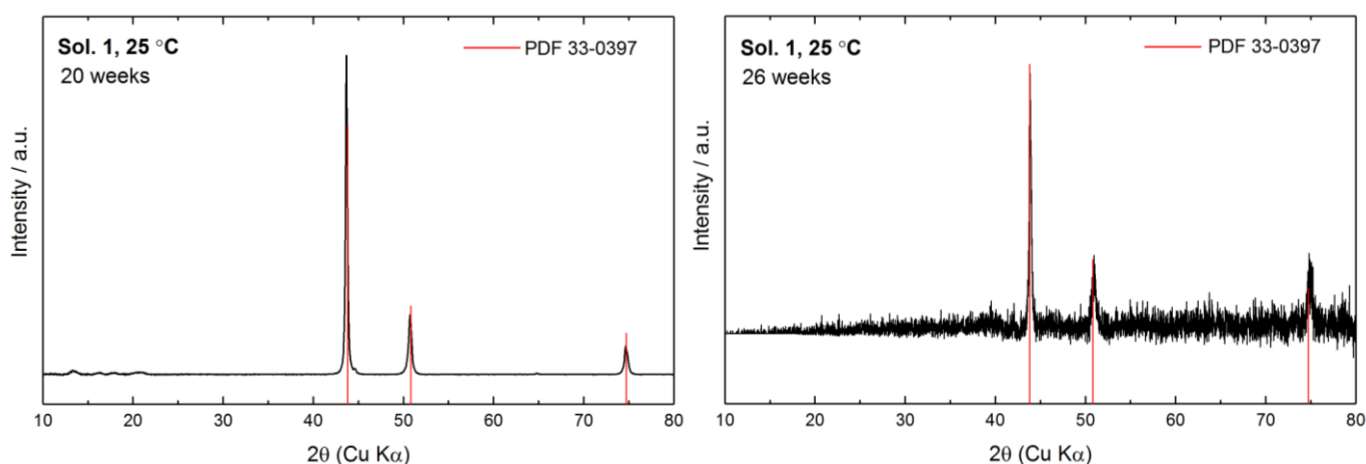


Figure A54: X-ray diffractograms of the Cr-Ni steel corroded in solution 1 ($I = 11.9$ M) for 20 and 26 weeks at 25 °C. PDF card 33-0397 refers to non-corroded steel surface.

The XPS analyses of the overall surface for sample in solution 1 at 25 °C showed the presence of Ni(0) and Cr(III), while the narrow Fe 2p spectra (**Figure A53**) showed the presence of Fe(III) in the crust after 20 weeks and a very weak Fe(III) peak along an Fe(0) peak after 26 weeks. The EDX analyses of the surface (**Table A15**) matches the initial steel composition after 20 and 26 weeks while the analysis of the layer shows the presence of Mg, O and Cl. Fe, Ni and Cr contributions are also found but it is likely from probing the surface below, so the exact composition of this layer cannot be determined. It may be a MgFe₂O₄ compound as Fe(III) is present but not Ni(II).

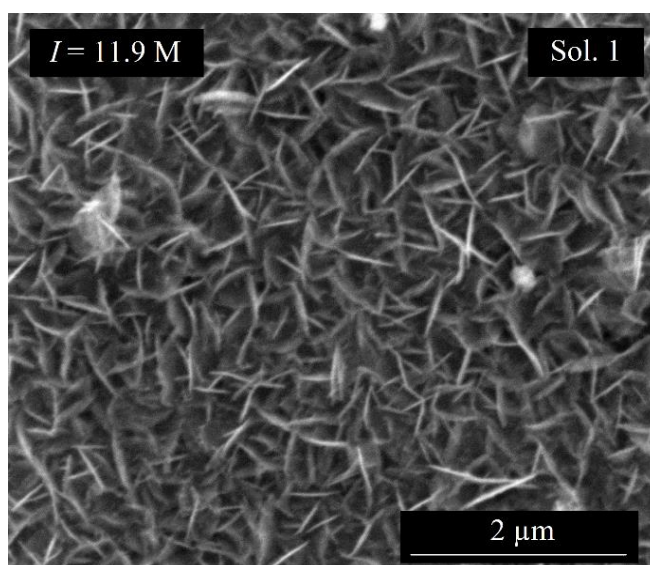


Figure A55: SEM image of the solid phase morphology in the solution 1, $I = 11.9$ M system after 26 weeks, $T = 90$ °C.

Corrosion under flowing conditions (in collaboration with SNL)

The Cr-Ni steel and SGI coupons have been prepared at INE following the same procedure as in our corrosion experiments. The dimensions were different, 5 cm x 5 cm, as requested by SNL to match their setup. The coupons were sent to SNL, USA and briefly repolished upon arrival to remove possible formed corrosion layers. The experiments were configured as a Single-Pass-Flow-Through setup. Three brine compositions were used in the experiments, 5 M NaCl, 3.4 M MgCl₂ and solution 3. The coupons were housed in a 120 mL Savillex Teflon vessel into which corresponding brines were continuously injected at a rate of 60 mL/day. The coupons were set in the holder assembly having contact with brine, which percolated over the sample and was collected at the bottom of the sample tube. The assemblies were contained in a specially designed aluminium casing and heated by a heater to achieve 90±2 °C. The experiments were carried out inside an inert atmosphere (nitrogen) glovebox.

Three different methods were applied on the system to obtain the corrosion rate: ICP-MS on the liquid phase, mass loss and 3-D interferometry on the coupon. Raman spectroscopy was applied to identify the formed corrosion products. The coupons were extracted upon termination of the experiments after 23 weeks of exposure. The leachate was collected, acidified and analysed by ICP-MS. The dissolution rate was then calculated from these results. As some of the dissolved iron is retained on the surface as a corrosion product, the calculated dissolution rate underestimates the true corrosion rate. The coupons were examined for weight loss using the same procedure as in case of our stagnant experiments following the ASTM G1-03 standards [2003]. The corrosion rates for each brine obtained by using the dissolved iron amounts measurements and weight loss technique are summarized in *Table A16*.

As weight loss is not indicative of dissolution in case of pitting corrosion, which may be the case particularly for Cr-Ni steels, a white light interferometry technique was applied on coupons, which can measure minute vertical distances. The strategy of this technique consists of application of silicone sealant to certain parts of the surface, which preserves the reference (initial) surface. After removal of the corrosion products from the coupon, the height difference between the reference and the reacted surface is proportional to the dissolution rate. The detection limit for the height difference is 20 nm. This is directly comparable to the corrosion rate obtained by weight loss or by dissolved iron measurements.

The interferometric measurement on the non-corroded surface revealed small height differences of 34 nm maximum. The *Figure A56* shows the 3-D interferometric images of the SGI corroded in 5 M

NaCl (A) and in solution 3 (B), while **Figure A57** shows the image of SGI corroded in 3.4 M MgCl₂. The interferometric images of the Cr-Ni steel showed little evidence of surface roughening and an absence of pitting. The corrosion products were scraped of the SGI coupon and placed in an anoxic sample holder for Raman spectroscopy measurements. The Cr-Ni steel had no corrosion products thus Raman analysis could not be performed on these samples.

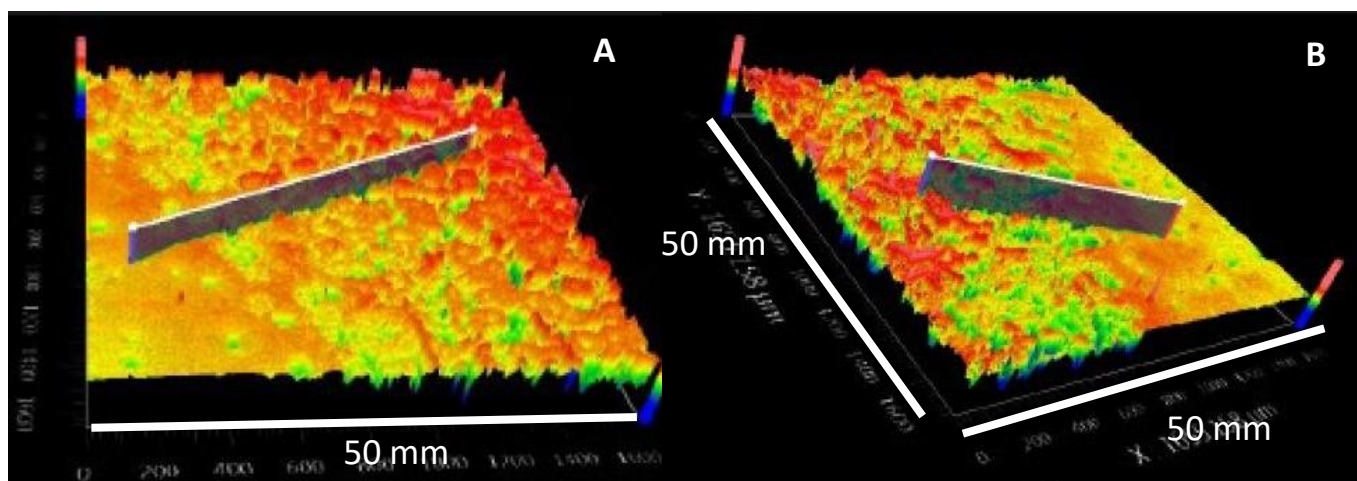


Figure A56: The 3-D interferometric image of SGI coupon after exposure to 5 M NaCl (A) and solution 3 (B) for 23 weeks.

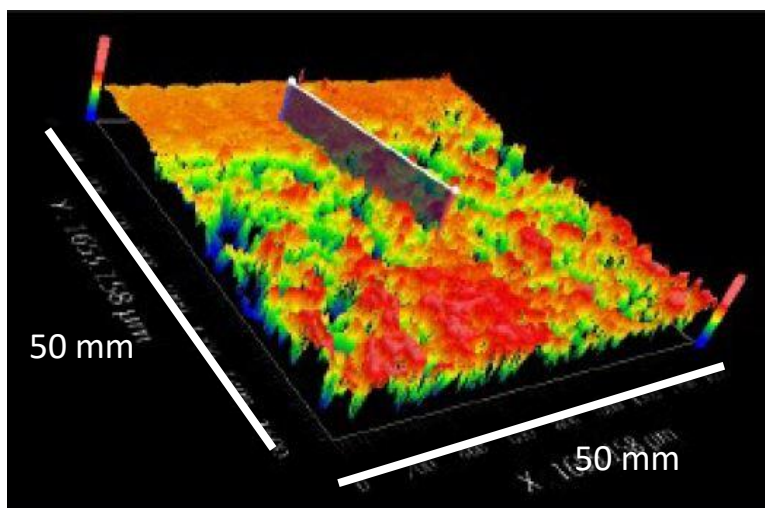


Figure A57: The 3-D interferometric image of SGI coupon after exposure to 3.4 M MgCl₂ for 23 weeks. The Raman spectra showed the presence of magnetite for SGI in 5 M NaCl, matching outcomes to our stagnant condition experiments. Interestingly, the Raman spectra of the SGI in solution 3 showed the presence of iron hydroxychloride, while SGI corroded in 3.4 M MgCl₂ showed the presence of green rust chloride. We have observed the formation of iron hydroxychloride in MgCl₂ brine, but under flowing conditions (or upon increase in redox potential), it seems to oxidize to green rust chloride. No

presence of iron silicate compounds was observed. This is likely due to a lack of saturation in the solution under flowing conditions. This may also explain the presence of iron hydroxychloride in solution 3, where we have identified cronstedtite.

The obtained corrosion rates for all techniques and the average corrosion rates are shown in **Table A16**.

Table A16: Corrosion rates (CR) obtained using various methods for both steels.				
Method / CR in $\mu\text{m/a}$	Dissolved iron	Weight loss	3-D interferometry	Average CR
SGI - 5 M NaCl	0.10 \pm 0.14	2.00 \pm 0.26	5.42 \pm 1.22	2.51 \pm 0.54
SGI - 3.4 M MgCl₂	14.98 \pm 6.69	7.90 \pm 0.62	10.13 \pm 2.29	11.0 \pm 3.2
SGI - Sol. 3	0.43 \pm 0.64	3.51 \pm 0.29	5.00 \pm 0.85	2.98 \pm 0.59
Cr-Ni steel - 5 M NaCl	0.05 \pm 0.04	0.2 \pm 0.1	0.17 \pm 0.16	0.14 \pm 0.10
Cr-Ni steel - 3.4 M MgCl₂	0.09 \pm 0.07	0.51 \pm 0.11	0.31 \pm 0.48	0.3 \pm 0.22
Cr-Ni steel - Sol. 3	0.11 \pm 0.23	0.82 \pm 0.12	0.08 \pm 0.04	0.34 \pm 0.13

Overall, this study has found that MgCl₂ is more corrosive medium for SGI, with corrosion rates 4 times higher than in NaCl medium. A similar corrosion rate was found for SGI in NaCl medium in the presence and in the absence of sulfate. For the Cr-Ni steel, the corrosion rates are very low, independent of the brine composition.

Considering our stagnant condition experiments, we have observed a lower corrosion rate for SGI in 5 M NaCl (1.01 \pm 0.05 $\mu\text{m/a}$), but 2 times higher corrosion rate for SGI corroded in 3.4 M MgCl₂ (23.13 \pm 1.5 $\mu\text{m/a}$) and 3 times higher corrosion rate for SGI in solution 3 (9.61 \pm 1.0 $\mu\text{m/a}$) compared to flowing conditions.

Sorption studies

Solubility and speciation of europium and americium in dilute to concentrated NaCl and MgCl₂ solutions

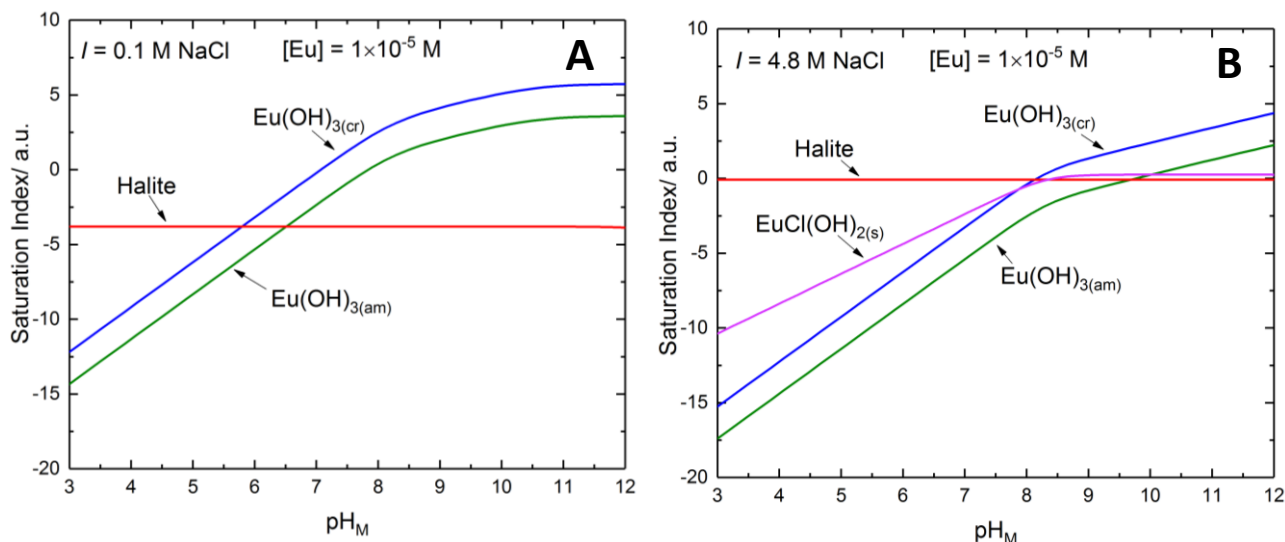


Figure A58: Saturation indices of europium solid phases vs. pH_M calculated using the SIT approach and [TC] database. $I = 0.1 \text{ M NaCl}$ (A) and $I = 4.8 \text{ M NaCl}$ (B), $[\text{Eu}] = 1 \times 10^{-5} \text{ M}$.

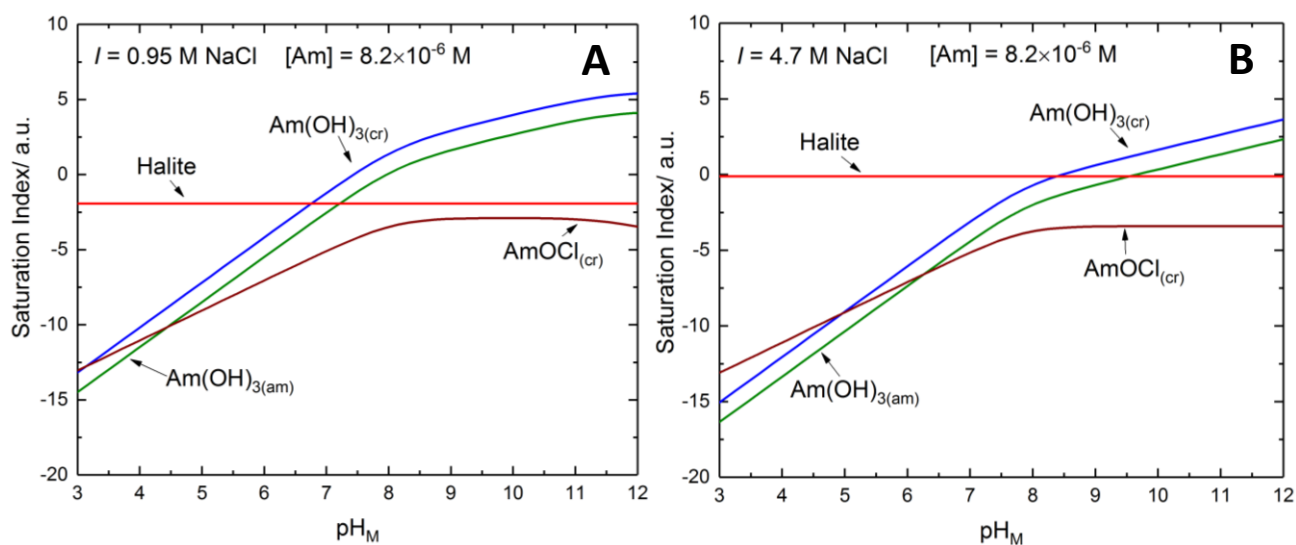


Figure A59: Saturation indices of americium solid phases vs. pH_M calculated using SIT approach and [TC] database. $I = 0.95 \text{ M NaCl}$ (A) and $I = 4.7 \text{ M NaCl}$ (B), $[\text{Am}] = 8.2 \times 10^{-6} \text{ M}$.

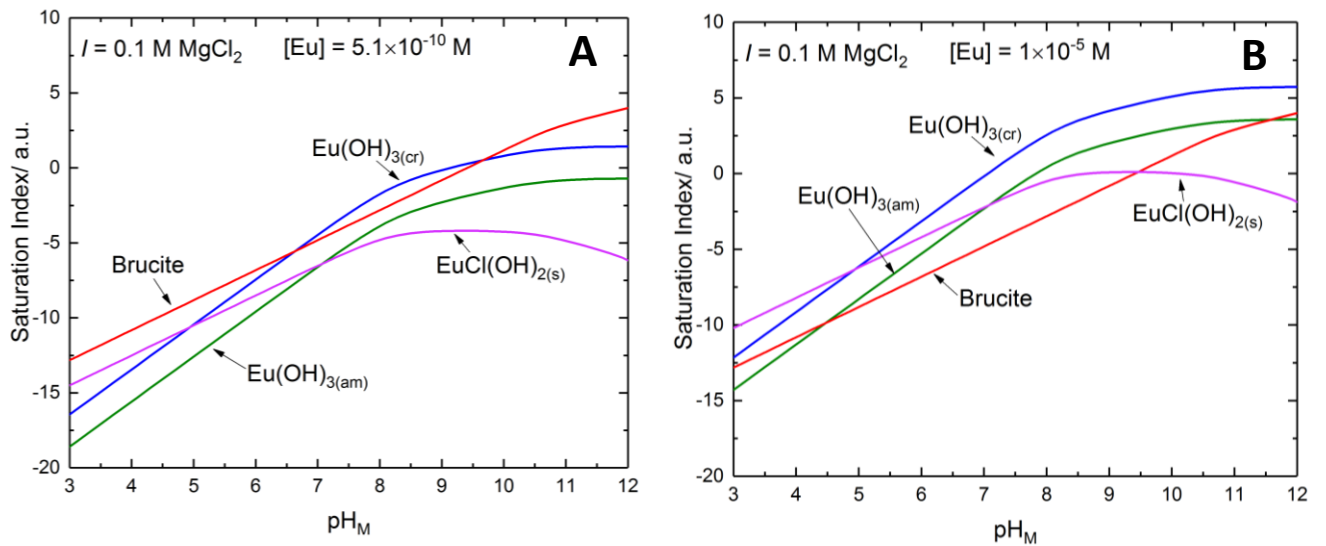


Figure A60: Saturation indices of europium solid phases vs. pH_M at $I = 0.1 \text{ M MgCl}_2$ for $[\text{Eu}] = 5.1 \times 10^{-10} \text{ M}$ (A) and $[\text{Eu}] = 1 \times 10^{-5} \text{ M}$ (B) calculated with SIT approach and [TC] database.

Uptake of europium/americium by magnetite

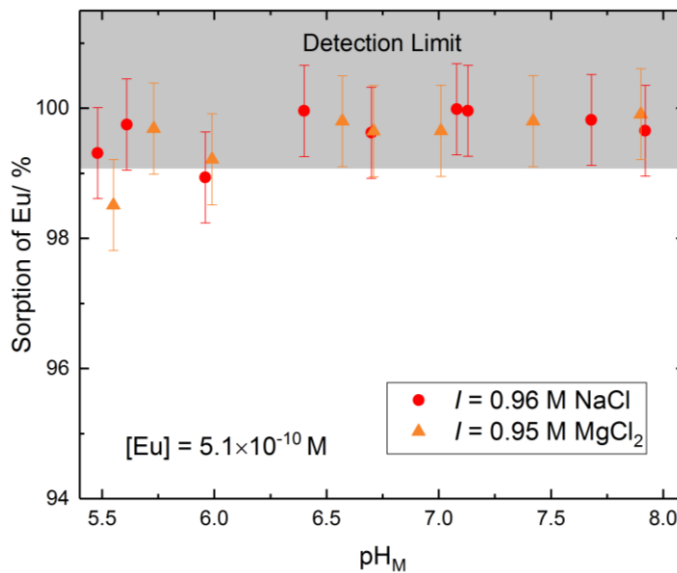


Figure A61: Sorption of europium $[\text{Eu}] = 5.1 \times 10^{-10} \text{ M}$ as percentage uptake on magnetite (0.5 g/L) as a function of pH_M and at ionic strengths of 0.96 M NaCl and 0.95 M MgCl_2 .